

*In situ* SABRE Polarisation of  $^1\text{H}$  and  $^{19}\text{F}$   
Nuclei with Earth's Field NMR Detection

Matheus Rossetto

PhD

University of York

Chemistry

September 2022



# Abstract

Demonstrated in this thesis is a route to directly explore ultra-low-field (ULF) polarisation transfer within Signal Amplification by Reversible Exchange (SABRE) without the need for a sample transfer step. Integration of an Earth's Field NMR (EFNMR) instrument that operates in the same field regime as SABRE polarisation transfer, with external solenoids and an automated  $p$ -H<sub>2</sub> gas flow system allows SABRE polarisation transfer to occur *in situ* of the detector. The rapid acquisition of SABRE-polarised NMR signals under the strong coupling conditions required for polarisation transfer offers a way to directly probe the transfer mechanism, thus providing a route toward maximising the efficiency of SABRE for different nuclei. A reproducible flow of  $p$ -H<sub>2</sub> into the EFNMR probe, combined with precise control over the timing and strength of the external field during SABRE polarisation transfer and NMR detection led to the acquisition of reproducible hyperpolarisation on the <sup>1</sup>H and <sup>19</sup>F nuclei of different fluorinated pyridine derivatives. Of the four different substrates, 3,5-difluoropyridine and 3-difluoromethylpyridine proved suitable candidates for interrogating the magnetic field dependence of SABRE polarisation transfer via ULF-cycling experiments, owing to their large heteronuclear  $J$ -coupling interactions of 9 and 55.4 Hz, respectively, that form hyperpolarised EFNMR signals with fine structure and minimal peak overlap. This was necessary to observe subtle changes to the signal shape under varying polarisation transfer conditions, where strong coupling and the collapse of chemical shift in the ULF regime led to the formation of complex NMR signals. The very strong coupling network of 3-difluoromethylpyridine exhibited polarisation transfer mechanics that differed from what was observed with the other more weakly coupled substrates. Numerical simulations were also employed to aid in interpreting the complex EFNMR spectra.



# Contents

<b>List of Figures</b>	<b>6</b>
<b>List of Tables</b>	<b>18</b>
<b>1 Introduction</b>	<b>21</b>
<b>2 Background Theory</b>	<b>29</b>
2.1 NMR Fundamentals . . . . .	29
2.1.1 Nuclei in a Magnetic Field . . . . .	29
2.1.2 NMR Relaxation . . . . .	33
2.2 NMR in the Ultra-Low-Field Regime . . . . .	36
2.2.1 Sensitivity . . . . .	36
2.2.2 Strong Coupling . . . . .	37
2.3 <i>Para</i> -Hydrogen . . . . .	39
2.4 Signal Amplification By Reversible Exchange . . . . .	42
<b>3 Earth's Field NMR System</b>	<b>48</b>
3.1 Introduction . . . . .	48
3.2 Terranova-MRI System . . . . .	49
3.2.1 Standard Operation and Procedures . . . . .	49
3.2.2 Probe Setup . . . . .	53
3.3 Improvements to Earth's Field NMR Instrument . . . . .	55
3.3.1 Alignment of Spin and Lab Frames of Reference . . . . .	55
3.3.2 Control of External Field . . . . .	57
3.3.3 Pulse Calibration . . . . .	60
3.3.4 Simultaneous Excitation of Different Nuclei . . . . .	65
3.4 Conclusion . . . . .	69
<b>4 <i>In situ</i> SABRE with Earth's Field NMR Detection</b>	<b>71</b>
4.1 Introduction . . . . .	71
4.2 Automated Gas Flow System . . . . .	73
4.2.1 Parahydrogen Generator . . . . .	73
4.2.2 Polariser Control Unit . . . . .	77
4.3 Monitoring Parahydrogen Flow and Diagnosing Problems . . . . .	80
4.3.1 Method . . . . .	80
4.3.2 Recovery of Parahydrogen Pressure . . . . .	84
4.3.3 Optimising the Parahydrogen Pressure Differential . . . . .	86
4.3.4 Blockage and Leak Tests . . . . .	87
4.4 Conclusion . . . . .	90

<b>5</b>	<b><i>In situ</i> SABRE Polarisation of Fluoropyridines</b>	<b>92</b>
5.1	Introduction . . . . .	92
5.2	SABRE-EFNMR Experiment . . . . .	95
5.3	SABRE Polarisation Transfer using Millitesla PTFs . . . . .	99
5.3.1	<i>In situ</i> SABRE Polarisation of 3-fluoropyridine . . . . .	99
5.3.2	SABRE-Polarised Solvent . . . . .	107
5.3.3	<i>In situ</i> SABRE Polarisation of 3,5-difluoropyridine . . . . .	109
5.3.4	<i>In situ</i> SABRE Polarisation of 3,5-bis(trifluoromethyl) pyridine . . . . .	114
5.3.5	<i>In situ</i> SABRE Polarisation of 3-difluoromethylpyridine . . . . .	116
5.3.6	Conclusion . . . . .	120
<b>6</b>	<b>Probing SABRE Polarisation Transfer with <i>in situ</i> EFNMR Detection</b>	<b>123</b>
6.1	Introduction . . . . .	123
6.2	SABRE Polarisation Transfer to 3,5-difluoropyridine . . . . .	124
6.2.1	Millitesla Polarisation Transfer Field Cycling . . . . .	124
6.2.2	<i>In situ</i> SABRE Polarisation Transfer using Microtesla Polarisation Transfer Fields . . . . .	127
6.2.3	Microtesla Polarisation Transfer Field Cycling . . . . .	130
6.3	SABRE Polarisation Transfer to 3-difluoromethylpyridine . . . . .	134
6.3.1	<i>In situ</i> SABRE Polarisation Transfer using Microtesla Polarisation Transfer Fields . . . . .	134
6.3.2	Microtesla Polarisation Transfer Field Cycling . . . . .	136
6.4	Conclusions . . . . .	137
<b>7</b>	<b><i>sel</i>-SHARPER on a Benchtop NMR System</b>	<b>139</b>
7.1	Introduction . . . . .	139
7.2	Selective Pulse Design . . . . .	142
7.2.1	Gaussian RF Pulse . . . . .	142
7.2.2	Synthesis of Gaussian RF Pulse . . . . .	145
7.2.3	Calibration of Gaussian Refocusing Pulse . . . . .	149
7.2.4	Selective Excitation of Fluorine . . . . .	152
7.3	<i>sel</i> -SHARPER of Fluoropyridines . . . . .	153
7.4	Conclusion and Future Work . . . . .	158
<b>8</b>	<b>Conclusions and Future Work</b>	<b>160</b>
<b>9</b>	<b>Experimental Details</b>	<b>166</b>
9.1	Sample Preparation . . . . .	166
9.2	Hyperpolarised EFNMR Data Acquisition . . . . .	166
9.3	EFNMR Data Processing . . . . .	167
9.4	Benchtop NMR Data Acquisition and Processing . . . . .	168
9.5	NMR Simulations . . . . .	168
	<b>List of Abbreviations</b>	<b>171</b>

# List of Figures

1.1	Illustration of a) hyperpolarisation of a heteronucleus X on a target molecule using PHIP and b) hyperpolarisation of nuclei on a target substrate using SABRE. The red and blue circles represent hyperpolarised and thermally polarised nuclei and molecules, respectively. . . . .	23
2.1	Illustration of nuclear Zeeman splitting in nuclei with different spin. . .	29
2.2	Nuclear Zeeman splitting of a single spin-1/2 nucleus inside of a magnetic field, $B^0$ . . . . .	30
2.3	The $T_1$ relaxation process causes the build-up of longitudinal magnetisation ( $M_z$ ) in a sample after it is exposed to a magnetic field $B^0$ . . . .	34
2.4	Plot of the x and y-components of the transverse magnetisation as a function of time, where the exponential damping of both traces is caused by $T_2$ relaxation. . . . .	35
2.5	The linewidth at half-height of an NMR signal is controlled by $T_2$ relaxation. . . . .	35
2.6	Illustration of the a) high-field $AX_2$ and b) EFNMR $AB_2$ spectrum of a $\text{CHF}_2$ functional group. The high-field $^{19}\text{F}$ and $^1\text{H}$ spectra show a doublet and triplet at their corresponding chemical shifts of $\omega_F^0$ and $\omega_H^0$ , respectively. The EFNMR spectrum shows four $^{19}\text{F}$ and $^1\text{H}$ peaks at their corresponding Larmor frequencies of $\nu_F$ and $\nu_H$ that are separated by around $\sim 130$ Hz at $\sim 50$ $\mu\text{T}$ . . . . .	39
2.7	Energy level diagram of $\text{H}_2$ when considering the spin state energies coupled to the rotational state energies (not drawn to scale). The ground state rotational level ( $J=0$ ) corresponds to the <i>para</i> -state and the second rotational level ( $J=1$ ) corresponds to the <i>ortho</i> -state. . . .	40
2.8	Temperature dependence of the percentage population of <i>p</i> - $\text{H}_2$ . The graph was plotted using $\theta_R = 87.57$ K (calculated from Eq. 2.33). . . . .	41
2.9	Illustration comparing the population dispersion across a thermally polarised and hyperpolarised nuclear spin system. The red spheres correspond to the NMR visible nuclei that contribute to the magnetic moment of the sample, $\mathbf{\mu}_{\text{sample}}$ . . . . .	42
2.10	SABRE catalytic cycle for the production of hyperpolarised substrate in solution using the Ir-IMes pre-catalyst. Reversible binding of $\text{H}_2$ and the substrate (Sub) is necessary to drive the catalytic reaction, and weak magnetic fields are required to drive SABRE polarisation transfer to the catalyst bound substrate molecules. Blue font denotes hyperpolarised atoms or molecules. . . . .	43

2.11	Illustration of the formation of an LAC between two strongly coupled nuclear spin states $ m\rangle$ (blue) and $ n\rangle$ (red) to allow coherent polarisation transfer between them. The strong coupling constant $J$ leads to an avoided crossing between the two states. . . . .	45
3.1	The Terranova-MRI probe (left) consists of 3 components (right): the polarising coil for polarisation of the sample before detection, the transmit-receive coil ( $B^1$ coil) for RF pulsing and NMR detection, and the gradient coils for shimming the probe to reduce local magnetic field inhomogeneities. . . . .	49
3.2	A schematic demonstrating the alignment and strength of the net magnetisation of the sample, $M^0$ , during the pre-polarising step, where a current is applied through the polarising coil to generate a magnetic field along the $x'$ -axis. The current is turned off adiabatically to maintain the hyperpolarisation of the spin system as the spins relax in the presence of the Earth's magnetic field. This figure has been adapted from a figure in the Terranova-MRI manual. <sup>1</sup> . . . . .	50
3.3	The simplest EFNMR experiment consisting of a pre-polarising pulse generated using the polarising coil, followed by a $\pi/2$ rad nutation of the spins and subsequent detection of their transverse magnetisation using the $B^1$ coil. . . . .	51
3.4	EFNMR spectrum acquired without a sample to observe the amplification range of the RLC circuit and the unsymmetrical and envelope-like shape of the amplified region. The data was acquired with a capacitance of 16.15 nF which tunes the RLC circuit to 1797 Hz. . . . .	52
3.5	Due to the Earth's axial tilt of $\theta \approx 23.5^\circ$ , the lab-frame and spin-frame axes do not align. $B^E$ has a longitudinal and transverse component with respect to the lab frame that is defined by angles $\theta$ and $\phi$ , respectively. . . . .	53
3.6	A shimmed $^1\text{H}$ spectrum of water in a 14 cm (H) x 7 cm (D) bottle displays a well resolved signal with a Full Width Half Max (FWHM) of 0.65 Hz. . . . .	54
3.7	The EFNMR-Helmholtz setup consisting of the Terranova-MRI probe at the centre of 3 equidistant and perpendicular coils, each producing a magnetic field in the $x'$ , $y'$ and $z'$ -directions, respectively. . . . .	55
3.8	Plot of $B_{eff}^2 - B_{H_x}^2$ against $B_{H_x}$ used to calculate the angle $\theta$ between the Earth's magnetic field and the $x'$ -axis, equal to $90^\circ$ . . . . .	56
3.9	A plot of the proton Larmor frequency, $\nu_{1H}$ , against the current through the y-Helmholtz coil, $I_{H_y}$ . The minimum of the curve shows that alignment of $B^0$ with the $z'$ -axis was achieved using a current of +70 mA to generate a magnetic field $B_{H_y} = 21.3$ uT along $+y'$ . An $\nu_{1H}$ of 1586.3 Hz indicates an external field of 37.3 uT. . . . .	57
3.10	Plot showing the linear relationship between the effective field, $B^0$ , and the magnetic field along the $z$ -axis, $B_{H_z}$ , generated by the $z$ -Helmholtz coil. This relationship is only possible if $B^0$ is parallel with the $z$ -Helmholtz coil along the vertical axis and enables control over the effective field from negative to positive values. The line of best fit indicates a $B^E$ of 36.7 $\mu\text{T}$ . . . . .	58

3.11	Image of the EFNMR-Helmholtz setup with a thick copper wire wrapped around it to block out electrical noise and improve the SNR of signals detected by the $B^1$ coil. . . . .	59
3.12	The improved EFNMR experiment contains the addition of the y and z-Helmholtz coil pairs that generate the $y'$ -cancelling field (21.3 $\mu\text{T}$ ) and the z-field (+15 $\mu\text{T}$ ), respectively. The y-Helmholtz coil pair aligns the spin-frame with the lab-frame to improve EFNMR detection. The z-Helmholtz coil makes use of this alignment and produces a field that constructively interferes with $B^0$ to increase the effective field to subsequently increase thermal polarisation and the signal intensity. . . . .	60
3.13	Illustration a) of the nutation of the net magnetisation of the sample, $M^0$ (blue), about $B^1$ toward the transverse plane, and b) of the precession of $M^0$ about $B^0$ at a frequency $\omega^0$ , which is detected by the $B^1$ coil also along the transverse plane (detection plane). The grey arrows represent the magnetic field with which $M^0$ rotates about. The precessing magnetisation generates a stronger NMR signal if it is in parallel with the transverse/detection plane and the $B^1$ coil, a condition that is met when the spin and lab-frames are aligned. . . . .	61
3.14	RF amplitude-sweep nutation curves track the nutation angle, $\theta_{nut}$ of the spins about the axis of the RF pulse through calculation and plotting of the signal intensity, S, at each iteration of $V_{RF}$ . The desired $\theta_{nut}$ can be read from the sinusoidal nutation curve. . . . .	63
3.15	Calibration of the $^1\text{H}$ $\pi/2$ pulse of water at 2210 Hz was performed by fitting the nutation curve (black) acquired from an RF amplitude-sweep experiment using a $t_{RF}$ of 8 cycles, to an exponentially decaying sine curve (red). The desired nutation of $\pi/2$ rad is achieved with a $V_{RF}$ of 0.99 V ( $V_{\pi/2}$ ), calculated from Eq. 3.6b. . . . .	64
3.16	The excitation profile of an RF pulse describes the RF amplitude with respect to frequency and is calculated from the Fourier Transform (FT) of the pulse shape which describes the RF amplitude with respect to time. A rectangular pulse shape of duration $t_{RF}$ (left) is equivalent to a sinc excitation profile with an approximate excitation bandwidth of $1/t_{RF}$ (right). . . . .	66
3.17	The $^1\text{H}$ and $^{19}\text{F}$ nutation curves of TFE at 2160 Hz were fit to Eq. 3.6a on Matlab and produced $V_{\pi/2}$ of $1.08 \pm 0.07$ V and $1.13 \pm 0.06$ V for the $^1\text{H}$ and $^{19}\text{F}$ nuclei, respectively. These were rounded to 1.1 V for use in future simultaneous excitation experiments. . . . .	67
3.18	The $^1\text{H}$ (2200 Hz) and $^{19}\text{F}$ (2069.5 Hz) signals of TFE were acquired from the improved EFNMR experiment using a) the TFE $^1\text{H}$ $\pi/2$ pulse at 2200 Hz ( $V_{\pi/2} = 1$ V, 8 cycles), b) the TFE $^{19}\text{F}$ $\pi/2$ pulse at 2069.5 Hz ( $V_{\pi/2} = 0.95$ V, 8 cycles) and c) the TFE $^1\text{H}$ and $^{19}\text{F}$ $\pi/2$ pulse at 2160 Hz ( $V_{\pi/2} = 1.1$ V, 8 cycles). The SNR values of each peak is displayed beside it and shows the off-resonance signals are much weaker than the on-resonance signals apart from the signals in c) where both nuclei were nutated by $\pi/2$ rad and therefore have very similar SNRs with a difference of 9.4. Roofing caused by the strong $J_{HF}^3$ coupling interaction is observed on all $^1\text{H}$ and $^{19}\text{F}$ signals and points toward the centre of the heteronuclear coupling pattern. . . . .	68

3.19	Illustration of the process for correcting the phase distortions displayed by the EFNMR spectra acquired using the EFNMR experiment that requires a long acquisition delay of 20 ms. A first-order phase of 276.5 rad is acquired by the $^1\text{H}$ TFE EFNMR signal (red) at 2200 Hz. Correction using Eq. 3.9 with $\nu^0 = 2202$ Hz generates a sinc oscillation in the baseline of the corrected spectrum (blue). Subtraction of a sinc curve (green) of matching frequency and amplitude to the oscillation on the baseline from the corrected spectrum yields a residual spectrum (black) with a well-phased $^1\text{H}$ EFNMR signal and improved baseline. . . . .	69
4.1	Schematic of the SABRE-EFNMR system comprised of the automated gas flow system integrated with the EFNMR-Helmholtz setup used to run SABRE experiments with <i>in situ</i> EFNMR detection. . . . .	73
4.2	Flow diagram of the automated gas flow system comprised of a $\text{H}_2$ generator, a Bruker BPHG 90 $p\text{-H}_2$ generator, a Bruker polariser control unit and a glass reaction cell. The $p\text{-H}_2$ generator enriches thermal $\text{H}_2$ gas in its lower energy para state with a conversion chamber operating at 38 K and lined with a paramagnetic catalyst. The $p\text{-H}_2$ is then fed into the Bruker polariser control unit which establishes a flow rate of $p\text{-H}_2$ through the reaction cell and SABRE sample. The polariser is controlled by commands within macros written on the Terranova-Expert software package (Magritek, Germany) that are delivered by the controlling PC outside of the EFNMR pulse sequence. . . . .	75
4.3	A plot of the pressure values recorded by pressure gauges PG1 and PG2 during a $p\text{-H}_2$ bubbling experiment that mimics the operation of the Bruker polariser control unit over the course of a SABRE-EFNMR experiment. . . . .	79
4.4	Image of the Bruker polariser control unit interface designed on the Terranova Expert software to facilitate access to the commands and pre-existing flow procedures of the polariser (red), and the newly designed flow procedures to aid in monitoring the flow of gas into the reaction cell (blue). The 'Monitoring Parameters' section of the interface offers control over the number of pressure values recorded by PG1 and/or PG2, and the length of time in seconds between each recording. The 'Regeneration' section is exclusive to the regenerate procedure to communicate to PR1 and PR2 the forward and back pressure, respectively, in bar. . . . .	81
4.5	Plot of forward pressure values of $p\text{-H}_2$ into the reaction cell from the end of the regenerate procedure to the end of the V1 Hold procedure which indicates the end of the SABRE-EFNMR experiment. The data shows the recovery of the output of $p\text{-H}_2$ from the $p\text{-H}_2$ generator across 15 different repetitions of the bubbling experiment. A good recovery of the $p\text{-H}_2$ generator is observed because the output pressure at the end of V1 hold is equilibrating to a value higher than the input pressure of the experiment of 4 bar, suggesting the $\text{H}_2$ and $p\text{-H}_2$ generators are keeping up with the $p\text{-H}_2$ demand by the SABRE-EFNMR experiment. . . . .	84

4.6	A plot of the $p$ -H <sub>2</sub> forward and back pressure, measured by PG1 and PG2, respectively, during the second stage of the regenerate procedure with a set pressure differential of a) 0.2 bar, b) 0.25 bar and c) 0.3 bar, from a forward pressure of 3.5 bar. . . . .	87
4.7	Plot of N <sub>2</sub> pressure during the different stages of the leak test procedure which aims to test the ability of the FEP tubing and components within the Bruker polariser control unit to hold pressure. The Hold 1 and Hold 2 procedures used to hold N <sub>2</sub> gas in between PR1 and V1, and PR1 and PR2, respectively, show that there are no leaks present within the polariser. The numbers in red next to the pressure regulators and switchable valves indicates their operating state. . . . .	89
5.1	Form of the SABRE-active catalyst when using the Ir-IMes SABRE precatalyst with pyridine as the SABRE substrate. . . . .	92
5.2	Pulse sequence of the a) mT and b) $\mu$ T SABRE-EFNMR experiments which are similar to the pulse sequence of the EFNMR experiment but include the addition of $p$ -H <sub>2</sub> bubbling made possible by integration of the EFNMR-Helmholtz setup with the automated gas flow system. The polarising coil (0.5- 18.8 mT) and the z-Helmholtz coil pair ( $\pm 64.5 \mu$ T) are used to generate the homonuclear and heteronuclear PTF, respectively, where heteronuclear SABRE polarisation transfer requires switching the current through the z-Helmholtz coil to generate both the PTF and detection field. . . . .	96
5.3	The SABRE-polarised EFNMR <sup>1</sup> H signal of 25 mM pyridine in 4 mL CD <sub>3</sub> OD acquired using the mT SABRE-EFNMR experiment overlaid with the less intense EFNMR <sup>1</sup> H signal of water (500 mL) acquired with the improved EFNMR experiment. The larger water sample experiences more inhomogeneities in the RF pulse and the external field across the sample volume which contributes to the larger linewidth of the water signal. Both <sup>1</sup> H peaks have equal Larmor frequencies of $\sim 2200$ Hz because chemical shift is not observed at $51.9 \mu$ T. . . . .	98
5.4	Activation curve of 5 mM Ir-IMes in 250 mM 3,5-DFP (50 equivalents relative to the catalyst) and 4 mL CD <sub>3</sub> OD showing the build-up of hyperpolarisation of the <sup>1</sup> H EFNMR signal as a function of $p$ -H <sub>2</sub> bubbling time and the formation of [Ir(IMes)(H) <sub>2</sub> (3,5-DFP) <sub>3</sub> ] <sup>+</sup> Cl <sup>-</sup> . Each data point represents a repetition of the mT SABRE-EFNMR experiment and 34.9 s of bubbling ( $t_{PTF} = 30$ s, $t_{RF} = 3.62$ ms, $t_{acq} = 4915.2$ ms, acquisition delay = 20 ms). Activation of the precatalyst was achieved at the plateau of the curve after $\sim 560$ s of $p$ -H <sub>2</sub> bubbling. The consistent intensity of the hyperpolarised <sup>1</sup> H signal following catalyst activation indicates good reproducibility in the hyperpolarisation achieved by the mT SABRE-EFNMR experiment. . . . .	98
5.5	SABRE-polarised EFNMR spectrum of 250 mM 3-FP (50 equivalents relative to 5 mM of Ir-IMes) in 4 mL CD <sub>3</sub> OD acquired with a PTF of 6.4 mT and a $t_{PTF}$ of 10 s with 1 scan of the mT SABRE-EFNMR experiment. . . . .	99

5.6	$^1\text{H}$ and $^{19}\text{F}$ NMR spectra of 3-FP acquired on a 500 MHz Bruker NMR spectrometer, overlaid with the high-field NMR simulation of 3-FP, generated with the $J$ -coupling values optimised by $J$ -opt 1. An $f$ -value of 2.10 and 1.03 was calculated from the fit of the simulation to the $^1\text{H}$ and $^{19}\text{F}$ experimental spectra, respectively. . . . .	102
5.7	Comparison between the SABRE-polarised $^1\text{H}$ EFNMR signal of 3-FP with the simulated $^1\text{H}$ EFNMR signal using the optimised $J$ -coupling values from the $J$ -opt 1 experiment. The simulation shows a goodness of fit of $f = 11.19$ . . . . .	103
5.8	Graph of $f$ -values for the 512 simulations produced from the $J$ -opt 2 experiment, where $f$ -values above 20 have been discarded. The EFNMR simulations from the 3 <sup>rd</sup> (green) and 175 <sup>th</sup> (red) combinations are included in the figure and represent the best and one of the worst fits to the experimental spectrum. The change in phase of only the $J\{\text{H}_1, \text{H}_4\}$ interaction of 3-FP was responsible for the optimal fit to the experimental $^1\text{H}$ signal which saw a change in $f$ -value from 11.19 (see FIGURE 5.7) to 5.31. . . . .	105
5.9	Comparison between the SABRE-polarised $^1\text{H}$ EFNMR signal of 3-FP with the simulated $^1\text{H}$ EFNMR signal using the optimised $J$ -coupling values from the $J$ -opt 1 and $J$ -opt 2 experiments, where the change in relative sign to the $J\{\text{H}_2, \text{H}_6\}$ coupling interaction improves the goodness of fit from $f = 11.19$ to $f = 5.31$ . . . . .	106
5.10	SABRE-polarised EFNMR spectrum of 3-FP (50 equivalents relative to 5 mM of Ir-IMes) acquired with a PTF of 6.4 mT overlaid with the simulated EFNMR spectrum of 3-FP. The $^1\text{H}$ signal has a good fit to the simulation ( $f = 5.31$ ) but significant splitting of the $^{19}\text{F}$ signal (backed up by simulations) and an inefficient pathway for its hyperpolarisation means the SABRE-polarised $^{19}\text{F}$ EFNMR signal of 3-FP was not observed.	107
5.11	Comparison of the simulated EFNMR spectrum of 3-FP with the SABRE-polarised $^1\text{H}$ EFNMR signals of 3-FP (50 equivalents relative to 5 mM of Ir-IMes) in 4 mL MeOH and $\text{CD}_3\text{OD}$ solvent, acquired with 1 scan using a PTF of 6.4 mT and a $t_{PTF}$ of 10 s. The sample containing MeOH displays a hyperpolarised $^1\text{H}$ signal with an intense negative singlet at its centre that is not observed in the simulated signal or in the hyperpolarised $^1\text{H}$ signal of the $\text{CD}_3\text{OD}$ sample. . . . .	108
5.12	SABRE-polarised $^1\text{H}$ and $^{19}\text{F}$ EFNMR signals of 3,5-DFP (30 equivalents relative to 5 mM of Ir-IMes) in 4 mL $\text{CD}_3\text{OD}$ acquired with a PTF of 9.0 mT and a $t_{PTF}$ of 20 s with 1 and 16 scans of the mT SABRE-EFNMR experiment, respectively. The experimental spectra are overlaid with simulated spectra of 3,5-DFP for comparison. The hyperpolarised $^1\text{H}$ and $^{19}\text{F}$ EFNMR signals have been acquired from different experiments and have been phased separately. Simulations were acquired with $\rho_0 = \sum_i \hat{I}_{zi}$ and $\hat{I}_{obs} = \sum_i \hat{I}_i^-$ for all nuclei. . . . .	109
5.13	NMR simulations of the <i>ortho</i> and <i>para</i> -proton signals of 3,5-DFP, acquired with $\hat{I}_{obs} = \sum_{i=2,6} \hat{I}_i^-$ and $\hat{I}_{obs} = \hat{I}_4^-$ , respectively at 51.9 $\mu\text{T}$ . The two signals allow observation of the individual contribution to the simulated $^1\text{H}$ signal by the <i>ortho</i> and <i>para</i> -proton environments. . . . .	111

- 5.14 Simulated splitting tree of the  $H_4$  signal of 3,5-DFP at  $51.9 \mu\text{T}$ . When considered separately, the dominant  $9 \text{ Hz } J\{H_4, F_{3,5}\}$  coupling interaction represents an  $AB_2$  spin system and forms a multiplet of four peaks. The two outer split peaks (green) are further split by the  $2.33 \text{ Hz } J\{H_{2,6}, H_4\}$  coupling interaction forming a set of multiplets of four peaks. The two central split peaks (grey) are further split by the  $2.33 \text{ Hz } J\{H_{2,6}, H_4\}$  coupling interaction forming a complex multiplet of several peaks. . . . 112
- 5.15 SABRE-polarised  $^1\text{H}$  and  $^{19}\text{F}$  EFNMR signals of 3,5-TFMP (50 equivalents relative to 5 mM of Ir-IMes) in 4 mL  $\text{CD}_3\text{OD}$  acquired with a PTF of 6.4 mT and a  $t_{PTF}$  of 30 s with 1 and 16 scans of the mT SABRE-EFNMR experiment, respectively, overlaid with the simulated EFNMR spectrum of 3,5-TFMP. The hyperpolarised  $^1\text{H}$  and  $^{19}\text{F}$  EFNMR signals have been acquired from different experiments and have been phased separately. Simulations were acquired with  $\rho_0 = \sum_i \hat{I}_{zi}$  and  $\hat{I}_{obs} = \sum_i \hat{I}_i^-$  for all nuclei. . . . . 114
- 5.16 SABRE-polarised  $^1\text{H}$  and  $^{19}\text{F}$  EFNMR signals of 3-DFMP (50 equivalents relative to 5 mM of Ir-IMes) in 4 mL  $\text{CD}_3\text{OD}$  acquired with a PTF of 6.0 mT and a  $t_{PTF}$  of 30 s with 1 and 8 scans of the mT SABRE-EFNMR experiment, respectively, overlaid with the simulated EFNMR spectrum of 3-DFMP. The hyperpolarised  $^1\text{H}$  and  $^{19}\text{F}$  EFNMR signals have been acquired from different experiments and have been phased separately. Simulations were acquired with  $\rho_0 = \sum_i \hat{I}_{zi}$  and  $\hat{I}_{obs} = \sum_i \hat{I}_i^-$  for all nuclei. The peaks labeled with a red and green stars are artefacts from the instrumentation. . . . . 116
- 5.17 The EFNMR simulation of 3-DFMP acquired with  $\rho_0 = \sum_i \hat{I}_{zi}$  over all  $^1\text{H}$  nuclei and  $\hat{I}_{obs} = \sum_i \hat{I}_i^-$  over all nuclei fits well to the SABRE-polarised EFNMR spectrum of 3-DFMP  $^{19}\text{F}$  and also replicates the phase of the hyperpolarised peaks at the  $^{19}\text{F}$  region of the spectrum. . . 119
- 5.18 The SABRE-polarised  $^1\text{H}$  and  $^{19}\text{F}$  EFNMR signals of 3,5-DFP, 3,5-TFMP and 3-DFMP acquired using the mT SABRE-EFNMR experiment. 121
- 6.1 The  $^1\text{H}$  and  $^{19}\text{F}$  mT PTF curves of 3,5-DFP acquired by repeating the mT SABRE-EFNMR experiment with 1 and 16 scans, respectively and a  $t_{PTF} = 10 \text{ s}$ . The curves illustrate the magnetic field dependence of the efficiency of SABRE polarisation transfer to the  $^1\text{H}$  and  $^{19}\text{F}$  nuclei. Polarisation transfer to  $^1\text{H}$  is maximal between 8.5 and 9.5 mT, and hyperpolarisation of  $^{19}\text{F}$  is maximal between 6 and 12 mT. The efficiency of polarisation transfer to  $^1\text{H}$  and  $^{19}\text{F}$  as a function of the PTF follows similar trends as  $^{19}\text{F}$  receives its hyperpolarisation from the SABRE-polarised  $^1\text{H}$  nuclei at mT PTFs. The normalised integrals represented by red circles were acquired from the same sample on a different day but replicate the shape of the PTF curve demonstrating good reproducibility in the SABRE results. . . . . 125

- 6.2 PTF curves plotted from the SABRE-polarised a)  $^1\text{H}$  and b)  $^{19}\text{F}$  signals of 3,5-DFP acquired via *ex situ* mT PTF-cycling experiments using an automated gas flow system for automated transfer from the PTF, generated by an external solenoid, to the 11.74 T detection field within the NMR spectrometer. Figures are reproduced without alteration from the SI of the publication by Olaru et al.<sup>2</sup> under the CC BY 4.0 license. 126
- 6.3 SABRE-polarised EFNMR spectrum of 3,5-DFP acquired using a) PTF = 8  $\mu\text{T}$  and  $t_{PTF} = 15\text{ s}$  with the  $\mu\text{T}$  SABRE-EFNMR experiment, and b) PTF = 9 mT with the mT SABRE-EFNMR experiment. The spectra have been phased so that the hyperpolarised signal from the target nucleus of SABRE polarisation transfer is an absorbance signal: a)  $^{19}\text{F}$  and b)  $^1\text{H}$ . . . . . 129
- 6.4 The hyperpolarised EFNMR spectra in b), and the corresponding PTF curves in a) of 3,5-DFP were acquired with 2 scans for each PTF iteration of the  $\mu\text{T}$  SABRE-EFNMR experiment. The PTF curves show the same magnetic field dependency of the efficiency of SABRE polarisation transfer to  $^{19}\text{F}$ , and the efficiency of indirect polarisation transfer from  $^{19}\text{F}$  to  $^1\text{H}$  across a PTF range of -14- 14  $\mu\text{T}$ . The stacked spectra have been aligned along the frequency axis for illustrative purposes. . . . . 131
- 6.5 PTF curve plotted from the SABRE-polarised  $^{19}\text{F}$  signal of 3,5-DFP acquired via *ex situ*  $\mu\text{T}$  PTF-cycling experiments using an automated gas flow system for automated transfer from the PTF, generated by an external solenoid, to the 11.74 T detection field within the NMR spectrometer. Figure is reproduced without alteration from the SI of the publication by Olaru et al.<sup>2</sup> under the CC BY 4.0 license. . . . . 132
- 6.6 SABRE-polarised EFNMR spectrum of 3-DFMP acquired using a) PTF = 5  $\mu\text{T}$  and  $t_{PTF} = 12\text{ s}$  with the  $\mu\text{T}$  SABRE-EFNMR experiment, and b) PTF = 6 mT with the mT SABRE-EFNMR experiment. The spectra have been phased so that the hyperpolarised signal from the target nucleus of SABRE polarisation transfer is an absorbance signal: a)  $^{19}\text{F}$  and b)  $^1\text{H}$ . . . . . 134
- 6.7 The hyperpolarised EFNMR spectra of 3-DFMP were acquired with 4 scans and a  $t_{PTF} = 12\text{ s}$  for each PTF iteration of the  $\mu\text{T}$  SABRE-EFNMR experiment. The magnetic field dependency of the efficiency of SABRE polarisation transfer to  $^{19}\text{F}$ , and the efficiency of indirect polarisation transfer from  $^{19}\text{F}$  to  $^1\text{H}$  is shown to be the same across a PTF range of 1- 8  $\mu\text{T}$ . The stacked spectra have been aligned along the frequency axis for illustrative purposes. . . . . 136

- 7.1 Pulse sequence for the a) SHARPER and b) *sel*-SHARPER experiment with the corresponding  $^{19}\text{F}$  SHARPER spectra of fluorobenzene and 2-deutero-1,3,4-trifluorophenyl displaying linewidths of 0.14 and 0.31 Hz, respectively. Solid rectangles represent hard  $\pi/2$  pulses and unfilled Gaussian shapes represent soft  $\pi$  pulses. Sine-shaped pulsed field gradients were applied at  $G_0 = 1\%$  for the SHARPER and *sel*-SHARPER experiments. The phase cycle:  $\phi_1 = 2x, 2(-x), 2y, 2(-y)$ ;  $\phi_2 = 2(y,-y), 2(x,-x)$ ;  $\phi_3 = 2(-y,y), 2(-x,x)$ ; and  $\Psi = 2x, 2(-x), 2y, 2(-y)$  was used for the SHARPER experiment. The phase cycle:  $\phi_1 = 4x, 4(-x), 4y, 4(-y)$ ;  $\phi_2 = 2y, 2x, 2(-y), 4(-x), 2y, 2x, 2(-y)$ ;  $\phi_3 = 4(y,-y), 4(x,-x)$ ;  $\phi_4 = 4(-y,y), 4(-x,x)$ ; and  $\Psi = 2x, 4(-x), 2x, 2y, 4(-y), 2y$  was used for the *sel*-SHARPER experiment.  $G_1$  was applied at 30%. Figures a) and b) have been reproduced with permission from the literature<sup>3</sup> (<https://pubs.acs.org/doi/10.1021/acs.analchem.7b02437>). Further permissions related to the material excerpted should be directed to the American Chemical Society. . . . . 140
- 7.2 Schematic illustrating the difference between the excitation profile shapes (right) of a) rectangular and b) shaped RF pulses, generated from the Fourier transform of the pulse shapes (left). The difference in the excitation bandwidth of rectangular ( $10^5$  Hz) and shaped pulses ( $10^3$  Hz) were calculated from typical  $t_{RF}$  values of 10  $\mu\text{s}$  and 1 ms, respectively. The sinc pulse shape is used here as the example of a shaped RF pulse. 143
- 7.3 Gaussian pulse shapes are very simple and easy to synthesise on low-field NMR systems that are less sophisticated than high-field NMR systems. The Gaussian pulse produces a Gaussian excitation profile in which active and passive spins experience only positive RF amplitude values at a frequency range calculated from the inverse of the pulse duration,  $t_{RF}$ . . . . . 144
- 7.4 Calibration curve showing the non-linear power output of the RF amplifier on the Spinsolve spectrometer in the a) dB scale and b) linear scale. Both sets of data were fit to a 5th order polynomial to calculate the amplitude value to be set on the spectrometer,  $\text{dB}_{set}$  or  $a_{Fset}$ , for execution of the desired pulse amplitude,  $\text{dB}_{ideal}$  or  $a_{Fideal}$ . The lowest 5 data points in b) were excluded from the fit because  $A_{RF}$  cannot be accurately defined below a linear attenuation of 0.01. The equation and corresponding polynomial coefficients of the fit to the data in plot a) can be found in Eq. 7.3 and Table 7.1, and in plot b) can be found in Eq. 7.7 and Table 7.2, respectively. . . . . 145
- 7.5 A plot of Gaussian curves with  $\text{dB}_{set} = 0$  and -12 dB plotted with Eq. 7.4 using 1000 amplitude values and a cut-off amplitude of  $b = 0.01$ . The curves represented by solid and dashed lines depict the ideal and corrected versions of the Gaussian, respectively, where the corrected versions involve passing the  $G_a$  values through the 5<sup>th</sup> order polynomial fit in Eq. 7.3 from the linear correction curve in FIGURE 7.4b. . . . . 149

7.6	Pulse sequence for the SPFGSE experiment, where the filled rectangle represents a hard $\pi/2$ RF pulse and the unfilled Gaussian shape represents a selective $\pi$ RF pulse. Repeating this experiment with a range of amplitude values allows calibration of the selective $\pi$ pulse for a given $t_{RF}$ . . . . .	150
7.7	Results from the SPFGSE amplitude sweep experiment showing that -33, -38.5 and -46 dB are required to achieve $\pi$ rad nutations for 2,3 and 4 ms Gaussian RF pulses, respectively. . . . .	150
7.8	Excitation profile of the 2, 3 and 4 ms Gaussian pulses showing that the Gaussian excitation profiles become narrower as $t_{RF}$ increases which is in agreement with the time-energy uncertainty relation. The excitation bandwidths (selectivity) of the Gaussian pulses are approximated from the FWHM of the Gaussian excitation profiles and are very close to the theoretical values calculated from the reciprocal of $t_{RF}$ . . . . .	151
7.9	Spectra of 3-FP acquired from 8 scans of a) a $^{19}\text{F}$ pulse-acquire experiment and b) a $^{19}\text{F}$ SPFGSE experiment using a 5 ms Gaussian $\pi$ pulse that offers a theoretical selectivity of 4.9 ppm. The lack of the background signal on the $^{19}\text{F}$ SPFGSE spectrum at -72.3 ppm and the observation of the 3-FP multiplet in both spectra at -127.2 ppm demonstrates the successful implementation of the Gaussian RF pulse which selectively interacted and refocused the $^{19}\text{F}$ nuclei in the sample only. . . . .	153
7.10	Pulse sequence for <i>sel</i> -SHARPER on the Spinsolve benchtop NMR spectrometer. A filled rectangle represents a hard $\pi/2$ pulse and the unfilled Gaussian shape represents a Gaussian $\pi$ pulse. The experiment is run with only one scan using phases of $\phi_1 = \Psi = x$ , and $\phi_2 = y$ , where $\Psi$ corresponds to the phase of the receiver. The homospoil gradients used for refocusing the active spins are labelled $G_1$ . . . . .	154
7.11	$^{19}\text{F}$ pulse acquire and <i>sel</i> -SHARPER spectra of a) 3-FP, b) 3,5-DFP and c) 3,5-TFMP acquired with 8 and 1 scan, respectively. The <i>sel</i> -SHARPER spectra show the collapse of the $^{19}\text{F}$ multiplets at -127.2, -125 and -63.9 ppm of 3,FP, 3,5-DFP and 3,5-TFMP, respectively, into narrow singlets with linewidths below 0.5 Hz. The background signal was also not observed in the <i>sel</i> -SHARPER spectra which utilised Gaussian $\pi$ pulses on resonance to the heteronuclear $^{19}\text{F}$ peaks with a selectivity of 4.9 ppm. Chunking artefacts were observed in the $^{19}\text{F}$ <i>sel</i> -SHARPER spectrum of 3,5-TFMP with separation of 48 Hz due to its stronger signal intensity. . . . .	155

7.12 Illustration of a) the pulse sequence for the SHARPER experiment for implementation on the Spinsolve NMR spectrometer where a filled thin and wide rectangle represents a hard  $\pi/2$  and  $\pi$  pulse, respectively. The corresponding SHARPER spectrum of 3-FP in b) shows collapse of the  $^{19}\text{F}$  multiplet into a singlet with linewidth = 1.2 Hz and SNR = 47.7. A series of intense FID chunking artefacts with a frequency of  $\pm 48.5$  Hz were observed between -90 and -60 ppm due to the collapse of the broad solid-state-like (background)  $^{19}\text{F}$  signal at -72.3 ppm. The same FID chunking artefacts are observed around the  $^{19}\text{F}$  peak of 3-FP with a much lower intensity as a consequence of the 48.5 Hz sampling rate of each FID chunk. The SHARPER experiment is performed with 1 scan using phases of  $\phi_1 = \Psi = x$  and  $\phi_2 = y$ . . . . . 157

# List of Tables

3.1	Table of coil constants, $C_c$ . . . . .	51
3.2	Table of $^1\text{H}$ and $^{19}\text{F}$ $V_{\pi/2}$ values for $\text{H}_2\text{O}$ and TFE acquired from RF amplitude-sweep nutation curves. . . . .	65
4.1	Table describing the commands and procedures available within the Bruker polariser interface. . . . .	83
5.1	Table of $J$ -coupling values of 3-FP. The optimised $J$ -coupling values were acquired using the $J$ -opt 1 experiment, using the measured $J$ -coupling values (acquired from high-field $^1\text{H}$ and $^{19}\text{F}$ spectra) as the starting point. The high-field NMR simulation of 3-FP in FIGURE 5.6 was generated using the optimised $J$ -coupling values. . . . .	103
5.2	Table of optimised $J$ -coupling values of 3-FP acquired from the $J$ -opt 1 and $J$ -opt 2 experiments. An improved fit to the SABRE-polarised $^1\text{H}$ spectrum of 3-FP was seen after the $J\{\text{H}_1, \text{H}_4\}$ interaction (bold and underlined) was given a negative phase. . . . .	106
5.3	Table of optimised $J$ -coupling values of 3,5-DFP. . . . .	110
5.4	Table of optimised $J$ -coupling values of 3,5-TFMP. . . . .	115
5.5	Table of optimised $J$ -coupling values of 3-DFMP. . . . .	117
7.1	Table of coefficients of the $5^{\text{th}}$ order polynomial that is fit to the calibration curve of the RF amplifier defined along a logarithmic (dB) attenuation scale. . . . .	147
7.2	Table of coefficients of the $5^{\text{th}}$ order polynomial that is fit to the calibration curve of the RF amplifier defined along a linear attenuation scale. . . . .	148
9.1	Table of values for the experimental parameters of the mT and $\mu\text{T}$ SABRE-EFNMR experiments. . . . .	167

## Acknowledgements

I would first like to thank my supervisor – Dr. Meghan Halse for her invaluable supervision, constant support and tutelage during the course of my PhD. Her continuous guidance both in and out of the lab was really influential in providing me with an excellent research experience, where I learnt much more than I thought I would. Thanks to her I have gained a stronger interest in, and passion for magnetic resonance and the desire to continue in the field. I would finally like to express my gratitude for her treasured guidance and reinforcement during the thesis write-up period, as I could always rely on her for helpful and detailed feedback, as well as reassurance that I was on track to finish the thesis, even though I didn't always believe it myself. My gratitude extends to EPSRC and the Department of Chemistry for the funding opportunity to undertake my studies at the University of York, and for Simon Duckett and the CHyM staff for access to their facilities. I also thank Dr. Fraser Hill-Casey for his mentorship and pool of knowledge on NMR and gas-flow instruments during his time with the group. I would like to thank the rest of my friends, lab mates, colleagues and research team – Alastair Robinson, Aminata Sakho, James McCall, Ana Silva Terra, Adrian Muller and Tom Guffick. I cherish the time spent together in the lab, Christmas ice-skating trips, the group trip to Aachen, Thursday nights at Spark and other good times we shared. A special shout out to Alastair who was always there when I needed to vent about anything that went wrong with my experiments or code. My appreciation also goes out in full force to my wonderful family and friends, particularly my girlfriend Gina and my twin brother Gabriel, whose hard work and dedication to their own PhDs was a constant source of motivation for me. Without their presence in my life over the last 4 years during weekends in Manchester, Birmingham or York, as well as holidays, my PhD experience would not have been one to remember. A special acknowledgement to my older brother Rodrigo for his major role in my attending university and pursuing chemistry, his friendship, and decision to have me plan his stag-do in the weeks leading to my thesis submission deadline, thanks bro! Finally, a huge thanks to my parents over the thesis write-up months: my Dad for funding my life during this period of unemployment whilst putting up with a caveman-like person in his house that resembles his son; and my Mum who, through her positivity and unwavering faith in me, always provided me with a space to relax, unwind and overcome periods of self doubt.

# Declaration

I declare that this thesis is a presentation of original work and I am the sole author. This work has not previously been presented for an award at this, or any other, University. All sources are acknowledged as References.

# 1 | Introduction

Nuclear Magnetic Resonance (NMR) is a powerful, quantitative and non-invasive analytical technique that is used for applications including structural elucidation of molecules and determination of the composition of complex mixtures. However, NMR spectroscopy suffers from poor sensitivity compared to other analytical techniques (e.g. optical spectroscopies and mass spectrometry) and as a consequence, relatively high sample concentrations ( $> \text{mM}$ ) are often required for routine detection. Sensitivity in NMR is proportional to the polarisation of the nuclear spin system. Polarisation arises from the population difference between nuclear spin states within a magnetic field. It is dictated by the Boltzmann distribution, and is dependent on the strength of the external field,  $B^0$ . Therefore, a brute force approach to enhance sensitivity in NMR is to use NMR instruments based on strong magnetic fields (7–28.2 T), typically generated using large superconducting magnets. Strong magnetic fields also help to separate NMR signals from spins in different chemical environments for improved chemical shift resolution. Careful engineering and shimming of these superconducting magnets achieves high magnetic field homogeneity within the sample region to maximise signal resolution.

Despite the many spectroscopic benefits of performing NMR with strong magnetic fields (high-field regime), there are a few practical drawbacks to this approach. High-field NMR instruments are extremely expensive to purchase and also expensive to operate as they must be kept under cryogenic temperatures and require specially trained personnel for maintenance. High-field NMR systems are heavy and have large spacial footprints, making them non-portable and complicating their setup inside of laboratories. As a consequence, there has been a growing demand for the development of NMR instruments that are cheaper, more compact and portable (benchtop NMR). However, achieving this requires the use of alternate magnet technologies<sup>4–6</sup> to generate  $B^0$ , such as permanent magnets. These magnets are a lot easier and cheaper to maintain than superconducting magnets; however, they are only capable of generating stable and homogeneous magnetic fields of approximately 1–2.4 T. The drop in field strength when moving from a high-field to a benchtop NMR instrument leads to a reduction in sensitivity and chemical shift resolution. Nonetheless, NMR in this regime can still provide good sensitivity and high spectral and chemical shift resolution, as well as greater  $J$ -coupling resolution, making it especially attractive for applications in an industrial setting where there may be a lack of NMR specialists and limitations to budget and/or lab space. Low-field NMR has demonstrated a wide range of applications in NMR<sup>7</sup> and imaging,<sup>8</sup> including applications in chemical and process monitoring,<sup>9–11</sup> due to their ability to be setup inside of fume-hoods and be easily integrated with

high-pressure flow systems.

Although stronger magnetic field strengths increase the thermal polarisation of the nuclear spin system to enhance the sensitivity of NMR detection, the extent of enhancement is small because the nuclear spin energy,  $\hbar\gamma B^0/2$ , where  $\gamma$  is the gyromagnetic ratio of a nucleus and  $\hbar$  is the reduced Planck's constant, is much weaker than the thermal energy,  $k_B T$ , where  $k_B$  is the Boltzmann constant. Thus only a slight population difference between the nuclear spin states is established at thermal equilibrium, even at low temperatures. For example, a thermal polarisation of  $3.1 \times 10^{-3} \%$  is achieved at 9.4 T and 298 K, corresponding to a population difference of 1 in 32,000. In other words, one spin out of every 32,000 will contribute to the detected NMR signal.

Therefore, there is great potential for the advancement of NMR as an analytical technique, especially for applications such as in *in-vivo* and *in-vitro* metabolomics<sup>12,13</sup> that require the detection of very small sample volumes ( $< \text{nL}$ ), if sensitivity can be decoupled from magnetic field strength. One solution to this is with the use of hyperpolarisation techniques that allow enhancement of the polarisation of the nuclear spin system far beyond thermal equilibrium conditions (generally by several orders of magnitude). Although many hyperpolarisation techniques have been developed over the last 60 years, most work in the same way, requiring a source of hyperpolarisation and a method to transfer it to a target molecule. The Dynamic Nuclear polarisation (DNP)<sup>14,15</sup> method relies on the very high Boltzmann polarisation of unpaired electrons at low temperatures and strong magnetic fields as the source of hyperpolarisation, owing to the large gyromagnetic ratio,  $\gamma$ , of electrons ( $\gamma[e] \approx 660\gamma[{}^1\text{H}]$ ). Polarisation transfer from the electrons to the nuclei is carried out by continuous microwave irradiation at a frequency near the Electron Paramagnetic Resonance (EPR) frequency. Spin-Exchange Optical Pumping (SEOP)<sup>16</sup> is another hyperpolarisation technique aimed at hyperpolarising noble gases ( ${}^3\text{He}$ ,  ${}^{129}\text{Xe}$ ,  ${}^{83}\text{Kr}$ , etc.) for applications in biomedical NMR<sup>17</sup> and imaging.<sup>18</sup> This method also relies on electronic spin polarisation, generated via irradiation of alkali metal vapour with resonant circularly polarized light. The polarisation is then transferred to the nuclear spins of target noble gas atoms through gas-phase collisions.<sup>19</sup>

*Para*-Hydrogen Induced Polarisation (PHIP)<sup>20-23</sup> is a hyperpolarisation technique that utilises *para*-hydrogen ( $p\text{-H}_2$ ), a magnetic spin isomer of  $\text{H}_2$ , as the source of hyperpolarisation.<sup>24</sup> The nuclear spin system of  $\text{H}_2$  becomes hyperpolarised by the enrichment of the *para*-state at low temperatures (preferably  $\leq 77 \text{ K}$ ) and in the presence of a paramagnetic catalyst (further details given in section 2.3). This polarisation is transferred to nuclei, usually heteronuclei (X), on the target analyte by chemical reactions involving both  $p\text{-H}_2$  and the target (see FIGURE 1.1a). PHIP is an especially attractive hyperpolarisation technique because the extent of hyperpolarisation amassed on the analyte is independent of  $B^0$ . Consequently, this allows for the effective implementation of PHIP with NMR systems operating in any detection field regime, from very low to ultra-high fields.<sup>25-27</sup> Furthermore, PHIP is very accessible because  $p\text{-H}_2$  is easy and inexpensive to generate and does not require complex and expensive instrumentation, with many research groups utilising  $p\text{-H}_2$  generators built in-house.<sup>28-30</sup> Practically speaking, the method for polarisation transfer in PHIP is also

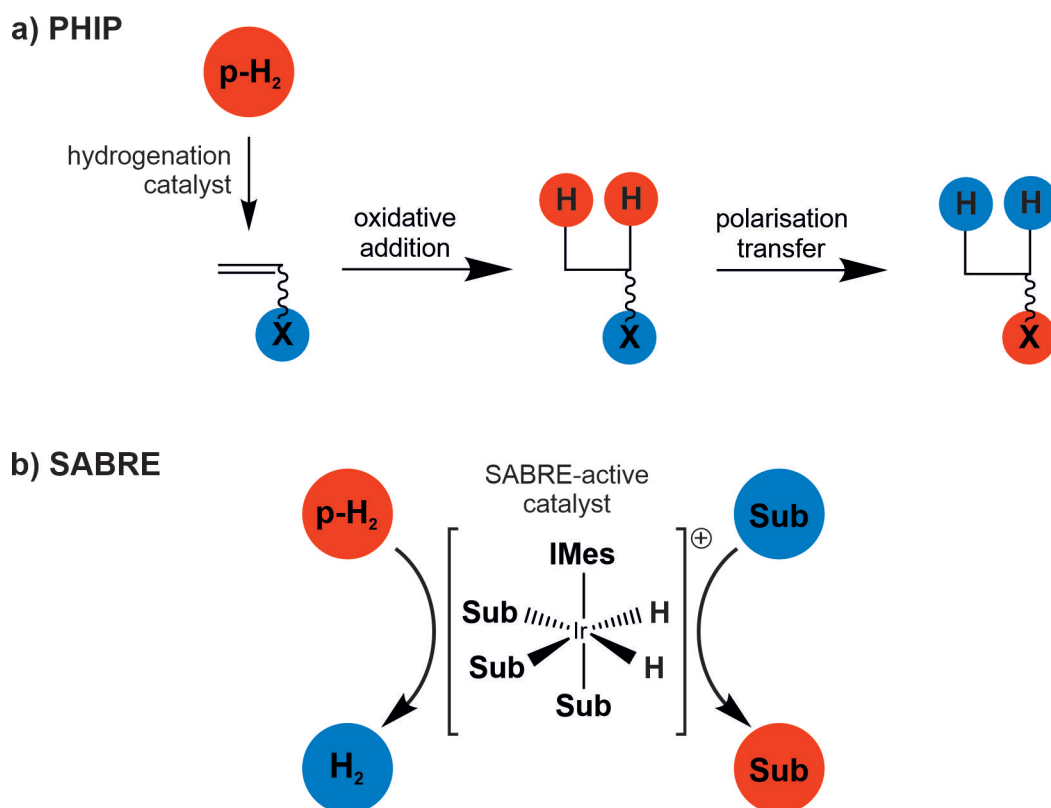


FIGURE 1.1: Illustration of a) hyperpolarisation of a heteronucleus X on a target molecule using PHIP and b) hyperpolarisation of nuclei on a target substrate using SABRE. The red and blue circles represent hyperpolarised and thermally polarised nuclei and molecules, respectively.

quick and easy to carry out. A hydrogenation catalyst (iridium, platinum, rhodium, ruthenium, etc.) is used to drive *para*-hydrogenation of an unsaturated bond on the starting material. The hyperpolarisation potential of *p*-H<sub>2</sub> is unlocked after its pairwise addition into the unsaturated bond, leading to enhanced NMR signals.

Relevant to this work is the Signal Amplification By Reversible Exchange<sup>31</sup> (SABRE) hyperpolarisation technique, which is a variant of PHIP as it also relies on *p*-H<sub>2</sub> as the source of hyperpolarisation. Unlike PHIP, SABRE does not achieve hyperpolarisation by chemically modifying the target molecule. Instead, a metal catalyst (SABRE-active catalyst) is used to mediate the transfer of hyperpolarisation from *p*-H<sub>2</sub> to the target by simultaneously and reversibly binding them, a process which unlocks the latent hyperpolarisation within *p*-H<sub>2</sub> (see FIGURE 1.1b). Reversibility in the binding enables replacement of the thermally polarised hydrides (depleted of hyperpolarisation due to transfer) and hyperpolarised molecules by fresh *p*-H<sub>2</sub> and thermally polarised molecules to allow build-up of hyperpolarised analyte in solution. As there is no chemical modification of the target molecules by the SABRE reaction, a single sample can be continuously hyperpolarised provided there is a supply of fresh *p*-H<sub>2</sub>. This broadens the range of SABRE-suitable molecules in comparison to PHIP because they are not required to contain an unsaturated bond for *para*-hydrogenation, but only the ability to bind reversibly to the metal catalyst.

A wide range of N-heterocyclic molecules have been successfully hyperpolarised by SABRE,<sup>32–36</sup> and a wide range of heteronuclei (<sup>19</sup>F,<sup>2,37</sup> <sup>13</sup>C,<sup>36</sup> <sup>31</sup>P,<sup>38</sup> <sup>15</sup>N,<sup>39</sup> <sup>33</sup>S,<sup>40</sup> <sup>119</sup>Sn

and  $^{29}\text{Si}$ ,<sup>41</sup> etc.). SABRE has also been utilised in a wide range of NMR experiments in both low and high-field regimes, such as pure-shift NMR,<sup>42,43</sup> reaction monitoring,<sup>44,45</sup> forensic drug chemistry<sup>46</sup> and quantitative trace analysis of complex mixtures,<sup>47</sup> among others.

The range of suitable molecules for SABRE was further extended by the method termed SABRE-RELAY,<sup>48</sup> in which ammonia or an amine is hyperpolarised by SABRE, and the hyperpolarisation is relayed via proton exchange onto a target analyte that cannot bind to the metal catalyst. Compatible analytes include amides, carboxylic acids, alcohols, phosphates and carbonates, all of which contain exchangeable protons and all of which have biological relevance. Combined with the fact that hyperpolarisation occurs without chemically altering the target molecule, SABRE-RELAY can provide a route toward advancing the use of NMR and MRI in metabolomics and *in-vivo* metabolic imaging (detection of such small sample volumes is significantly improved with hyperpolarisation). The challenge in these applications is overcoming the toxicity of the iridium SABRE catalyst which complicates its use within living organisms. There are ongoing developments on the design of biocompatible SABRE catalysts,<sup>49</sup> and on methods to remove the SABRE catalyst from solution,<sup>50</sup> both of which, when coupled with the ability to perform continuous SABRE polarisation in solution,<sup>51</sup> will help to accomplish the implementation of SABRE for improved *in-vivo* analysis by NMR. Nevertheless, recent studies have also shown the *in-vitro* hyperpolarisation of pyruvate<sup>52,53</sup> and anticancer agents<sup>53</sup> using SABRE.

Of interest to this project is the method of polarisation transfer in SABRE, occurring between the catalyst bound *p*-H<sub>2</sub> derived hydrides and the catalyst bound target molecules. The transfer process is mediated by the *J*-coupling network of the catalyst and occurs most efficiently in the Ultra-Low-Field (ULF) regime ( $\mu\text{T}$  -  $\text{mT}$ ) under the strong coupling condition, when the Larmor frequency difference between two nuclei is comparable to the coupling between them. In a weak magnetic field denoted the Polarisation Transfer Field (PTF), the hyperpolarised singlet (*para*) state of H<sub>2</sub>,  $|S_0\rangle$ , experiences Level Anti-Crossings (LACs)<sup>54</sup> with the nuclear spin states of the molecule, enabling the transfer of spin polarisation. Moreover, the theory of Level Anti-Crossing (LAC) shows that homonuclear SABRE polarisation transfer, from the *p*-H<sub>2</sub> derived hydrides to  $^1\text{H}$  nuclei on the molecule, is maximal at  $\text{mT}$  PTFs, whereas heteronuclear SABRE polarisation transfer to heteronuclei on the molecule is maximal at  $\mu\text{T}$  PTFs.

An understanding of the spin physics behind the SABRE polarisation transfer mechanism is necessary to optimise its efficiency, but to also progress toward directing the transfer onto target nuclei of different species ( $^1\text{H}$ ,  $^{19}\text{F}$ ,  $^{13}\text{C}$ ,  $^{31}\text{P}$ , etc.) on the analyte. As a consequence, a considerable amount of research<sup>54-56</sup> has been carried out with the use of polarisation transfer field-cycling (PTF-cycling) experiments to investigate and observe the magnetic field dependency of SABRE polarisation transfer.

The majority of research into SABRE polarisation transfer has been conducted with high-field NMR detection ( $> 1\text{ T}$ ), where the fixed nature of the  $B^0$  field generated by benchtop and high-field NMR instruments prevents exposure of the sample to weak magnetic fields whilst inside the NMR probe. Therefore, SABRE polarisation transfer

has to take place outside of the spectrometer (*ex situ*) and a sample transfer step is required to transport the sample between the two field regimes. Manual transfer is commonly employed via the "shake and drop" experiment,<sup>44,57,58</sup> which requires shaking the sample under a *p*-H<sub>2</sub> atmosphere in the presence of the PTF to initiate the SABRE reaction and drive polarisation transfer to the analyte, before being dropped into the high-field NMR probe for detection. Automated transfer can also be employed to improve the reproducibility of sample transfer. One example is with the use of an automated gas flow system<sup>59-62</sup> to shuttle the liquid SABRE sample from a mixing chamber, that hosts *p*-H<sub>2</sub> bubbling of the sample in the presence of the PTF, into an empty cell within the high-field NMR probe. Other examples include automated pneumatic shuttles<sup>63</sup> to transport the sample through a vertical path from the bore of a high-field NMR spectrometer, where the sample is exposed to a strong magnetic field for detection, to a magnetic shield placed above the bore, where the sample can be exposed to  $\mu\text{T}$ -0 T PTFs. This method therefore enables automated magnetic field cycling between the high-field and ULF regimes.

Minimising the duration of sample transfer is vital to minimise the loss of molecule hyperpolarisation through relaxation mechanisms such as  $T_1$ . Manual and automated transfer times are typically between 2-3 and 4-5 s, respectively, where automated transfer must include a short delay (< 1 s) to allow settling of the SABRE sample before the NMR experiment. Although *ex situ* SABRE with any sample transfer method has yielded signal enhancements by up to four orders of magnitude, automated sample transfer is preferred as it provides more control over the polarisation transfer conditions, such as the rate of dissolution of *p*-H<sub>2</sub> (different dissolution rates are achieved with the "shake and drop" experiment if the sample is shaken differently between experiments), transfer time and duration of exposure to the PTF, the result of which is more reproducible SABRE and signal enhancement. The pathway of the sample from the PTF to the NMR probe is also important in *ex situ* SABRE because it can be exposed to stray position dependent magnetic fields that promote  $T_1$  relaxation and the loss of hyperpolarisation (nonadiabatic sample transfer). While neither manual nor automated sample transfer removes exposure to these stray fields, the consistent pathway of the sample in automated transfer allows for a more consistent loss of hyperpolarisation and helps to achieve more reproducible SABRE results.<sup>61</sup>

High-field NMR systems provide good signal and chemical shift resolution, however, SABRE polarisation transfer cannot be interrogated until the sample reaches the probe, at which point hyperpolarisation has been lost to  $T_1$  relaxation, and the transfer of polarisation is already in effect. Methods such as Low-Irradiation Generation of High Tesla-SABRE (LIGHT-SABRE)<sup>64</sup> and RF-SABRE<sup>65</sup> utilise low-power CW pulses and high-power Radio Frequency (RF) pulses, respectively, to drive SABRE polarisation transfer in the high-field regime, removing the need for sample transfer by performing SABRE polarisation transfer *in situ* of NMR detection. Such pulses are necessary to drive SABRE polarisation transfer in the high-field regime where the LAC condition cannot be met. Signal enhancements of 480 for <sup>15</sup>N in free pyridine were recorded using LIGHT-SABRE,<sup>64</sup> whereas signal enhancements of about 1600 for <sup>15</sup>N in free pyridine was recorded with RF-SABRE,<sup>66</sup> and in a much shorter transfer time (0.5 s versus 7.5 s).

The goal of this project is to directly probe the SABRE polarisation transfer mechanism to  $^1\text{H}$  and heteronuclei under weak magnetic fields by detecting hyperpolarisation on the target molecule immediately after the polarisation transfer step without the need to transport the sample to a high-field detector. This is achieved by detecting the SABRE hyperpolarisation in the ULF regime. Carrying out SABRE polarisation transfer *in situ* within the NMR detector will allow us to better understand the SABRE polarisation transfer mechanism so that it may be optimised and more effectively directed to target nuclei on the chosen analyte. ULF NMR systems operate at magnetic fields of  $\mu\text{T}$  -  $\text{mT}$ , and unlike high-field and benchtop NMR systems, do not require the use of permanent or superconducting magnets to generate a  $B^0$  field. These systems are therefore portable and cost efficient and permit the use of external solenoids to access magnetic fields across the entire PTF range ( $\mu\text{T}$  -  $\text{mT}$ ). With NMR detection and SABRE polarisation transfer occurring in the same magnetic field regime, control of the current through these solenoids during an NMR experiment allows facile switching between the PTF and the detection field whilst the sample remains inside the probe (*in situ* magnetic field cycling).

The principal driving force for the development and implementation of ULF detection has been the wide range of applications offered by the ability to perform NMR and MRI outside of the lab.<sup>67,68</sup> Since sensitivity scales approximately with  $(B^0)^2$ , NMR signals in the ULF regime are many orders of magnitude weaker than those acquired with traditional high-field NMR systems, and ULF NMR detection heavily depends upon the use of hyperpolarisation methods to enhance signal intensity. The prepolarisation method, which achieves hyperpolarisation by increasing thermal polarisation of the nuclear spin system, is one of the most common approaches used in ULF NMR. It was first developed by Packard and Varian<sup>69</sup> during the early stages of NMR to enable the detection of a Free Induction Decay (FID) signal in the highly homogeneous, free and naturally available Earth's magnetic field ( $\sim 50 \mu\text{T}$ ). Prepolarisation works by thermally polarising a sample under a stronger ( $\text{mT}$ ) but not necessarily homogeneous magnetic field (prepolarising field), prior to detection in the weaker but more homogeneous Earth's magnetic field. The prepolarising field is oriented perpendicular to the Earth's magnetic field and is switched off adiabatically (slowly on the timescale of NMR evolution;  $\sim 10 \text{ ms}$ ) to ensure the induced polarisation is preserved during alignment of the spin system to the Earth's magnetic field. After realignment, the sample is excited by an RF pulse for detection. The implementation of prepolarisation has enabled the application of Earth's Field NMR (EFNMR) to areas such as diffusion NMR,<sup>70</sup> 2D NMR<sup>71</sup> and 3D MRI.<sup>72</sup> Hyperpolarisation techniques such as DNP,<sup>73,74</sup> SEOP<sup>75-77</sup> and PHIP,<sup>78,79</sup> that achieve hyperpolarisation of the nuclear spin system far beyond thermal equilibrium conditions have also been implemented with ULF NMR instruments to improve detection.

Presented in this report is the implementation of SABRE with EFNMR, not to enhance the accessibility and applicability of EFNMR as an analytical technique, but to carry out SABRE polarisation transfer *in situ* of NMR detection to probe the process directly and hence more reliably. Along with high signal resolution (linewidths  $< 1 \text{ Hz}$ ) provided by the highly homogeneous Earth's magnetic field ( $B^0$ ) which is not as easy to achieve on the other ULF systems, EFNMR systems offer easy access to the bore, making them suitable for integration with an automated gas flow system for *in*

*in situ*  $p$ -H<sub>2</sub> bubbling of the sample. The drop in sensitivity due to low levels of thermal polarisation at the Earth’s magnetic field is compensated for by hyperpolarisation via PHIP, as the amassed hyperpolarisation on the target molecule is independent of  $B^0$ .

First presented in Chapter 3 is an introduction into the commercially available EFNMR instrument utilised for the *in situ* detection of SABRE polarisation, covering methods and built-in procedures to maximise the acquisition of non-SABRE-polarised signals in the ULF regime. Demonstrated in this chapter is also the implementation of a triaxial Helmholtz coil array to improve the performance of the EFNMR system. These external solenoids enable more accurate RF pulse calibration, as well as precise control over the external magnetic field to maximise signal intensity and permit *in situ* magnetic field cycling. Chapter 4 illustrates the automated gas flow system, made-up of a  $p$ -H<sub>2</sub> generator, a flow controller and a reaction cell that when integrated with the EFNMR probe allows *in situ*  $p$ -H<sub>2</sub> bubbling of the sample during exposure to the PTF, the RF pulse experiment and NMR detection. A detailed description of the operation of the  $p$ -H<sub>2</sub> generator and Bruker polariser control unit (flow controller) is given, along with the built-in and designed (in-house) flow procedure macros that ensure a reproducible flow and pressure of  $p$ -H<sub>2</sub> into the sample for reproducible SABRE, and help to troubleshoot and diagnose flow problems within the automated gas flow system due to leaks and blockages in the  $p$ -H<sub>2</sub> path.

The bespoke EFNMR system, which now offers control over the external magnetic field across the ULF regime and *in situ*  $p$ -H<sub>2</sub> flow into the sample, is implemented for interrogation of the polarisation transfer mechanism by observing and comparing homonuclear and heteronuclear polarisation transfer to <sup>1</sup>H and <sup>19</sup>F in N-heterocyclic substrates. Fluorine is the heteronucleus of choice here because it is 100% abundant in the NMR-active <sup>19</sup>F isotope ( $I = 1/2$ ) with the highest gyromagnetic ratio ( $\gamma = 40.078 \text{ MHz T}^{-1}$ ) behind <sup>1</sup>H. Additionally, SABRE polarisation transfer to <sup>19</sup>F is well established<sup>2</sup> using  $\mu\text{T}$  PTFs and PTF-cycling experiments. As the focus of this work is not improving the SABRE reaction for higher signal enhancements, a model and well documented SABRE catalyst, solvent and molecule combination is utilised. This ensures the acquired hyperpolarised EFNMR results, which can be hard to interpret, are a consequence of an ideal SABRE reaction.

The successful acquisition of SABRE-polarised <sup>1</sup>H and <sup>19</sup>F EFNMR signals in four different fluorinated pyridines using mT PTFs for optimal transfer to <sup>1</sup>H, is shown in Chapter 5. NMR in the ULF is still dominated by the nuclear Zeeman effect, but there is strong coupling between the nuclei. Coupled with the loss of chemical shift resolution, EFNMR spectra are complex and challenging to interpret. NMR simulations are utilised here as a powerful tool in assigning and interpreting the acquired EFNMR signals as they can be dissected in a way that is not possible with experimental spectra. With an understanding of the observed hyperpolarised <sup>1</sup>H and <sup>19</sup>F EFNMR signals, the results from the PTF-cycling experiments demonstrated in Chapter 6 for two of the four target analytes, can be interpreted for insight into the magnetic field dependence of SABRE polarisation transfer. Simulations can also offer insight into the nuclear spin states of the molecule that are involved in the SABRE polarisation transfer mechanism across varying polarisation transfer conditions, to further aid in probing the transfer mechanism.

Presented in Chapter 7 is the design and implementation of a Gaussian RF pulse on a benchtop NMR spectrometer to perform the *sel*-SHARPER experiment on more compact NMR systems. This work was part of a collaborative project with the Dusan Uhrin group at the University of Edinburgh and was carried out over the first COVID-19 lockdown when lab access was not permitted, thus preventing the undertaking of hydrogen flow experiments (required for work related to the thesis). The design of the Gaussian RF pulse required only a water sample and could therefore be performed remotely. Illustrated in this chapter is the method used to correct for the non-linearity of the RF amplifier in the benchtop NMR spectrometer to accurately synthesise a Gaussian shaped pulse. Methods for the calibration of selective and non-selective RF pulses is also demonstrated. Successful design of the Gaussian pulse enabled the acquisition of *sel*-SHARPER spectra on a range of fluorinated pyridine derivatives.

Chapter 8 includes a conclusion of the work presented in this thesis with a discussion about the future of this research. This includes comments on how the work can be improved, predominantly focusing on maximising the Signal to Noise Ratio (SNR) by achieving higher levels of hyperpolarisation. Potential improvements to the instrumentation is also mentioned to allow further optimisation of the SABRE-EFNMR experiments as well as the design of new experiments to widen understanding of the SABRE polarisation transfer mechanism.

## 2 | Background Theory

### 2.1 NMR Fundamentals

#### 2.1.1 Nuclei in a Magnetic Field

Nuclei with spin  $I > 0$  possess spin angular momentum,  $\mathbf{S}$ , and a magnetic moment,  $\boldsymbol{\mu}$ . The relationship between the two is shown below:

$$\hat{\boldsymbol{\mu}} = \gamma \hat{\mathbf{S}} \quad (2.1)$$

where the proportionality constant,  $\gamma$ , is the gyromagnetic ratio of the nucleus and the hats above the symbols denote a quantum mechanical operator.

The spin state of a nucleus with spin  $I$  is  $(2I + 1)$ -fold degenerate. In the presence of an external magnetic field,  $B^0$ , the degeneracy is broken by nuclear Zeeman splitting and  $2I + 1$  energy levels ( $m_I \in \{-I, -I + 1, \dots, I - 1, I\}$ ) are formed. FIGURE 2.1 illustrates the nuclear Zeeman splitting for nuclei of different spin. Splitting of the spin states is shown to increase with the strength of  $B^0$ . The weaker splitting of  $^{13}\text{C}$  compared to  $^1\text{H}$ , both of which are spin  $I = 1/2$ , is because the latter has a much larger gyromagnetic ratio ( $\gamma_{\text{H}}/\gamma_{\text{C}} \approx 4$ ) and thus interacts more strongly with  $B^0$ .

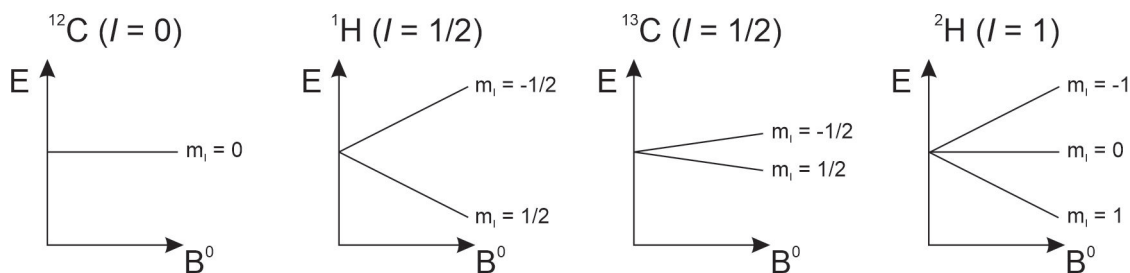


FIGURE 2.1: Illustration of nuclear Zeeman splitting in nuclei with different spin.

These split spin states can be expressed as wave functions in Bra-Ket notation:

$$|\Psi\rangle = |I, m_I\rangle \quad (2.2)$$

These wave functions are eigenfunctions of the Zeeman Hamiltonian operator,  $\hat{\mathbf{H}}_{\mathbf{Z}}$ , such that:

$$\hat{\mathbf{H}}_{\mathbf{Z}} |I, m_I\rangle = E |I, m_I\rangle = -\gamma B^0 \hat{I}_z |I, m_I\rangle \quad (2.3)$$

where  $\hat{I}_z$  is the z-angular momentum operator which projects the z-component of the angular momentum of a nuclear spin state by the following eigenequation:

$$\hat{I}_z |I, m_I\rangle = m_I |I, m_I\rangle \quad (2.4)$$

The  $m_I$  parameter, denoted the azimuthal quantum number, is therefore an eigenvalue of the  $\hat{I}_z$  operator. Its value represents the magnitude of z-angular momentum and its sign represents the alignment of z-angular momentum along  $B^0$ . It is important to note that Eq. 2.3 does not include the reduced Plank's constant,  $\hbar$ , as the energy is being quoted in units of angular frequency ( $\text{rad s}^{-1}$ ).

Magnetic nuclei ( $I > 0$ ) also undergo Larmor precession about  $B^0$  (conventionally along the z-axis) with a Larmor frequency,  $\omega^0$ , equal to:

$$\omega^0 = -\gamma B^0 \quad (2.5)$$

Taking a single spin-1/2 nucleus ( $I = 1/2$ ) as an example, its interaction with the external field causes nuclear Zeeman splitting of the degenerate spin states into a lower energy  $|\alpha\rangle$  ( $|1/2, 1/2\rangle$ ) state, and a higher energy  $|\beta\rangle$  ( $|1/2, -1/2\rangle$ ) state that represent parallel and anti-parallel alignment of the nuclei to  $B^0$ , respectively (see FIGURE 2.1). The energy of the  $|\alpha\rangle$  and  $|\beta\rangle$  spin state is calculated using Eq. 2.3 and Eq. 2.4 to be:

$$\hat{\mathbf{H}}_Z |\alpha\rangle = \frac{1}{2} \omega^0 \quad (2.6a)$$

$$\hat{\mathbf{H}}_Z |\beta\rangle = -\frac{1}{2} \omega^0 \quad (2.6b)$$

The red arrows in FIGURE 2.2 illustrate the alignment of the nuclear magnetic moment to  $B^0$  (along the vertical axis). The Larmor frequency of the nucleus turns out to be equal to the energy difference between the spin states.

Within a molecule, the Larmor frequency of a nucleus varies depending on its chemical environment because electrons in the molecule induce local magnetic fields across a submolecular distance that combine with  $B^0$ . Therefore, depending on the molecular location of a nucleus, it will experience an effective field,  $\mathbf{B}_{eff}$ , such that:

$$\mathbf{B}_{eff} = B^0(1 + \delta_{CS}) \quad (2.7)$$

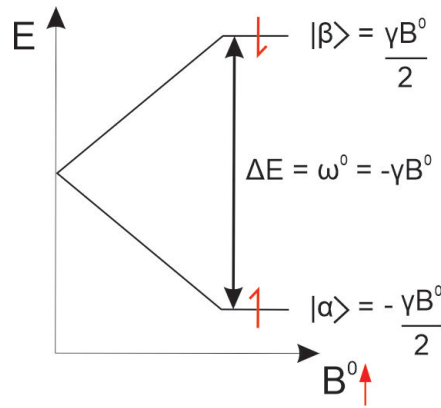


FIGURE 2.2: Nuclear Zeeman splitting of a single spin-1/2 nucleus inside of a magnetic field,  $B^0$ .

where  $\delta_{CS}$  is the isotropic chemical shift. The Larmor frequency of a nucleus is therefore expressed as:

$$\omega^0 = \gamma \mathbf{B}_{eff} \quad (2.8)$$

leading to the definition of the chemical shift Hamiltonian operator,  $\hat{\mathbf{H}}_{CS}$ :

$$\hat{\mathbf{H}}_{CS} = \omega^0 \hat{I}_z \quad (2.9)$$

The intramolecular magnetic interactions between nuclei has not been considered thus far, but is necessary to more accurately represent the energy of a nuclear spin system. In a sample the nuclei in a molecule also interact magnetically with each other and these interactions are independent of  $B^0$ . One example is the through-space interaction between nuclear magnetic fields known as dipole-dipole coupling. Another example is the indirect through-bond interaction between nuclear spins that is mediated by the electrons in chemical bonds, known as  $J$ -coupling. In an isotropic liquid, the scalar  $J$ -coupling interactions survive the rotational motion of the molecule, but the orientation-dependent dipole-dipole couplings average to zero.

The magnitude of the  $J$ -coupling interaction is proportional to the number of bonds between the coupled nuclei, becoming stronger when they are separated by a smaller number of bonds. The  $J$ -coupling also has a sign, where a positive sign indicates that the energy of the interaction between two nuclei is lower if their magnetic moments are antiparallel, and conversely if the sign is negative. For a coupled pair of spin-1/2 nuclei the energy of the interaction is calculated from the  $J$ -coupling Hamiltonian operator,  $\hat{\mathbf{H}}_J$ :

$$\begin{aligned} \hat{\mathbf{H}}_J &= 2\pi J_{jk} \hat{\mathbf{I}}_j \cdot \hat{\mathbf{I}}_k \quad (2.10) \\ \mathbf{I}_j \cdot \mathbf{I}_k &= (\hat{I}_{jx}\hat{I}_{kx} + \hat{I}_{jy}\hat{I}_{ky} + \hat{I}_{jz}\hat{I}_{kz}) \end{aligned}$$

The complete Hamiltonian operator is derived from the sum of the Zeeman and  $J$ -coupling Hamiltonian operators, and for a coupled pair of spin-1/2 nuclei, it is equal to:

$$\hat{\mathbf{H}} = \hat{\mathbf{H}}_{CS} + \hat{\mathbf{H}}_J = \omega_1^0 \hat{I}_{1z} + \omega_2^0 \hat{I}_{2z} + 2\pi J_{12} \hat{\mathbf{I}}_1 \cdot \hat{\mathbf{I}}_2 \quad (2.11)$$

where the Zeeman Hamiltonian operator must include the Larmor frequency of nucleus-1 and nucleus-2. If the two nuclei have the same chemical shift, they are said to be chemically equivalent and the Zeeman term of the complete Hamiltonian simplifies to  $\omega^0(\hat{I}_{1z} + \hat{I}_{2z})$ .

The Hamiltonian operator can be expressed more generally for a nuclear spin system of  $n$  coupled spins as:

$$\hat{\mathbf{H}} = \sum_n \omega_n^0 \hat{I}_{zn} + \sum_j \sum_{j>k} 2\pi J_{jk} \hat{\mathbf{I}}_j \cdot \hat{\mathbf{I}}_k \quad (2.12)$$

where  $j$  and  $k$  refer to groups of magnetically inequivalent spins.

Under strong magnetic fields the  $J$ -coupling interactions between nuclei can become weak. The condition for weak coupling is:

$$|\omega_j^0 - \omega_k^0| \gg |\pi J_{jk}| \quad (2.13)$$

As the Larmor frequency scales with  $B^0$  but the  $J$ -coupling does not, strong magnetic fields can separate the Larmor frequencies of coupled nuclei several orders of magnitude above the size of their  $J$ -coupling interactions. Within this condition, the nuclear spin interactions are dominated by the Zeeman effect (magnetic field interactions along the  $z$ -axis). As such, the  $\hat{I}_{jx}\hat{I}_{kx}$  and  $\hat{I}_{jy}\hat{I}_{ky}$   $J$ -coupling terms become very small and hence have a negligible contribution to the Hamiltonian. Using the secular approximation to remove low energy terms, the Hamiltonian can be simplified to:

$$\hat{\mathbf{H}} = \sum_n \omega_n^0 \hat{I}_{zn} + \sum_j \sum_{j>k} 2\pi J_{jk} \hat{I}_{jz} \hat{I}_{kz} \quad (2.14)$$

In the presence of much weaker magnetic fields ( $\mu\text{T}$  -  $\text{mT}$ ) the complete form of the Hamiltonian (see Eq. 2.12) is used because while the nuclear spin system is still dominated by the Zeeman effect, the  $J$ -coupling interactions between nuclei have a much larger contribution to the Hamiltonian and the secular approximation cannot be employed. The  $J$ -coupling interaction between nuclei is considered strong when the following condition is met:

$$|\omega_j^0 - \omega_k^0| \gtrsim |\pi J_{jk}| \quad (2.15)$$

Heteronuclear  $J$ -coupling interactions are therefore always weak in the high-field regime because the difference in Larmor frequency arises from the difference in gyromagnetic ratio between different types of spins. By contrast, for homonuclear  $J$ -coupling interactions, the Larmor frequency difference between coupled nuclei is due to differences in chemical shift. The strength of the coupling can lie somewhere in between strongly and weakly coupled, depending on the size of the chemical shift difference in ppm, the strength of the magnetic field, and the size of their  $J$ -coupling interactions.

Pople nomenclature is a notation proposed by Bernstein and Pople<sup>80</sup> to classify nuclear spin interactions based on the relative strength of the  $J$ -coupling interactions within molecules. In this notation, each spin in the system is denoted by a capital letter. Spins that are chemically inequivalent, i.e. that have different chemical shift values, are given different letters. Pairs of nuclei with Larmor frequency differences comparable to the  $J$ -coupling value between them are assigned to adjacent letters in the alphabet to indicate that they are strongly coupled (e.g. AB). The use of letters well separated in the alphabet indicates a pair of nuclei that have a difference in Larmor frequency that is orders of magnitude higher than their  $J$ -coupling interaction, indicating weak coupling (e.g. AX). Chemically equivalent nuclei are labelled with the same letter; however, the prime symbol is used within Pople nomenclature to denote magnetic inequivalence between two chemically equivalent nuclei e.g.  $AA'$ . A set of spins are magnetically equivalent if they are chemically equivalent and have identical  $J$ -coupling interactions to the other nuclei in the spin system. Chemical equivalence combined with non-identical coupling interactions to other nuclei represents magnetic inequivalence. The nuclear spin systems of molecules such as methane ( $\text{CH}_4$ ), 2,2,2-trifluoroethanol ( $\text{F}_3\text{C}-\text{H}_2\text{C}-\text{OH}$ ) and 1-bromo-1-fluoroethene ( $\text{H}_2\text{C}=\text{CBrF}$ ) are examples of  $A_4$ ,  $A_2X_3$  and  $ABX$  in the high-field regime, respectively. The carbon and bromine nuclei are not included as they are considered to be non-magnetic.

## 2.1.2 NMR Relaxation

In a sample containing multiple magnetic nuclei ( $I > 0$ ), exposure to a magnetic field generates a net magnetic moment that is aligned parallel to  $B^0$ . This is because a thermal equilibrium population difference (thermal spin polarisation), dictated by the Boltzmann distribution, is established between the spin states, with more spins populating the lower energy spin states. The direction and strength of the net magnetic moment is related to the spin state with excess population and the size of the excess, respectively.

In the absence of a magnetic field the net magnetic moment of a sample is very close to zero. This is because the nuclear energy levels are degenerate and therefore equally populated at thermal equilibrium (isotropic distribution of spin polarisation). As there is no preference for alignment of the nuclear magnetic moment to any particular direction, the magnetic moments point in all possible directions and cancel each other out. Sudden exposure of the sample to a magnetic field causes Zeeman splitting of the degenerate spin states and the spins undergo Larmor precession about the field. However, initially there is no effect on the population of the energy levels and the spin polarisation remains isotropic.

Over time, tiny fluctuations in the magnetic environment of the liquid sample due to thermal motion (e.g. molecular rotation and collisions) leads to the generation of tiny fluctuating magnetic fields that break the isotropy of the spin states. The energetic preference for aligning parallel to  $B^0$  allows the slow build-up of polarisation and hence longitudinal magnetisation ( $M_z$ ) until it plateaus to a thermal equilibrium magnetisation,  $M_{eq}$ . This process is known as longitudinal relaxation (more commonly referred to as  $T_1$  relaxation) and is expressed mathematically as:

$$M_z(t) = M_{eq} \left( 1 - \exp\left\{ \frac{-t}{T_1} \right\} \right) \quad (2.16)$$

where  $T_1$  is an exponential time constant known as the longitudinal relaxation time constant. The plot of longitudinal magnetisation build-up as a function of time and  $B^0$  is illustrated in FIGURE 2.3.

Transverse relaxation (more commonly referred to as  $T_2$  relaxation) describes the decay of magnetisation along the transverse plane which is perpendicular to  $B^0$ . When a sample at thermal equilibrium with net longitudinal magnetisation ( $M_{eq}$ ) interacts with an RF pulse, the vector of the magnetisation is rotated about the axis of the RF pulse (nutations) and, assuming the pulse is accurately calibrated for a  $\pi/2$  rad nutation, is placed along the transverse plane. Transverse magnetisation is essential to NMR detection as the Larmor precession of nuclei along the transverse plane permits electromagnetic induction on the  $B^1$  coil for digitisation of the NMR signal.

The precession of transverse magnetisation can be described in terms of magnetisation along the x and y-axis:

$$\begin{aligned} M_x &= M_{eq} \sin(\omega^0 t) \\ M_y &= -M_{eq} \cos(\omega^0 t) \end{aligned} \quad (2.17)$$

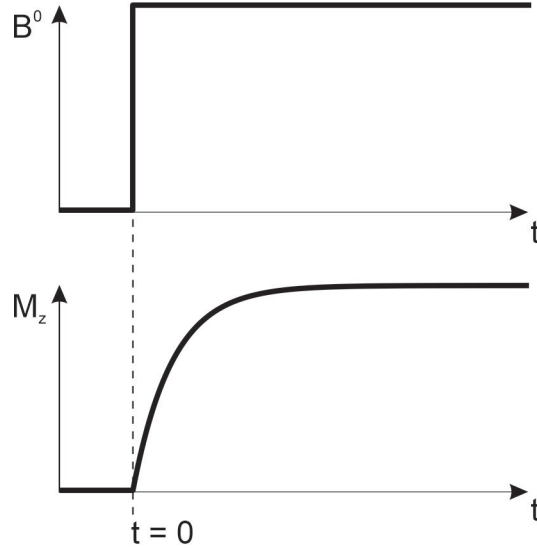


FIGURE 2.3: The  $T_1$  relaxation process causes the build-up of longitudinal magnetisation ( $M_z$ ) in a sample after it is exposed to a magnetic field  $B^0$ .

The above equations describe Larmor precession of magnetisation that begins along the -y-axis and precedes to rotate toward the x-axis ( $-y \rightarrow x \rightarrow y \rightarrow -x$ ). This is achieved by a  $\pi/2$  nutation of the net longitudinal magnetic moment with an RF pulse applied along the x-axis. This description of precession along the transverse plain is not complete because in practice there is decay of the transverse magnetisation. Just as the strength of the net magnetic moment along  $B^0$  depends on the longitudinal polarisation of the nuclei, the net magnetic moment along the transverse plain depends on the transverse polarisation of the nuclei. However, the transverse polarisation decays over time due to the nuclei experiencing slightly different local magnetic fields that shift their Larmor frequencies. This loss in synchrony between the nuclear magnetic moments over time occurs with an exponential decay characterised by the exponential time constant,  $T_2^*$ , known as the transverse relaxation time constant.

There are two distinct sources of  $T_2$  relaxation: inhomogeneity in  $B^0$  across the sample volume due to instrumental imperfections ( $\Delta B^0$ ) and the presence of local magnetic fields that arise as a consequence of natural intramolecular and intermolecular interactions within the sample; considered the 'true' or natural  $T_2$  ( $T_{2(nat)}$ ).  $T_2^*$  is a combination of both sources of relaxation and is therefore considered as the 'effective' or 'observed'  $T_2$ , such that:

$$\frac{1}{T_2^*} = \frac{1}{T_{2(nat)}} + \gamma \Delta B^0 \quad (2.18)$$

The precession of transverse magnetisation can therefore be more accurately described as:

$$\begin{aligned} M_x &= M_{eq} \sin(\omega^0 t) \exp\left(\frac{-t}{T_2^*}\right) \\ M_y &= -M_{eq} \cos(\omega^0 t) \exp\left(\frac{-t}{T_2^*}\right) \end{aligned} \quad (2.19)$$

where the exponential term causes damping of transverse magnetisation. The plot of

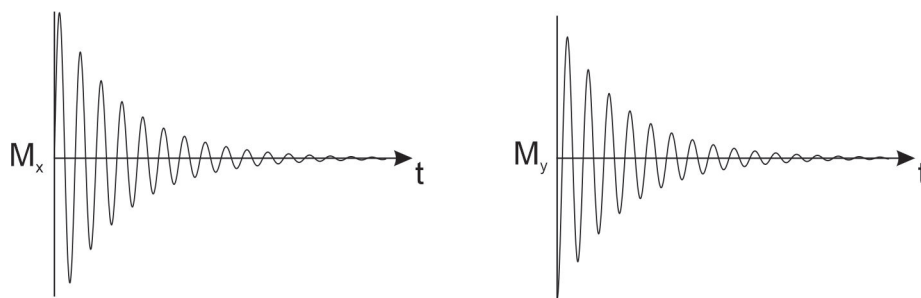


FIGURE 2.4: Plot of the x and y-components of the transverse magnetisation as a function of time, where the exponential damping of both traces is caused by  $T_2$  relaxation.

transverse magnetisation as a function of time in FIGURE 2.4 replicates the form of an FID.

The magnetisation along the x and y-axis replicates the real and imaginary components of the FID, respectively. As  $T_2$  relaxation manifests in the FID it impacts the shape of the acquired NMR signal. The linewidth at half-height of the Lorentzian NMR peak in the frequency domain ( $\Delta\nu_{1/2}$ ), after the Fourier transform of the FID in the time domain, is dictated by  $T_2^*$  (see FIGURE 2.5) through the following equation:

$$\Delta\nu_{1/2} = \frac{1}{\pi T_2^*} \quad (2.20)$$

A longer  $T_2^*$  value represents slower  $T_2$  relaxation and a weaker damping of the FID. In turn, a narrower Lorentzian NMR signal is acquired. Minimising the linewidth of NMR signals is crucial to minimise peak overlap and maximise signal resolution.

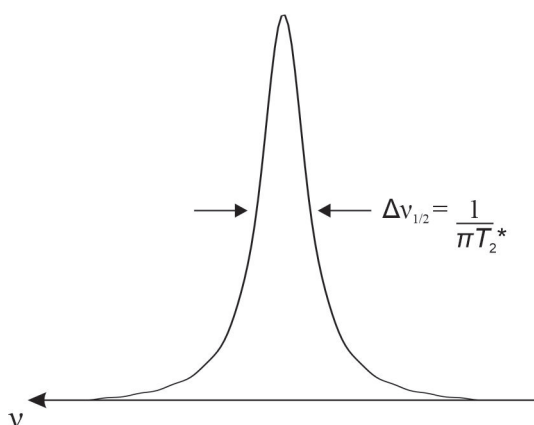


FIGURE 2.5: The linewidth at half-height of an NMR signal is controlled by  $T_2$  relaxation.

## 2.2 NMR in the Ultra-Low-Field Regime

### 2.2.1 Sensitivity

The sensitivity of NMR is measured by the strength or intensity of the NMR signal, which is directly proportional to the polarisation ( $P$ ) of the nuclear spin system. Polarisation arises from the population difference between the nuclear spin states, and for a sample of spin-1/2 nuclei at thermal equilibrium,  $P$  is expressed as:

$$P = \frac{p_{|\alpha\rangle} - p_{|\beta\rangle}}{p_{|\alpha\rangle} + p_{|\beta\rangle}} \quad (2.21)$$

where  $p$  is the Boltzmann population of a spin state:

$$p_r = \frac{\exp(-\hbar\omega_r^0/k_B T)}{\sum_s \exp(-\hbar\omega_s^0/k_B T)} \quad (2.22)$$

and where  $\omega_r^0$  refers to the energy of spin state  $|r\rangle$ . For a spin-1/2 nucleus the energy of the  $|\alpha\rangle$  and  $|\beta\rangle$  spin state is:

$$\begin{aligned} \omega_\alpha^0 &= -\omega^0/2 \\ \omega_\beta^0 &= \omega^0/2 \end{aligned} \quad (2.23)$$

Using the high temperature approximation which accounts for the fact that the magnetic energy ( $\omega^0$ ) of a nuclear spin system is several orders of magnitude weaker than the thermal energy of the system ( $k_B T$ ) for temperatures above a few mK, the Boltzmann distribution (Eq. 2.22) can be simplified by the following approximations:

$$\exp\left(\frac{-\hbar\omega_r^0}{k_B T}\right) \cong 1 - \frac{\hbar\omega_r^0}{k_B T} \quad (2.24)$$

and

$$\sum_s \exp\left(\frac{-\hbar\omega_s^0}{k_B T}\right) \cong 2I + 1 \quad (2.25)$$

to give:

$$p_{|\alpha\rangle} = \frac{1}{2} + \frac{\hbar\omega^0}{4k_B T} \quad (2.26a)$$

$$p_{|\beta\rangle} = \frac{1}{2} - \frac{\hbar\omega^0}{4k_B T} \quad (2.26b)$$

Substituting Eq. 2.26a and 2.26b into Eq. 2.21 produces the the thermal polarisation of a spin-1/2 system:

$$P = \frac{\hbar\omega^0}{2k_B T}, \quad \text{at high } T \quad (2.27)$$

The thermal polarisation of  $^1\text{H}$  nuclei at 11.74 T and 295 K is calculated to be  $4.0 \times 10^{-5}$  (3.5 ppm  $\text{T}^{-1}$ ) and corresponds to an excess of 40 nuclei in every million that

populate the lower energy state. Thus, NMR is an insensitive spectroscopic technique that requires relatively large sample volumes ( $> \mu\text{L}$ ) even with the use of the strongest magnetic field strengths available.

Since thermal polarisation of the nuclear spin system is proportional to  $B^0$ , moving from the high-field to the ULF regime ( $\text{T} \rightarrow \mu\text{T}$ ) leads to a drop in  $B^0$  by several orders of magnitude that is accompanied by a significant loss in sensitivity. Furthermore, traditional acquisition of the NMR signal via Faraday detection (precession of magnetic spins in a sample induces a voltage in an RF pick-up coil through electromagnetic induction) becomes significantly less effective since the induced voltage in the RF coil scales with  $\sim (B^0)^{1/2}$ . Therefore, while sensitivity is a challenge when working in the high-field regime ( $\geq 1 \text{ T}$ ), in the ULF regime it is too low to observe thermal polarisation without some type of sensitivity enhancement. Alternative acquisition methods such as those with SQUID devices<sup>81</sup> and atomic magnetometers<sup>79</sup> have been developed to provide an alternative to Faraday detection for the improved acquisition of NMR signals at ULFs.

## 2.2.2 Strong Coupling

The exposure of a nuclear spin system to a strong external field leads to satisfaction of the weak coupling condition (see Eq. 2.13) by the heteronuclear  $J$ -coupling interactions and also by the homonuclear coupling interactions in some cases. When the nuclear spin system is exposed to the ULF regime, all  $J$ -coupling interactions within it satisfy the strong coupling condition (see Eq. 2.15). The Hamiltonian to describe the energy of this system cannot be simplified via the secular approximation and retains its complete form (see Eq. 2.12).

In the Earth's magnetic field ( $\sim 50 \mu\text{T}$ ) the chemical shift collapses. As a consequence, all nuclei of the same species precess at the same Larmor frequency and hence become very strongly coupled ( $|\omega_j^0 - \omega_k^0| < |\pi J_{jk}|$ ). Heteronuclear  $J$ -coupling interactions between  $^1\text{H}$  and  $^{19}\text{F}$  also become strong as their Larmor frequency difference drops to  $\sim 130 \text{ Hz}$  at  $50 \mu\text{T}$  in comparison to  $\sim 30 \text{ MHz}$  at  $11.74 \text{ T}$ . Therefore, for the example molecules given in section 2.1.1:  $\text{CH}_4$ ;  $\text{F}_3\text{C-H}_2\text{C-OH}$ ; and  $\text{H}_2\text{C=CBrF}$ , they are labelled in the Earth's magnetic field as  $A_4$ ,  $A_3B_2$  and  $ABC$ , as opposed to  $A_4$ ,  $A_2X_3$  and  $ABX$  in the high-field regime, respectively.

As a result of the loss in chemical shift at the Earth's magnetic field and the very strong homonuclear couplings, all nuclei of the same species become magnetically equivalent. For example, pyridine becomes an  $A_5$  nuclear spin system and yields a  $^1\text{H}$  EFNMR spectrum that displays only a singlet. Homonuclear  $J$ -coupling interactions can only be observed in a spectrum if the magnetic equivalence of these nuclei is broken. This requires the use of a heteronucleus as illustrated by Appelt et al.<sup>82</sup> on a sample of tetramethylsilane (TMS) with chemical structure  $\text{Si}(\text{CH}_3)_4$  and natural abundance  $^{13}\text{C}$  (1 %) and silicon  $^{29}\text{Si}$  (4.7 %). A major singlet peak was observed that corresponds to the 12 magnetically equivalent protons in molecules of TMS that did

not contain a magnetic isotope of carbon and silicon. Minor peaks from homonuclear  $J$ -coupling interactions were observed for  $^1\text{H}$  nuclei whose symmetry were broken by heteronuclear  $J$ -coupling interactions to  $^{13}\text{C}$  and  $^{29}\text{Si}$ .

The strength of the  $J$ -coupling interaction has a major influence on the shape of the multiplet produced by each chemical environment, as well as the relative signal intensities of the split peaks within that multiplet. Under weak coupling conditions the secular approximation allows the Hamiltonian operator to be defined by the Zeeman eigenbasis. For a pair of spin-1/2 nuclei the Zeeman basis is written as:

$$|\Psi\rangle = c_{\alpha\alpha} |\alpha\alpha\rangle + c_{\alpha\beta} |\alpha\beta\rangle + c_{\beta\alpha} |\beta\alpha\rangle + c_{\beta\beta} |\beta\beta\rangle \quad (2.28)$$

where  $c$  are the superposition coefficients for each eigenstate which must be normalised:

$$|c_1|^2 + |c_2|^2 + |c_3|^2 + |c_4|^2 = 1 \quad (2.29)$$

Under strong coupling conditions the complete Hamiltonian operator is defined by the singlet-triplet eigenbasis:

$$|\Psi\rangle = c_{T_1} |T_1\rangle + c_{T_0} |T_0\rangle + c_{T_{-1}} |T_{-1}\rangle + c_{S_0} |S_0\rangle \quad (2.30)$$

where,

$$\begin{aligned} |T_1\rangle &= |\alpha\alpha\rangle \\ |T_0\rangle &= \frac{1}{\sqrt{2}}(|\alpha\beta\rangle + |\beta\alpha\rangle) \\ |T_{-1}\rangle &= |\beta\beta\rangle \\ |S_0\rangle &= \frac{1}{\sqrt{2}}(|\alpha\beta\rangle - |\beta\alpha\rangle) \end{aligned} \quad (2.31)$$

The singlet-triplet eigenbasis is therefore a superposition (or mixing) of the eigenstates in the Zeeman eigenbasis. For chemically equivalent nuclear spins, the mixing can break the degeneracy of certain Zeeman states (e.g.  $|\alpha\beta\rangle$  and  $|\beta\alpha\rangle$ ) which consequently leads to more (-1) quantum coherences in the nuclear spin system (refers to the flipping of one nuclear spin, e.g.  $|\alpha\alpha\rangle \rightarrow |\alpha\beta\rangle$  which is an NMR-observable transition) and the formation of more complex multiplets with a higher number of split peaks.

The 3-spin difluoromethyl functional group,  $\text{CHF}_2$ , is encountered in this thesis and is an example of a nuclear spin system that gives rise to drastically different NMR signals under weak ( $AX_2$ ) and strong ( $AB_2$ ) heteronuclear coupling conditions in the high-field and ULF regime, respectively. FIGURE 2.6 illustrates the NMR spectra for such a spin system at both regimes, where the ULF spectrum corresponds to NMR detection in the Earth's magnetic field ( $\sim 50 \mu\text{T}$ ). At high-field, the  $^1\text{H}$  signal is a triplet due to coupling to two equivalent  $^{19}\text{F}$  nuclei ( $2NI + 1 = 3$ , where  $I$  is spin and  $N$  is the number of magnetically equivalent nuclei), and the  $^{19}\text{F}$  signal is a doublet due to coupling to a single  $^1\text{H}$  nucleus ( $2NI + 1 = 2$ ). In the Earth's magnetic field, the  $^1\text{H}$  and  $^{19}\text{F}$  signals each form a multiplet of four peaks, giving a total of eight (-1) quantum coherences in  $AB_2$ , in comparison to five in  $AX_2$ .

The EFNMR spectrum in FIGURE 2.6 demonstrates the close proximity ( $\sim 130 \text{ Hz}$ ) in Larmor frequency of  $^1\text{H}$  ( $\nu_H$ ) and  $^{19}\text{F}$  ( $\nu_F$ ) which allows simultaneous excitation of the two nuclei with a single RF pulse, followed by simultaneous acquisition. This concept will be explored in more detail in Chapter 3.

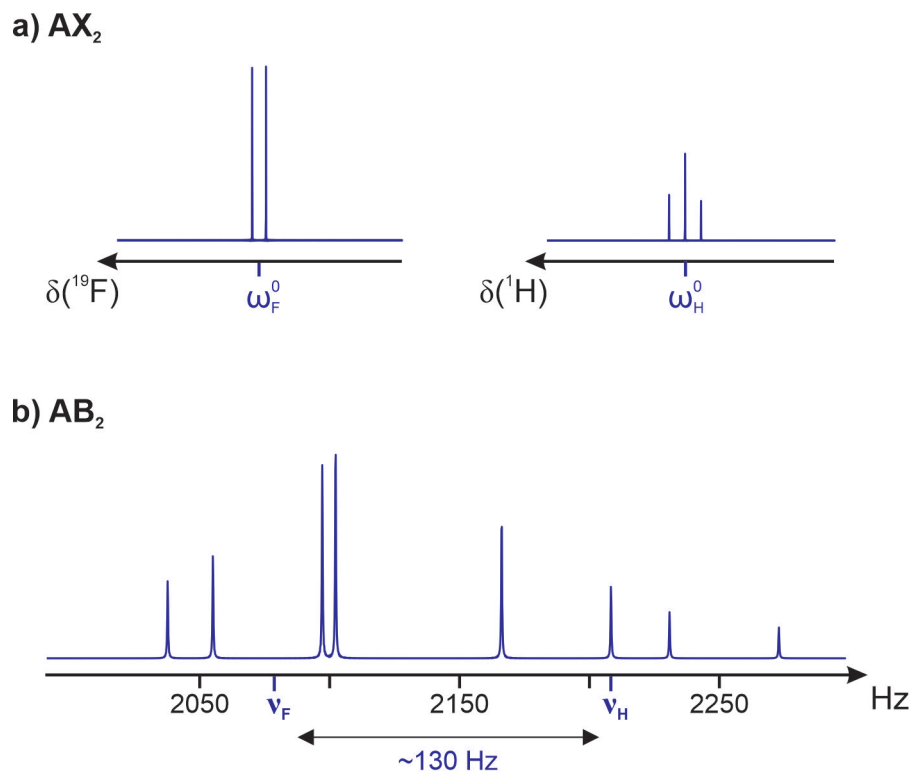


FIGURE 2.6: Illustration of the a) high-field  $AX_2$  and b) EFNMR  $AB_2$  spectrum of a  $\text{CHF}_2$  functional group. The high-field  $^{19}\text{F}$  and  $^1\text{H}$  spectra show a doublet and triplet at their corresponding chemical shifts of  $\omega_F^0$  and  $\omega_H^0$ , respectively. The EFNMR spectrum shows four  $^{19}\text{F}$  and  $^1\text{H}$  peaks at their corresponding Larmor frequencies of  $\nu_F$  and  $\nu_H$  that are separated by around  $\sim 130$  Hz at  $\sim 50$   $\mu\text{T}$ .

## 2.3 *Para*-Hydrogen

The hydrogen molecule ( $\text{H}_2$ ) is made-up of two spin-1/2  $^1\text{H}$  nuclei that have four different combinations of the nuclear spin states:

$$\begin{aligned}
 |S_0\rangle &= \frac{1}{\sqrt{2}}(|\alpha\beta\rangle - |\beta\alpha\rangle) && \text{antisymmetric} \\
 |T_1\rangle &= |\alpha\alpha\rangle && \text{symmetric} \\
 |T_0\rangle &= \frac{1}{\sqrt{2}}(|\alpha\beta\rangle + |\beta\alpha\rangle) && \text{symmetric} \\
 |T_{-1}\rangle &= |\beta\beta\rangle && \text{symmetric}
 \end{aligned} \tag{2.32}$$

These can be separated by their nuclear spin state symmetry with respect to particle exchange; one antisymmetric state, the 'singlet' state ( $|S_0\rangle$ ), and three symmetric states, the 'triplet' states ( $|T_1\rangle$ ,  $|T_0\rangle$  and  $|T_{-1}\rangle$ ). The subscript represents the total spin angular momentum of the combined nuclear spin state. The singlet state of  $\text{H}_2$  is named the *para*-state, meaning abnormal, and the triplet state is named the *ortho*-state, meaning dominant, referring to their 1:3 degeneracy ratio.

The *para* and *ortho*-states populate different rotational energy levels,  $J$  (rotational quantum number), and have different energies. The even ( $J=0,2,4,\dots$ ) and odd

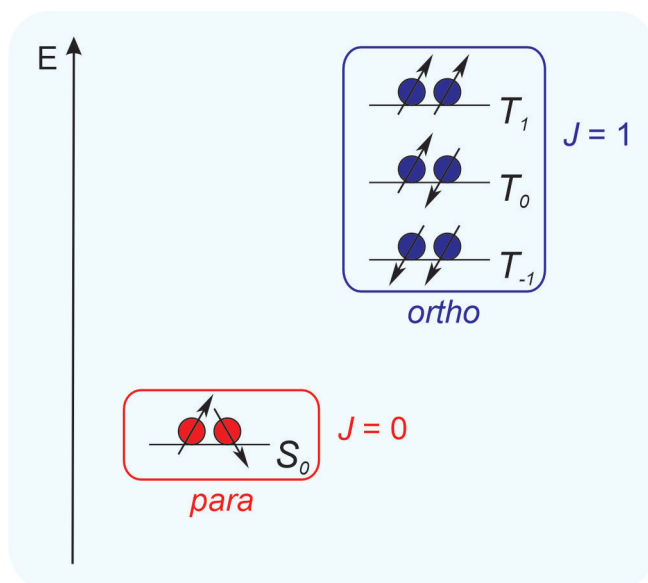


FIGURE 2.7: Energy level diagram of H<sub>2</sub> when considering the spin state energies coupled to the rotational state energies (not drawn to scale). The ground state rotational level ( $J = 0$ ) corresponds to the *para*-state and the second rotational level ( $J = 1$ ) corresponds to the *ortho*-state.

( $J = 1, 3, 5..$ ) rotational energy levels correspond to symmetric and antisymmetric spatial states with respect to particle exchange, respectively. As H<sub>2</sub> is made-up of fermions (spin-1/2 particles), its total quantum state must be antisymmetric with respect to particle exchange (Pauli principle). Therefore, the antisymmetric *para*-state must populate a symmetric (even) spatial state, and the symmetric *ortho*-state must populate an antisymmetric (odd) spatial state (assuming the system is symmetric with respect to populations of the vibrational and electronic states).

Illustrated in FIGURE 2.7 are the energy levels of H<sub>2</sub> at  $J = 0$  and  $J = 1$ , where the black arrows and spheres depict the relative alignment of the magnetic moments of each <sup>1</sup>H nucleus in H<sub>2</sub>. Population of the *para*-state in an H<sub>2</sub> molecule represents the existence of *para*-hydrogen (*p*-H<sub>2</sub>), whereas population of the *ortho*-state represents the existence of *ortho*-hydrogen (*o*-H<sub>2</sub>).

Occupation of the rotational energy levels of a molecule is dictated by Boltzmann's distribution law for a rotational state:<sup>83</sup>

$$N_J = N g_J \exp\left(-\frac{J(J+1)\theta_R}{T}\right) \quad (2.33)$$

$$\theta_R = \frac{h^2}{8\pi^2 I k_B}$$

where  $N_J$  is the occupation of the  $J^{\text{th}}$  rotational energy state,  $N$  is the total number of states,  $g_J$  is the degeneracy of the  $J^{\text{th}}$  rotational energy state and  $T$  is the temperature. The rotational constant,  $\theta_R$ , is also defined in Eq. 2.33, where  $h$  is the Plank's constant,  $I$  is the moment of inertia and  $k_B$  is the Boltzmann constant. The ratio of *p*-H<sub>2</sub> to

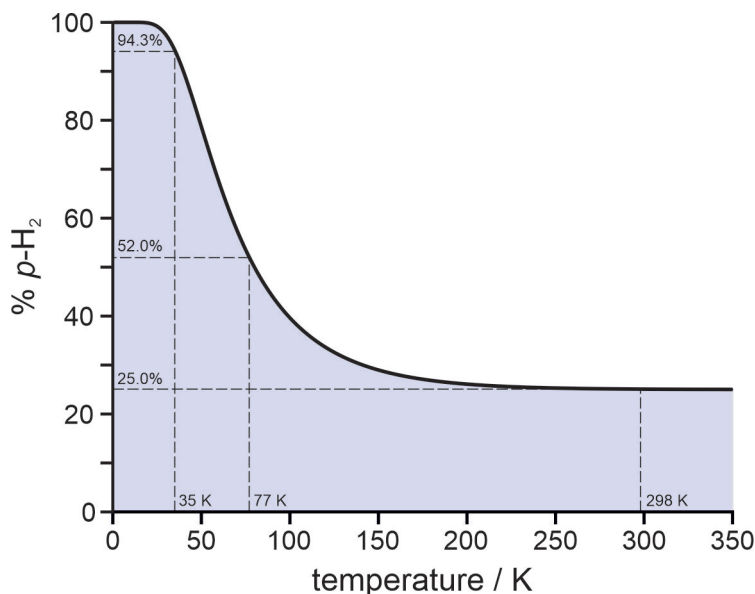


FIGURE 2.8: Temperature dependence of the percentage population of  $p$ -H<sub>2</sub>. The graph was plotted using  $\theta_R = 87.57$  K (calculated from Eq. 2.33).

$o$ -H<sub>2</sub> is therefore calculated as:

$$\frac{N_{para}}{N_{ortho}} = \frac{\sum_{J=even} (2J + 1) \exp\left(-\frac{J(J+1)\theta_R}{T}\right)}{3 \sum_{J=odd} (2J + 1) \exp\left(-\frac{J(J+1)\theta_R}{T}\right)} \quad (2.34)$$

Using Eq. 2.34 the percentage occupation of  $p$ -H<sub>2</sub> can be plotted as a function of temperature (see FIGURE 2.8). This trend was reproduced experimentally via detection of the <sup>1</sup>H NMR signal of  $p$ -H<sub>2</sub> enriched H<sub>2</sub> gas dissolved in toluene.<sup>84</sup>

H<sub>2</sub> gas at 298 K (room temperature) is made-up of 75%  $o$ -H<sub>2</sub> and 25%  $p$ -H<sub>2</sub>, indicating a 3:1 *ortho* to *para* population dispersion (see FIGURE 2.8). The population of the *para*-state of H<sub>2</sub> drastically increases below 150 K. 94.3% and 52%  $p$ -H<sub>2</sub> enrichment is achieved at 35 K and 77 K which corresponds to the use of compressed helium and liquid nitrogen, respectively.

The conversion of  $o$ -H<sub>2</sub> to  $p$ -H<sub>2</sub> is symmetry-forbidden because one of the <sup>1</sup>H nuclei must undergo spin reversal. Therefore, conversion requires cooling H<sub>2</sub> in the presence of an inhomogeneous magnetic field to perturb the molecular symmetry. This was successfully demonstrated using a magnetic dipole as the source of magnetic field inhomogeneity.<sup>85</sup> Paramagnetic species such as iron(III) oxide<sup>86,87</sup> or activated charcoal<sup>88,89</sup> have been used for many years and work very well. Once conversion is complete, the attained  $p$ -H<sub>2</sub> enrichment can be warmed up for use at room temperature and stored for several weeks,<sup>83,90</sup> provided the gas is not in contact with a paramagnetic species as this will permit the symmetry forbidden conversion of  $p$ -H<sub>2</sub> back to  $o$ -H<sub>2</sub> to re-establish the thermal equilibrium populations of the rotational energy states. The *para*-state is therefore a long-lived state.

Applications of  $p$ -H<sub>2</sub> include rocket fuel<sup>91</sup> and liquid hydrogen storage.<sup>92</sup> In NMR, the spin polarisation of  $p$ -H<sub>2</sub> enriched H<sub>2</sub> gas is exploited. Conversion of  $o$ -H<sub>2</sub>

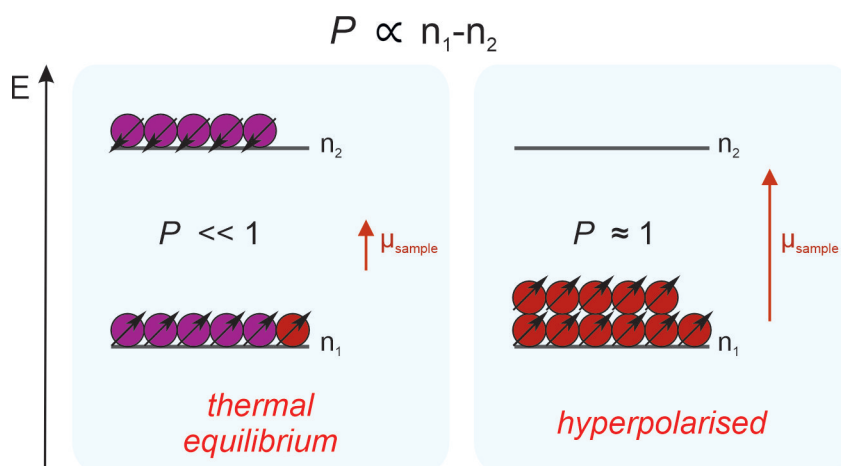


FIGURE 2.9: Illustration comparing the population dispersion across a thermally polarised and hyperpolarised nuclear spin system. The red spheres correspond to the NMR visible nuclei that contribute to the magnetic moment of the sample,  $\mu_{\text{sample}}$ .

to  $p\text{-H}_2$  corresponds to population transfer from the  $\text{H}_2$  triplet states to the pure singlet state  $S_0$ , creating a highly polarised nuclear spin system; at compressed helium temperatures ( $\sim 35\text{ K}$ ) 94.3%  $p\text{-H}_2$  enrichment is achieved, corresponding to almost 100% spin polarisation. The PHIP hyperpolarisation techniques<sup>24,31</sup> provide a route toward increasing the spin polarisation of target nuclear spin systems far beyond the limits of thermal equilibrium, as illustrated in FIGURE 2.9, to massively enhance SNR and overcome the poor sensitivity of NMR detection.

## 2.4 Signal Amplification By Reversible Exchange

SABRE is a variant of PHIP that was first demonstrated by Adams et al. in 2009.<sup>31</sup> As a  $p\text{-H}_2$  based hyperpolarisation technique, SABRE relies on the transfer of polarisation from the singlet state  $S_0$  of  $\text{H}_2$  to nuclear spin states on the target analyte. Achieving this requires breaking the symmetry of the two  $p\text{-H}_2$ -derived hydrides to unlock their hyperpolarisation, and requires the introduction of magnetic inequivalence between them. The conversion process of  $o\text{-H}_2$  to  $p\text{-H}_2$  utilises a paramagnetic species as the source of magnetic inequivalence. In SABRE, magnetic inequivalence is achieved when  $p\text{-H}_2$  binds via oxidative addition to the metal centre of a SABRE catalyst which has been specially designed to ensure the bound hydrides experience different  $J$ -coupling interactions with neighbouring nuclei (e.g.  $\text{AA}'\text{B}$  or  $\text{AA}'\text{BB}'$  spin system, where A corresponds to the  $p\text{-H}_2$  derived hydrides).

SABRE relies on a catalytic cycle to achieve continuous hyperpolarisation of a target analyte. FIGURE 2.10 outlines the SABRE catalytic cycle using the Ir-IMes ( $[\text{IrCl}\{\text{COD}\}\{\text{IMes}\}]$ , where IMes = 1,3-bis{2,4,6-trimethylphenyl}imidazol-2-ylidene and COD = cis,cis-1,5-cyclooctadiene) pre-catalyst. Mixing of the pre-catalyst with  $p\text{-H}_2$  gas and the substrate of interest in the presence of an organic solvent leads to the formation of the SABRE-active catalyst. Exposure of this species to a weak magnetic field in the ULF regime ( $\mu\text{T}$  -  $\text{mT}$ ) drives polarisation transfer from the  $p\text{-H}_2$

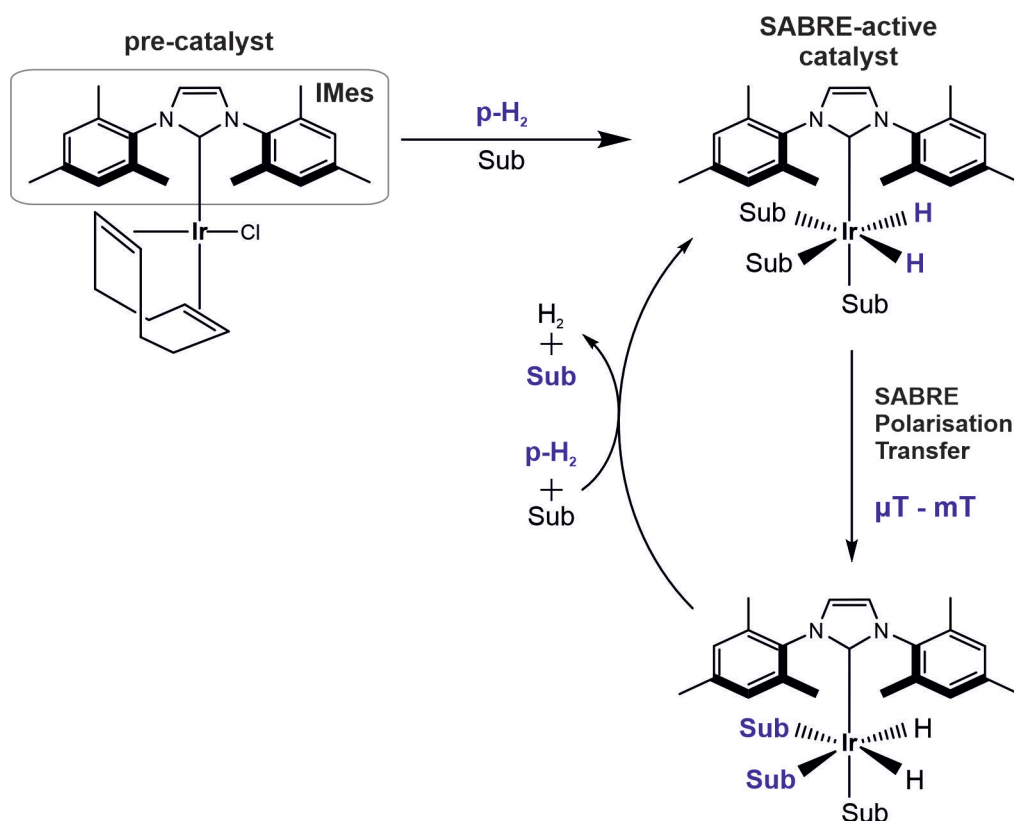


FIGURE 2.10: SABRE catalytic cycle for the production of hyperpolarised substrate in solution using the Ir-IMes pre-catalyst. Reversible binding of  $\text{H}_2$  and the substrate (Sub) is necessary to drive the catalytic reaction, and weak magnetic fields are required to drive SABRE polarisation transfer to the catalyst bound substrate molecules. Blue font denotes hyperpolarised atoms or molecules.

derived hydrides to the substrate. At this point, hyperpolarisation of the hydrides is depleted and the hyperpolarised substrate ligands detach from the SABRE-active catalyst, leaving behind an empty binding site that  $p\text{-H}_2$  and the substrate compete for. When there is oxidative addition of fresh  $p\text{-H}_2$  into the binding site, the 'old' hydrides reductively eliminate to form  $\text{H}_2$  gas and again leave behind an empty binding site. In the case where this is followed by the binding of a new substrate molecule, the initial form of the SABRE active catalyst is regained (see FIGURE 2.10). Since the binding of  $p\text{-H}_2$  and substrate molecules is reversible and the substrate molecule is not chemically altered over the course of the catalytic cycle, the SABRE reaction can be continuously repeated with a fresh supply of  $p\text{-H}_2$  to build hyperpolarised substrate in solution.

As already stated, the binding of  $p\text{-H}_2$  to the SABRE pre-catalyst unlocks its hyperpolarisation. If this occurs in the ULF regime and in unison with the binding of a substrate molecule, the polarisation on the singlet state, which is NMR silent, can be efficiently transferred to the substrate (SABRE polarisation transfer) where it can be detected by NMR for the acquisition of hyperpolarised signals. This is because in the ULF regime the energy of the nuclear spin states approach each other, and at certain magnetic fields they cross. The strong coupling interactions (see Eq. 2.15) between nuclei in the ULF regime lead to a Level Anti-Crossing (LAC), also known as an avoided crossing, between the nuclear spin states. The LAC provides a pathway for

coherent polarisation transfer in the ULF regime.<sup>93</sup>

The work by Pravdivtsev et al. in 2012<sup>54</sup> provided an understanding of the role of LACs in the experimentally observed magnetic field dependence of SABRE. The sign and enhancement level of the SABRE-polarised NMR signal for a range of N-heterocyclic substrates was shown to follow the magnetic field dependence predicted by the theory of LACs. Since this theory was constructed from a model  $AA'MM'$  4-spin system, it cannot be used to accurately calculate the magnetic fields required for LACs within the complexity of a real SABRE system that contains many nuclear spin states from the three substrate molecules and ligand. A major simplification of LAC theory gives rise to a general equation that provides a good approximation of the magnetic field strength required for an LAC involving the singlet state and target nuclei on the substrate. This equation is known as the Polarisation Transfer Condition (PTC):<sup>39,55</sup>

$$\begin{aligned} J_{H_A H_{A'}} &= \Delta\nu_{H_A B_{(H,X)}} & (2.35) \\ \Delta\nu_{H_A B_{(H)}} &= \frac{\gamma_H B_{PTF} (\delta_{H_A} - \delta_{B_H})}{2\pi} \\ \Delta\nu_{H_A B_{(X)}} &= \frac{B_{PTF} (\gamma_H - \gamma_{B_X})}{2\pi} \end{aligned}$$

where  $J_{H_A H_{A'}}$  is the dominant  $J$ -coupling interaction between the magnetically inequivalent  $p$ -H<sub>2</sub> derived hydrides,  $\Delta\nu_{H_A B_{(H,X)}}$  is the frequency difference between the hydride and target nucleus-B which can either be a proton ( $B_H$ ) or heteronucleus ( $B_X$ ),  $\delta_{H_A}$  and  $\delta_{B_H}$  are the chemical shifts of the <sup>1</sup>H nuclei containing and receiving hyperpolarisation, respectively, and  $\gamma_{B_X}$  is the gyromagnetic ratio of the heteronucleus receiving hyperpolarisation.

The condition states that the transfer of polarisation from the singlet state on the hydride to a target nucleus on the substrate is most efficient when the dominant  $J$ -coupling interaction within the SABRE-active catalyst coupling network, which is generally  $J_{H_A H_{A'}}$ , is matched to the Larmor frequency difference between the source and target of SABRE polarisation transfer. Therefore, the magnetic field strength that satisfies the matching condition,  $B_{PTF}$ , is approximated to be the magnetic field at which an LAC between the singlet state and the target substrate nuclei occurs. FIGURE 2.11 demonstrates the occurrence of an LAC between nuclear spin states  $|m\rangle$  and  $|n\rangle$  at  $B_{PTF}$ .

Relevant to the nuclei investigated in this thesis, the PTC predicts an optimal PTF of  $\sim 6.6$  mT for coherent homonuclear polarisation transfer to <sup>1</sup>H ( $\gamma_H B^0 \{\delta_{H_A} - \delta_{B_H}\} \approx 32$  ppm,  $J_{H_A H_{A'}} \approx 9$  Hz), and  $3.6$   $\mu$ T for coherent heteronuclear polarisation transfer to <sup>19</sup>F ( $\gamma_H - \gamma_{B_X} = 15.7 \times 10^6$  rad s<sup>-1</sup> T<sup>-1</sup>).

While optimising the PTF is crucial to maximise the efficiency of SABRE polarisation transfer from  $S_0$  to the substrate, optimisation of the chemistry of the SABRE reaction is first required to ensure  $p$ -H<sub>2</sub> and the substrate molecules can bind simultaneously and reversibly to the pre-catalyst to drive the SABRE catalytic cycle. This requires the careful design of a pre-catalyst containing ligands that are labile enough to dissociate, after which the catalyst must have sufficient vacant sites

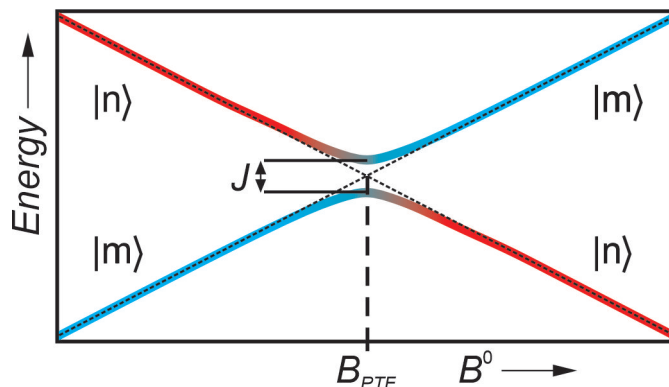


FIGURE 2.11: Illustration of the formation of an LAC between two strongly coupled nuclear spin states  $|m\rangle$  (blue) and  $|n\rangle$  (red) to allow coherent polarisation transfer between them. The strong coupling constant  $J$  leads to an avoided crossing between the two states.

to coordinate the substrate and  $p$ -H<sub>2</sub>, where these must also bind to the catalyst but be labile enough to dissociate. Reversibility in their binding is dictated by the catalyst-substrate and catalyst-hydride binding strength, parameters that can be altered and tuned with the use of ligands on the pre-catalyst of different sizes (steric hindrance) and electronegativity.

Crabtree's catalyst,  $[\text{Ir}(\text{COD})(\text{PCy}_3)(\text{Py})][\text{BF}_4]$  (Ir-based hydrogenation catalyst), was first implemented for SABRE.<sup>31,94</sup> A modified version of Crabtree's catalyst containing an N-heterocyclic carbene (NHC) ligand<sup>95</sup> was later implemented, where the Ir-IMes catalyst and slightly different variants of it<sup>96</sup> were found to yield the best SABRE results for a range of target substrates. Ir-IMes (see FIGURE 2.10), which has been employed for SABRE in this work is therefore a well documented pre-catalyst. The reaction kinetics of reversible binding of the substrates to Ir-IMes is relatively slow on an NMR timescale and allows for the resolved detection of the hyperpolarised bound and free forms of the substrate. Two equatorial and one axial position is filled by substrate molecules in the activated form of the SABRE-catalyst, where they have different chemical shifts and experience different  $J$ -coupling interactions with the hydrides that are on the equatorial position. The equatorial substrate molecules are much more strongly hyperpolarised by SABRE in the ULF regime as they have a larger  $J$ -coupling to the hydrides (*trans*-coupling) than the axial substrate (*cis*-coupling). Furthermore, the axial substrate has a much slower exchange rate with free substrate molecules than the equatorial substrate.

The lifetime of the active SABRE complex is a key parameter that must also be optimised, and depends on the binding strength of the substrate to the catalyst. Hyperpolarisation of the substrate requires both it and  $p$ -H<sub>2</sub> be bound to the catalyst so that the unlocked hyperpolarisation on the hydride is directed to the substrate. However, the amount of polarisation that is transferred varies with time and is related to the strong  $J$ -coupling interaction between the hydride and the target nucleus on the substrate,  $J_{HX}$ , which mediates the transfer. The optimal lifetime of the active SABRE complex depends on the dissociation rate of the bound substrate, as it is this step that subsequently drives dissociation (reductive elimination) of the bound hydrides, and is equal to a 1/2-cycle of the  $J$ -evolution ( $1/2J_{HX}$ ).<sup>97,98</sup> If the lifetime of the active SABRE complex is much shorter than  $1/2J$  it will not receive sufficient

polarisation before substrate dissociation, but if it is much longer, the transferred polarisation will decay via  $T_1$  relaxation and also begin transferring back to the singlet state. The estimated optimal dissociation rate for pyridine is therefore equal to  $2\text{ s}^{-1}$  (500 ms) due to the  $\sim 1\text{ Hz}$  J coupling between the  $p\text{-H}_2$  derived hydride and the substrate *ortho*-proton.

N-heterocyclic substrates bind to Ir-IMes with an optimal lifetime for SABRE polarisation transfer. It has therefore been employed for the hyperpolarisation of many pyridine derivatives.<sup>2,52,56,84,99–103</sup> Fluoropyridines are the substrates chosen in this work as they provide an optimal chemical SABRE system to allow focus on the polarisation transfer mechanisms to  $^1\text{H}$  and  $^{19}\text{F}$ . The substrates used are 3-fluoropyridine (3-FP), 3,5-difluoropyridine (3,5-DFP), 3,5-bis(trifluoromethyl)pyridine (3,5-TFMP) and 3-difluoromethylpyridine (3-DFMP).

The choice in solvent for SABRE is also important as the pre-catalyst and substrate must be soluble in it. The effective Ir-IMes pre-catalyst is compatible with a wide range of organic solvents, however, it is not soluble in water, thus limiting its use in bio-compatible hyperpolarised SABRE experiments.<sup>104</sup> Protio solvents are generally avoided in the acquisition of thermally polarised spin systems because they produce very intense  $^1\text{H}$  signals that saturate the  $^1\text{H}$  spectrum and can overlap with analyte peaks. More expensive deuterated solvents are used instead as they produce significantly weaker  $^1\text{H}$  solvent signals. Hyperpolarised spin systems that produce analyte peaks several orders of magnitude stronger than the solvent peak are compatible with protio solvents, however, the protio solvent can sometimes compete with the substrate in binding to the catalyst and consequently become hyperpolarised and generate a SABRE-polarised  $^1\text{H}$  signal. This was observed using MeOH.<sup>2</sup> The use of co-solvents that bind with a higher affinity to the catalyst were shown to prevent solvent hyperpolarisation and thus increase the efficiency of SABRE.<sup>105</sup>

Solvents play a role in the relaxation of nuclear spin systems, and can therefore influence the hyperpolarised lifetimes of the substrate molecules in solution. The use of deuterated solvents increases the  $T_1$  relaxation time of the nuclei on the substrate to allow an increase in SABRE efficiency.<sup>102,106</sup> This is because there is a reduction in the dipole–dipole interactions between the  $^1\text{H}$  nuclei on the solvent and substrate, where dipole–dipole interactions act as a source of  $T_1$  relaxation. The same effect was observed when substrates and pre-catalyst ligands were deuterated.<sup>102,107</sup>

A key aspect of the SABRE experiment is activation of the pre-catalyst to form the SABRE-active catalyst. A detailed account of the reaction pathways involved in the activation of the Ir-IMes pre-catalyst via mixing of the precatalyst, substrate and solvent in the presence of  $p\text{-H}_2$  pressure (see FIGURE 2.10) to form the SABRE-active catalyst,  $\text{Ir}[(\text{IMes})(\text{H})_2(\text{sub})_3]^+ \text{Cl}^-$ , is given in the literature.<sup>98,99,101</sup> Acquisition of reproducible and comparable SABRE results requires complete activation of the pre-catalyst since it is the active-catalyst that mediates SABRE polarisation transfer. The concentration ratio of precatalyst to substrate must be at least 1:3 (3 equivalents of substrate) to ensure full activation, however, higher equivalents are typically used to yield stronger hyperpolarised signal intensities as there is more substrate available for hyperpolarisation, and hence a larger concentration of hyperpolarised substrate in

solution is established. For this reason, the SABRE experiments in this work have used relatively large substrate excesses (20 - 50 fold) to maximise the absolute hyperpolarised signal intensity and achieve sufficient SNR. Nonetheless, whilst increasing substrate concentration increases the absolute signal intensity, the hyperpolarisation of the substrate as a fraction of its thermal polarisation decreases, indicating a reduction in SABRE efficiency.<sup>55,99</sup>

## 3 | Earth's Field NMR System

### 3.1 Introduction

All EFNMR experiments in this work were performed on the commercial Terranova-MRI system (Magritek, Germany) which was originally designed as a teaching tool to help users run and understand simple NMR and Magnetic Resonance Imaging (MRI) experiments. The excellent homogeneity of the Earth's magnetic field that leads to longer spin relaxation times and high spectral resolution motivated the use of the Terranova-MRI system in executing a range of NMR techniques in the ULF regime.<sup>71, 72, 108-111</sup> It is also beneficial in this work for the interpretation of SABRE-polarised  $^1\text{H}$  and  $^{19}\text{F}$  signals in the ULF, where strong coupling between nuclei and the lack of chemical shift resolution produces EFNMR signals with complex splitting patterns. The homonuclear couplings in fluorinated pyridines ( $< 1$  Hz) therefore requires sub-hertz spectral resolution to be accurately observed.

As previously mentioned, studying the SABRE polarisation transfer mechanism and optimising it requires the *in situ* detection of SABRE-polarised signals without the need to transfer the sample between the polarisation transfer and detection field. The Terranova-MRI instrument is crucial to this as the compact and accessible nature of its probe makes it possible to integrate external solenoids that can provide control over the magnitude and orientation of the external field to enable switching between the polarisation transfer and detection fields. The bore can also be easily attached to an automated  $p\text{-H}_2$  gas flow system for *in situ* bubbling of the sample during the EFNMR experiment. Included with the Terranova-MRI probe is a solenoid (polarising coil) that was designed to generate mT magnetic fields along the transverse plane to polarise the sample before EFNMR detection and improve sensitivity. This is no longer necessary when SABRE is the method of hyperpolarisation as it can induce a much larger polarisation of the nuclear spin system, thus freeing up the polarising coil to generate mT PTFs for homonuclear polarisation transfer ( $\sim 6.6$  mT). With the addition of an external solenoid, the Terranova-MRI system will also have control over the external field in the  $\mu\text{T}$  regime for heteronuclear polarisation transfer to  $^{19}\text{F}$  ( $\sim 3.6$   $\mu\text{T}$ ). Together, both coils provide access to the full SABRE PTF range ( $\mu\text{T}$ -mT).

The work presented in section 3.2 briefly describes the technology underpinning the Terranova-MRI instrument, including the built-in experiments and procedures involved in setting up the Terranova-MRI probe for the acquisition of EFNMR signals

with sub-hertz linewidths from hundreds of millilitres of sample. However, in order for the EFNMR system to successfully carry out *in situ* SABRE polarisation, a BH600-3-B triaxial Helmholtz coil array (Serviciencia, S.L, Spain) was added to the Terranova-MRI setup. The work presented in section 3.3 describes the procedure for aligning the external field, naturally orientated  $\sim 23.5^\circ$  from the vertical axis due to the Earth's axial tilt, using the Helmholtz coil array, and how this enables linear shifting of the detection field to higher magnetic fields for greater conductivity of the  $B^1$  coil to improve the efficiency of EFNMR detection. The alignment of the external field was also taken advantage of to improve RF pulse calibration to optimise an RF pulse that is able to excite both the  $^1\text{H}$  and  $^{19}\text{F}$  spins simultaneously. This will be beneficial for the acquisition of the SABRE polarised  $^1\text{H}$  and  $^{19}\text{F}$  EFNMR signals of the target fluorinated pyridines.

## 3.2 Terranova-MRI System

### 3.2.1 Standard Operation and Procedures

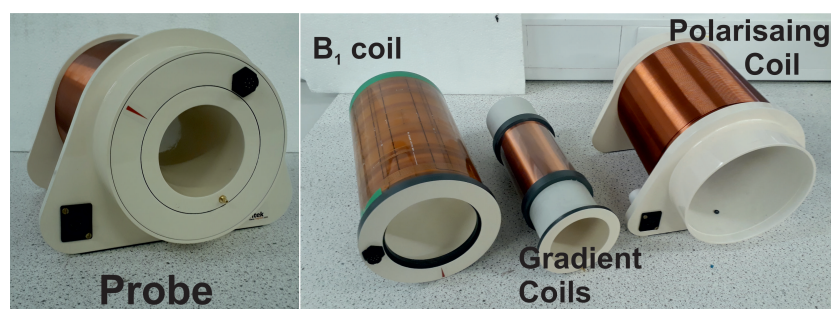


FIGURE 3.1: The Terranova-MRI probe (left) consists of 3 components (right): the polarising coil for polarisation of the sample before detection, the transmit-receive coil ( $B^1$  coil) for RF pulsing and NMR detection, and the gradient coils for shimming the probe to reduce local magnetic field inhomogeneities.

The Terranova-MRI probe shown in FIGURE 3.1 is made up of three coils: the polarising coil on the outside of the probe; the transmit-receive ( $B^1$ ) coil and the gradient coils, where the  $B^1$  and gradient coils are located inside the bore of the probe (see FIGURE 3.1). The gradient coils consist of x, y and z-coils that generate magnetic fields along the z-direction whose magnitudes vary linearly along the x, y and z directions. Such magnetic fields are referred to as magnetic field gradients. Magnetic field inhomogeneities can be removed from a sample by exposing it to the magnetic field gradients produced by the gradient coils in a process called 'shimming', whereby the current through the three coils iteratively samples across a user-defined range until the signal linewidth is minimised. Shimming the probe helps to improve spectral resolution and hence the quality of the NMR data. The gradient coils can also be used to create position encoded precession for MRI. The  $B^1$  coil is a transmit-receive coil used to transmit Audio Frequency (AF) radiation and detect the precession of magnetisation in the transverse plane.

Unlike the  $B^1$  and gradient coils, the polarising coil is generally not found in standard high-field NMR probes but is essential to detection on the Terranova-MRI system. Its purpose is to generate a temporary magnetic field that is much stronger than  $B^E$  to increase the thermal polarisation of the sample nuclear spin system and improve the sensitivity of EFNMR detection. A current is passed through the polarising coil to generate a millitesla magnetic field (6 A provides an 18.8 mT field). It is important to note that the polarising coil lies along the transverse plane, and since nuclear spins always align with the dominant field, the polarisation produced by the polarising coil will also lie along the transverse plane. For this reason, the current through the polarising coil must be switched-off adiabatically to allow the spins to re-align with  $B^E$  whilst maintaining their hyperpolarisation (see FIGURE 3.2) so that they may be detected with enhanced sensitivity. Pre-polarisation is essential for EFNMR detection because even samples with large volumes are not observed without it (e.g. a 500 mL water sample).

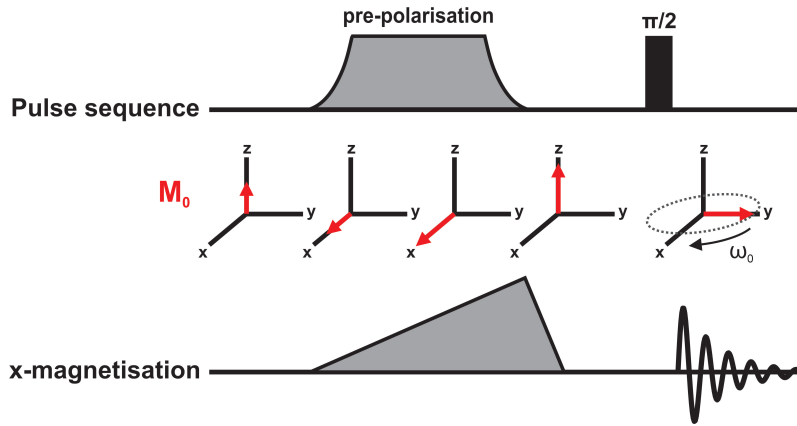


FIGURE 3.2: A schematic demonstrating the alignment and strength of the net magnetisation of the sample,  $M^0$ , during the pre-polarising step, where a current is applied through the polarising coil to generate a magnetic field along the  $x'$ -axis. The current is turned off adiabatically to maintain the hyperpolarisation of the spin system as the spins relax in the presence of the Earth's magnetic field. This figure has been adapted from a figure in the Terranova-MRI manual.<sup>1</sup>

FIGURE 3.3 displays the simplest EFNMR experiment that is used for the acquisition of EFNMR signals. The experiment is initiated with the turning on of the shims, followed by the pre-polarisation step to hyperpolarise the sample. A  $\pi/2$  ( $90^\circ$ ) RF pulse is generated by the  $B^1$  coil immediately after pre-polarisation and is used to place the net magnetisation ( $M_0$ ) along the transverse plane where NMR detection is maximised. This is followed by an acquisition delay,  $t_{acq}$ , which allows the current through the  $B^1$  coil to dissipate (coil ring down) before the  $B^1$  coil is used to detect transverse magnetisation for acquisition of the FID. Without  $t_{acq}$  the acquired NMR signal would be saturated by the resultant current in the coil from the RF pulse because it is significantly larger than the NMR response.

The parameters  $A_{pol}$  and  $t_{pol}$  represent the pre-polarising pulse amplitude and duration and are equal to 6 A and 4 s, respectively. An amplitude of 6 A corresponds to a pre-polarising field of 18.8 mT, calculated using Eq. 3.1, where  $I$  is the current through the coil,  $B_{mag}$  is the induced magnetic field and  $C_c$  is the coil constant, equal to  $3.13 \text{ mT A}^{-1}$  for the polarising coil (see Table 3.1). The parameters  $A_{RF}$  and  $t_{RF}$

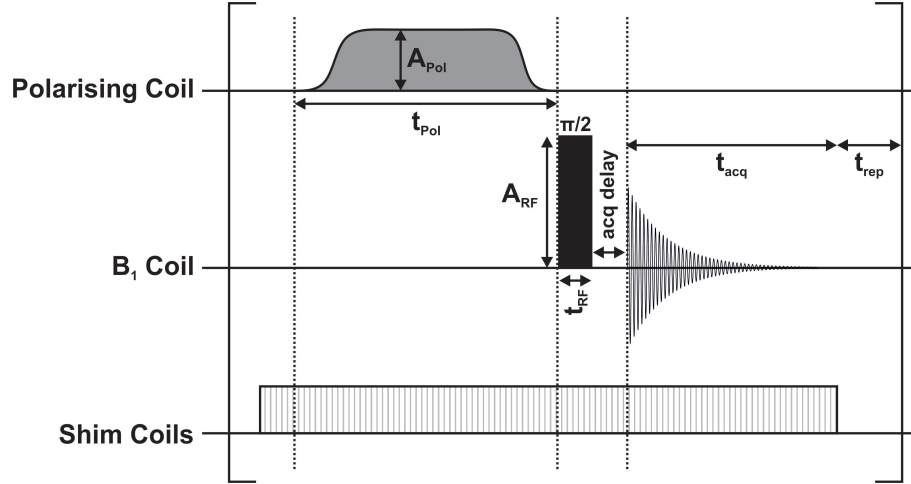


FIGURE 3.3: The simplest EFNMR experiment consisting of a pre-polarising pulse generated using the polarising coil, followed by a  $\pi/2$  rad nutation of the spins and subsequent detection of their transverse magnetisation using the  $B^1$  coil.

represent the RF pulse amplitude and duration, respectively, which must be optimised to achieve a  $\pi/2$  rad nutation (see section 3.3.3). The experiment ends with a repetition delay,  $t_{rep}$ , which, for traditional NMR experiments, is given a duration of  $5 T_1$  to allow the nuclear spin system to return to equilibrium under  $B^0$  before the start of the next experiment. For EFNMR experiments on the Terranova-MRI spectrometer, the nuclear spin system equilibrates in the presence of the pre-polarising pulse with an ideal duration,  $t_{Pol}$ , of  $5 T_1$ . The  $t_{rep}$  delay is instead used to prevent over-heating of the polarising coil as a consequence of a large duty cycle and typically takes values of 5-15 s, where stronger currents through the polarising coil to generate stronger fields require longer  $t_{rep}$  delays.

$$B_{mag} = C_c I \quad (3.1)$$

Table 3.1: Table of coil constants,  $C_c$ .

Coil	Coil Constant, $C_c$ (mT A <sup>-1</sup> )
Polarising	3.133
Helmholtz (x,y,z)	0.3224

The sensitivity of EFNMR detection may be further improved via amplification of the acquired signal. One method of amplification is through tuning of the RLC circuit within the probe. This requires altering the capacitance of the RLC circuit until it oscillates at a frequency that resonates with the precession frequency of the signal of interest. Eq. 3.2 describes the relationship between the precession frequency,  $\nu$ , and capacitance,  $C$ , of the Terranova-MRI probe RLC circuit, where  $L$  is the inductance ( $0.3972 \pm 0.0007$  H) of the  $B^1$  coil and  $C_p$  ( $3.73 \pm 0.02$  nF) is the parasitic capacitance of the RLC circuit.

$$C = \frac{1}{(2\pi\nu)^2 L} - C_p \quad (3.2)$$

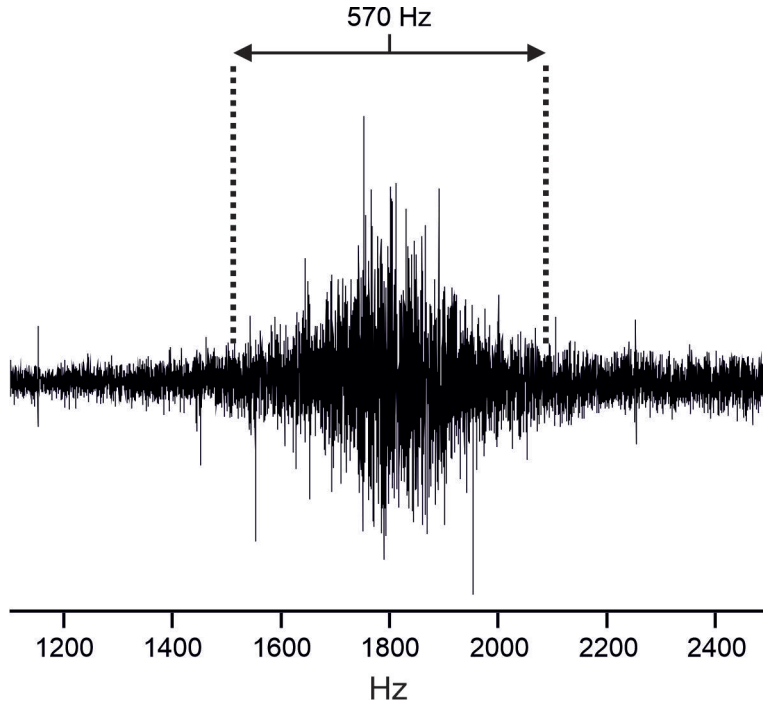


FIGURE 3.4: EFNMR spectrum acquired without a sample to observe the amplification range of the RLC circuit and the unsymmetrical and envelope-like shape of the amplified region. The data was acquired with a capacitance of 16.15 nF which tunes the RLC circuit to 1797 Hz.

The RLC circuit amplifies a range of frequencies, with the region of largest amplification being at the tuned frequency  $\nu$ . The amplification of the electrical signals detected by the  $B^1$  coil is shown in FIGURE 3.4, where the RLC circuit is shown to exhibit an unsymmetrical envelope shape with a rough amplification range of  $\pm 285$  Hz from  $\nu$ . The spectrum corresponds to an RLC circuit tuned to 1797 Hz with a capacitance of 16.15 nF. The range of frequencies amplified is much larger than  $\pm 285$  Hz but the level of signal amplification outside this range is minimal. Amplification is also achieved using a pre-amplifier, found in all NMR spectrometers that scales up the weak electrical signal to a higher voltage level.

An inherent problem with NMR detection in the Earth's magnetic field is that there is a misalignment between the spin and lab frames of reference. The lab frame is represented in 3D-space by  $x'y'z'$ -axes, with the  $B^1$  coil acting as the point of reference along the  $x'y'$  (transverse) plane. NMR convention states that  $B^0$  is aligned positively along the longitudinal plane of the spin frame, represented in 3D-space by  $xyz$ -axes. The misalignment between the two is demonstrated in FIGURE 3.5 and occurs because  $B^E$  is tilted away from the longitudinal plane of the lab frame ( $z'$ -axis) by an angle  $\theta$ , approximately equal to  $23.5^\circ$  which corresponds to the Earth's axial tilt. Angle  $\phi$  represents the position of  $B^E$  along the transverse plane. High-field NMR spectrometers do not have this issue because they are designed to generate fixed magnetic fields along the positive  $z'$ -axis that create a net longitudinal magnetisation of the sample at thermal equilibrium.

The issue of misalignment was managed previously in the literature<sup>72</sup> by rotating the probe about the  $z'$ -axis so as to place  $B^E$  along the  $x'z'$  plane ( $\phi = 0$ ). This

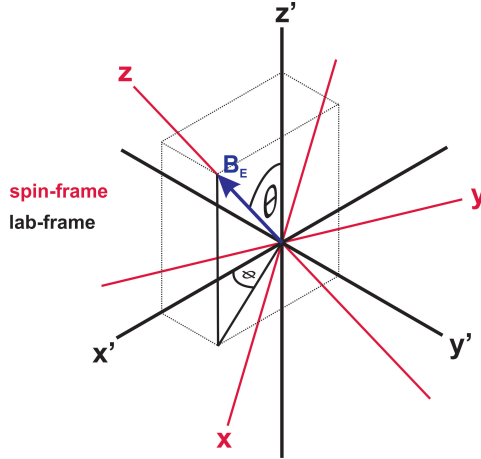


FIGURE 3.5: Due to the Earth's axial tilt of  $\theta \approx 23.5^\circ$ , the lab-frame and spin-frame axes do not align.  $B^E$  has a longitudinal and transverse component with respect to the lab frame that is defined by angles  $\theta$  and  $\phi$ , respectively.

simplified the picture as the  $y'$  component of  $B^E$  was removed and only the  $x'$  and  $z'$  components needed to be considered. In this project misalignment was overcome with the addition of triaxial (xyz) Helmholtz coil pairs to the Terranova-MRI system to shift  $B^0$  and position it along the vertical axis. The method is described in section 3.3.1. Alignment of the spin and lab frames creates a system in which there is an orthogonal (ideal) interaction between the spins in the sample and  $B^1$  during the RF pulse which helps to improve RF pulse calibration (see section 3.3.3). This in turn enables enhancement of the sensitivity of EFNMR detection and the design of more complex pulse sequences. Alignment also allows linear control of the effective field by the z-Helmholtz coil which generates magnetic fields along the  $z'$ -axis. Positive magnetic fields generated by the z-Helmholtz coil add onto  $B^0$  and increase the effective field experienced by the spins in the sample. This increases the Larmor frequency of the spins which in turn increases the conductivity of the  $B^1$  coil and therefore enhances the efficiency of NMR detection. Negative magnetic fields generated by the z-Helmholtz coil cancel with  $B^0$  and decrease the effective field. This is key for probing SABRE polarisation transfer to  $^{19}\text{F}$ , where the transfer is maximised at magnetic fields below  $B^E$ . SABRE polarisation transfer is covered in more detail in Chapter 5. The process of aligning the effective field with the vertical axis, and the corresponding improvements in RF pulses and EFNMR detection are covered in section 3.3.

### 3.2.2 Probe Setup

All experiments during the setup and optimisation of the EFNMR system were performed on a 14 cm (H) x 7 cm (D) bottle of water (500 mL).

The probe makes use of the naturally available Earth's magnetic field ( $\sim 50 \mu\text{T}$ ) for polarisation of the spin system and hence detection of the sample as described in section 3.2.1. Unlike high-field instruments, magnetic shielding cannot be implemented

on the Terranova-MRI probe as this would block out the Earth's magnetic field which acts as the external field ( $B^0$ ). The Terranova-MRI probe is therefore location sensitive and the quality of the EFNMR experiment will depend on minimising the effects of local magnetic field inhomogeneity and noise caused by the presence of magnetic materials and electronic equipment in the vicinity of the EFNMR probe. Stray magnetic fields and the instability of the Earth's magnetic field will cause small shifts in the nuclear Larmor frequencies during and between experiments, as well as reduce the local magnetic field homogeneity. This leads to broadening of the NMR signal and hence a loss of spectral resolution. An increase in the electrical noise picked up by the probe will lead to a lower SNR of the NMR signals further reducing sensitivity.

Once a location for the Terranova-MRI probe is chosen, it must be kept isolated from any sources of magnetic and electrical interference. The built-in 'Monitor Noise' experiment is used to help locate a spot for the probe where there is minimal electrical noise. In this experiment the probe detects the background electrical signal for a user-defined duration and calculates its Root Mean Square (RMS) in  $\mu\text{V}$ . The probe is moved around the lab and rotated horizontally until an RMS noise value of  $< 10 \mu\text{V}$  is detected. A signal can then be acquired on the probe to ensure it is located in a region of local magnetic field homogeneity. Acquiring a signal with a sub-Hertz linewidth after shimming on the probe indicates the presence of a homogeneous field. FIGURE 3.6 shows the  $^1\text{H}$  peak of water with a linewidth of 0.61 Hz after shimming. The Terranova-MRI probe is distanced by at least 1 m from sources of stray magnetic fields so that sub-hertz linewidths can be achieved with the very basic shimming procedure available to the instrument, utilising a set of x, y and z-gradient coils that only generate linear shims.

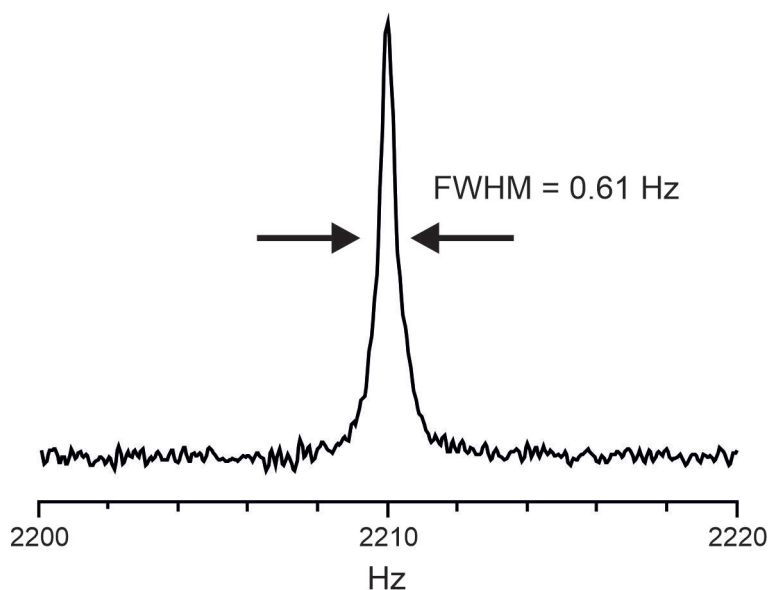


FIGURE 3.6: A shimmed  $^1\text{H}$  spectrum of water in a 14 cm (H) x 7 cm (D) bottle displays a well resolved signal with a Full Width Half Max (FWHM) of 0.65 Hz.

## 3.3 Improvements to Earth's Field NMR Instrument

### 3.3.1 Alignment of Spin and Lab Frames of Reference

Using a set of tri-axial Helmholtz coils the Earth's magnetic field can be directed away from its natural position and aligned with the  $z'$ -axis. The Helmholtz setup consists of 3 pairs of equidistant and perpendicular coils that form a cage around the Terranova-MRI probe which sits at the centre (see FIGURE 3.7). Applying a current through the x, y or z-coil pair generates a magnetic field in the  $x'$ ,  $y'$  or  $z'$  direction, respectively, that will add to the Earth's magnetic field to generate an effective magnetic field. The Helmholtz coils therefore offer control over the magnitude and orientation of the magnetic field experienced by the spins in the sample. The probe must be placed precisely in the middle of Helmholtz coil array as this is the region that experiences the best field homogeneity.

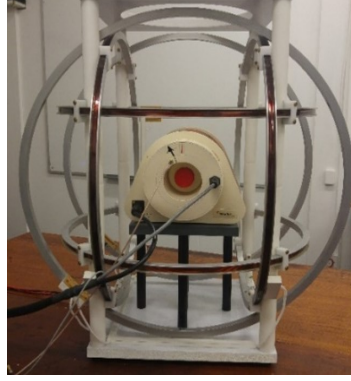


FIGURE 3.7: The EFNMR-Helmholtz setup consisting of the Terranova-MRI probe at the centre of 3 equidistant and perpendicular coils, each producing a magnetic field in the  $x'$ ,  $y'$  and  $z'$ -directions, respectively.

To align  $B^0$  with the  $z'$ -axis the EFNMR-Helmholtz setup was first rotated about the  $z'$ -axis to position  $B^E$  perpendicular to the  $x'$ -axis so that it lies in the  $y'z'$  plane ( $\phi = 90^\circ$  or  $270^\circ$ ). The angle,  $\phi$ , between  $B^E$  and the  $x'$ -axis was calculated by applying a range of current values through the x-Helmholtz coil to generate varying magnetic fields,  $B_{H_x}$ , along the  $x'$ -axis, while measuring the corresponding  $^1\text{H}$  Larmor frequency,  $\nu_H$ . The effective field,  $B^{eff}$ , experienced by the spins at each iteration of the current is calculated by dividing  $\nu_H$  by the proton gyromagnetic ratio,  $\gamma_H = 42.577 \text{ MHz T}^{-1}$ .  $B_{H_x}$  is calculated from the current through the x-Helmholtz coil. Plotting the data as  $(B^{eff})^2 - B_{H_x}^2$  against  $B_{H_x}$  exhibits a linear relationship that can be fit to Eq 3.3 (derived from the cosine rule), where  $(B^E)^2$  and  $-2B^E \cos \theta$  represent the y-intercept and gradient of the fit, respectively.  $\phi$  is extracted from the gradient and if it is not equal to  $90^\circ$ , the Helmholtz setup is rotated again and the procedure repeated.

$$(B^{eff})^2 - B_{H_x}^2 = (B^E)^2 - 2B^E B_{H_x} \cos \theta \quad (3.3)$$

The data in FIGURE 3.8 was acquired using current values through the x-Helmholtz coil of  $-15$ - $15$  mA in steps of  $5$  mA. The linear fit of the plot displays a y-intercept of  $1847.8 \mu\text{T}^2$  and a gradient value of  $0.1286 \mu\text{T}$ , signifying a  $B^E = 43.0 \mu\text{T}$  and an angle  $\theta = 90 \pm 0.3^\circ$ . The flat nature of the line of best fit indicates that  $B_{H_x}$  is perpendicular to the effective field, and that  $B_{\text{eff}}^2 - B_{H_x}^2$  is constant for all values of  $B_{H_x}$ .

Once  $B^E$  is along the  $y'z'$  plane, the y-Helmholtz coil can be used to generate a magnetic field,  $B_{H_y}$ , that is equal in magnitude but opposite in direction to its  $y'$ -component to cancel it out, thus aligning the external field with the  $z'$ -axis. A Magnoprobe<sup>TM</sup> 3 axis compass determined the direction of the  $y'$ -component to be along the  $-y'$ -axis. With the equation:  $B_{y'} = B_E \sin \theta$ , where  $B^E = 43 \text{ uT}$  (see FIGURE 3.8) and  $\theta = 23.5^\circ$  (Earth's axial tilt), an initial guess of the field along the  $y'$ -axis required to cancel-out the  $y'$ -component of  $B^E$  was made. The field required was estimated to equal  $-17.15 \mu\text{T}$  and corresponds to a current of  $+56.4 \text{ mA}$  (converted using the Helmholtz coil constant,  $C_c = 324.4 \mu\text{T A}^{-1}$ ) through the y-Helmholtz coil.

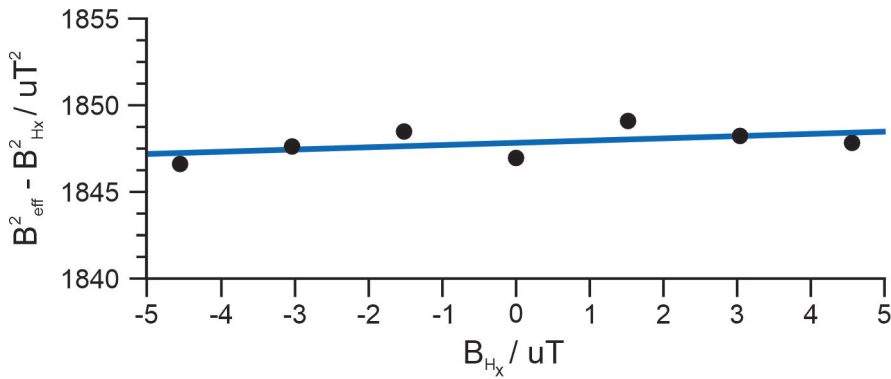


FIGURE 3.8: Plot of  $B_{\text{eff}}^2 - B_{H_x}^2$  against  $B_{H_x}$  used to calculate the angle  $\theta$  between the Earth's magnetic field and the  $x'$ -axis, equal to  $90^\circ$ .

The actual current required to align  $B^0$  with the  $z'$ -axis was calculated by measuring  $\nu_H$  at multiple current values through the y-Helmholtz coil, ranging from  $60$ - $85$  mA. The results were plotted and produced a U-shaped curve that is shown in FIGURE 3.9. The minimum of this curve indicates the current required to cancel-out the  $y'$ -component of  $B^E$  and align  $B^0$  with the  $z'$ -axis because this is the point where  $B^0$  is weakest.  $I_{H_y}$  values of  $70$ ,  $71$ ,  $72$  and  $73$  mA all gave the lowest  $\nu_H$  value of  $1586.3$  Hz.  $70$  mA was chosen as the minimum value and corresponds to a  $B_{H_y}$  ( $B_{y'}$ ) of  $21.3 \mu\text{T}$ . All EFNMR experiments were modified to include the implementation of this  $B_{y'}$  field throughout the entire experiment so as to maintain a constant alignment of the spin and lab frames of reference.

Although  $B^0$  was shifted to the  $z'$ -axis in this work from the  $y'z'$  plane, it is also possible to leave the probe in an arbitrary position and use the x and y-Helmholtz coil pairs together to cancel out the  $x'$  and  $y'$ -components of  $B^E$  in the same way.

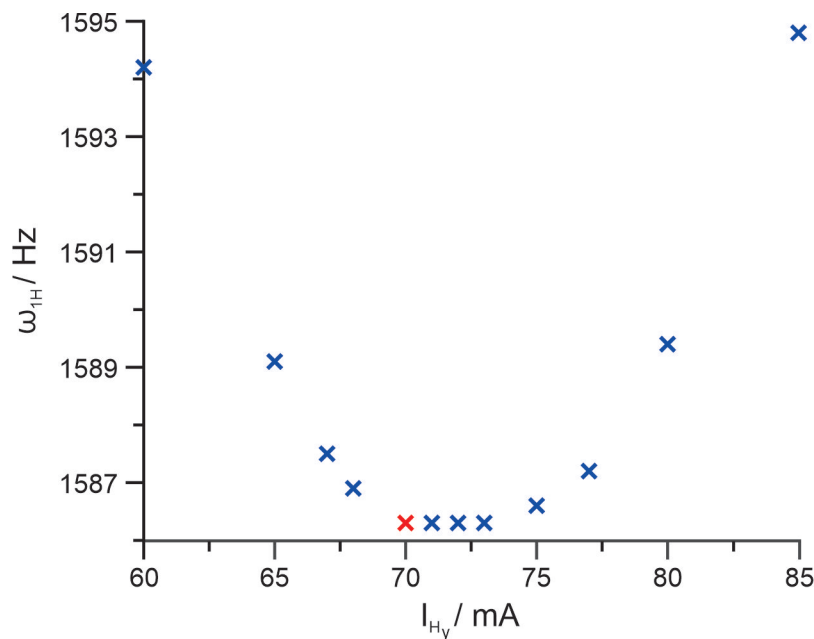


FIGURE 3.9: A plot of the proton Larmor frequency,  $\nu_{1H}$ , against the current through the y-Helmholtz coil,  $I_{H_y}$ . The minimum of the curve shows that alignment of  $B^0$  with the  $z'$ -axis was achieved using a current of +70 mA to generate a magnetic field  $B_{H_y} = 21.3 \text{ uT}$  along  $+y'$ . An  $\nu_{1H}$  of 1586.3 Hz indicates an external field of 37.3 uT.

### 3.3.2 Control of External Field

Access to the current through the z-Helmholtz coil offers control over the effective field experienced by the sample within the Terranova-MRI probe at different stages of an EFNMR experiment. The sensitivity of EFNMR detection can be slightly improved by using a positive current through the z-Helmholtz coil during NMR detection to generate a magnetic field,  $B_{H_z}$ , along the  $z'$ -axis that combines with  $B^0$  to increase the effective field experienced by the spins in the sample and hence improve the conductivity of the  $B^1$  coil (electrical induction increases with higher Larmor frequencies). This is carried out on a much larger scale in the high-field regime with the use of expensive NMR spectrometers that generate very strong magnet fields ( $\nu_H \geq 300 \text{ MHz}$ ). A negative current through the z-Helmholtz coil generates a  $B_{H_z}$  that counteracts  $B^0$  to weaken the effective field, and is used during heteronuclear SABRE polarisation transfer which requires a PTF below  $B^E$ . Stronger negative currents produce  $B_{H_z}$  values that overcome  $B^E$  to produce a negative effective field. This can be used to study how crossing zero-field from a negative to positive effective field, or vice versa, affects the non-equilibrium polarisation of a spin system by measuring  $T_1$  relaxation across the zero-field point. For EFNMR experiments that do not rely on SABRE polarisation, only positive  $B_{H_z}$  values to improve the sensitivity of EFNMR detection are required.

Alignment of  $B^0$  with the vertical axis simplifies control over the effective field as it develops a linear relationship with the magnetic field generated by the z-Helmholtz coil and  $B^0$ . The plot in FIGURE 3.10 shows this linear relationship over a  $B_{H_z}$  range of  $-53.53$  -  $19.46 \text{ uT}$ , produced by current values of  $-165$  -  $60 \text{ mA}$  in  $15 \text{ mA}$  steps. The  $B_{H_z}$  values of  $-43.79$ ,  $-48.66$  and  $-53.53 \text{ uT}$ , corresponding to current values of  $-165$ ,  $-150$ ,

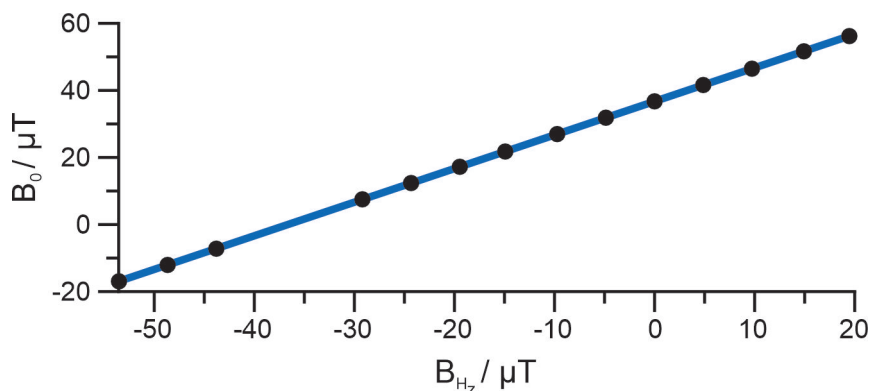


FIGURE 3.10: Plot showing the linear relationship between the effective field,  $B^0$ , and the magnetic field along the  $z$ -axis,  $B_{H_z}$ , generated by the  $z$ -Helmholtz coil. This relationship is only possible if  $B^0$  is parallel with the  $z$ -Helmholtz coil along the vertical axis and enables control over the effective field from negative to positive values. The line of best fit indicates a  $B^E$  of  $36.7 \mu\text{T}$ .

$-135 \text{ mA}$ , respectively, were strong enough to overcome  $B^E$  of  $36.7 \mu\text{T}$  (calculated from  $y$ -intercept of line of best fit in FIGURE 3.10) and generate a negative  $B^0$  where the effective field is pointing along the  $-z'$ -axis and the direction of precession is reversed. The gap in data points is due to difficulties in locating the  $^1\text{H}$  signal of water at a Larmor frequency of  $113.3 \text{ Hz}$  ( $B_{H_z} = -34.06 \mu\text{T}$ ) and  $-93.6 \text{ Hz}$  ( $B_{H_z} = -38.9 \mu\text{T}$ ).  $B^0$  was calculated from the  $\nu_H$  of water at each iteration of  $B_{H_z}$ .

A GW Instek GPP 4323 power supply was used to power the  $x$  and  $y$ -Helmholtz coils for alignment of  $B^0$  with the  $z'$ -axis. The minimum timing of the GW Instek GPP 4323 power supply is  $1 \text{ s}$  and it cannot invert the flow of current to switch between positive and negative current values. For this reason, an alternative power supply was used with the  $z$ -Helmholtz coil since it requires a supply of both positive and negative current, as well as the ability to switch between current values with millisecond precision. These conditions must be met to carry out heteronuclear SABRE polarisation transfer which requires first generating a negative  $B_{H_z}$  to counteract  $B^0$  and produce a PTF below  $B^E$ , and then instantly switch to a  $+z'$ -field that adds onto  $B^0$  to set the detection field. Millisecond precision is necessary to ensure the switch occurs before the RF pulse.

Within the Terranova-MRI spectrometer are four power supplies that can carry out commands on a millisecond time frame. Three of these power supplies are assigned to the  $x$ ,  $y$  and  $z$ -shim coils and one to the offset coil, designed to generate a positive magnetic field along the  $z'$ -axis to increase  $B^0$  and shift the Larmor frequency of the nuclei in the sample. Since the  $z$ -Helmholtz coil can also do this but with a more homogeneous field, the offset coil and its power supply were unused. Unlike the power supply of the offset coil which produces only positive currents at a maximum allowable current of  $2 \text{ A}$ , the power supply of each shim coil produces positive and negative currents at a maximum allowable current of  $\pm 200 \text{ mA}$ . The power supply of the  $y$ -shim coil was therefore connected to the  $z$ -Helmholtz coil and the offset coil power supply was connected to the  $y$ -shim coil where it could now only perform shimming with a positive field gradient along the  $y'$ -axis. Using an internal power supply to power the  $z$ -Helmholtz coil also has the benefit of simplifying the switching of currents during



FIGURE 3.11: Image of the EFNMR-Helmholtz setup with a thick copper wire wrapped around it to block out electrical noise and improve the SNR of signals detected by the  $B^1$  coil.

EFNMR experiments because they can be pre-defined in the pulse program macro within the Terranova-Expert software that operates the Terranova-MRI spectrometer.

Since NMR detection becomes more efficient at higher Larmor frequencies, a maximum allowable current of  $\pm 200$  mA through the z-Helmholtz coil allows for a maximum positive  $B_{H_z}$  of  $65 \mu\text{T}$  to create an effective field of  $108 \mu\text{T}$  and shift  $\nu_H$  to  $4598$  Hz. However, detection of signals at this frequency was avoided because the capacitor in the RLC circuit of the probe is limited to  $4.4$  nF which is equal to a maximum tuning frequency of  $2800$  Hz. Further limitations to increasing  $\nu_H$  were imposed by the EFNMR-Helmholtz setup which became a source of internal electrical noise for the Terranova-MRI probe after rewiring of the power supplies, especially at frequencies above  $2300$  Hz. A thick copper wire was wrapped around the EFNMR-Helmholtz setup and shorted to create a continuous current path that acts as a Faraday cage to limit the intensity of the noise introduced into the system by the z-Helmholtz coil and so improve SNR (see FIGURE 3.11). A  $\nu_H$  of  $2210$  Hz was settled on, requiring a  $B_{H_z}$  of around  $14.9 \mu\text{T}$  to generate a  $B^0$  of  $51.9 \mu\text{T}$  ( $\omega^0 = 1.39 \times 10^4 \text{ rad s}^{-1}$ ). Due to the natural instability of  $B^E$ , the exact current value required to produce a  $B^0$  of  $51.9 \mu\text{T}$  changed throughout the day, but was generally around  $46$  mA. Rewiring of the internal power supplies and implementation of the Faraday cage was carried out by James McCall, under the supervision of Dr Meghan Halse, as part of a Master's project.

The EFNMR experiment in FIGURE 3.3 can now be improved on to include the use of the y-Helmholtz coil pair in generating the  $y'$ -cancelling field of  $21.3 \mu\text{T}$  to align the spin and lab frames of reference (see section 3.2.1), and the addition of the z-Helmholtz coil pair which makes use of the spin and lab frame alignment to shift  $B^0$  to  $51.9 \mu\text{T}$  to improve the efficiency of NMR detection (see FIGURE 3.12). Both fields are implemented throughout the entirety of the EFNMR experiment. The positive  $B_{H_z}$  generated by the z-Helmholtz coil overlaps with the pre-polarising pulse ( $18.8$  mT) but has a negligible effect on the net field experienced by the spins during pre-polarisation as it is 3 orders of magnitude smaller. The detection field must be set before the RF pulse, but applying  $B_{H_z}$  at this point is problematic because when a

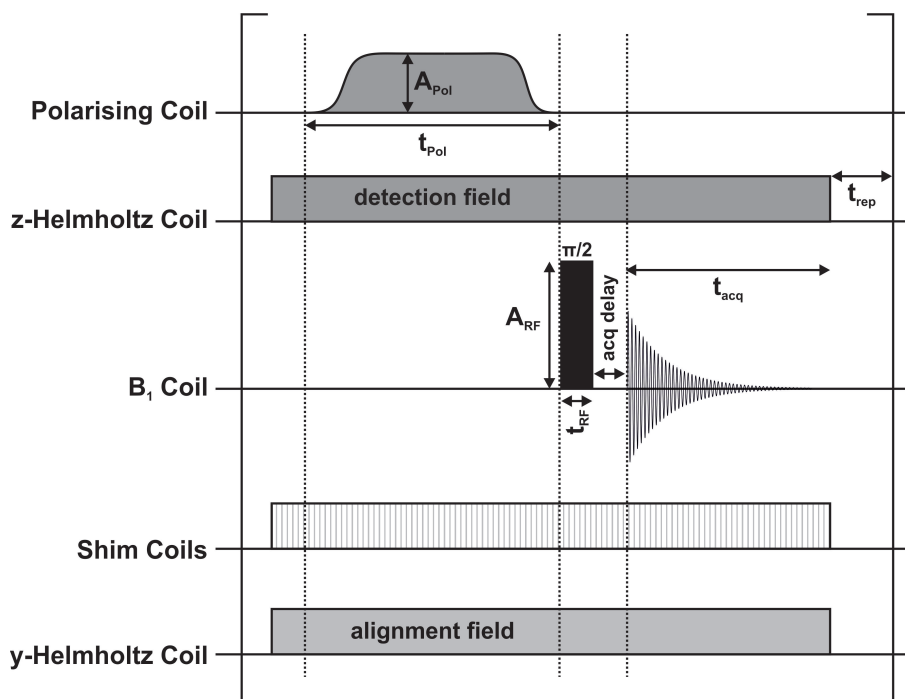


FIGURE 3.12: The improved EFNMR experiment contains the addition of the y and z-Helmholtz coil pairs that generate the  $y'$ -cancelling field ( $21.3 \mu\text{T}$ ) and the z-field ( $+15 \mu\text{T}$ ), respectively. The y-Helmholtz coil pair aligns the spin-frame with the lab-frame to improve EFNMR detection. The z-Helmholtz coil makes use of this alignment and produces a field that constructively interferes with  $B^0$  to increase the effective field to subsequently increase thermal polarisation and the signal intensity.

change in current is implemented by the power supply there is always an overshoot which generates a slightly stronger magnetic field. A few milliseconds is necessary to allow the current and subsequent field to stabilise to the desired value in a process referred to as coil ring down. During this time the sample will be exposed to a varying magnetic field that disrupts the nutation and subsequent detection process. Therefore it is preferable to apply this field at the start of the experiment at the same time as the application of the polarising field.

### 3.3.3 Pulse Calibration

Detection occurs when the  $B^1$  coil converts precessing transverse magnetisation of the spins in the NMR sample to an electrical signal via electromagnetic induction (Faraday detection). Detectable (transverse) magnetisation is created when  $M^0$ , which is originally positioned along the z-axis, interacts with a magnetic field,  $B^1$ , generated by the  $B^1$  coil, and is rotated (nutation) about its axis toward the transverse ( $x'y'$ ) plane (see FIGURE 3.13). When the spin-frame is aligned to the lab-frame,  $M^0$  is orientated along the  $z'$ -axis and the interaction with  $B^1$  is orthogonal, leading to an ideal (circular) nutation of  $M^0$ . When the spin and lab-frame are misaligned,  $M^0$  is orientated along the z-axis with a smaller  $z'$  component that interacts with  $B^1$  and the nutation follows a cone-like trajectory. After nutation,  $M^0$  precesses along the xy

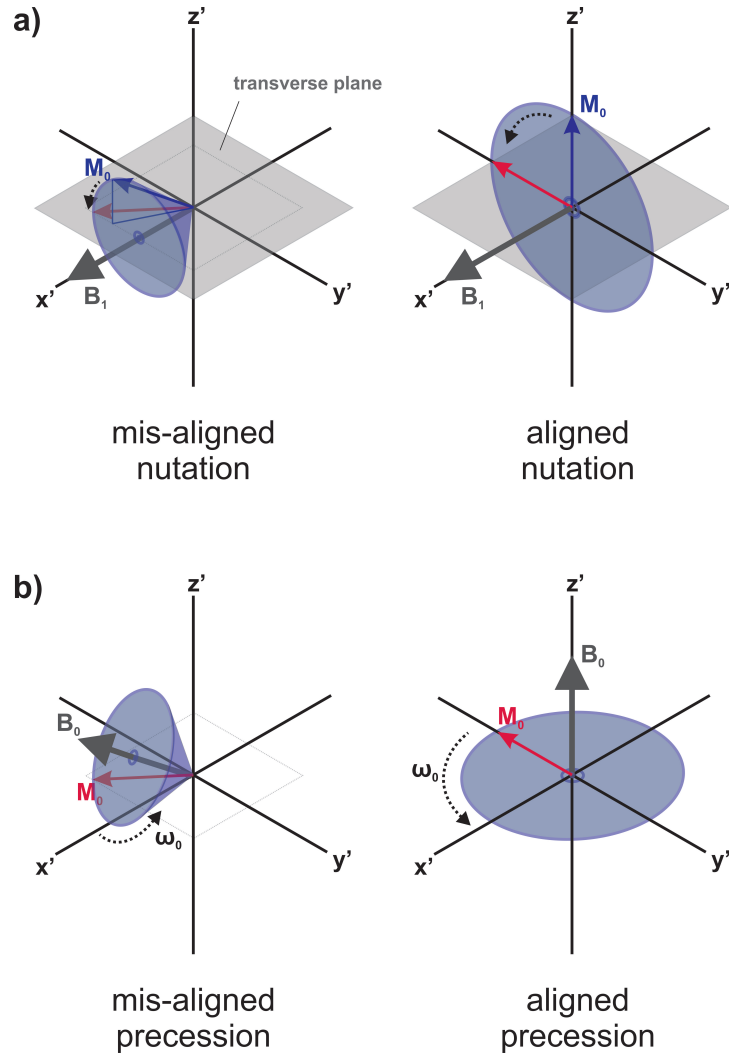


FIGURE 3.13: Illustration a) of the nutation of the net magnetisation of the sample,  $M^0$  (blue), about  $B^1$  toward the transverse plane, and b) of the precession of  $M^0$  about  $B^0$  at a frequency  $\omega^0$ , which is detected by the  $B^1$  coil also along the transverse plane (detection plane). The grey arrows represent the magnetic field with which  $M^0$  rotates about. The precessing magnetisation generates a stronger NMR signal if it is in parallel with the transverse/detection plane and the  $B^1$  coil, a condition that is met when the spin and lab-frames are aligned.

plane about  $B^0$  at a frequency  $\omega^0$ . Only the transverse component of  $M^0$  is picked up by the  $B^1$  coil, therefore, NMR detection is maximised when the  $xy$  and  $x'y'$  planes are aligned. A cone like precession of  $M^0$  occurs when the  $xy$  and transverse planes are not aligned and leads to the detection of a weaker NMR signal.

$B^1$  is better thought of as a pulse since the duration of its interaction with the sample is finite. The interaction is most effective when the  $B^1$  pulse is in resonance with  $\omega^0$ . This means that an RF pulse is used in the high-field regime (MHz) and an AF pulse in the ULF regime (kHz). Nonetheless, it is convention in NMR to refer to  $B^1$  as an RF pulse regardless of its frequency.

The angle of nutation,  $\theta_{nut}$  in radians, is equal to the product of pulse duration,  $t_{RF}$ , and pulse amplitude,  $A_{RF}$ , which can be expressed in terms of the angular nutation frequency,  $\omega_1$  (see Eq. 3.4a). Eq. 3.4b shows the relationship of  $\omega_1$  and  $\theta_{nut}$  with the

voltage,  $V_{RF}$ , through the  $B^1$  coil, where  $P_{RF}$  is the power of the RF pulse and  $\alpha$  is the proportionality constant in  $\text{s}^{-1} \text{V}^{-1}$ . Calibrating RF pulses requires experimentally calculating the values of  $V_{RF}$  and  $t_{RF}$  that produce the desired  $\theta_{nut}$ . This is carried out on the Terranova-MRI system with an RF amplitude-sweep experiment, where the improved EFNMR experiment in FIGURE 3.12 is repeated under a range of  $V_{RF}$  values but a fixed  $t_{RF}$ . Signal intensity is then plotted as a function of  $V_{RF}$  to produce a nutation curve (see FIGURE 3.14).

$$\theta_{nut} = t_{RF} \omega_1 \quad (3.4a)$$

$$\begin{aligned} \text{since } \omega_1 &\propto \sqrt{P_{RF}} \propto V_{RF}, \\ \theta_{nut} &= t_{RF} V_{RF} \alpha \end{aligned} \quad (3.4b)$$

$$S \propto M_+ = M^0 \sin [t_{RF} V_{RF} \alpha] e^{-\frac{V_{RF}}{T_{1\rho}}} \quad (3.5)$$

The RF amplitude-sweep experiment tracks the nutation path of  $M^0$  at each iteration of  $V_{RF}$  via acquisition of the signal intensity,  $S$ , which is proportional to the transverse magnetisation,  $M_+$ , and represents the projection of  $M^0$  onto the transverse plane. The nutation curve is an exponentially decaying sine curve described by Eq. 3.5. The first-order relaxation constant,  $T_{1\rho}$ , describes  $T_1$  relaxation of the nutating magnetisation in the presence of an RF field when in the rotating frame. The nutation angle that is achieved at each iteration of  $V_{RF}$  is read off from the nutation curve as illustrated by FIGURE 3.14. For example, a  $\pi/2$  rad nutation occurs at the first maximum of the sine curve which was achieved with a particular  $V_{RF}$  value, referred to as  $V_{\pi/2}$ .  $V_\pi$  is the voltage required for a  $\pi$  rad nutation and is found at the second node,  $V_{3\pi/2}$  is found at the first minimum and so on. Alignment of the spin and lab frames of reference is key for accurately calibrating RF pulses because the nutation shown in FIGURE 3.14 and described by Eq. 3.5 is dependent on the ideal nutation of  $M^0$ , caused by the orthogonal interaction between  $B^1$ , along the  $x'y'$  plane, and  $M^0$ , along the  $z'$ -axis.

Nutation angles can be more accurately calibrated by fitting the nutation curve to an exponentially decaying sine curve to acquire a calibration value in  $\text{V rad}^{-1}$  that allows  $V_{RF}$  to be calculated for any  $\theta_{nut}$ . EFNMR RF pulses on the Terranova-MRI system were calibrated by normalising the nutation curve and fitting it to Eq. 3.6a (see FIGURE 3.14), where  $\alpha_{cal}$  is the calibration constant in  $\text{V rad}^{-1}$ , and  $V^0$  and  $C$  are offsets in  $V_{RF}$  and  $S$  that account for the slow ramping up of the voltage through the  $B^1$  coil from 0-0.3 V and do not restrict the origin of the fit at coordinates of (0,0). The  $V_{RF}$  required for a desired  $\theta_{nut}$  is calculated from  $\alpha_{cal}$  and  $V^0$  using Eq. 3.6b. Fitting is performed on Matlab R2020a using the 'Curve Fitting' tool which optimises the experimental parameters ( $V^0$ ,  $C$ ,  $\alpha_{cal}$  and  $T_{1\rho}$ ) over a user-defined range until a fit with a minimal R-square value (measures goodness of fit) is achieved.

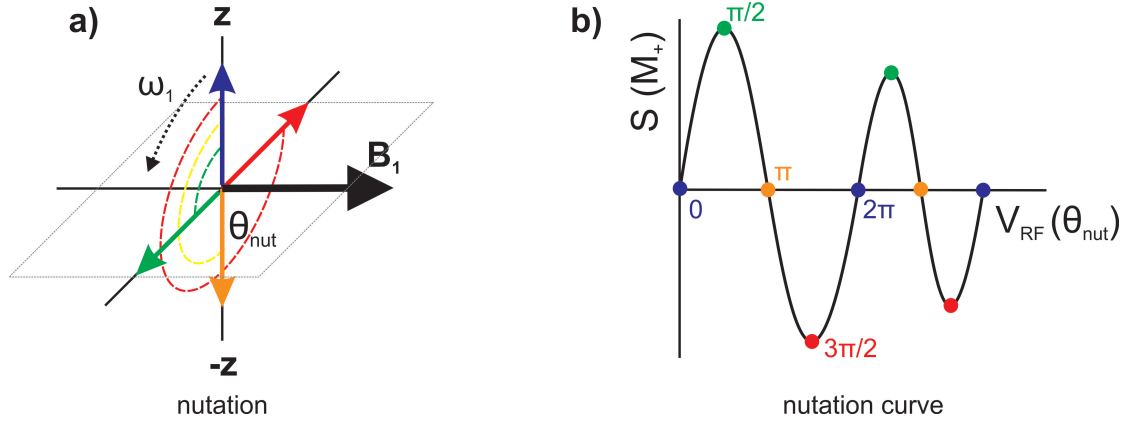


FIGURE 3.14: RF amplitude-sweep nutation curves track the nutation angle,  $\theta_{nut}$  of the spins about the axis of the RF pulse through calculation and plotting of the signal intensity,  $S$ , at each iteration of  $V_{RF}$ . The desired  $\theta_{nut}$  can be read from the sinusoidal nutation curve.

$$S = \sin \left[ (V_{RF} - V^0) \frac{1}{\alpha_{cal}} \right] \exp \left( -\frac{V_{RF}}{T_{1\rho}} \right) + C \quad (3.6a)$$

$$\begin{aligned} \text{since } \theta_{nut} &= (V_{RF} - V^0) \frac{1}{\alpha_{cal}} \\ V_{RF} &= V^0 + (\theta_{nut} \alpha_{cal}) \end{aligned} \quad (3.6b)$$

Choosing a  $t_{RF}$  value for the RF pulse on the Terranova-MRI system requires consideration of the pulse duration and the accuracy of its implementation by the spectrometer. RF pulses in high-field NMR have frequencies between  $10^6 - 10^8$  Hz. In a few microseconds the RF pulse will complete thousands of cycles and hence have a good interaction with the spins in the sample. ULF RF pulses of  $10^3$  Hz require durations of a few milliseconds to interact with the sample because an RF pulse with a duration of  $10 \mu\text{s}$  at 2000 Hz completes 0.02 cycles, but a pulse with a duration of 1 ms at 2000 Hz completes 2 cycles and will interact more effectively with the spins. Pulse durations should be kept as short as possible to minimise relaxation during the NMR experiment. The accuracy of  $t_{RF}$  depends on the instruments ability to efficiently turn-on/off the RF radiation from the  $B^1$  coil. On the Terranova-MRI system, energy from the  $B^1$  coil is dissipated very slowly and leads to continued emission of RF radiation for an indeterminate amount of time, even after the current through the coil is switched off. During this time the spins in the sample continue to nutate and do so at unknown frequencies which leads to inaccuracy and unreliability in  $t_{RF}$ . Using pulse durations of integer or half integer cycles of the RF frequency minimises this effect because the amplitude at these points is zero and energy dissipation is more efficient. Calibrating the RF pulse with an RF duration-sweep experiment is avoided on the Terranova-MRI system because of limitations imposed by the requirement of half or integer cycles of  $t_{RF}$  that complicate this calibration experiment. It is important to note that when defining the RF pulse duration in cycles, pulses with different frequencies but the same number of cycles will have different  $t_{RF}$  values ( $t_{RF} = \text{cycles}/\nu_{RF}$ ).

$\theta_{nut}$  is also proportional to the nuclear gyromagnetic ratio,  $\gamma$ , and the  $B^1$  field

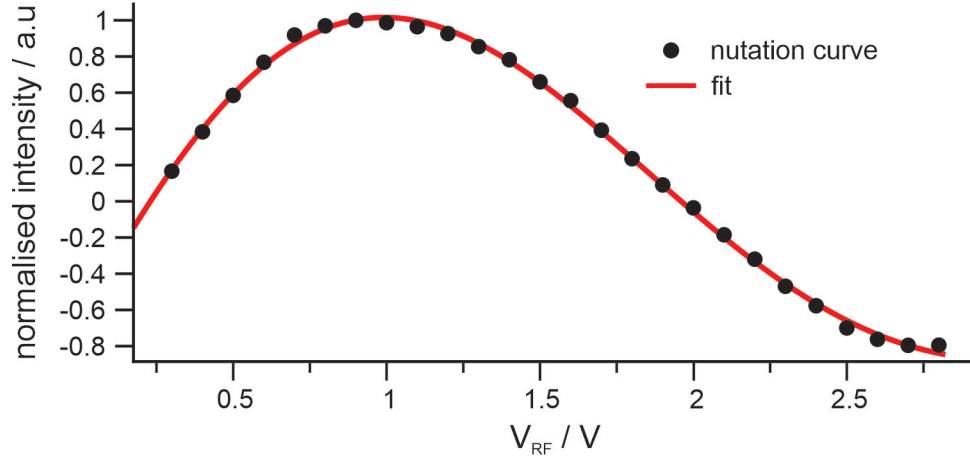


FIGURE 3.15: Calibration of the  $^1\text{H}$   $\pi/2$  pulse of water at 2210 Hz was performed by fitting the nutation curve (black) acquired from an RF amplitude-sweep experiment using a  $t_{RF}$  of 8 cycles, to an exponentially decaying sine curve (red). The desired nutation of  $\pi/2$  rad is achieved with a  $V_{RF}$  of 0.99 V ( $V_{\pi/2}$ ), calculated from Eq. 3.6b.

(see Eq. 3.7). This means that each nucleus type in the sample interacts differently with the RF pulse and experience different nutation frequencies. It also means that samples of different sizes and volumes experience different nutation frequencies since the spins in those samples will experience slightly different  $B^1$  fields. The RF pulse therefore has to be calibrated for each nucleus and sample type.

$$\theta_{nut} = t_{RF} \omega_1 = t_{RF} \gamma B^1 \quad (3.7)$$

Calibration of the  $\pi/2$  pulse was carried out on water and 2,2,2-trifluoroethanol (TFE) samples with  $^1\text{H}$  and  $^{19}\text{F}$  signals at 2210 Hz and 2078.9 Hz, respectively. The  $V_{\pi/2}$  values shown in Table 3.2 were calculated by fitting each nutation curve, acquired through  $V_{RF}$  sweeps of 0.3–2.8 V in 0.1 V steps using a  $t_{RF}$  of 8 cycles, to Eq. 3.6a on Matlab (see  $^1\text{H}$   $\text{H}_2\text{O}$  example in FIGURE 3.15). The nutation curves of  $\text{H}_2\text{O}$  were acquired with 1 scan and those of TFE were acquired with 16 scans due to its smaller volume and more complicated peak patterns that lead to a lower SNR. The fit to each nutation curve produced  $V^0$  and  $\alpha_{cal}$  values that were put into Eq. 3.6b for the calculation of  $V_{\pi/2}$ . The 8 cycle  $^1\text{H}$  RF pulse at 2210 Hz has a duration of 3.62 ms, whereas the 8 cycle  $^{19}\text{F}$  RF pulse at 2078.9 Hz has a duration of 3.85 ms. The  $^{19}\text{F}$  RF pulse is slightly longer and therefore should require a lower  $V_{\pi/2}$  value. However, the gyromagnetic ratio of  $^{19}\text{F}$  is lower than of  $^1\text{H}$  which means the  $^{19}\text{F}$  spins have a weaker interaction with  $B^1$  and require a higher  $V_{\pi/2}$  value. Since the difference in  $\omega^0$  of the  $^1\text{H}$  and  $^{19}\text{F}$  nuclei is due to the differences in their gyromagnetic ratios, and contributes towards the difference in their pulse duration, the two effects cancel each other out. This explains the small difference of 0.05 V in the  $V_{\pi/2}$  of the  $^1\text{H}$  ( $1.00 \pm 0.04$  V) and  $^{19}\text{F}$  ( $0.95 \pm 0.03$  V) signals in TFE, where the two values are also within error. The same is true for the difference of 0.04 V in the  $^1\text{H}$   $V_{\pi/2}$  value of water ( $1.04 \pm 0.04$  V) and TFE. The slightly larger  $V_{\pi/2}$  of water is due to the difference in sample volume and sample size. Larger samples occupy more volume across the bore of the Terranova-MRI probe and experience more inhomogeneity in  $B^1$  and a reduced average RF pulse amplitude for the same input voltage.

Table 3.2: Table of  $^1\text{H}$  and  $^{19}\text{F}$   $V_{\pi/2}$  values for  $\text{H}_2\text{O}$  and TFE acquired from RF amplitude-sweep nutation curves.

Sample	Volume (mL)	Dimensions (H cm x D cm)	Nucleus	$t_{RF}$ (cycles   ms)	$V_{\pi/2}$ (V)
$\text{H}_2\text{O}$	500	14 x 7	$^1\text{H}$	8   3.62	$1.04 \pm 0.04$
TFE	250	10 x 6	$^1\text{H}$	8   3.62	$1.00 \pm 0.04$
			$^{19}\text{F}$	8   3.85	$0.95 \pm 0.03$

### 3.3.4 Simultaneous Excitation of Different Nuclei

The time-energy uncertainty relation states that uncertainty in time,  $\Delta T$ , is inversely proportional to uncertainty in energy,  $\Delta E$ . In NMR terms, the excitation bandwidth of an RF pulse,  $\Delta\nu$  is inversely proportional to  $t_{RF}$  and may be estimated as  $1/t_{RF}$  (see Eq. 3.8). The difference in Larmor frequency,  $\delta\nu$ , between the  $^1\text{H}$  and  $^{19}\text{F}$  nucleus is proportional to  $B^0$ , and at  $51.9\ \mu\text{T}$  (detection field) is equal to  $131.1\ \text{Hz}$  ( $\nu_H = 2210\ \text{Hz}$ ,  $\nu_{^{19}\text{F}} = 2078.9\ \text{Hz}$ ). On a TFE sample, an RF pulse that completes 8 cycles at a frequency of  $2210\ \text{Hz}$  is on-resonance with the  $^1\text{H}$  spins and has a duration of  $3.62\ \text{ms}$ , corresponding to a  $\Delta\nu$  of around  $276\ \text{Hz}$  or  $\pm 138\ \text{Hz}$  from the pulse centre.  $\Delta\nu/2$  is larger than  $\delta\nu$  and so the pulse has a broad enough excitation bandwidth to have an off-resonance interaction with the  $^{19}\text{F}$  spins at  $2078.9\ \text{Hz}$ . If the same pulse is centred at the  $^{19}\text{F}$  Larmor frequency of  $2078.9\ \text{Hz}$ , there will be an on-resonance interaction with the  $^{19}\text{F}$  spins and a off-resonance interaction with the  $^1\text{H}$  spins.

$$\Delta\nu \approx \frac{1}{t_{RF}} \quad (3.8)$$

The interaction between the spins and the RF pulse can be better understood from the excitation profile of the pulse. This describes  $A_{RF}$  as a function of the offset frequency and can be calculated by the Fourier transform (FT) of the pulse shape, which describes  $A_{RF}$  as a function of time. Rectangular pulses have been used thus far and are generated by the application of a fixed current through the  $B^1$  coil for a duration  $t_{RF}$ . Shaped pulses are more complicated and require passing a range of currents through the  $B^1$  coil for a duration  $t_{RF}$ . The implementation of shaped pulses is further discussed in Chapter 7.

The excitation profile of a rectangular pulse is a sinc function centred at the pulse frequency and with an approximate  $\Delta\nu$  equal to the inverse of  $t_{RF}$  (see FIGURE 3.16). Therefore, if the pulse is on-resonance with a  $^1\text{H}$  signal at  $2210\ \text{Hz}$ , the  $^1\text{H}$  nuclei will interact with the maximum of the sinc function where the frequency offset is zero. The  $^{19}\text{F}$  signal at  $2078.9\ \text{Hz}$  has an offset frequency of  $131.1\ \text{Hz}$  to the RF pulse and lies within  $\pm \Delta\nu/2 = 138\ \text{Hz}$  and will interact with a lower amplitude of the sinc function, thus experiencing a less efficient nutation with an unknown  $\text{rad } V^{-1}$  value.

Simultaneous excitation of different types of nuclei is not possible in the high-field

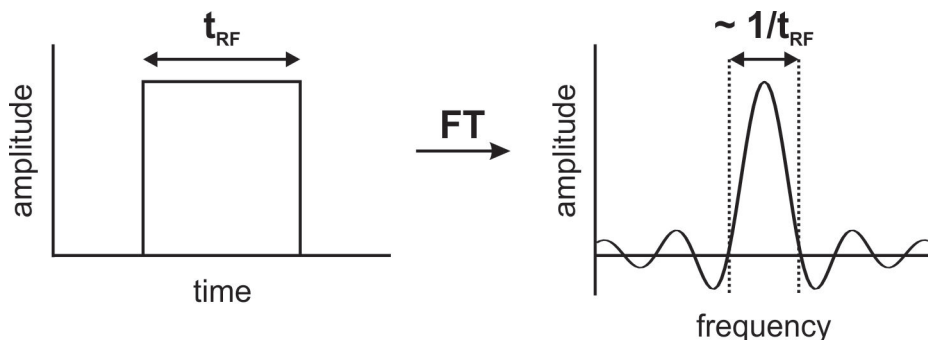


FIGURE 3.16: The excitation profile of an RF pulse describes the RF amplitude with respect to frequency and is calculated from the Fourier Transform (FT) of the pulse shape which describes the RF amplitude with respect to time. A rectangular pulse shape of duration  $t_{RF}$  (left) is equivalent to a sinc excitation profile with an approximate excitation bandwidth of  $1/t_{RF}$  (right).

regime ( $\geq 1$  T) because  $\delta\nu$  values are much larger than  $\Delta\nu$ . The RF pulse duration is typically between  $1 - 10 \mu\text{s}$  and corresponds to a  $\Delta\nu$  of  $10^6 - 10^7$  Hz. A nanosecond RF pulse would be required to interact simultaneously with the  $^1\text{H}$  and  $^{19}\text{F}$  nuclei at 9.4 T where a  $\delta\nu$  of 24 MHz ( $6 \times 10^4$  ppm) is observed. High-field NMR probes therefore contain RF channels that are designed to interact with a specific nuclear species by emitting RF pulses with frequencies at and around their Larmor frequency. Access to multiple channels on high-field NMR instruments enables the excitation of multiple nuclei independently of each other and allows for the design of complex heteronuclear NMR experiments.

Many of the SABRE experiments in this work required simultaneous  $\pi/2$  rad nutation of the  $^1\text{H}$  and  $^{19}\text{F}$  nuclei in fluorinated pyridines (see chapter 5/6). These experiments had to be carried out with a single RF pulse at a fixed frequency because the Terranova-MRI probe contains only one channel and the RF frequency cannot be changed during the experiment. A single RF pulse that simultaneously nutates the  $^1\text{H}$  and  $^{19}\text{F}$  nuclei by  $\pi/2$  rad was calibrated via a trial and error method. RF amplitude-sweep nutation curves were acquired for the  $^1\text{H}$  and  $^{19}\text{F}$  nuclei of TFE at a range of RF frequencies between  $\nu_{^1\text{H}} = 2210$  Hz and  $\nu_{^{19}\text{F}} = 2078.9$  Hz (both nuclei placed off-resonance to the pulse) until the fit of both nutation curves exhibited the same  $V_{\pi/2}$  value. The nutation curves were acquired with 16 scans at a fixed  $t_{RF}$  of 8 cycles and a sweep of 0.3-2.8 V in 0.125 V steps. A capacitance of 10.15 nF which tunes the probe to 2038 Hz was also used to acquire the nutation curves as this is able to amplify both the  $^1\text{H}$  and  $^{19}\text{F}$  signals.

The nutation curves at 2160 Hz showed the best synchronicity across  $V_{RF}$  (see FIGURE 3.17) and so were fit to Eq. 3.6a for calculation of  $V_{\pi/2}$ . The fit to the  $^1\text{H}$  nutation produced an  $\alpha_{cal} = 0.548 \pm 0.033 \text{ V rad}^{-1}$  and a  $V^0 = 0.215 \pm 0.054 \text{ V}$ , corresponding to a  $V_{\pi/2} = 1.08 \pm 0.07 \text{ V}$ . The fit to the nutation of the  $^{19}\text{F}$  nucleus displayed an  $\alpha_{cal} = 0.480 \pm 0.027 \text{ V rad}^{-1}$  and a  $V^0 = 0.380 \pm 0.039 \text{ V}$ , corresponding to a  $V_{\pi/2} = 1.13 \pm 0.06 \text{ V}$ . The  $V_{\pi/2}$  values were within error and so were rounded to 1.1 V for future simultaneous excitation experiments of TFE.

The  $^1\text{H}$  and  $^{19}\text{F}$  signals of TFE were acquired from the improved EFNMR ex-

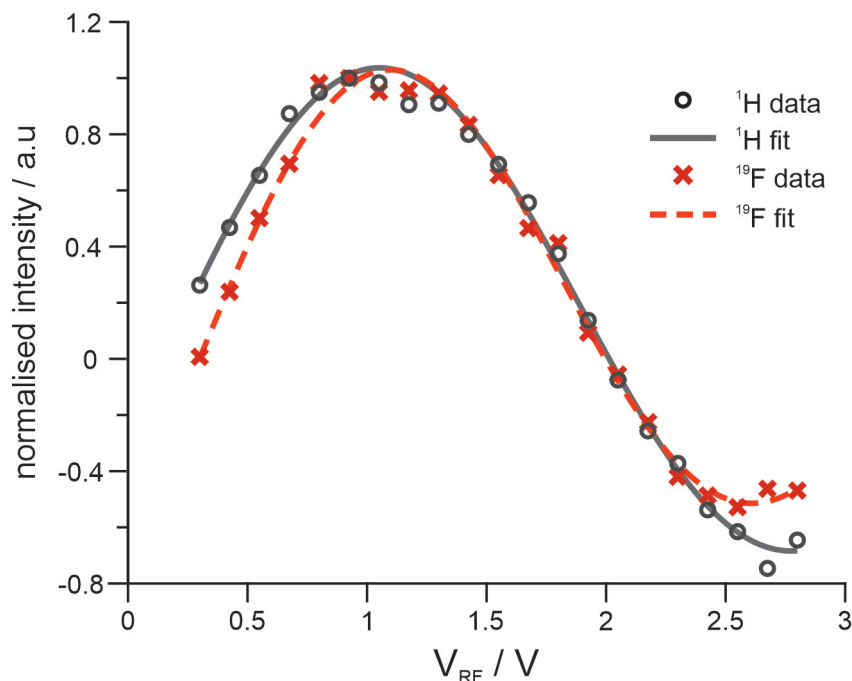


FIGURE 3.17: The  $^1H$  and  $^{19}F$  nutation curves of TFE at 2160 Hz were fit to Eq. 3.6a on Matlab and produced  $V_{\pi/2}$  of  $1.08 \pm 0.07$  V and  $1.13 \pm 0.06$  V for the  $^1H$  and  $^{19}F$  nuclei, respectively. These were rounded to 1.1 V for use in future simultaneous excitation experiments.

periment using the three different  $\pi/2$  RF pulses that have been calibrated on TFE. The results are plotted in FIGURE 3.18. Spectrum a) shows the TFE spectrum acquired from the  $\pi/2$  pulse on resonance with the  $^1H$  signal at 2200 Hz ( $V_{\pi/2} = 1$  V, 8 cycles), spectrum b) from the  $\pi/2$  pulse on resonance with the  $^{19}F$  signal at 2069.5 Hz ( $V_{\pi/2} = 0.95$  V, 8 cycles) and spectrum c) from the  $\pi/2$  pulse at 2160 Hz which simultaneously nutates the  $^1H$  and  $^{19}F$  by  $\pi/2$  rad ( $V_{\pi/2} = 1.1$  V, 8 cycles). The SNR of each peak was calculated and used to compare the response of the  $^1H$  and  $^{19}F$  nuclei to the RF pulses, where a larger SNR is expected for signals derived from nuclei that have experienced a  $\pi/2$  rad nutation. The  $^1H$  and  $^{19}F$  signals have an SNR of 186.1 and 124.7 in spectrum a), and 138.9 and 193.8 in spectrum b), respectively. The lower SNR of the  $^{19}F$  and  $^1H$  signals in spectrum a) and b), respectively, was expected because the spins that are off-resonance to the  $\pi/2$  RF pulse do not experience a  $\pi/2$  rad nutation and hence display a lower SNR. Spectrum c) shows much similar SNR values of 195.2 and 185.6 for the  $^1H$  and  $^{19}F$  signals, respectively, as both spins experience a near  $\pi/2$  rad nutation that gives rise to maximal transverse magnetisation.

It is important to note that the SNR of each signal depends heavily on the amplification by the Terranova-MRI probe's RLC circuit. Although the range of amplification spans 570 Hz and can encapsulate the  $^1H$  and  $^{19}F$  signals, the unsymmetrical and envelope-shaped nature of the amplification region means that the signals may not be amplified by the same amount. The three spectra in FIGURE 3.18 were therefore acquired with a capacitance of 10.25 nF to tune the probe to 2130 Hz, which is a region in between the two signals that ensures they both experience a near-equal amplification.

The spectra displayed in FIGURE 3.18 have been processed with a first-order

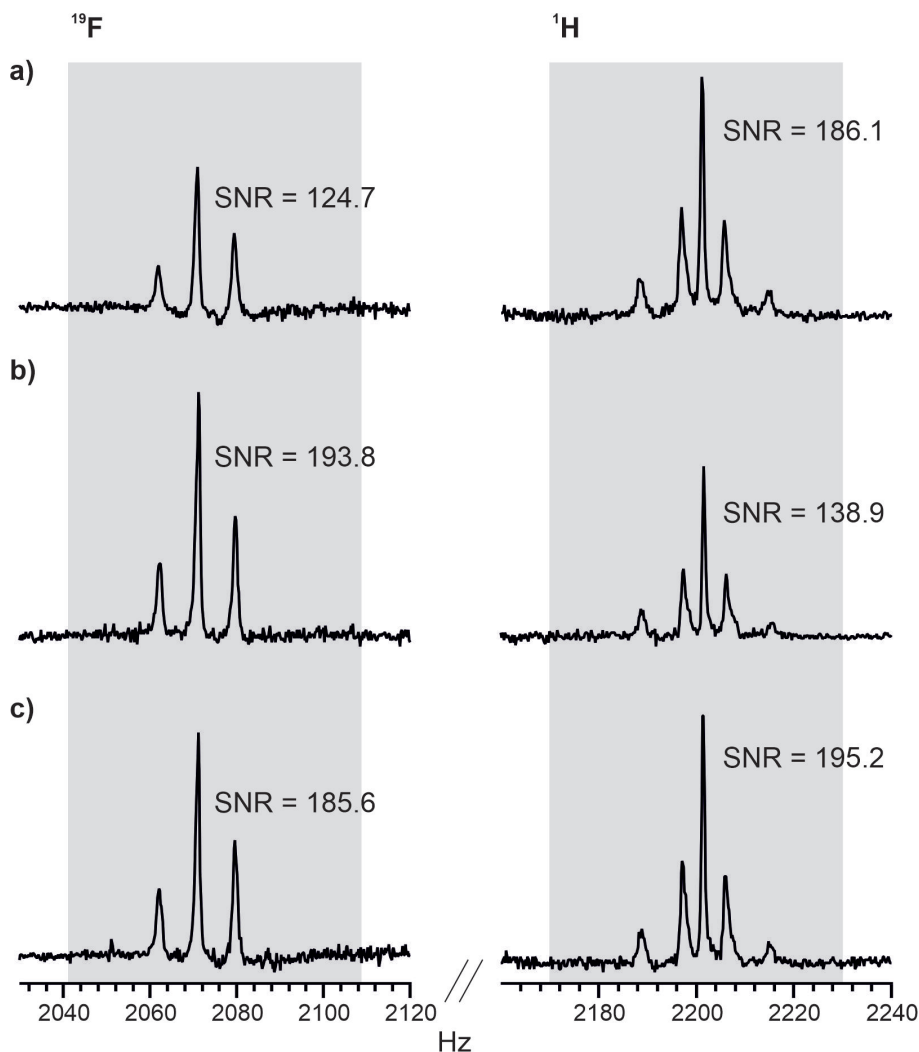


FIGURE 3.18: The  $^1\text{H}$  (2200 Hz) and  $^{19}\text{F}$  (2069.5 Hz) signals of TFE were acquired from the improved EFNMR experiment using a) the TFE  $^1\text{H}$   $\pi/2$  pulse at 2200 Hz ( $V_{\pi/2} = 1$  V, 8 cycles), b) the TFE  $^{19}\text{F}$   $\pi/2$  pulse at 2069.5 Hz ( $V_{\pi/2} = 0.95$  V, 8 cycles) and c) the TFE  $^1\text{H}$  and  $^{19}\text{F}$   $\pi/2$  pulse at 2160 Hz ( $V_{\pi/2} = 1.1$  V, 8 cycles). The SNR values of each peak is displayed beside it and shows the off-resonance signals are much weaker than the on-resonance signals apart from the signals in c) where both nuclei were nutated by  $\pi/2$  rad and therefore have very similar SNRs with a difference of 9.4. Roofing caused by the strong  $J_{HF}^3$  coupling interaction is observed on all  $^1\text{H}$  and  $^{19}\text{F}$  signals and points toward the centre of the heteronuclear coupling pattern.

phase correction shown in Eq. 3.9, where  $S_p(\nu)$  and  $S(\nu)$  are the phased and unphased spectra, respectively,  $t_{acq}$  is the acquisition delay and  $(\nu - \nu_0)$  is the frequency offset relative to the pivot point ( $\nu^0$ ) of the first-order phase correction. This correction was implemented to remove phase distortions exhibited by the multiplets as a consequence of the relatively long 20 ms acquisition delay of the EFNMR experiment, during which the spins complete multiple cycles of precession before acquisition (a  $^1\text{H}$  nucleus with a Larmor frequency of 2200 Hz completes  $\sim 44$  cycles in 20 ms) and gain a linear first-order phase across the spectrum of  $\phi = 2\pi t_{acq}\nu$ .

$$S_p(\nu) = S(\nu) \exp\{i2\pi t_{acq}(\nu - \nu^0)\} \quad (3.9)$$

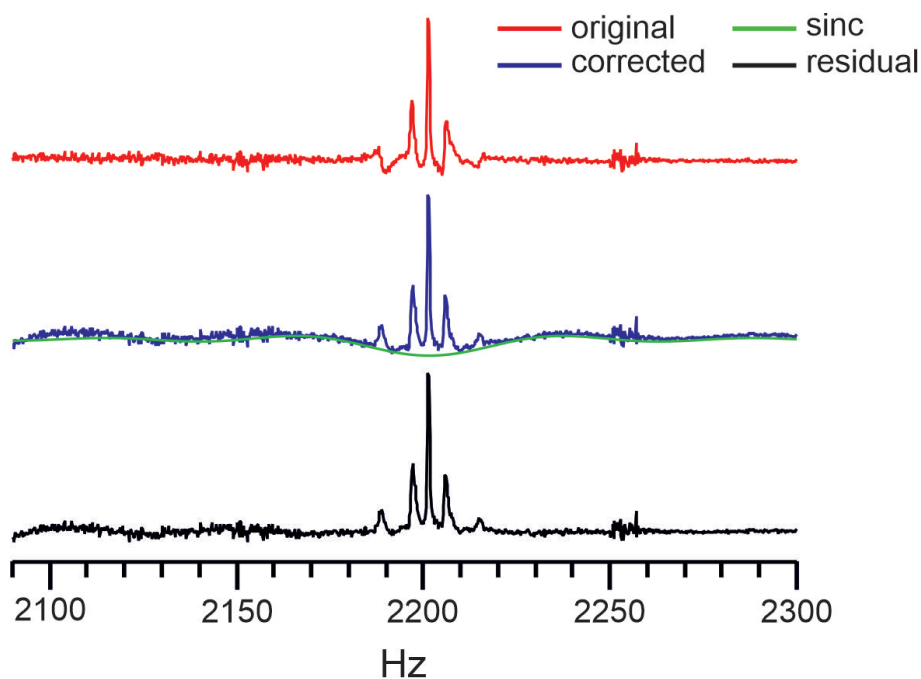


FIGURE 3.19: Illustration of the process for correcting the phase distortions displayed by the EFNMR spectra acquired using the EFNMR experiment that requires a long acquisition delay of 20 ms. A first-order phase of 276.5 rad is acquired by the  $^1\text{H}$  TFE EFNMR signal (red) at 2200 Hz. Correction using Eq. 3.9 with  $\nu^0 = 2202$  Hz generates a sinc oscillation in the baseline of the corrected spectrum (blue). Subtraction of a sinc curve (green) of matching frequency and amplitude to the oscillation on the baseline from the corrected spectrum yields a residual spectrum (black) with a well-phased  $^1\text{H}$  EFNMR signal and improved baseline.

The uncorrected  $^1\text{H}$  peak of TFE from FIGURE 3.18c is shown in FIGURE 3.19 (red). Application of the first-order phase correction to this signal, where  $t_{acq} = 20$  ms and  $\nu^0 = 2202$  Hz, corresponding to the centre frequency of the  $^1\text{H}$  signal, removes the phase distortions created by the acquisition delay but creates a sinc oscillation in the baseline of the spectrum (blue). The baseline is then corrected by subtracting a sinc function of equal frequency and amplitude (green) from the phase-corrected signal to yield the residual signal that displays first-order phase and baseline correction (black). The residual spectra in Figures 3.18 and 3.19 still show non-linear baselines meaning the correction is not perfect, however, a more accurate representation of the signal shape and multiplicity is observed which is vital for interpretation.

### 3.4 Conclusion

Integrating the Terranova-MRI probe with the triaxial Helmholtz coil pairs allowed alignment of the spin and lab frames of reference (from now on the lab and spin frames of reference will be described using the xyz axes only). This was shown to improve EFNMR experiments with the Terranova-MRI probe by facilitating the calibration of EFNMR RF pulses and the design of an RF pulse that simultaneously nutates the  $^1\text{H}$  and  $^{19}\text{F}$  nuclei in TFE by  $\pi/2$  rad. Such a pulse provides a starting point toward simultaneous nutation and detection of SABRE-polarised  $^1\text{H}$  and  $^{19}\text{F}$  nuclei in

fluorinated pyridines.

Linear shifting of the effective field experienced by the spins in the sample was also made possible with the alignment of  $B^0$  to the  $z'$ -axis. This can be taken advantage of to shift the Larmor frequency to higher frequencies to improve the sensitivity of EFNMR, as was demonstrated in this chapter, but more importantly, it provides access to the entire PTF range via control of the current through the  $z$ -Helmholtz coil pair and polarising coil during an EFNMR experiment. The polarising coil can generate mT fields to drive homonuclear polarisation transfer to protons on the substrate, whereas the  $z$ -Helmholtz coil pair can generate  $\mu$ T fields to drive heteronuclear polarisation transfer to  $^{19}\text{F}$  nuclei on the SABRE substrate. The ability to expose the spins in the sample to both the PTF and detection field without having to transport the sample means that the improved EFNMR system is able to carry out SABRE *in situ* of NMR detection in the ULF regime.

The EFNMR setup has therefore been optimised and is suited for probing of the SABRE polarisation transfer mechanism to  $^1\text{H}$  and  $^{19}\text{F}$  nuclei *in situ* of NMR detection. The next chapter discusses the design and optimisation of the automated gas flow system that introduces  $p\text{-H}_2$  into the sample containing the SABRE catalyst and the substrate to initiate the SABRE catalytic cycle.

# 4 | *In situ* SABRE with Earth's Field NMR Detection

## 4.1 Introduction

The goal of this chapter is to develop a robust instrument for generating reproducible SABRE polarisation with *in situ* NMR detection in the ULF regime. This *in situ* approach will provide a novel route toward probing the SABRE polarisation transfer step as it can be observed, via signal acquisition, immediately after the SABRE catalyst is exposed to the substrate and  $p\text{-H}_2$  within the limits of the time required for the RF pulse and the acquisition delay. The EFNMR-Helmholtz setup described in Chapter 3 utilises the polarising coil of the Terranova-MRI probe and the z-Helmholtz coil pair to provide control over the external field experienced by the spins in the sample and therefore enable access to the desired PTF range ( $\mu\text{T}$  -  $\text{mT}$ ), as well as a common detection field (e.g.  $51.9\ \mu\text{T}$ ) whilst the sample remains fixed inside the probe. In order to carry out the SABRE reaction inside the Terranova-MRI probe, the EFNMR-Helmholtz setup must be integrated with an automated gas flow system for *in situ*  $p\text{-H}_2$  bubbling of the sample during the PTF.

A schematic of the SABRE-EFNMR system is presented in FIGURE 4.1. The flow of  $p\text{-H}_2$  into the reaction cell within the Terranova-MRI probe is controlled and executed by the Bruker polariser control unit. It was first developed as part of a collaboration between the University of York and Bruker (Massachusetts, United States) to perform SABRE experiments with high-field NMR detection under an automated flow of  $p\text{-H}_2$ .<sup>59,60,95,112</sup> In these experiments, the SABRE signals were detected using Bruker NMR systems that use superconducting magnets to generate very strong but fixed external fields, meaning that the SABRE polarisation transfer step had to take place outside of the detection field (*ex situ*). Therefore, as well as controlling the flow of  $p\text{-H}_2$  into the SABRE sample, the polariser was also designed to use high pressure nitrogen gas to quickly transport the sample from a reaction chamber where SABRE polarisation transfer takes place under a weak magnetic field generated by an external solenoid, to an NMR flow cell within the Bruker probe for detection in the high-field regime. Commands to control the flow of  $p\text{-H}_2$  and nitrogen through the polariser, by manipulation of the valves and pressure regulators inside it, were written in macros in the Bruker TopSpin software tool<sup>113</sup> that runs the Bruker NMR spectrometer, and passed from a controlling PC using Transistor-Transistor Logic (TTL) pulses. Introducing  $p\text{-H}_2$  into the reaction chamber required attaching

the polariser to a  $p$ -H<sub>2</sub> generator which is also attached to an H<sub>2</sub> source (either a H<sub>2</sub> cylinder or an electrolytic H<sub>2</sub> generator). The combination of these instruments made-up the automated gas flow system for performing SABRE with high-field NMR detection.

The automated gas flow system was later combined with a 1 T (43 MHz) benchtop NMR spectrometer (Spinsolve Carbon, Magritek).<sup>61</sup> This required communicating with the Bruker polariser control unit via commands written in macros on the Prospa software tool that operates all Magritek spectrometers, carried out by the controlling PC through an RS232 serial interface. Adaptation of the Bruker polariser control unit for use with the Prospa software provided a platform to interface the automated gas flow system, originally developed for the *ex situ* detection of SABRE-polarisation on high and low-field NMR spectrometers, with the Terranova-MRI spectrometer to achieve SABRE hyperpolarisation with *in situ* EFNMR detection.

An *in situ* approach toward the detection of SABRE polarisation required a modification of the automated gas flow system. The flow cell used on high-field NMR systems for *ex situ* polarisation transfer, consisting of an external reaction chamber linked to an NMR tube, was replaced with a glass reaction cell that can host the SABRE reaction inside the Terranova-MRI probe during polarisation transfer and NMR detection. Operation of the polariser was simplified by this change since the flow of nitrogen gas for sample transfer was no longer needed. Several generations of the glass reaction cell were developed, the latest of which was used in this work (see FIGURE 4.1). The employed glass reaction cell has dimensions of 2.4 cm x 2.8 cm and contains an inlet and outlet at the bottom and top of the cell, respectively, for the flow of  $p$ -H<sub>2</sub> gas. A porous frit was fitted into a glass capillary which was fused to the cell inlet to act as a sparger to bubble  $p$ -H<sub>2</sub> through the liquid sample within the reaction cell designed to hold a maximum sample volume of 4 mL.  $p$ -H<sub>2</sub> bubbling promotes the dissolution of the gas into the liquid SABRE sample for a more effective SABRE reaction.

The *in situ* detection of SABRE-polarised pyridine on the Terranova-MRI spectrometer was published by the Meghan Halse group in 2019<sup>106</sup> using the glass reaction cell as part of the modified automated gas flow system. As a co-author on this publication, I contributed toward the development and optimisation of the EFNMR experiments designed to detect the SABRE polarisation of pyridine. It is worth noting that SABRE polarisation transfer could only be carried out under a mT PTF on this SABRE-EFNMR system since the triaxial Helmholtz coil array had not yet been integrated with the Terranova-MRI probe.

The SABRE-EFNMR system illustrated in FIGURE 4.1 is a combination of the automated gas flow system with the EFNMR-Helmholtz setup to achieve homonuclear and heteronuclear SABRE polarisation transfer *in situ* of EFNMR detection. The access to  $\mu$ T and mT PTFs is necessary for fully probing and optimising the SABRE polarisation transfer mechanism. The H<sub>2</sub> and  $p$ -H<sub>2</sub> generators, the Bruker polariser control unit and the glass reaction cell make-up the automated gas flow system, with all components attached by Fluorinated Ethylene Propylene (FEP) tubing.

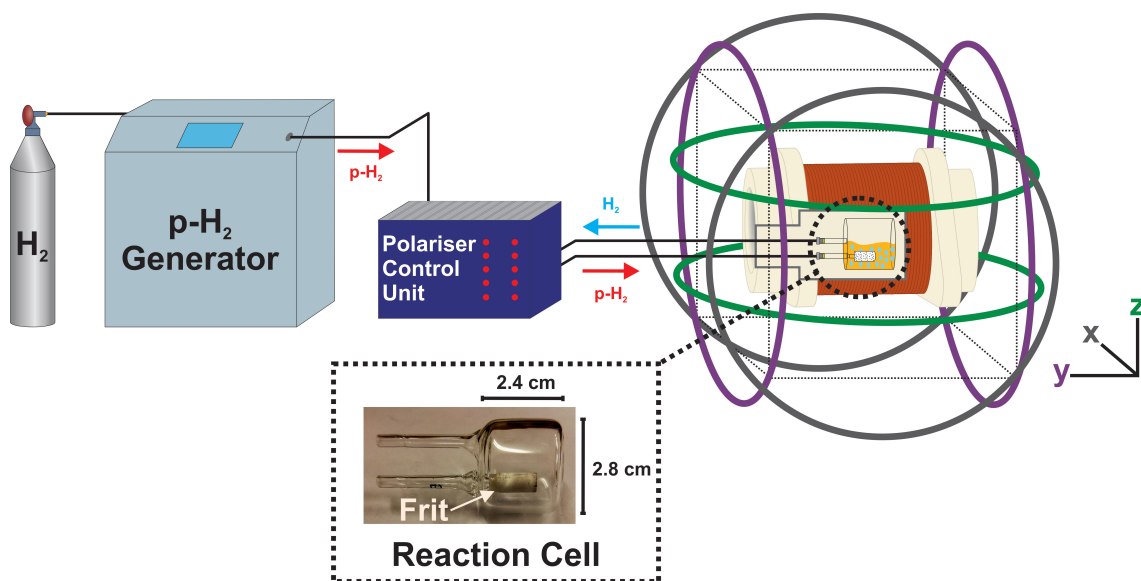


FIGURE 4.1: Schematic of the SABRE-EFNMR system comprised of the automated gas flow system integrated with the EFNMR-Helmholtz setup used to run SABRE experiments with *in situ* EFNMR detection.

Many issues were encountered with the automated gas flow system at the start of the project, such as blockages and leaks in the  $p\text{-H}_2$  path toward the reaction cell, due to uncertainties in the operation of the  $p\text{-H}_2$  generator and the Bruker polariser control unit. These issues led to a gradual decay in the production rate of  $p\text{-H}_2$ , where the  $p\text{-H}_2$  generator could not keep up with the  $p\text{-H}_2$  pressure demands of the SABRE experiment. A lack of reproducibility in the flow rate of  $p\text{-H}_2$  into the reaction cell led to inconsistent SABRE results. The work presented in the first section of this chapter provides a detailed description of the  $p\text{-H}_2$  generator and Bruker polariser control unit with the help of flow diagrams. The built-in procedures of these instruments that are used to establish  $p\text{-H}_2$  bubbling are discussed, together with the changes implemented for the development of a new and robust operation of the automated gas flow system. The method behind diagnosing and fixing problems such as leaks, blockages and a decline in the supply of  $p\text{-H}_2$  is provided in the second section of the chapter, as well as the boundaries for the experimental parameters required to ensure the  $\text{H}_2$  and  $p\text{-H}_2$  generators can keep up with the demands of  $p\text{-H}_2$  bubbling for the SABRE experiment.

## 4.2 Automated Gas Flow System

### 4.2.1 Parahydrogen Generator

The flow of  $p\text{-H}_2$  begins at the  $\text{H}_2$  generator which forms  $\text{H}_2$  gas from the electrolysis of water and feeds it into the Bruker BPHG 90  $p\text{-H}_2$  generator. Here the  $\text{H}_2$  gas is cooled down in the presence of a paramagnetic catalyst to form  $p\text{-H}_2$ , which is then transferred to the Bruker polariser control unit, before making its way to the reaction

cell.

The flow diagram of the  $p$ -H<sub>2</sub> generator is displayed in FIGURE 4.2. H<sub>2</sub> gas enters at solenoid valve SV1 at the inlet of the generator, and the input pressure is measure by the pressure gauge, PG. From here there are two paths the H<sub>2</sub> can take. The path through SV2 takes H<sub>2</sub> to the conversion chamber where it can be cooled in order to be enriched with  $p$ -H<sub>2</sub>. The alternative path through SV7 takes the H<sub>2</sub> gas to the outlet of the  $p$ -H<sub>2</sub> generator, bypassing the conversion chamber. Conversion of  $o$ -H<sub>2</sub> to  $p$ -H<sub>2</sub> increases at lower temperatures and requires a paramagnetic catalyst to enable the symmetry forbidden transition of nuclear spins in the higher energy ortho-state ( $I = 1$ ) to the lower energy para-state ( $I = 0$ ). Generating  $p$ -H<sub>2</sub> requires passing H<sub>2</sub> gas through the conversion chamber, which is lined with a paramagnetic catalyst and cooled to 38 K to produce an estimated  $p$ -H<sub>2</sub> content of 92% from 25% at room temperature. The conversion chamber is attached to a cryocooler cold head inside of a vacuum enclosure and is cooled down using a closed loop water cooling circuit.

Before the  $p$ -H<sub>2</sub> generator is cooled down, all gases other than H<sub>2</sub> must be evacuated from the internal tubing to prevent them from freezing inside the conversion chamber when it is operating at 38 K as this blocks it and interrupts the flow of  $p$ -H<sub>2</sub>. A gas purifier cartridge is fitted downstream of SV2 (see FIGURE 4.2) to remove the undesirable gases from the path toward the reaction chamber. The built-in 'purge' procedure is also used for this and works by first using the vacuum pump to evacuate the entire working volume of the  $p$ -H<sub>2</sub> generator, before refilling the evacuated volume with H<sub>2</sub> gas from the H<sub>2</sub> generator to prepare the  $p$ -H<sub>2</sub> generator for cooling. In the case where an H<sub>2</sub> generator that produces H<sub>2</sub> gas from the electrolysis of water is integrated with the  $p$ -H<sub>2</sub> generator, the gas purifier cartridge helps to remove water vapour that may travel into the  $p$ -H<sub>2</sub> generator with the H<sub>2</sub> gas.

The purge procedure is automated and lasts about 10 minutes; however, it was found that it was not effectively evacuating the working volume as the conversion chamber would be repeatedly blocked by frozen gases after a few days of use, even when the purge procedure was run at the start of each day. To ensure complete evacuation of the working volume, a new manual procedure for purging the system was developed. This procedure requires accessing the generator's manufacturer settings to allow for manual opening and closing of the solenoid valves, as well as switching on and off of the vacuum pump. At the end of each day of experiments the vacuum pump was turned on and valves SV4, SV3 and SV2 were opened (in the written order, see FIGURE 4.2) to allow evacuation of the entire working volume. The procedure would be left running for a minimum of  $\sim 15$  h. At the start of each day, the valves and vacuum pump are closed and turned off to prepare for cooling. The manual purge procedure does not need to include filling of the working volume with H<sub>2</sub> gas after vacuum pumping because the cooling procedure already does this.

Cooling of the conversion chamber is initiated by pressing the 'start' option on the screen of the Bruker BPHG 90 which becomes available after purging, and takes around 40 minutes to complete. During cooling, SV1 and SV2 open to allow H<sub>2</sub> from the H<sub>2</sub> generator to fill up the  $p$ -H<sub>2</sub> path. The flow rate of H<sub>2</sub> into the  $p$ -H<sub>2</sub> generator

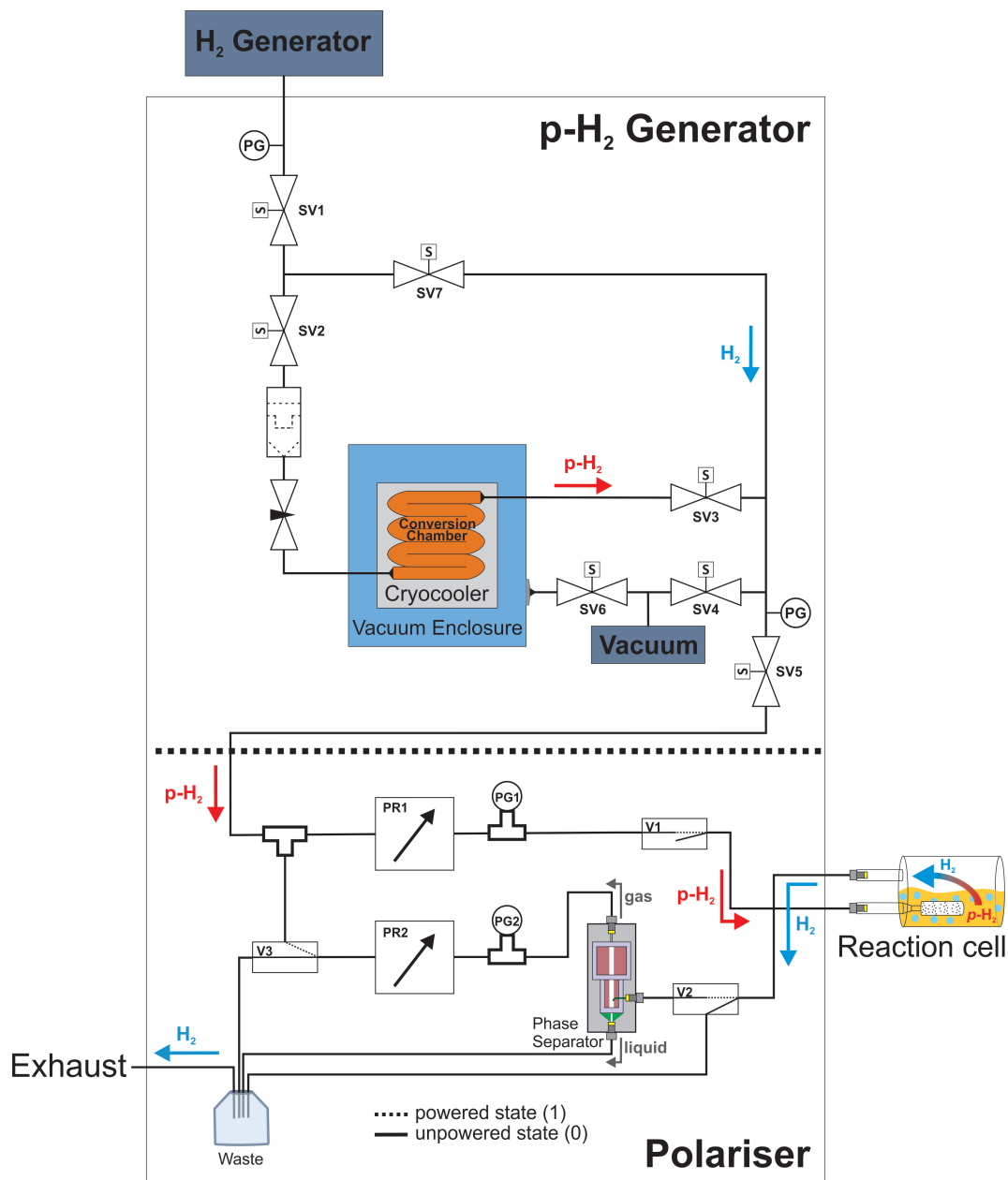


FIGURE 4.2: Flow diagram of the automated gas flow system comprised of a  $H_2$  generator, a Bruker BPHG 90  $p$ - $H_2$  generator, a Bruker polariser control unit and a glass reaction cell. The  $p$ - $H_2$  generator enriches thermal  $H_2$  gas in its lower energy para state with a conversion chamber operating at 38 K and lined with a paramagnetic catalyst. The  $p$ - $H_2$  is then fed into the Bruker polariser control unit which establishes a flow rate of  $p$ - $H_2$  through the reaction cell and SABRE sample. The polariser is controlled by commands within macros written on the Terranova-Expert software package (Magritek, Germany) that are delivered by the controlling PC outside of the EFNMR pulse sequence.

is dependant on the output pressure of the H<sub>2</sub> generator, however, the flow of H<sub>2</sub> into the conversion chamber is limited to 0.2 L min<sup>-1</sup> (at standard temperature and pressure) by the needle valve located between SV2 and the conversion chamber. The flow through the needle valve must be slow enough to ensure the retention time of the H<sub>2</sub> in the conversion chamber is long enough to allow optimal *p*-H<sub>2</sub> enrichment. Once the conversion chamber reaches 38 K the cooling procedure terminates and the 'continuous flow' procedure can be selected to initiate delivery of *p*-H<sub>2</sub> into the polariser. The procedure begins by opening SV4 and turning on the vacuum pump to evacuate the space between SV3 and the outlet of the *p*-H<sub>2</sub> generator. This lasts for approximately 15 s and ensures the *p*-H<sub>2</sub> held at SV3 is the first thing to make contact with the reaction cell once the *p*-H<sub>2</sub> bubbling experiment begins. Finally, SV3 and SV5 are opened and a continuous flow of *p*-H<sub>2</sub> into the polariser is established.

The Bruker BPHG 90 *p*-H<sub>2</sub> generator allows the user to set the maximum output pressure of *p*-H<sub>2</sub> from SV5, thus providing control over the pressure within the Bruker polariser control unit. A maximum output pressure of 6 bar was set for the automated gas flow system as a safety precaution to prevent leaking of *p*-H<sub>2</sub> from the plastic connectors and valves within the polariser, some of which can only handle gas pressures of 8 bar. The *p*-H<sub>2</sub> generator maintains this output pressure by closing SV5 once the output pressure, measured by the outlet pressure gauge, PG, reaches 6 bar. This will stop the flow of *p*-H<sub>2</sub> into the polariser, however, when and if the outlet pressure drops below 6 bar as the *p*-H<sub>2</sub> is used up, SV5 opens again to re-introduce *p*-H<sub>2</sub> into the polariser.

When the continuous flow procedure is first activated after purging of the *p*-H<sub>2</sub> generator, the *p*-H<sub>2</sub> pressure reading at the outlet begins to increase as the *p*-H<sub>2</sub> that was held at SV3 during the cooling procedure flows through it toward the Bruker polariser. Typically it takes ~120 s for the output pressure to reach 6 bar; however, if the *p*-H<sub>2</sub> flow has been interrupted, due to a block within the reaction chamber for example, the build-up time is much slower (minutes). Depending on the extent of the block, the output pressure may not even reach 6 bar. Also, if there is a block, it will get worse as more *p*-H<sub>2</sub> bubbling experiments are run. In this case the build-up of *p*-H<sub>2</sub> pressure at the outlet of the *p*-H<sub>2</sub> generator between experiments will progressively get slower. This is discussed further in section 4.3.2. If a slow build-up of output pressure is observed, it is necessary to immediately stop the continuous flow procedure in order to warm up the *p*-H<sub>2</sub> generator via the 'warm-up' procedure. This procedure initiates the heater within the cryocooler to speed up the warm-up process of the reaction chamber to 301 K, during which the vacuum pump is activated and valves SV2, SV3 and SV4 are opened. This process allows removal of the frozen gases within the reaction chamber as they melt. The improved purge procedure is then left running until the next working day to make sure that the *p*-H<sub>2</sub> generator has been fully purged and the reaction chamber will not block again.

The warm-up procedure is also activated at the end of the working day so that the *p*-H<sub>2</sub> generator can be re-purged and therefore re-cooled at the start of the next working day. This is a safety precaution to avoid leaving the lab with an unattended instrument containing pressurised H<sub>2</sub> gas.

## 4.2.2 Polariser Control Unit

The Bruker polariser control unit is used to dictate the flow of  $p$ -H<sub>2</sub> into the glass reaction cell by controlling the  $p$ -H<sub>2</sub> pressure at its inlet (forward pressure) and outlet (back pressure). A consistent flow of  $p$ -H<sub>2</sub> into the SABRE sample is key for acquiring reproducible hyperpolarisation data. Between periods of  $p$ -H<sub>2</sub> bubbling, the pressure in the cell is reduced to atmospheric pressure. This allows for an out-gassing of used H<sub>2</sub> from solution between experiments, where it is assumed that at the end of a bubbling experiment there is reductive elimination of the  $p$ -H<sub>2</sub> derived hydrides from the SABRE catalyst to give H<sub>2</sub> gas which naturally diffuses out of the SABRE solution as thermal H<sub>2</sub> (75 %  $o$ -H<sub>2</sub> and 25 %  $p$ -H<sub>2</sub>).

There is not much flexibility in when to initiate and terminate  $p$ -H<sub>2</sub> bubbling during the SABRE-EFNMR experiment because communication with the Bruker polariser control unit, via macros written on Prospa, is only possible outside the operation of the Terranova-MRI spectrometer DSP, which carries out the EFNMR pulse sequence. Therefore,  $p$ -H<sub>2</sub> bubbling of the SABRE sample may only be initiated before the NMR pulse sequence begins and turned off after acquisition of the EFNMR FID. Bubbling of a sample during NMR detection is generally avoided in the high-field regime because of magnetic field inhomogeneities introduced into the sample at the gas-liquid interface due to their differences in magnetic susceptibility. The impact of magnetic susceptibility on the homogeneity of the local magnetic field scales with magnetic field strength, such that it becomes negligible in the ULF regime. Therefore,  $p$ -H<sub>2</sub> bubbling of the SABRE sample during EFNMR detection does not reduce spectral resolution.

The polariser's switchable valves V1, V2 and V3 (see FIGURE 4.2) operate in a powered or unpowered state defined by the number 1 or 0, respectively, where the state of each valve is chosen depending on the desired path of the  $p$ -H<sub>2</sub> through the polariser. Pressure regulators PR1 and PR2 in the polariser contain a valve on a spring that reduces the input pressure to a desired output pressure. PR1 is used to restrict the flow of  $p$ -H<sub>2</sub> from the  $p$ -H<sub>2</sub> generator at its inlet and establish a forward pressure of  $p$ -H<sub>2</sub> into the reaction cell. PR2 is attached to the flow system in reverse (gas flows into its outlet and out of its inlet, see FIGURE 4.2) and is used to restrict the flow of H<sub>2</sub> out of the reaction cell to establish a back pressure. The output pressure of PR1 and the input pressure of PR2 is recorded by the adjacent pressure gauges PG1 and PG2, respectively. The extent of flow restriction by the pressure regulators is defined by values ranging from 0 to 5. A value of 0 closes the valve in PR1 so that  $p$ -H<sub>2</sub> does not flow through and 0 bar relative output pressure is established. A value of 0 opens the valve in PR2 so that there is free flow of H<sub>2</sub> to achieve 0 bar relative input pressure. A value of 5 opens the valve in PR1 but closes the valve in PR2. Values between 0 and 5 define the output and input pressures of PR1 and PR2 in units of bar. For example, if PR1 is set to 3 and PR2 is set to 2, pressure gauge PG1 would read 3 bar and PG2 would read 2 bar and a pressure differential of 1 bar would be established across the reaction cell.

Together, PR1 and PR2 create and maintain a pressure differential across the

reaction cell to initiate  $p\text{-H}_2$  bubbling of the SABRE sample. A larger pressure at PR1 than at PR2 is required to flow  $p\text{-H}_2$  through the porous frit at the inlet of the reaction cell and out through the outlet. The pressure at PR1 determines the concentration of  $p\text{-H}_2$  in the reaction cell and dissolved in the SABRE sample during bubbling. A higher concentration of dissolved  $p\text{-H}_2$  leads to a higher concentration of hyperpolarised substrate in solution and a stronger hyperpolarised signal.<sup>39,60,99</sup> The pressure differential determines the flow/bubbling rate of  $p\text{-H}_2$  through the SABRE sample, where a faster bubbling rate also improves the dissolution of  $p\text{-H}_2$  into the SABRE sample to increase the concentration of dissolved  $p\text{-H}_2$ .

The polariser commences in stand-by mode where valves V1, V2 and V3 are in their unpowered states (represented as [000]), and pressure regulators PR1 and PR2 are set to 0. In this state,  $p\text{-H}_2$  is held at PR1 at the regulated outlet pressure of the  $p\text{-H}_2$  generator. The first step of a SABRE-EFNMR experiment is to initiate  $p\text{-H}_2$  bubbling of the sample with the built-in 'regenerate' procedure which is made-up of 2 stages: the first stage fills the reaction cell with  $p\text{-H}_2$  to quickly establish the back pressure and hence the desired pressure differential; the second stage maintains the pressure differential to achieve reproducible  $p\text{-H}_2$  bubbling of the SABRE sample. The back pressure is established in the first stage by setting PR1 and PR2 to the desired forward and back pressure values, and setting a valve state of [1 1 1] (V1 = 1, V2 = 1, V3 = 1) for a user defined period, typically 1 s. This short lived state allows  $p\text{-H}_2$  to flow into the cell from its inlet via PR1 and V1, and its outlet via V3, PR2 and V2 (see FIGURE 4.2). The back pressure can alternatively be achieved by flowing  $p\text{-H}_2$  into the cell through the inlet only and waiting for it to build-up at PR2, but this is much slower. The second stage maintains the pressure differential across the reaction cell and creates a continuous flow of  $p\text{-H}_2$  through the SABRE sample by changing to a valve state of [1 1 0]. The second stage of the regenerate procedure is left running for the duration of the SABRE-EFNMR experiment, after which the built-in 'stop' procedure, which returns the polariser to stand-by mode (PR1 = 0, PR2 = 0, valve state: [000]) is used to terminate  $p\text{-H}_2$  flow through the reaction cell. At this point, any gas downstream from V1 is flushed toward the exhaust, which is open to atmospheric pressure, causing out-gassing of the SABRE sample in preparation for the next SABRE-EFNMR bubbling experiment.

Due to aggressive bubbling that agitates the sample, small amounts of the SABRE sample can also flow out from the outlet of the reaction cell. A phase separator (see FIGURE 4.2) is used to ensure any liquid that flows out from the cell is transferred directly to waste, bypassing PG2, PR2 and V3. This is necessary because the SABRE sample contains solvent which is harmful to the inner mechanics of pressure regulators and the electronic pressure gauges. The  $\text{H}_2$  gas from the cell is transferred by the phase separator toward PR2 (see FIGURE 4.2) to allow the build-up of back pressure.

When  $p\text{-H}_2$  bubbling is terminated at the end of a SABRE-EFNMR experiment and the polariser returns to stand-by mode, some  $p\text{-H}_2$  becomes trapped between PR1 and V1. The gas in this region must be removed before the start of the next experiment to ensure a clear and reproducible path toward the reaction cell for the fresh  $p\text{-H}_2$  in the following experiment. When the trapped gas was not removed between SABRE-EFNMR experiments, the intensity of the acquired hyperpolarised signal was

seen to vary significantly ( $\pm 5 \mu\text{V}$ ) across delays of a few seconds between experiments. This occurs because the trapped  $p\text{-H}_2$  slowly diffuses out through the FEP tubing and leaks out from the plastic connectors, therefore if the pressure is not cleared, the  $p\text{-H}_2$  flowing into the reaction cell from PR1 will experience a different pressure differential and corresponding flow rate into the SABRE sample as a function of differing delays between experiments. Removing all the trapped  $\text{H}_2$  before the start of the next SABRE experiment ensures identical starting conditions of the EFNMR-SABRE experiment to attain reproducible hyperpolarisation. After the polariser returns to stand-by mode, the valve state [1 0 0] is set to initiate the 'vent' procedure which opens a path for the trapped  $p\text{-H}_2$  towards the exhaust via the reaction cell and V2. The polariser is held at this state for 0.5 s, before the 'stop' procedure is used to return the system to stand-by for the start of the next SABRE-EFNMR experiment. The vent procedure must also be included at the start of the SABRE-EFNMR experiment so that the  $p\text{-H}_2$  bubbling conditions of the first experiment are consistent with that of subsequent ones.

The plot in FIGURE 4.3 shows the forward and back pressure readings of PG1 (blue) and PG2 (orange), respectively, during a  $p\text{-H}_2$  bubbling experiment that mimics the operation of the polariser control unit during a SABRE-EFNMR experiment. The SABRE-EFNMR experiment is mimicked because the process of reading and printing pressure values requires communication with PG1 and PG2 by the controlling PC which, during a SABRE-EFNMR experiment, is only possible outside the operation of the Terranova-MRI spectrometer. The method by which this data was collected is described in detail in section 4.3.1.

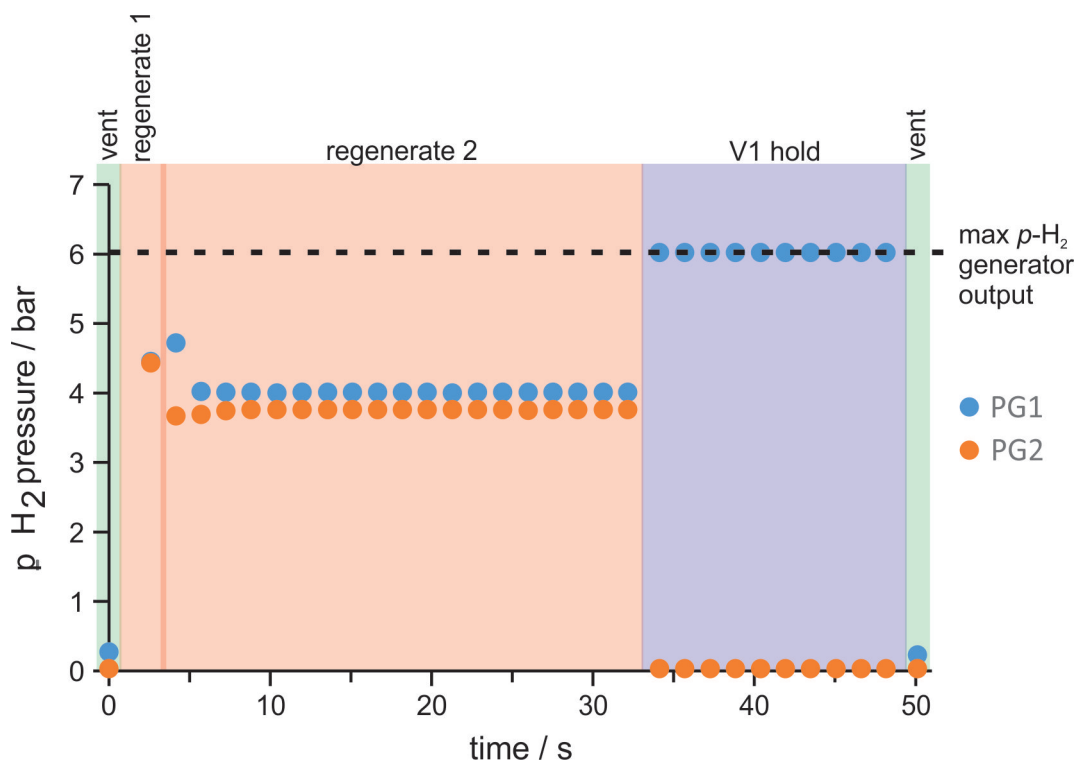


FIGURE 4.3: A plot of the pressure values recorded by pressure gauges PG1 and PG2 during a  $p\text{-H}_2$  bubbling experiment that mimics the operation of the Bruker polariser control unit over the course of a SABRE-EFNMR experiment.

The initial pressure reading of 0.27 and 0.03 bar at PG1 and PG2, respectively,

was recorded immediately after the vent procedure and verifies that there was no gas inside the polariser at the start of the experiment. The regenerate procedure was then performed with a forward pressure of 4 bar and a back pressure of 3.75 bar (+0.25 bar pressure differential). The second pressure reading shows that within 2.5 s the pressure at PG1 increased to 4.45 bar and the pressure at PG2 increased to 4.43 bar which corresponds to the first stage of the regenerate procedure where the reaction cell is filled with  $p\text{-H}_2$  from its inlet and outlet. The first stage lasts for 1 s in a standard SABRE-EFNMR experiment, however it was increased to 2.5 s to demonstrate the build-up in the figure. From this point, the second stage of the regenerate procedure was initiated, whereby the pressure differential of +0.25 bar was maintained by PR1 and PR2 for 28 s to allow  $p\text{-H}_2$  bubbling of the SABRE sample. It can be seen from the plot that it took around 4.65 s from the start of the second stage for PR1 and PR2 to regulate to their set pressures of 4 and 3.75 bar, respectively. The 'V1 hold' procedure then terminates  $p\text{-H}_2$  bubbling and holds the  $p\text{-H}_2$  from the  $p\text{-H}_2$  generator at V1. This procedure is identical to the stop procedure, apart from the role of PR1 which is set to 5 instead of 0 to allow the  $p\text{-H}_2$  flow into V1 where its pressure can be recorded by PG1. This step is used to observe the output of the  $p\text{-H}_2$  generator at the end of a  $p\text{-H}_2$  bubbling experiment to ensure it is high enough to keep up with the demand of the next one (4 bar forward pressure and +0.25 bar pressure differential in this case).

The recovery of the  $p\text{-H}_2$  generator depends on whether the rate of formation of  $p\text{-H}_2$  by the conversion chamber in the  $p\text{-H}_2$  generator ( $0.2\text{ L min}^{-1}$ ), which is also dependent on the rate of production of  $\text{H}_2$  gas by the  $\text{H}_2$  generator, can keep up with the rate of bubbling which is proportional to the pressure differential across the reaction cell. During the V1 hold procedure the pressure at PG1 immediately rose to 6.02 bar, and the pressure at PG2 immediately dropped to 0.03 bar. The pressure of 6.02 bar at V1 is equal to the regulated output pressure of the  $p\text{-H}_2$  generator and shows that the  $p\text{-H}_2$  was able to fully recover and very quickly. This suggests that the rate of production of  $\text{H}_2$  and the rate of formation of  $p\text{-H}_2$  were fast enough to keep up with the bubbling rate associated with the +0.25 bar pressure differential across the reaction cell, after one experiment. The final data point shows a return of PG1 and PG2 to 0.27 and 0.03 bar, respectively, after the vent procedure was run to remove any gas still present within the polariser control unit to ready it for the start of the next experiment.

## 4.3 Monitoring Parahydrogen Flow and Diagnosing Problems

### 4.3.1 Method

The flow of  $p\text{-H}_2$  through the polariser can be visualised using the electric pressure gauges PG1 and PG2, as shown by the example in FIGURE 4.3. They enable the recording and printing of pressure readings at the inlet and outlet of the reaction

cell under the different stages of gas flow, through the incorporation of the necessary commands into the pulse program macro of the Terranova Expert software. The pressure values can be saved as Comma Separated Values (CSV) files for processing of the pressure data in programs such as Microsoft Excel or Matlab. Printing of other parameters, including the time and valve state at each pressure reading was implemented to help with interpreting the pressure data.

Access to these commands during operation of the Bruker polariser allows for the creation of specially designed gas flow procedures to diagnose issues with the  $p\text{-H}_2$  flow into the reaction cell, caused by problems such as blockages and leaks within the working volume of the Bruker polariser itself, and the  $p\text{-H}_2$  generator. Furthermore, these commands were incorporated into the pulse program macros of the SABRE-EFNMR experiments to keep track of the performance of the automated gas flow system to aid in the post processing of the SABRE-polarised data and identify potential problems with the  $p\text{-H}_2$  flow.

A Bruker polariser interface was created in the Terranova-Expert software (see FIGURE 4.4) to provide easy access to the gas flow monitoring procedures and commands available to the user; procedures involve multiple steps and utilise multiple commands that are sent to the pressure regulators and switchable valves. The red box in FIGURE 4.4 outlines the commands for communicating with the switchable valves and the pressure gauges, as well as built-in procedures made up of multiple steps that involve commands to the polariser to initiate and terminate  $p\text{-H}_2$  flow into

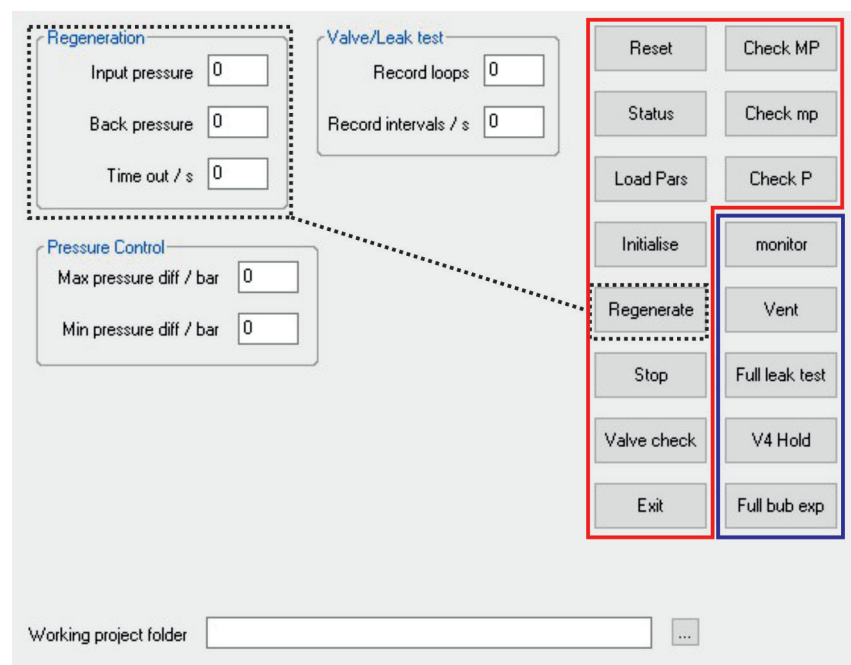


FIGURE 4.4: Image of the Bruker polariser control unit interface designed on the Terranova Expert software to facilitate access to the commands and pre-existing flow procedures of the polariser (red), and the newly designed flow procedures to aid in monitoring the flow of gas into the reaction cell (blue). The 'Monitoring Parameters' section of the interface offers control over the number of pressure values recorded by PG1 and/or PG2, and the length of time in seconds between each recording. The 'Regeneration' section is exclusive to the regenerate procedure to communicate to PR1 and PR2 the forward and back pressure, respectively, in bar.

the reaction cell. The procedures inside of the blue box were developed in this work to allow monitoring of  $p\text{-H}_2$  flow through the Bruker polariser to improve the diagnosis of issues, and therefore the robustness and reproducibility of the SABRE-EFNMR experiment. The plot in FIGURE 4.3 was generated from the gas flow procedure labelled 'Full bub exp' and is an example of the way the recorded data is interpreted.

Information on the commands and procedures within the interface is provided in Table 4.1. The user input parameters labelled 'Record loops' and 'Record intervals / s' in the 'Monitoring Parameters' section of the interface control the total number of pressure values recorded by PG1 and/or PG2 in each step of the chosen flow procedure and the delay in seconds between each recording, respectively.

The 'Input pressure' and 'Back pressure' user-input parameters in the 'Regenerate' section of the interface are used to set the forward and back pressure of  $p\text{-H}_2$  through the reaction cell during the built-in regenerate procedure. All of the SABRE-EFNMR experiments utilise the regenerate procedure, as well as some of the gas flow monitoring procedures (see Table 4.1). The forward and back pressures of gas through the reaction cell for the other gas flow procedures are defined explicitly in their pulse program. The 'Time-out / s' user-input parameter sets the time in seconds to build-up the desired back pressure at the start of the regenerate procedure. Access to all of the  $p\text{-H}_2$  flow parameters during the regenerate procedure is therefore easily accessible within the Bruker polariser interface.

Access to built-in safety measures is also provided by the interface in FIGURE 4.4 via the 'Pressure Control' section. The 'Max pressure diff / bar' user-input parameter prevents too large a pressure differential and corresponding flow rate of gas through the working volume of the polariser from being set. This is done to prevent vigorous bubbling and spraying of the sample in the reaction cell which will lead to rapid loss through the outlet. The 'Min pressure diff / bar' parameter ensures there is always a positive pressure differential through the reaction cell and gas is always flowing from the polariser inlet to the exhaust. This prevents a build-up of pressure inside the polariser and the reaction cell which can lead to the damaging of both. Values of 0.7 bar and 0.15 bar were inputted for the max and min pressure differential parameters, respectively, in this work.

Table 4.1: Table describing the commands and procedures available within the Bruker polariser interface.

<b>Command (C) / Procedure (P)</b>	<b>Description</b>
Check MP (C)	Prints the maximum pressure differential value that has been set within 'Pressure Control' onto the CLI.
Check mp (C)	Prints the minimum pressure differential value that has been set within 'Pressure Control' onto the CLI.
Check P (C)	Prints the maximum pressure differential value that has been set within 'Pressure Control' onto the CLI.
Reset (P)	Forces the unit to perform a soft reset of the application program.
Status (P)	Prints a description of the current operation phase of the polariser onto the CLI (e.g. Idle, Regeneration Start, Regeneration Over, etc.).
Load Pars (P)	Loads 'Regeneration' and 'Pressure Control' parameters from the Bruker polariser to update the GUI.
Initialise (p)	Update polariser with 'Regeneration' and 'Pressure Control' parameters from the GUI and write result to a parameter file in project directory. Parameters must be re-updated whenever there is a change to the parameters.
Regenerate (P)	Starts regenerate procedure (p-H <sub>2</sub> bubbling).
Stop (P)	Terminates any running procedure and returns polariser to stand-by mode.
Exit (P)	Close Bruker polariser interface.
monitor (P)	Initiates the regenerate procedure to test how well the pressure differential is held by PR1 and PR2. Pressure values at PG1 and PG2, valve state and time are recorded in intervals throughout the procedure and are printed onto file pVals(n).csv (n = 0,1,2,3...) in the project directory.
Vent (P)	Reaction cell is opened to exhaust for degassing of the sample and working volume of the Bruker polariser.
Full leak test (P)	Gas pressure is held in different sections of the working volume of the Bruker polariser to test for leaks. Pressure values at PG1 and PG2, valve state and time are recorded in intervals throughout the procedure and are printed onto file FullLeakTest(n).csv (n = 0,1,2,3...) in the project directory.
V4 Hold (P)	PR1 is opened and gas pressure is held at V1.
Full bub exp (P)	Replicates the SABRE-EFNMR experiment to test the performance of the Bruker polariser and the p-H <sub>2</sub> generator. Pressure values at PG1 and PG2, valve state and time are recorded in intervals throughout the procedure and are printed onto file fullBubbling_test(n).csv (n = 0,1,2,3...) in the project directory.

### 4.3.2 Recovery of Parahydrogen Pressure

A consistent flow rate of  $p\text{-H}_2$  through the SABRE sample is essential in acquiring reproducible and comparable SABRE polarised data, and depends on the absence of leaks and blockages in the  $p\text{-H}_2$  flow path, as well as the correct functioning of all components of the automated gas flow system (pressure regulators, solenoid valves, etc.). FIGURE 4.5 shows the monitoring of  $p\text{-H}_2$  pressure at PG1 over 15 repetitions of a SABRE-EFNMR experiment with a pressure differential of +0.25 bar, achieved using a forward pressure at PR1 of 4 bar and a back pressure at PR2 of 3.75 bar. Pressure data was not acquired during the first and second stages of the regenerate procedure, as was done in FIGURE 4.3, because communication with the polariser control unit is only possible outside the operation of the EFNMR experiment. Therefore, the plot shows the pressure readings from the point immediately after the second stage of the regenerate procedure when  $p\text{-H}_2$  bubbling is terminated, to the end of the SABRE-EFNMR experiment. The pressure readings from the initial and final vent procedures were ignored.

The  $p\text{-H}_2$  forward pressure over the course of the V1 hold procedure tracks the rate of recovery of the  $p\text{-H}_2$  generator for 32 s, after  $\sim 47$  s of  $p\text{-H}_2$  bubbling. It

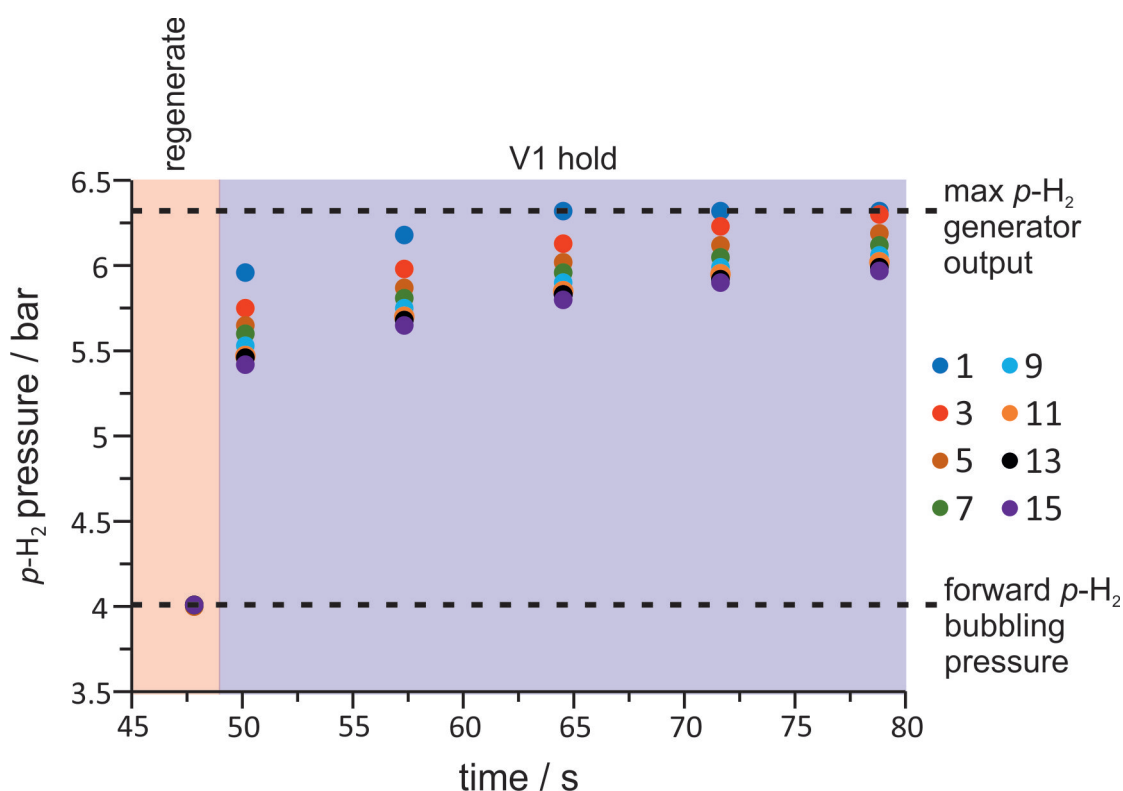


FIGURE 4.5: Plot of forward pressure values of  $p\text{-H}_2$  into the reaction cell from the end of the regenerate procedure to the end of the V1 Hold procedure which indicates the end of the SABRE-EFNMR experiment. The data shows the recovery of the output of  $p\text{-H}_2$  from the  $p\text{-H}_2$  generator across 15 different repetitions of the bubbling experiment. A good recovery of the  $p\text{-H}_2$  generator is observed because the output pressure at the end of V1 hold is equilibrating to a value higher than the input pressure of the experiment of 4 bar, suggesting the  $\text{H}_2$  and  $p\text{-H}_2$  generators are keeping up with the  $p\text{-H}_2$  demand by the SABRE-EFNMR experiment.

is important to note that the V1 hold procedure has replaced what would be the repetition delay between experiments in a standard SABRE-EFNMR experiment. The recovery of the generator is dependent on a combination of the  $p\text{-H}_2$  flow rate through the cell dictated by the pressure differential, the  $p\text{-H}_2$  formation rate limited to  $0.2\text{ L min}^{-1}$ , the  $\text{H}_2$  gas production rate and the V1 hold duration (repetition delay). Since the  $\text{H}_2$  production rate and the  $p\text{-H}_2$  formation rate are fixed, and the  $p\text{-H}_2$  bubbling rate is chosen to maximise the SABRE reaction, the repetition delay must be optimised to ensure the  $p\text{-H}_2$  generator sufficiently recovers between experiments in order to maintain the required pressure differential across the cell.

The first data point of the PG1 monitor experiment shows that the forward pressure was successfully maintained at the set value of 4 bar for all repetitions indicating that PR1 is correctly regulating the pressure (the same is true for PR2). The first 3 repetitions of the SABRE-EFNMR experiment show a full recovery of the output of the  $p\text{-H}_2$  generator to the regulated value of 6.3 bar (a reading of 6 bar on the pressure gauge at the outlet of the  $p\text{-H}_2$  generator is read as 6.3 bar on PG1) by the end of the V1 hold procedure. The recovery rate of the  $p\text{-H}_2$  generator was unchanged for all repetitions of the SABRE-EFNMR experiment, however, its output pressure at the start and end of the V1 hold procedure consistently decreased with each repetition until the generator no longer fully recovered after the third repetition. Since the recovery rate depends on the formation rate of  $p\text{-H}_2$  which depends on the production rate of  $\text{H}_2$ , and the inlet pressure of the  $p\text{-H}_2$  generator continuously dropped during the regenerate and V1 hold procedures across all repetitions (observed on the screen of the  $p\text{-H}_2$  generator whilst on 'diagram' view), the production of  $\text{H}_2$  was concluded to be the limiting factor in the recovery rate. This means that the production rate of  $\text{H}_2$  is slowing down the formation of  $p\text{-H}_2$  required to maintain a  $+0.25$  bar pressure differential.

When the regenerate procedure is initiated, the output pressure of the  $p\text{-H}_2$  generator drops rapidly (also observed on the screen of the  $p\text{-H}_2$  generator whilst on 'diagram' view) as the reaction cell fills up with  $p\text{-H}_2$ . Once the pressure differential is established, the outlet pressure of the  $p\text{-H}_2$  generator slowly increases, provided the rate of formation of  $p\text{-H}_2$  is faster than the bubbling rate. This was the case for the PG1 monitor experiment in FIGURE 4.5, however, the plot shows that although the  $p\text{-H}_2$  pressure at the start and end of the V1 hold procedure decreases with every repetition, the amount at which it drops by also decreases. This indicates that the flow rate of  $p\text{-H}_2$  through the cell is slower than the  $0.2\text{ L min}^{-1}$  formation rate of  $p\text{-H}_2$ . It also indicates that the performance of the automated gas flow system is reaching a state of equilibrium, where the output pressure of the  $p\text{-H}_2$  generator at the start and end of the V1 hold procedure appears to be converging toward 5.3 and 5.8 bar, respectively. The large drop in output pressure of the  $p\text{-H}_2$  generator, due to the initial filling of the reaction cell with  $p\text{-H}_2$  also equilibrates to a certain value, and as long as it is at least 0.5 bar higher than the set forward pressure at PR1, the flow system can keep up with the  $p\text{-H}_2$  demand for the SABRE-EFNMR experiment over many repetitions. If not, the repetition time (or duration of the V1 hold procedure in this case) must be increased to allow the production rates of  $\text{H}_2$  and  $p\text{-H}_2$  to keep up with the desired pressure differential, as all other parameters that effect the  $p\text{-H}_2$  generator's recovery are fixed.

For the case when the output pressure of the  $p$ -H<sub>2</sub> generator drops below the forward pressure set by PR1 during the SABRE-EFNMR experiment, there will be more pressure in the reaction chamber than in the polariser control unit and the  $p$ -H<sub>2</sub> generator, thus creating an unfavourable pressure differential that forces  $p$ -H<sub>2</sub> and small amounts SABRE solution into the  $p$ -H<sub>2</sub> generator via the polariser. The SABRE sample contains iridium catalyst and CH<sub>3</sub>OH/CD<sub>3</sub>OD solvent which is not only harmful to valves, pressure gauges and pressure regulators in the polariser control unit and  $p$ -H<sub>2</sub> generator, but will also freeze inside the generator causing a block. Damage to the flow system can be minimised if the experiment is terminated quickly and the generator is immediately warmed to room temperature and purged. It is therefore imperative for the person operating the system or someone who understands it to be close by to continuously check on the recovery of the  $p$ -H<sub>2</sub> generator's output in between experiments. This can be done by either keeping an eye on the inlet and outlet pressures of the  $p$ -H<sub>2</sub> generator during the SABRE-EFNMR experiment (shown on its screen when in 'diagram' view), or by recording and saving the pressure values at PG1 and PG2 after each repetition of the SABRE-EFNMR experiment, as shown in FIGURE 4.5.

### 4.3.3 Optimising the Parahydrogen Pressure Differential

The forward pressure of  $p$ -H<sub>2</sub> into the reaction cell, regulated at PR1, determines the concentration of  $p$ -H<sub>2</sub> in the SABRE sample during  $p$ -H<sub>2</sub> bubbling. The combination of the forward and back pressure regulated at PR1 and PR2 determines the pressure differential and corresponding flow rate of  $p$ -H<sub>2</sub> through the reaction cell. Maximising the forward pressure and the pressure differential maximises the dissolution of  $p$ -H<sub>2</sub> into the SABRE sample and hence the hyperpolarisation of the substrate. However, the values of these parameters must be chosen in consideration with the limited production of H<sub>2</sub> and limited formation of  $p$ -H<sub>2</sub> (0.2 L min<sup>-1</sup>) because too high a forward pressure and pressure differential will use up too much  $p$ -H<sub>2</sub> at each repetition of the SABRE-EFNMR experiment.

A pressure differential of +0.25 bar from a forward and back pressure of 4 and 3.75 bar, respectively, was used in FIGURE 4.5 which demonstrated sufficient recovery of the  $p$ -H<sub>2</sub> generator over 15 repetitions. To observe the effect of the pressure differential on the output of the  $p$ -H<sub>2</sub> generator, PG1 and PG2 were used to record the forward and back pressures of  $p$ -H<sub>2</sub> during the second stage of the regenerate procedure under pressure differentials of 0.2, 0.25 and 0.3 bar, from a forward pressure of 3.5 bar (see FIGURE 4.6). When a 0.2 and 0.25 bar pressure differential were used, a consistent flow of  $p$ -H<sub>2</sub> through PR1 and PR2 was observed, and the pressure differential was successfully established and maintained. When a 0.3 bar pressure differential was set, the flow of  $p$ -H<sub>2</sub> through PR1 and PR2 was very inconsistent and could not be regulated to the set pressure of 3.5 bar at PR1 and 3.2 bar at PR2. This result suggests that the production rate of H<sub>2</sub> or the 0.2 L min<sup>-1</sup> formation rate of  $p$ -H<sub>2</sub> is slower than the flow rate of  $p$ -H<sub>2</sub> through the reaction cell that is associated with a 0.3 bar pressure differential. Therefore, a lower pressure differential must be used for SABRE-EFNMR

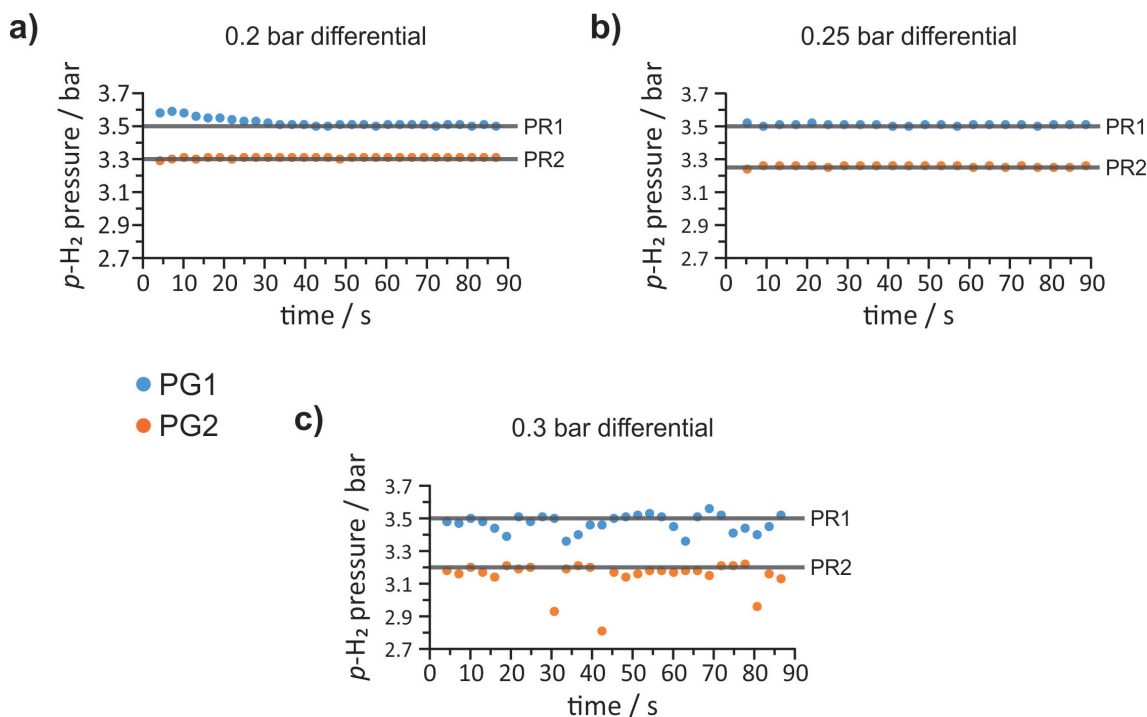


FIGURE 4.6: A plot of the  $p\text{-H}_2$  forward and back pressure, measured by PG1 and PG2, respectively, during the second stage of the regenerate procedure with a set pressure differential of a) 0.2 bar, b) 0.25 bar and c) 0.3 bar, from a forward pressure of 3.5 bar.

experiments to achieve reproducible SABRE hyperpolarisation.

#### 4.3.4 Blockage and Leak Tests

Insufficient vacuuming of the  $p\text{-H}_2$  generator working volume introduces gases other than  $\text{H}_2$  into the conversion chamber which freeze at the operating temperature of 38 K. The frozen gas blocks the path of the  $p\text{-H}_2$  through the conversion chamber and reduces its flow rate by an amount that is proportional to the severity of the block. A block can be diagnosed by observing the generator's output pressure, displayed on the screen of the generator in 'diagram' view, after initiation of the continuous flow procedure which transfers  $p\text{-H}_2$  toward a closed PR1 (if polariser is in stand-by mode) and leads to a pressure build up at the outlet of the generator. If the observed pressure build-up is significantly slower than under normal operating conditions, the  $p\text{-H}_2$  generator is blocked and the continuous flow procedure must be terminated in order to run the manual purge procedure. In some cases blocking due to freezing can take time to occur, especially if there is a leak in the generator that is slowly introducing air into the reaction chamber, where the block may then occur in the middle of the day and could get worse as more and more  $p\text{-H}_2$  bubbling experiments are run.

Leaks in the working volume of the  $p\text{-H}_2$  generator, as well as faulty components within it such as solenoid valves, etc., which act as blockages if they are unintentionally

limiting the flow of  $p\text{-H}_2$  through them, can disrupt the build-up of pressure at the outlet of the generator after initiating the continuous flow procedure. This can easily be tested for by using the path through SV7 (see FIGURE 4.2) that bypasses the conversion chamber to flow thermal hydrogen gas into the polariser. A clean flow through the polariser operating at room temperature means that blockages are only occurring when its cooled down and must be due to gases freezing within the conversion chamber. However, if the output of the generator is compromised when warm, the issue is due to a faulty part or a leak. Manual switching of the solenoid valves in the  $p\text{-H}_2$  generator to hold the  $\text{H}_2$  gas within different sections of the working volume can help to locate the issue.

Leaks within the Bruker polariser control unit were encountered much more frequently than on the Bruker BPHG 90  $p\text{-H}_2$  generator, and occurred due to improper tightening of its plastic connectors that link the FEP tubing to all of the components. Therefore, the first form of action if a leak was suspected within the polariser was to hand tighten all of the accessible connectors, followed by the use leak detector during gas flow through the polariser. Care should be taken when spraying leak detector on the inside of the polariser as liquids can damage the circuit board. One could also visually check for punctures or bends in the FEP tubing that could be affecting the flow of gas. A more reliable way of testing for leaks was with a leak test experiment written on the Terranova Expert software that allow gas to be held within different sections of the polariser's working volume, and observing how well the gas pressure is held using PG1 or PG2, as illustrated in FIGURE 4.7. The procedure is initiated with the polariser on stand-by mode (PR1 = 0, PR2 = 0, valve state: [0 0 0]), and begins by first setting PR1 to 5 to build-up gas pressure at V1. The system is left in this state for a few seconds to allow the pressure at V1 to build-up to the pressure of gas going into the polariser. The 'Hold 1' procedure is then run which sets PR1 to 0 to hold the  $\text{N}_2$  gas between PR1 and V1, and test for gas leaks within this isolated section of the polariser working volume. After the Hold 1 procedure finishes, the polariser changes to a valve state of [1 1 0] and PR2 is set to 5. This allows gas to flow through PR1, the reaction cell and the phase separator to achieve a pressure build-up at PR2. The system is held in this state for a few seconds to allow the pressure at PR1 and PR2 to equilibrate, after which the 'Hold 2' procedure is run which sets PR1 to 5. This traps the  $\text{N}_2$  gas between PR1 and PR2 to test for leaks in the rest of the working volume of the polariser. The leak test procedure does not test for leaks between the T piece and V3, but this can be achieved by repeating the first part of the leak test procedure where gas is allowed to build-up at V1, and then turning off the flow of  $\text{N}_2$  from the source. This traps  $\text{N}_2$  gas between the outlet of the  $\text{N}_2$  source and V1, which includes the T piece and V3. At this point, PG1 can be used to track any changes in the  $\text{N}_2$  pressure to determine whether there is a leak present.

FIGURE 4.7 demonstrates the results from a leak test experiment that was run with 5.8 bar of  $\text{N}_2$  gas and with pressure readings from PG1 and PG2 recorded every 2.3s. An instant build-up of  $\text{N}_2$  pressure at V1 to 5.8 bar is observed at PG1 when the leak test is initiated. The results from PG1 during the Hold 1 procedure show that the tubing between V1 and PR1, and the connections to V1 and PR1 themselves are well sealed as the pressure remained mostly consistent. A negligible loss of  $\text{N}_2$  pressure was observed, however this is attributed to the unavoidable escape of  $\text{N}_2$  gas

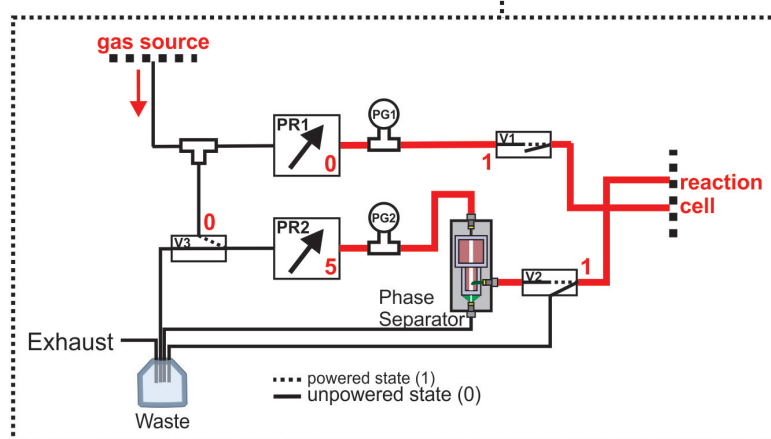
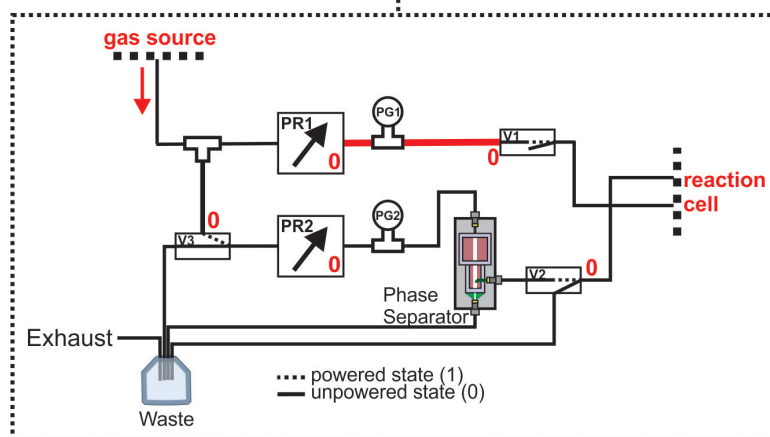
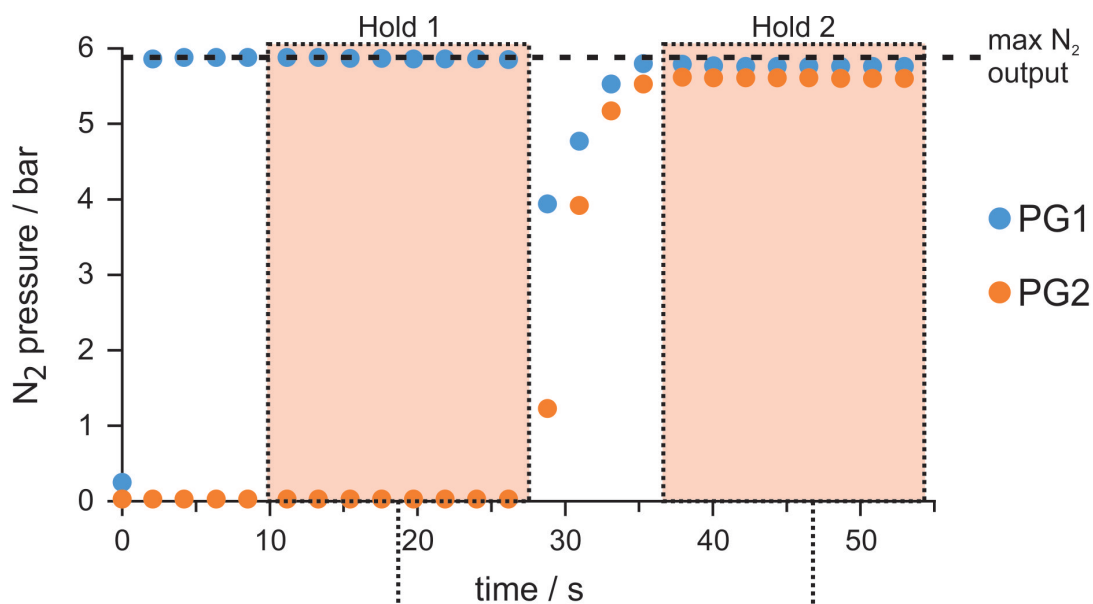


FIGURE 4.7: Plot of N<sub>2</sub> pressure during the different stages of the leak test procedure which aims to test the ability of the FEP tubing and components within the Bruker polariser control unit to hold pressure. The Hold 1 and Hold 2 procedures used to hold N<sub>2</sub> gas in between PR1 and V1, and PR1 and PR2, respectively, show that there are no leaks present within the polariser. The numbers in red next to the pressure regulators and switchable valves indicates their operating state.

from the plastic connectors. A pressure build-up at PG2 and pressure loss at PG1 was then observed as the N<sub>2</sub> gas is pushed toward PR2. The N<sub>2</sub> pressure equilibrated to 5.7 and 5.55 bar at PG1 and PG2, respectively, after 12 s. The final pressure results from PG1 and PG2 for the Hold 2 procedure shows that the tubing, as well as the connectors to the components, between PR1 and PR2 were also well sealed as there was no significant change in pressure. The insignificant and unavoidable escape of N<sub>2</sub> gas was again observed.

## 4.4 Conclusion

Integration of the EFNMR-Helmholtz system with the automated gas flow system formed the SABRE-EFNMR system which is capable of carrying out SABRE experiments *in situ* of the polarising and detection fields. This system is an upgrade on the *in situ* system published previously by the Meghan Halse group.<sup>106</sup> Although the hyperpolarised pyridine data in the paper demonstrated a good level of reproducibility, the conversion chamber within the *p*-H<sub>2</sub> generator was prone to blocking, and the *p*-H<sub>2</sub> flow rate into the SABRE sample was not always consistent across multiple experiments.

Improvements to the operating procedures of the Bruker BPHG 90 *p*-H<sub>2</sub> generator and the Bruker polariser control unit meant that SABRE experiments could be optimised and performed with much more consistency to give a higher reproducibility of hyperpolarisation. The purge procedure carried out by the *p*-H<sub>2</sub> generator was enhanced to ensure blocking of the conversion chamber by the freezing of unwanted gases within it at 38 K did not occur, especially during a SABRE-EFNMR experiment when a continuous flow of *p*-H<sub>2</sub> into the polariser is required. Macros on the Terranova-Expert software were written to test for leaks in the polariser's internal FEP tubing in order to prevent the escape of H<sub>2</sub> gas into the lab and to maintain a consistent flow of *p*-H<sub>2</sub> into the reaction cell across all experiments. Procedures that monitor the flow of gas through the Bruker polariser control unit using PG1 and PG2 were also written, and together with the real-time pressure readings displayed on the screen of the *p*-H<sub>2</sub> generator, the forward pressure of *p*-H<sub>2</sub> into the reaction cell and the flow rate of *p*-H<sub>2</sub> through the SABRE sample could be optimised. Optimal flow conditions are key to ensuring the automated gas flow system can maintain the desired flow rate of *p*-H<sub>2</sub> over consecutive SABRE-EFNMR experiments. Finally, the very simple addition of the vent procedure to the start and end of all repetitions of the SABRE-EFNMR experiments aided in creating identical starting conditions for the flow of *p*-H<sub>2</sub> into the reaction cell.

All of the improvements to the automated gas flow system used previously by the group to perform *in situ* SABRE with EFNMR detection<sup>106</sup> have helped to establish a reproducible, user-controlled flow of *p*-H<sub>2</sub> into the reaction cell. In addition, the previous *in situ* system was also limited by its ability to only perform homonuclear SABRE polarisation transfer using the built-in polarising coil, however, the EFNMR-Helmholtz system which has been integrated with the automated gas flow system,

is able to overcome this. In the next chapter, the SABRE-EFNMR system will be used to achieve mT and  $\mu$ T SABRE polarisation transfer with *in situ* detection in the ultra-low-field regime. The benefits of rapid detection of the SABRE hyperpolarisation after the polarisation transfer step due to our in situ detection approach will be explored and demonstrated for a range of fluoropyridines with different  $J$ -coupling properties.

# 5 | *In situ* SABRE Polarisation of Fluoropyridines

## 5.1 Introduction

In chapters 2 and 3, a system for *in situ* SABRE polarisation with EFNMR detection was described that provides a robust and reproducible set of experimental conditions for performing hyperpolarisation measurements. In this chapter, we will use this system to demonstrate the *in situ* SABRE polarisation of  $^1\text{H}$  and  $^{19}\text{F}$  nuclei with EFNMR detection. The goal is to develop an improved understanding of the spin-physics that underpins SABRE polarisation transfer in the ULF regime.

Since it is not the chemistry behind the SABRE process that is being probed, but the spin-physics behind the SABRE polarisation transfer mechanism, a well documented SABRE catalyst-substrate combination was employed, and involved the use of N-heterocyclic substrates with the Ir-IMes ( $[\text{IrCl}\{\text{COD}\}\{\text{IMes}\}]$ ) metal complex as the SABRE precatalyst.<sup>2,52,56,84,99–103</sup> Pyridine is a well studied SABRE substrate that is often used with the Ir-IMes precatalyst<sup>32,55,100,114,115</sup> (see FIGURE 5.1), however, its EFNMR spectrum shows only a singlet because the  $^1\text{H}$  nuclei are magnetically equivalent in the ULF regime and produce overlapping singlet peaks. Introduction of a heteronuclear coupling breaks the equivalence, and a  $J$ -coupling network comprised of strong  $^1\text{H}$ - $^1\text{H}$  and  $\text{X}$ - $^1\text{H}$  interactions is formed, giving rise to complicated peak shapes that are nonetheless specific to the substrate under investigation. As a consequence, information about the chemical system of the substrate and the form of the SABRE polarisation is provided. Further complexity is added to the SABRE-polarised EFNMR

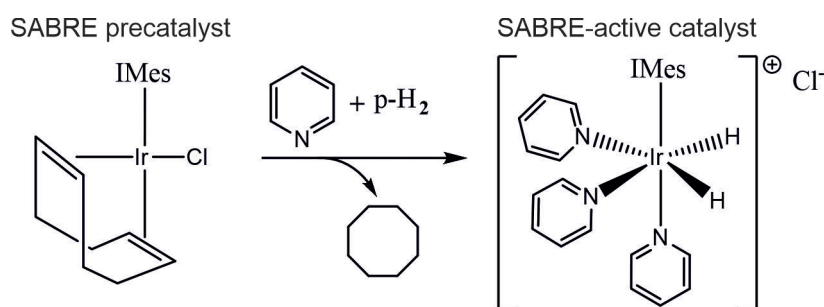


FIGURE 5.1: Form of the SABRE-active catalyst when using the Ir-IMes SABRE precatalyst with pyridine as the SABRE substrate.

spectrum by the poor signal resolution due to overlapping peaks with equal chemical shifts.

The absence of chemical shift resolution combined with strong homonuclear and heteronuclear coupling, inherent to NMR detection in the ULF regime, presents a challenge for spectral interpretation. Even so, the complete and successful analyses of strongly coupled  $^1\text{H}$ -X spin systems has been demonstrated in the literature in the Earth's magnetic field on a range of substrates containing spin-1/2<sup>82</sup> and quadrupolar<sup>111</sup> heteronuclei. The complex EFNMR spectra produced by these substrates were analysed using perturbation theory and NMR simulations based on a quantum mechanical method first proposed by Bernstein and Pople.<sup>80</sup> The studies show that although difficult, more structural information can be extracted from signals acquired in the ULF regime. This is beneficial in regards to probing of the SABRE polarisation transfer mechanism as the EFNMR signal shape will be more sensitive to changes in the polarisation transfer pathway.

The SABRE-polarised EFNMR spectra acquired in this report have been analysed using NMR simulations that represent theoretical spectra for comparison to facilitate interpretation. Simulations also allow deconvolution of the observed SABRE-polarised signal with the ability to isolate certain nuclei for detection in order to assign the hyperpolarised peaks to chemical environments on the substrate. As a consequence of the SABRE polarisation transfer pathway, many magnetic states in the substrate spin system receive hyperpolarisation, but it is not obvious by looking at the SABRE-polarised signals, which states those are. Choosing which magnetic states are allowed to evolve under the simulated NMR experiment and which are detected is an effective way to replicate the SABRE-polarised signals to estimate which magnetic states on the substrate are involved in the SABRE polarisation transfer pathway.

This work has focused on the use of fluorinated pyridine derivatives as the N-heterocyclic substrates of choice. Fluorine was chosen as the heteronucleus because it is 100% abundant in the spin-half  $^{19}\text{F}$  isotope which has a gyromagnetic ratio that is close to that of proton. This leads to a difference in Larmor frequency between the two nuclei of  $\sim 131.1$  Hz at the preferred EFNMR detection field of  $51.9$   $\mu\text{T}$ . The two nuclei can therefore be simultaneously excited and detected (see Chapter 3) which facilitates the acquisition of their SABRE-polarised signals on the Terranova-MRI probe. Fluorinated pyridine substrates with a varying number of  $^{19}\text{F}$  nuclei were used to maximise the intensity of the SABRE-polarised  $^{19}\text{F}$  EFNMR signal. Substrates with and without symmetry, containing varying magnitudes of  $^{19}\text{F}$ - $^1\text{H}$   $J$ -coupling interactions were also used in order to observe how the substrate  $J$ -coupling network influences the SABRE polarisation transfer mechanism.

The acquisition and observation of SABRE-polarised  $^1\text{H}$  and  $^{19}\text{F}$  signals in this chapter have made use of the direct and indirect transfer of polarisation from the  $p$ - $\text{H}_2$  derived hydrides on the SABRE catalyst to a target nucleus on the substrate. Indirect transfer refers to the transfer of polarisation to one type of nucleus on the substrate before being relayed onto the target nucleus which is also on the substrate but is of a different type (e.g. from the hydrides to a  $^1\text{H}$  nucleus on the substrate, and then from the  $^1\text{H}$  nucleus to a  $^{13}\text{C}$  nucleus on the substrate). Both transfer pathways are mediated

by the  $J$ -coupling in the presence of a weak magnetic field. The PHIP method is heavily dependent on indirect polarisation transfer to hyperpolarise heteronuclei ( $^{13}\text{C}$ ,  $^{19}\text{F}$ , etc.) on the hydrogenated substrate. This can occur spontaneously,<sup>116,117</sup> albeit not very efficiently. Magnetic field cycling<sup>118,119</sup> and RF pulse sequences<sup>120,121</sup> have been developed with PHIP to improve the efficiency of indirect polarisation transfer.

In a publication by Hill-Casey et al. on SABRE-polarised pyridine derivatives with EFNMR detection,<sup>106</sup> the monitoring of the activation of the Ir-IMes catalyst, hyperpolarisation build-up in mT PTFs as a function of  $p\text{-H}_2$  bubbling time, and polarisation transfer as a function of mT PTF strength via *in situ* EFNMR detection was demonstrated for the first time. PTF sweep experiments in the mT regime, implemented using the polarising coil, found that a PTF of 6.5 mT is optimal for direct polarisation transfer to the protons on pyridine, pyrazine, and isonicotinamide. This is in agreement with the PTFs used widely across the literature for mT SABRE polarisation transfer to protons on a substrate,<sup>2,35,99,101</sup> chosen based on the PTC<sup>39,55</sup> derived from the theory of LAC.<sup>54</sup> The SABRE-EFNMR experiments in this work have been adapted for implementation of the triaxial Helmholtz coil array.

The work by Hill-Casey et al.<sup>106</sup> also presented a method for quantitatively assessing the level of SABRE polarisation of pyridine. At high field, SABRE enhancements are calculated by dividing the intensity of the hyperpolarised signal by the intensity of the same signal, from the same sample, at thermal equilibrium. However, the pyridine SABRE sample contained too low a concentration of protons (mM) to produce an observable thermal pyridine  $^1\text{H}$  signal on the Terranova-MRI system. Therefore, the pyridine signal intensity at thermal equilibrium was estimated from the extrapolation of a fit to the plot of signal intensity against the concentration of  $^1\text{H}$  nuclei in multiple water samples of different volumes and with pre-polarisation at 18.8 mT. This method provides an estimate of the polarisation levels achieved, but the precision is poor due to the high level of uncertainty inherent in this approach. Therefore, in the following work no estimates of absolute polarisation level were made. Instead, a qualitative analysis of the SABRE-polarised results is presented. This is suitable because changes in the shape of the SABRE-polarised signal, as well as relative changes to its signal intensity under varying experimental conditions (PTF, RF pulse sequence, etc.) is of more importance to probing the SABRE polarisation transfer mechanism than measures of the absolute polarisation level.

The first section of this chapter outlines the SABRE-EFNMR experiments that were developed for the SABRE-EFNMR system to achieve the *in situ* detection of SABRE polarisation on the target substrates. The second section displays the successful hyperpolarisation of  $^1\text{H}$  and  $^{19}\text{F}$  nuclei in target fluorinated pyridines using the mT SABRE-EFNMR experiment. With the use of NMR simulations to aid in interpreting the complex EFNMR spectra and qualitatively judge the success of the mT SABRE-EFNMR experiment, a detailed discussion and comparison of the SABRE-polarised spectra is given. Hyperpolarisation of the SABRE solvent was observed and is also briefly discussed in this section.

## 5.2 SABRE-EFNMR Experiment

The mT and  $\mu\text{T}$  SABRE-EFNMR experiments in FIGURE 5.2 were developed from the improved EFNMR experiment by the addition of  $p\text{-H}_2$  bubbling into the NMR pulse sequence and the replacement of the pre-polarising pulse with the PTF pulse, produced by either the polarising coil or the z-Helmholtz coil pair. Instead of hyperpolarising the sample with an 18.8 mT pre-polarising field, the polarising coil achieves hyperpolarisation by satisfying the SABRE PTC for the coherent transfer of polarisation from the singlet state of the  $p\text{-H}_2$  derived hydride to  $^1\text{H}$  nuclei on the substrate, equal to around 6.6 mT (this value is only a prediction, the exact PTF varies depending on the substrate). The z-Helmholtz coil pair uses negative currents to generate  $\mu\text{T}$  PTFs below  $B_E$  (0-50  $\mu\text{T}$ ) to satisfy the SABRE PTC for efficient SABRE polarisation transfer to  $^{19}\text{F}$  nuclei on the substrate of around 3.6  $\mu\text{T}$  (also just a prediction). The role of the  $B^1$  coil, the shim coils and the y-Helmholtz coil pair coil is unchanged in the SABRE-EFNMR experiments.

Regardless of the polarisation transfer pathway, a positive current is passed through the z-Helmholtz coil pair after the PTF to generate the detection field ( $\sim +46$  mA shifts  $\nu_{^1\text{H}}$  to 2210 Hz). Therefore, instantaneous switching from negative to positive currents through the z-Helmholtz coil pair is required. As mentioned in section 3.2.2, instantaneous changes to the current through a coil leads to an overshoot which eventually stabilises to the set value, but in the process, generates a fluctuating magnetic field that is picked up by the  $B^1$  coil. A delay,  $t_{RD}$ , of 20 ms is added after the switch in current to allow the z-Helmholtz coil to ring down to prevent disruption to RF pulses and EFNMR detection.

$p\text{-H}_2$  bubbling of the sample in the reaction cell is initiated and terminated by the polariser control unit, marking the start of the SABRE-EFNMR experiment and the end of EFNMR detection. Communication between the controlling PC and the polariser control unit is external of the operation of the polarising and  $B^1$  coil, and means that the SABRE polarisation transfer step, the RF pulse sequence and NMR detection are encapsulated within  $p\text{-H}_2$  bubbling. The main contributor to the duration of  $p\text{-H}_2$  bubbling,  $t_{bub}$ , is the duration of the PTF,  $t_{PTF}$ . The longer  $p\text{-H}_2$  is bubbled through the SABRE solution under the PTF, the greater the build-up of hyperpolarisation. This is because longer  $p\text{-H}_2$  bubbling increases the build-up of hyperpolarised substrate in solution. A plateau is reached when a steady state is established between the production and relaxation rate ( $1/T_1$ ) of the hyperpolarised substrate. The point at which the plateau is reached is dictated by multiple parameters such as the concentration of  $p\text{-H}_2$  in solution and the rate at which the  $p\text{-H}_2$  and substrate molecules bind and unbind from the metal centre, as this determines the lifetime of the active SABRE complex. The plateau point is therefore considered as the optimal  $t_{PTF}$ , and varies with different substrates since they have different binding strengths to the SABRE catalyst. The  $t_{PTF}$  is optimised by repeating the mT and  $\mu\text{T}$  SABRE-EFNMR experiments with a linear variation in  $t_{PTF}$ . A typical duration sweep involves ranging  $t_{PTF}$  from 0-30 s.

The repetition time,  $t_{rep}$ , is not dictated by  $T_1$  relaxation time of the spin system

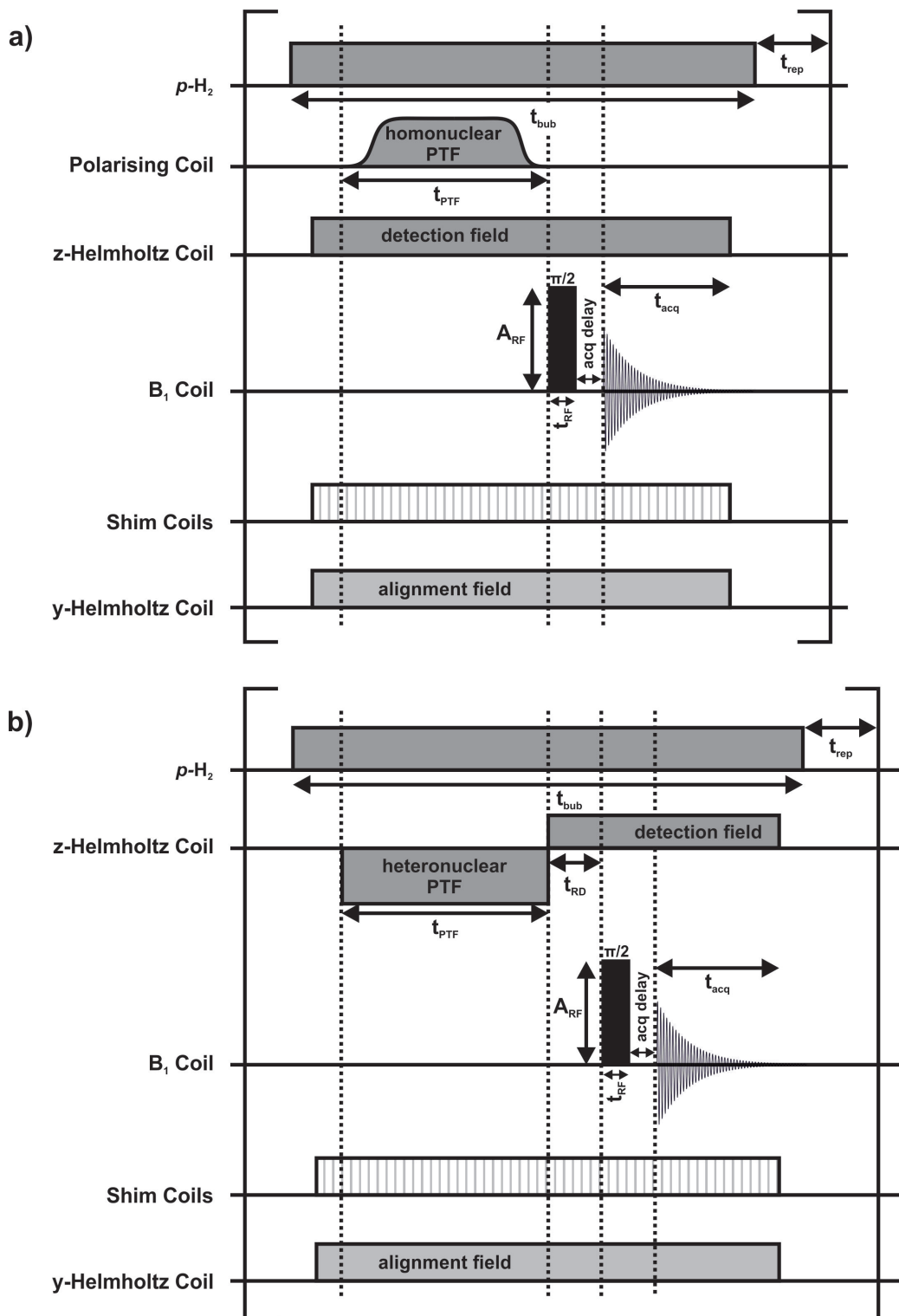


FIGURE 5.2: Pulse sequence of the a) mT and b)  $\mu\text{T}$  SABRE-EFNMR experiments which are similar to the pulse sequence of the EFNMR experiment but include the addition of  $p\text{-H}_2$  bubbling made possible by integration of the EFNMR-Helmholtz setup with the automated gas flow system. The polarising coil (0.5-18.8 mT) and the z-Helmholtz coil pair ( $\pm 64.5 \mu\text{T}$ ) are used to generate the homonuclear and heteronuclear PTF, respectively, where heteronuclear SABRE polarisation transfer requires switching the current through the z-Helmholtz coil to generate both the PTF and detection field.

but by the recovery time of the  $p$ -H<sub>2</sub> generator. With the automated gas flow system described in chapter 4, recovery times are typically more than 40 s which is much longer than  $5T_1$ . Whilst long  $t_{rep}$  times increase experimental times, it also allows time for the degassing of the sample, where dissolved H<sub>2</sub> from the current bubbling experiment is removed from solution in preparation for the next one. Degassing helps to maintain consistent starting conditions for each experiment and a maximal dissolution of fresh  $p$ -H<sub>2</sub> to increase the efficiency of the SABRE reaction.

The amplitude of the RF pulses for the on-resonance and simultaneous  $\pi/2$  nutation of the <sup>1</sup>H and <sup>19</sup>F nuclei should ideally be calibrated for each substrate to maximise EFNMR detection of their hyperpolarised signals. However, only the on resonance interaction between the RF pulse and <sup>1</sup>H nuclei for each substrate could be calibrated because it was not possible to acquire good quality RF amplitude-sweep nutation curves from the hyperpolarised <sup>19</sup>F signals. The nutation experiment produced very weak hyperpolarised <sup>19</sup>F signals that also exhibited complex splitting patterns. Both factors made integration of the hyperpolarised <sup>19</sup>F signals challenging. Instead, the amplitude value from the calibration of the on resonance <sup>19</sup>F  $\pi/2$  pulse on TFE ( $V_{\pi/2} = 0.95$  V) was used for the on-resonance  $\pi/2$  rad nutation of the hyperpolarised <sup>19</sup>F nuclei. The amplitude value from the calibration of the simultaneous  $\pi/2$  pulse on TFE was also used on all the substrates to simultaneously nutate the hyperpolarised <sup>1</sup>H and <sup>19</sup>F nuclei by  $\pi/2$  rad ( $V_{\pi/2} = 1.1$  V). This could be done because the RF amplitude of the  $\pi/2$  <sup>1</sup>H pulses calibrated on SABRE samples of varying concentrations, were very close to those calibrated on H<sub>2</sub>O and TFE. By this logic the same should follow for the <sup>19</sup>F pulse and the simultaneous nutation pulse.

A SABRE-polarised <sup>1</sup>H spectrum of 25 mM pyridine in 4 mL of deuterated MeOH (CD<sub>3</sub>OD) is shown in FIGURE 5.3. It was acquired in 1 scan using the mT SABRE-EFNMR experiment (see 5.2a) with a PTF = 6.4 mT and a  $t_{PTF} = 20$  s. The hyperpolarised pyridine singlet is overlaid with the singlet acquired from a 500 mL water sample in 1 scan using the improved EFNMR experiment with pre-polarisation at 18.8 mT. Linewidths of 0.2 and 0.6 Hz, respectively, were observed. The wider linewidth of the water signal is attributed to the larger size of the 500 mL water bottle in comparison to the glass reaction cell, causing the <sup>1</sup>H spins of water to experience a less homogeneous external field and RF pulse across the sample volume. A SABRE enhancement factor cannot be calculated directly for this sample because 25 mM of pyridine in 4 mL of solvent cannot be observed with standard EFNMR. However, the observed SABRE-polarised signal level is of the same order of magnitude as the water signal, despite the fact that there are ca. 110,000 times more <sup>1</sup>H nuclei in the water sample compared to the pyridine sample. Therefore, the level of signal enhancement that has been achieved is on the order of 10<sup>5</sup>-fold.

For each new SABRE sample, the Ir-IMes precatalyst must first be activated, since it is the active form that is involved in the SABRE catalytic cycle. Catalyst activation is monitored by repeating the mT SABRE-EFNMR experiment (see FIGURE 5.2) and plotting the integral of the acquired <sup>1</sup>H EFNMR signal at each repetition against the  $p$ -H<sub>2</sub> bubbling time to give the catalyst activation curve. The shape of the curve is unique to the precatalyst-substrate combination, their relative quantities, and the pressure and flow rate of  $p$ -H<sub>2</sub>. An example activation curve is shown in FIGURE

5.4 acquired from a sample containing 5 mM Ir-IMes and 250 mM 3,5-DFP. This catalyst activation experiment is therefore monitoring the conversion of the Ir-IMes to  $[\text{Ir}(\text{IMes})(\text{H})_2(3,5\text{-DFP})_3]^+ \text{Cl}^-$ .

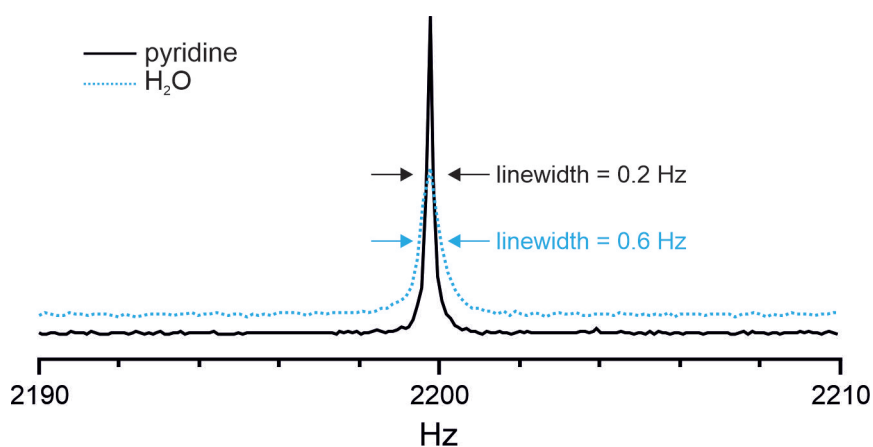


FIGURE 5.3: The SABRE-polarised EFNMR  $^1\text{H}$  signal of 25 mM pyridine in 4 mL  $\text{CD}_3\text{OD}$  acquired using the mT SABRE-EFNMR experiment overlaid with the less intense EFNMR  $^1\text{H}$  signal of water (500 mL) acquired with the improved EFNMR experiment. The larger water sample experiences more inhomogeneities in the RF pulse and the external field across the sample volume which contributes to the larger linewidth of the water signal. Both  $^1\text{H}$  peaks have equal Larmor frequencies of  $\sim 2200$  Hz because chemical shift is not observed at  $51.9\mu\text{T}$ .

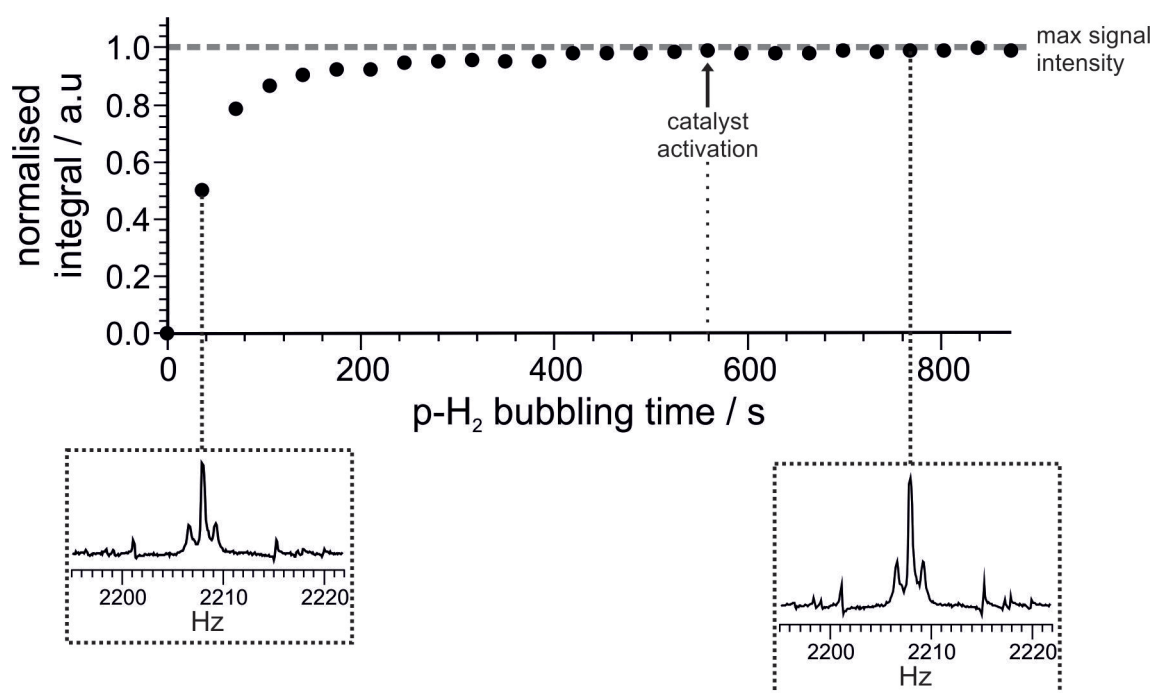


FIGURE 5.4: Activation curve of 5 mM Ir-IMes in 250 mM 3,5-DFP (50 equivalents relative to the catalyst) and 4 mL  $\text{CD}_3\text{OD}$  showing the build-up of hyperpolarisation of the  $^1\text{H}$  EFNMR signal as a function of  $p\text{-H}_2$  bubbling time and the formation of  $[\text{Ir}(\text{IMes})(\text{H})_2(3,5\text{-DFP})_3]^+ \text{Cl}^-$ . Each data point represents a repetition of the mT SABRE-EFNMR experiment and 34.9 s of bubbling ( $t_{PTF} = 30$  s,  $t_{RF} = 3.62$  ms,  $t_{acq} = 4915.2$  ms, acquisition delay = 20 ms). Activation of the precatalyst was achieved at the plateau of the curve after  $\sim 560$  s of  $p\text{-H}_2$  bubbling. The consistent intensity of the hyperpolarised  $^1\text{H}$  signal following catalyst activation indicates good reproducibility in the hyperpolarisation achieved by the mT SABRE-EFNMR experiment.

A rapid increase in the intensity of the hyperpolarised  $^1\text{H}$  signal of 3,5-DFP is observed at the start of the experiment for the first 3 repetitions ( $\sim 105\text{ s}$   $p\text{-H}_2$  bubbling). The next 13 repetitions saw a much slower increase in the hyperpolarised signal intensity, where the 16<sup>th</sup> repetition, equivalent to  $\sim 560\text{ s}$  of  $p\text{-H}_2$  bubbling, appears to reach a plateau. This indicates that the SABRE catalyst has been fully activated and an equilibrium has been established between the various parameters that contribute toward the hyperpolarised signal intensity (e.g. binding/dissociation rate of  $p\text{-H}_2$  and substrate to the active catalyst, production and relaxation rate of hyperpolarised substrate, etc.).

## 5.3 SABRE Polarisation Transfer using Millitesla PTFs

### 5.3.1 *In situ* SABRE Polarisation of 3-fluoropyridine

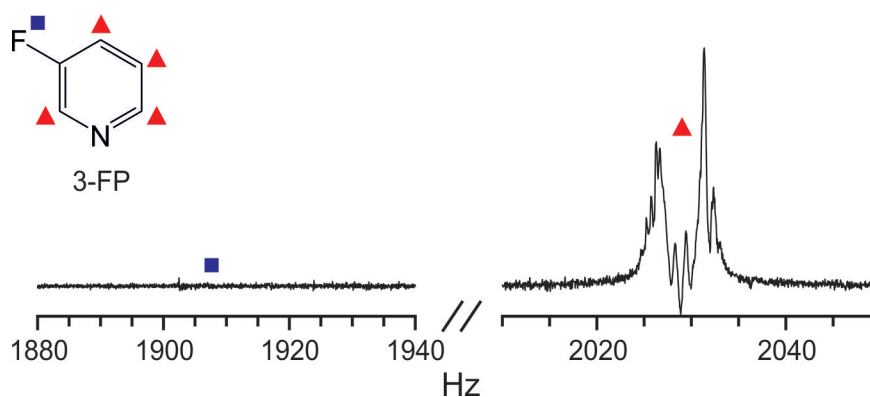


FIGURE 5.5: SABRE-polarised EFNMR spectrum of 250 mM 3-FP (50 equivalents relative to 5 mM of Ir-IMes) in 4 mL  $\text{CD}_3\text{OD}$  acquired with a PTF of 6.4 mT and a  $t_{PTF}$  of 10 s with 1 scan of the mT SABRE-EFNMR experiment.

The mT SABRE-EFNMR experiment was run using a 6.4 mT PTF to successfully acquire the SABRE-polarised EFNMR spectrum of 3-FP (see FIGURE 5.5). A complex and unsymmetrical hyperpolarised  $^1\text{H}$  signal was observed as a consequence of the multiple homonuclear and heteronuclear strong coupling interactions, however a hyperpolarised  $^{19}\text{F}$  signal was not. One of the suspected reasons for this is the presence of only one  $^{19}\text{F}$  nucleus in 3-FP that is strongly coupled to 4 magnetically inequivalent  $^1\text{H}$  nuclei, causing significant signal splitting and hence distribution of the signal intensity. Another reason is that a mT PTF promotes direct SABRE polarisation transfer to  $^1\text{H}$  nuclei on the substrate, therefore, the  $^{19}\text{F}$  nucleus is more likely to receive hyperpolarisation indirectly from the  $^1\text{H}$  nuclei which is a less efficient polarisation transfer pathway. The combination of these factors contributes to a hyperpolarised  $^{19}\text{F}$  EFNMR signal that is inherently weak, especially in comparison to the  $^1\text{H}$  signal, and may explain why it does not appear.

Simulations are a useful tool to aid in the non-trivial interpretation of SABRE-

polarised EFNMR spectra that exhibit complex signal shapes due to strong coupling and a lack of chemical shift resolution, and in this case, can also help to explain the missing SABRE-polarised  $^{19}\text{F}$  EFNMR signal.

NMR simulations were acquired on Matlab (version R2020a) using the Spinach library<sup>122</sup> (version 2.4.5157). The product operator terms used to construct the spin density matrix are first defined from the total number of NMR-active isotopes within the molecule of interest. From the species and chemical shift (in ppm) of each nucleus, the  $J$ -coupling interactions between them and the detection field (in tesla), all of which are supplied by the user, the Spinach library builds the Hamiltonian operator shown in Eq. 5.1). Kinetic and relaxation operators can also be built from relevant user-defined parameters, and the linear combination of these operators produces the Liouvillian superoperator, however, only the Hamiltonian was used for the acquisition of NMR simulations in this work.

$$\hat{\mathbf{H}} = \sum_n \omega_n^0 \hat{I}_{zn} + \sum_j \sum_{j>k} 2\pi J_{jk} \hat{\mathbf{I}}_j \cdot \hat{\mathbf{I}}_k \quad (5.1)$$

The Spinach library allows the user to define the starting state of the spin density matrix,  $\rho_0$ , as a single or sum of product operator terms (e.g.  $\hat{I}_{zj}$ ,  $\hat{I}_{zj}\hat{S}_{xk}$ ,  $\hat{I}_{zj} + \hat{S}_{zk}$ , etc.). A Matlab function within the Spinach library that is made-up of elements such as evolution periods, RF pulses and field gradients, is applied to the  $\rho_0$  parameter to simulate an NMR experiment. The Hamiltonian operator is used to evolve  $\rho_0$  in the presence of external fields, and rotation operators are used to nutate  $\rho_0$  in the presence of RF pulses, where the angle and axis of the nutation are controllable parameters. The resultant spin density matrix,  $\rho(0)$ , is combined with the observation operator,  $\hat{I}_{obs}$ , as shown in Eq. 5.2, to calculate the first data-point of the simulated FID,  $S(0)$ . The entire simulated FID is constructed by calculating a new  $S$ -value for every iteration of the  $\rho$  parameter as it is repeatedly evolved under the Hamiltonian for a duration dictated by the dwell-time parameter,  $t_d$ . This is a replication of the practical NMR detection process whereby the FID is acquired in intervals as the spins precess about the  $B^0$  field.

$$S(t_d) = \text{Tr} \left\{ \hat{U}_{obs} \rho(t_d) \right\} \quad (5.2)$$

Similarly to the  $\rho_0$  parameter, the Spinach library allows the user to define the  $\hat{I}_{obs}$  parameter as a single or sum of product operator term to select which states of the spin density matrix and which nuclei will be detected in the simulated FID. This control enables the user to chose which nuclei and which states within the spin density matrix experience the NMR experiment, and of those, which are detected during acquisition of the FID. Such selectivity is impossible in practice and is why NMR simulations are such a powerful tool for interpreting EFNMR spectra and assigning the SABRE-polarised EFNMR peaks to nuclei on the substrate when there is no chemical shift and high peak density.

Unless otherwise stated, NMR simulations in this report were acquired with

$\hat{I}_{obs} = \sum_i \hat{I}_i^-$ , and  $\rho_0 = \sum_i \hat{I}_{zi}$ , where the sum is over all NMR-active nuclei in the simulated molecule. The  $\hat{I}^-$  product operator term represents a (-1) quantum coherence describing the negative precession of the nuclei along the transverse plane as a combination of the  $\hat{I}_x$  and  $\hat{I}_y$  product operator terms ( $\hat{I}^- = \hat{I}_x - i\hat{I}_y$ ). A simulated pulse-acquire experiment with a hard  $\pi/2$  pulse that interacts with all spins was also implemented for acquisition of simulations in this work. This experiment is required to generate transverse magnetisation ( $\hat{I}^-$ ) from a starting state of  $\hat{I}_z$ .

The Spinach library can also make use of the assumption of weak coupling between heteronuclei in the high-field regime ( $|\nu_H - \nu_X| \gg J_{H,X}/2$ ) to simplify the Hamiltonian since only the longitudinal  $J$ -coupling interactions between nuclei are considered (see Eq. 5.3), thus simplifying calculations for the evolution of the spin density matrix. This allows for faster simulation times and was used for all high-field NMR simulations in this work. In the ULF regime there is strong coupling between heteronuclei ( $|\nu_H - \nu_X| \gtrsim J_{H,X}/2$ ) meaning  $J$ -coupling interactions across all three axes must be considered and the original form of the Hamiltonian is used (see Eq. 5.1). EFNMR simulations in this work were run without the weak coupling assumption to accurately generate EFNMR spectra. The assumption can be toggled on or off in the Spinach library through use of the "nmr" or "labframe" input parameter within the function that runs the simulated NMR experiment (more details provided in Chapter 9).

$$\hat{\mathbf{H}} = \sum_i \omega^0 \hat{I}_{zi} + \sum_j \sum_{j>k} 2\pi J_{jk} \hat{I}_{zj} \hat{I}_{zk} \quad (5.3)$$

Before acquiring a simulation of a chosen substrate, the chemical shift of all the magnetic isotopes and the  $J$ -coupling interactions between them must be known to construct the Hamiltonian. These are the only user-input parameters required to run the Spinach Matlab script that must be acquired experimentally. This information can sometimes be found for certain substrates on, for example, online databases, but it is much more reliable to measure the  $J$ -coupling and chemical shift values from high-field NMR spectra, which provide excellent chemical shift resolution and sufficiently high SNRs. A  $^1\text{H}$  and  $^{19}\text{F}$  spectrum of 3-FP was recorded on a 500 MHz Bruker NMR spectrometer (see FIGURE 5.6). The  $J$ -coupling interactions between the  $^1\text{H}$  and  $^{19}\text{F}$  nuclei were measured from the separation of the split peaks, and the chemical shifts of all the proton and fluorine environments were read-off from the ppm axis as the centre frequency of each multiplet. While values for all of the  $J$ -coupling interactions of 3-FP were acquired, manually measuring the separation between split peaks limits accuracy. To optimise these values,  $^1\text{H}$  and  $^{19}\text{F}$  simulations of 3-FP were carried out and compared to the experimental spectra to refine the measured  $J$ -coupling and chemical shift parameters.

An optimisation experiment ( $J$ -opt 1) that uses the Nelder-Mead method to fine-tune the measured  $J$ -coupling values was written on Matlab. Each  $J$ -coupling interaction within the coupling network of the substrate is varied across a user-defined range, and at each iteration of the coupling network, a simulated spectrum is acquired. A goodness of fit,  $f$ , to the experimental spectrum is calculated using Eq. 5.4, where  $A_{s_i}$  and  $A_{e_i}$  are the amplitude value of the normalised simulated and experimental

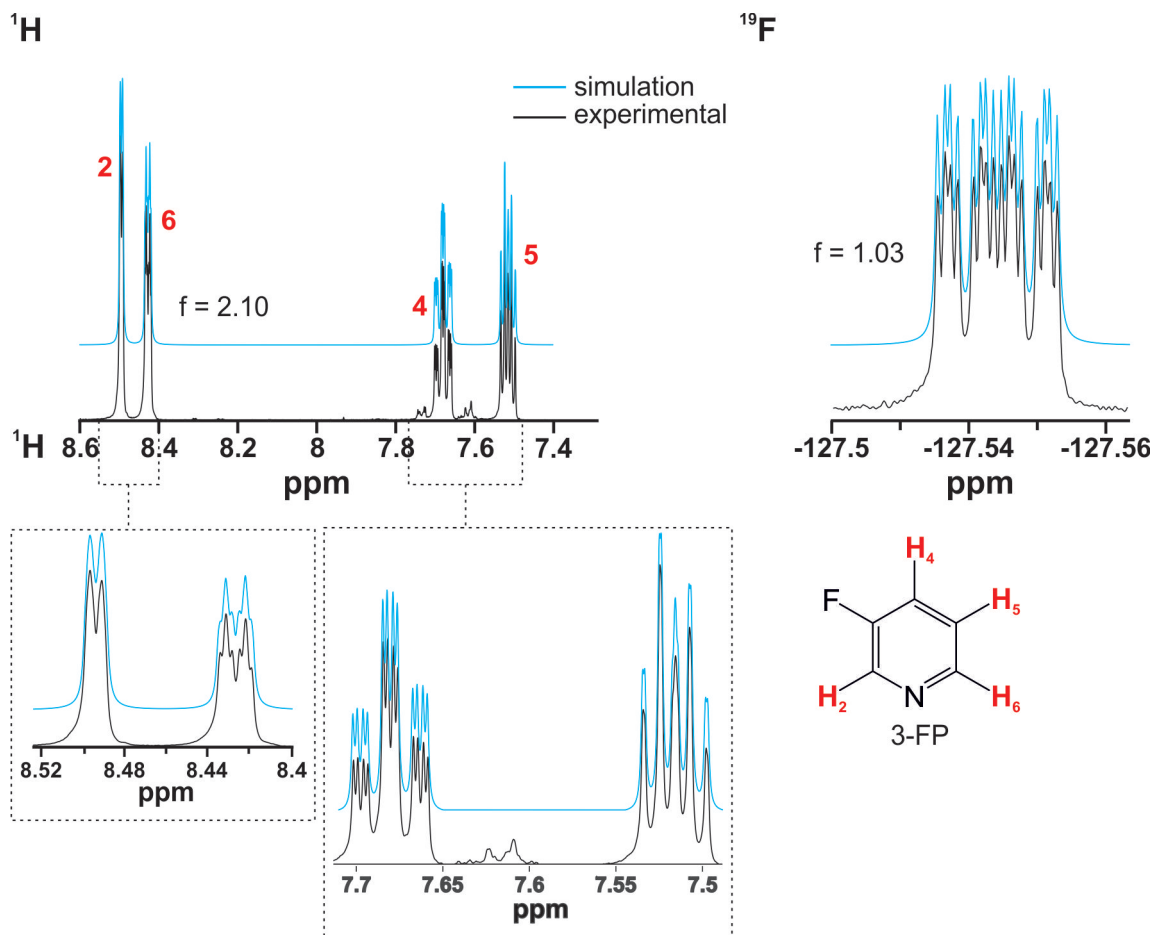


FIGURE 5.6:  $^1\text{H}$  and  $^{19}\text{F}$  NMR spectra of 3-FP acquired on a 500 MHz Bruker NMR spectrometer, overlaid with the high-field NMR simulation of 3-FP, generated with the  $J$ -coupling values optimised by  $J$ -opt 1. An  $f$ -value of 2.10 and 1.03 was calculated from the fit of the simulation to the  $^1\text{H}$  and  $^{19}\text{F}$  experimental spectra, respectively.

spectra, respectively, at each data point,  $i$ , on their trace. The  $J$ -coupling values that give rise to the smallest  $f$ -value are considered to be optimal.

$$f = \sum_i (A_{s_i} - A_{e_i})^2 \quad (5.4)$$

$J$ -opt 1 was carried out on the measured  $J$ -coupling values in Table 5.1, by comparison with the experimental  $^1\text{H}$  spectrum of 3-FP at 500 MHz in FIGURE 5.6. Small upper and lower bounds of  $\pm 0.5$  Hz were set for each  $J$ -coupling parameter since the simulation generated from the measured  $J$ -couplings already fit quite well to the experimental  $^1\text{H}$  spectrum. The output of the optimisation experiment was the optimised  $J$ -coupling values in Table 5.1 which are only slightly different to the measured  $J$ -coupling values, and produced the simulated  $^1\text{H}$  spectrum of 3-FP in FIGURE 5.6 which has an  $f$ -value of 2.10 that perfectly replicates the experimental  $^1\text{H}$  signals of 3-FP. The simulated  $^{19}\text{F}$  spectrum of 3-FP was then acquired with the optimised  $J$ -coupling values and fit the experimental  $^{19}\text{F}$  spectrum with an  $f$ -value of 1.03, indicating an excellent fit.

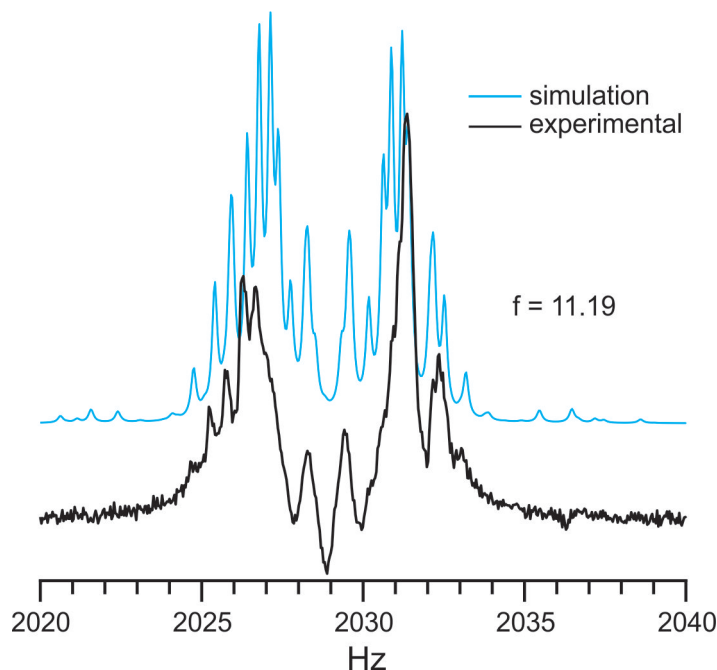


FIGURE 5.7: Comparison between the SABRE-polarised  $^1\text{H}$  EFNMR signal of 3-FP with the simulated  $^1\text{H}$  EFNMR signal using the optimised  $J$ -coupling values from the  $J$ -opt 1 experiment. The simulation shows a goodness of fit of  $f = 11.19$ .

The optimised  $J$ -coupling values were then used to acquire the EFNMR simulation of 3-FP (chemical shift has a negligible effect on the shape of EFNMR spectra and is not a necessary parameter). FIGURE 5.7 shows the SABRE-polarised  $^1\text{H}$  EFNMR signal of 3-FP overlaid with the optimised simulation. The fit between the two spectra has an  $f$ -value of 11.19, and it is clear by looking at the spectra that the fit is worse than what was observed with the high-field data in FIGURE 5.6 ( $f = 2.10$ ).

Table 5.1: Table of  $J$ -coupling values of 3-FP. The optimised  $J$ -coupling values were acquired using the  $J$ -opt 1 experiment, using the measured  $J$ -coupling values (acquired from high-field  $^1\text{H}$  and  $^{19}\text{F}$  spectra) as the starting point. The high-field NMR simulation of 3-FP in FIGURE 5.6 was generated using the optimised  $J$ -coupling values.

<b><math>J</math>-Coupling Interaction</b>	<b>Measured Couplings (Hz)</b>	<b>Optimised Couplings w/<math>J</math>-opt 1 (Hz)</b>
$J\{\text{H}_2, \text{H}_4\}$	3.00	2.96
$J\{\text{H}_2, \text{H}_5\}$	0.63	0.70
$J\{\text{H}_2, \text{H}_6\}$	0.50	0.50
$J\{\text{H}_2, \text{F}\}$	0.66	1.03
$J\{\text{H}_4, \text{H}_5\}$	8.40	8.55
$J\{\text{H}_4, \text{H}_6\}$	1.32	1.26
$J\{\text{H}_4, \text{F}\}$	8.80	8.75
$J\{\text{H}_5, \text{H}_6\}$	4.60	4.74
$J\{\text{H}_5, \text{F}\}$	4.83	4.88
$J\{\text{H}_6, \text{F}\}$	2.00	1.76

Further optimisation of the  $J$ -coupling values was attempted by considering the relative signs of the  $J$ -coupling interactions. The sign has no effect on the shape of signals produced under weak coupling conditions; however, it does play a role in the shape of signals produced under strong coupling conditions, such as those in the ULF regime. This optimisation required the design of a different Matlab experiment ( $J$ -opt 2) to generate an EFNMR simulation from the optimised  $J$ -coupling values in Table 5.1, and detection of the  $\hat{I}^-$  state, but where a negative sign is introduced into each interaction in the  $J$ -coupling network, until all of the different combinations of positive and negative phases of the  $J$ -coupling interactions have produced an EFNMR simulation. In the same way as the previous optimisation experiment, an  $f$ -value is calculated to evaluate how well the simulation fits to the SABRE-polarised EFNMR spectrum.

The number of combinations,  $N$ , was calculated from Eq.5.5, where  $n_J$  is the number of  $J$ -coupling interactions within the  $J$ -coupling network of the substrate of interest. The equation is valid under the assumption that the relative sign of the coupling values cause a change in the observed multiplicity, e.g.  $J_{AX} = 1$  Hz,  $J_{BX} = -1$  Hz is equivalent to  $J_{AX} = -1$  Hz,  $J_{BX} = 1$  Hz, but different to  $J_{AX} = 1$  Hz and  $J_{BX} = 1$  Hz.

$$N = 2^{n_J-1} \quad (5.5)$$

The  $J$ -coupling network of 3-FP is made up of ten  $J$ -coupling interactions, meaning there are 512 different phase combinations. A plot of  $f$ -value against combination number is shown in FIGURE 5.8, where combinations with  $f$ -values above 20 have been discarded. From the remaining combinations, the spectra with  $f$ -values below 10 were observed individually in order to visually decide on the  $^1\text{H}$  EFNMR simulation with the best fit. This brute force approach was taken because the simulated spectrum with the lowest  $f$ -value was not necessarily the one with the best fit to the experimental data. This is due to the fact that the central region of the SABRE-polarised  $^1\text{H}$  EFNMR signal of 3-FP ( $\sim 2027.5$ - $2030.5$  Hz) is distorted by the hyperpolarised solvent peak which appears at the centre of the signal and has a negative phase (discussed later in this section). Therefore, a good fit to this region has a heavy influence on minimising the  $f$ -value but may not represent a good fit to the rest of the signal shape.

The third phase combination of the  $J$ -coupling network of 3-FP corresponds to the optimised set of  $J$ -coupling values from the  $J$ -opt 2 experiment (see Table 5.2), where the sign of the  $J$ -coupling interaction between the *ortho*-protons ( $J\{\text{H}_2, \text{H}_6\}$ ) has been changed. The EFNMR simulation of the  $^1\text{H}$  signal of 3-FP from this  $J$ -coupling network is outlined in green in FIGURE 5.8 and has a fit of  $f = 5.31$  to the SABRE-polarised  $^1\text{H}$  EFNMR signal. The simulation from the 175<sup>th</sup> phase combination is outlined in red and represents a bad fit of  $f = 19.15$  to the experimental signal, demonstrating the drastic effect that changes to the relative sign of the  $J$ -coupling interaction has on the form of the signal in the ULF regime. The optimised  $J$ -coupling values from the  $J$ -opt 1 and  $J$ -opt 2 experiment are slightly different, however the latter has a better fit to the SABRE-polarised  $^1\text{H}$  EFNMR signal of 3-FP (see FIGURE 5.9).

With the  $J$ -coupling values optimised by the  $J$ -opt 2 experiment, the simulated  $^1\text{H}$  and  $^{19}\text{F}$  EFNMR signals of 3-FP were acquired and compared with the SABRE-polarised EFNMR spectrum of 3-FP in FIGURE 5.10. The simulated  $^{19}\text{F}$  signal is very broad (20 Hz) as it splits multiple times due to the extensive  $J$ -coupling experienced by the  $^{19}\text{F}$  nucleus. This significantly reduces its signal intensity as it is heavily distributed between the split peaks. As a consequence, the simulated  $^{19}\text{F}$  signal intensity is a factor of 6 lower than the simulated  $^1\text{H}$  signal, even though there is a 4:1 ratio of  $^1\text{H}$  to  $^{19}\text{F}$  nuclei in the substrate. Combining this information provided by the simulation with the fact that experimentally, SABRE polarisation of the  $^{19}\text{F}$  nucleus occurs via the less efficient indirect polarisation transfer pathway, in which the SABRE-polarised  $^1\text{H}$  nuclei spontaneously transfer their hyperpolarisation to neighbouring heteronuclei through the  $J$ -coupling network, it is not surprising that the  $^{19}\text{F}$  EFNMR signal of 3-FP is not observed from the mT SABRE-EFNMR experiment.

The close fit between the SABRE-polarised  $^1\text{H}$  EFNMR signal of 3-FP, acquired from a mT SABRE-EFNMR experiment, and the simulated  $^1\text{H}$  signal of 3-FP, acquired with  $\hat{I}_{obs} = \sum_i \hat{I}_i^-$  for all  $^1\text{H}$  nuclei, suggests that the SABRE polarisation transfer

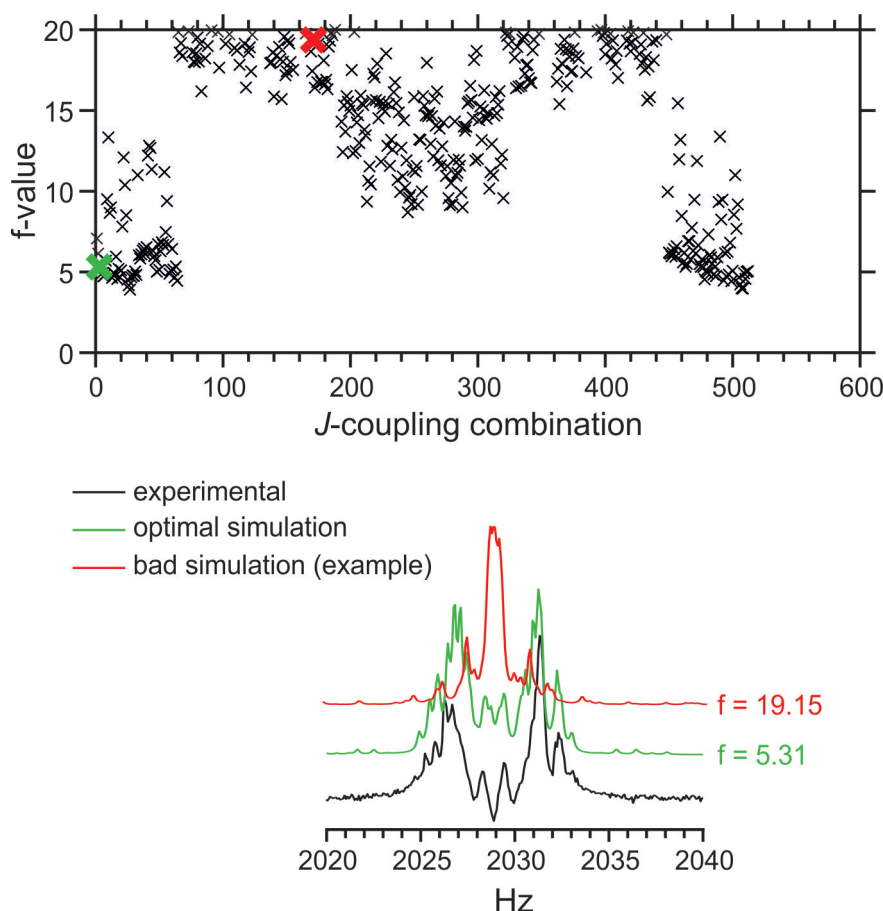


FIGURE 5.8: Graph of  $f$ -values for the 512 simulations produced from the  $J$ -opt 2 experiment, where  $f$ -values above 20 have been discarded. The EFNMR simulations from the  $3^{rd}$  (green) and  $175^{th}$  (red) combinations are included in the figure and represent the best and one of the worst fits to the experimental spectrum. The change in phase of only the  $J\{\text{H}_1, \text{H}_4\}$  interaction of 3-FP was responsible for the optimal fit to the experimental  $^1\text{H}$  signal which saw a change in  $f$ -value from 11.19 (see FIGURE 5.7) to 5.31.

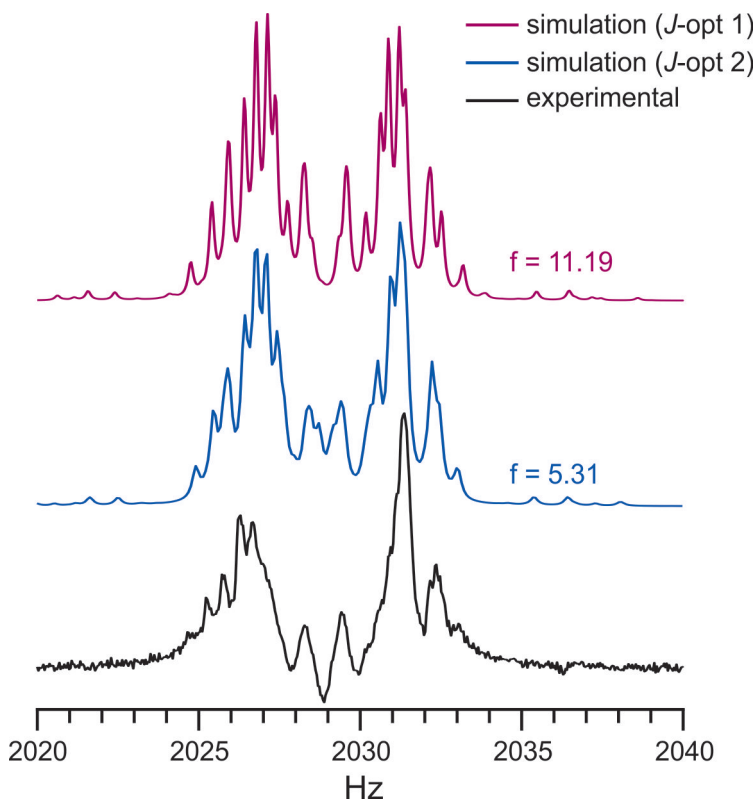


FIGURE 5.9: Comparison between the SABRE-polarised  $^1\text{H}$  EFNMR signal of 3-FP with the simulated  $^1\text{H}$  EFNMR signal using the optimised  $J$ -coupling values from the  $J$ -opt 1 and  $J$ -opt 2 experiments, where the change in relative sign to the  $J\{\text{H}_2, \text{H}_6\}$  coupling interaction improves the goodness of fit from  $f = 11.19$  to  $f = 5.31$ .

pathway at 6.4 mT is predominantly from the  $\mathbf{I}_1 \cdot \mathbf{I}_2$  ( $S_0$ ) state of the  $p\text{-H}_2$  derived hydrides to the  $\hat{I}_z$  state on the protons, which is later transformed into the  $\hat{I}^-$  state by the  $\pi/2$   $^1\text{H}$  pulse in the mT SABRE-EFNMR experiment (see FIGURE 5.2).

Table 5.2: Table of optimised  $J$ -coupling values of 3-FP acquired from the  $J$ -opt 1 and  $J$ -opt 2 experiments. An improved fit to the SABRE-polarised  $^1\text{H}$  spectrum of 3-FP was seen after the  $J\{\text{H}_1, \text{H}_4\}$  interaction (bold and underlined) was given a negative phase.

<b><math>J</math>-Coupling Interaction</b>	<b>Optimised Couplings w/<math>J</math>-opt 1 (Hz)</b>	<b>Optimised Couplings w/<math>J</math>-opt 2 (Hz)</b>
$J\{\text{H}_2, \text{H}_4\}$	2.96	2.96
$J\{\text{H}_2, \text{H}_5\}$	0.70	0.7
$J\{\text{H}_2, \text{H}_6\}$	0.50	<b><u>-0.5</u></b>
$J\{\text{H}_2, \text{F}\}$	1.03	1.03
$J\{\text{H}_4, \text{H}_5\}$	8.55	8.55
$J\{\text{H}_4, \text{H}_6\}$	1.26	1.26
$J\{\text{H}_4, \text{F}\}$	8.75	8.75
$J\{\text{H}_5, \text{H}_6\}$	4.74	4.74
$J\{\text{H}_5, \text{F}\}$	4.88	4.88
$J\{\text{H}_6, \text{F}\}$	1.76	1.76

Since the SABRE-polarised  $^{19}\text{F}$  EFNMR signal of 3-FP was not observed from the mT SABRE-EFNMR experiment, 3,5-DFP, 3-DFMP and 3,5-TFMP were used as alternate substrates. All three have a higher concentration of  $^{19}\text{F}$  nuclei and therefore are likely to boost the SNR of the  $^{19}\text{F}$  signal. 3,5-DFP and 3,5-TFMP have the  $^{19}\text{F}$  nuclei and the  $\text{CF}_3$  functional groups, respectively, in the meta positions (3,5). This adds symmetry to the substrates which simplifies the  $J$ -coupling network, reducing signal splitting and further increasing the SNR. Although 3-DFMP is not symmetrical, it makes use of the large  $^2J_{\text{HF}}$  coupling of 55.4 Hz ( $J\{\text{H}_7,\text{F}\}$ ) between the nuclei in the methyl group to separate the peaks of the  $^1\text{H}$  and  $^{19}\text{F}$  EFNMR signals. This reduces peak overlap and allows the spectra to exhibit more chemical and structural information. The  $J\{\text{H}_7,\text{F}\}$  coupling also promotes the indirect transfer of polarisation from the methyl proton to the  $^{19}\text{F}$  nuclei to boost the SNR of the  $^{19}\text{F}$  signal.

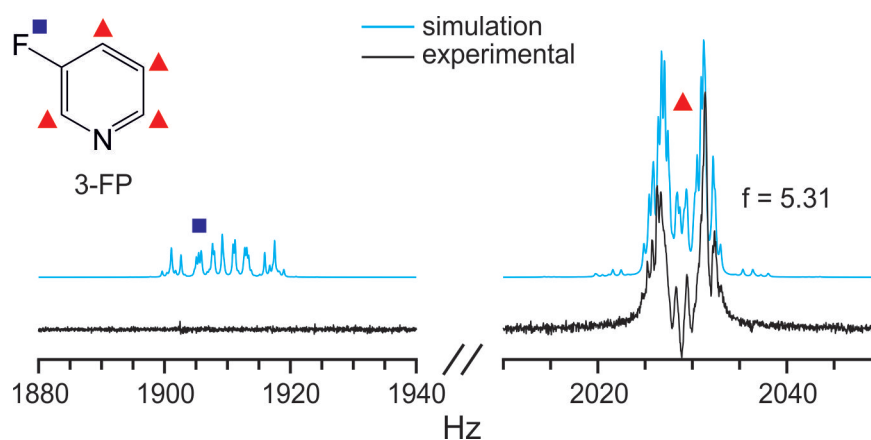


FIGURE 5.10: SABRE-polarised EFNMR spectrum of 3-FP (50 equivalents relative to 5 mM of Ir-IMes) acquired with a PTF of 6.4 mT overlaid with the simulated EFNMR spectrum of 3-FP. The  $^1\text{H}$  signal has a good fit to the simulation ( $f = 5.31$ ) but significant splitting of the  $^{19}\text{F}$  signal (backed up by simulations) and an inefficient pathway for its hyperpolarisation means the SABRE-polarised  $^{19}\text{F}$  EFNMR signal of 3-FP was not observed.

### 5.3.2 SABRE-Polarised Solvent

The SABRE polarisation of 3-FP was first carried out on a sample containing protio methanol (MeOH) solvent. Protio solvents are generally avoided in NMR as they produce very intense  $^1\text{H}$  signals that disrupt the interpretation of  $^1\text{H}$  spectra, however, the SABRE-EFNMR samples used in this work contain such a low volume of solvent (4 mL) that it is not detected by the Terranova-MRI probe, even when the sample was pre-polarised at 18.8 mT.

The SABRE-polarised  $^1\text{H}$  signal of 3-FP in MeOH is displayed in FIGURE 5.11 and contains an intense negative singlet peak at its centre, however, comparison to the simulated 3-FP EFNMR signal shows that it cannot be assigned to the substrate since it is not observed. When the experiment was repeated on a sample containing deuterated methanol ( $\text{CD}_3\text{OD}$ ) the negative singlet peak disappeared (see FIGURE 5.11), indicating that the peak likely corresponds to hyperpolarised methanol in

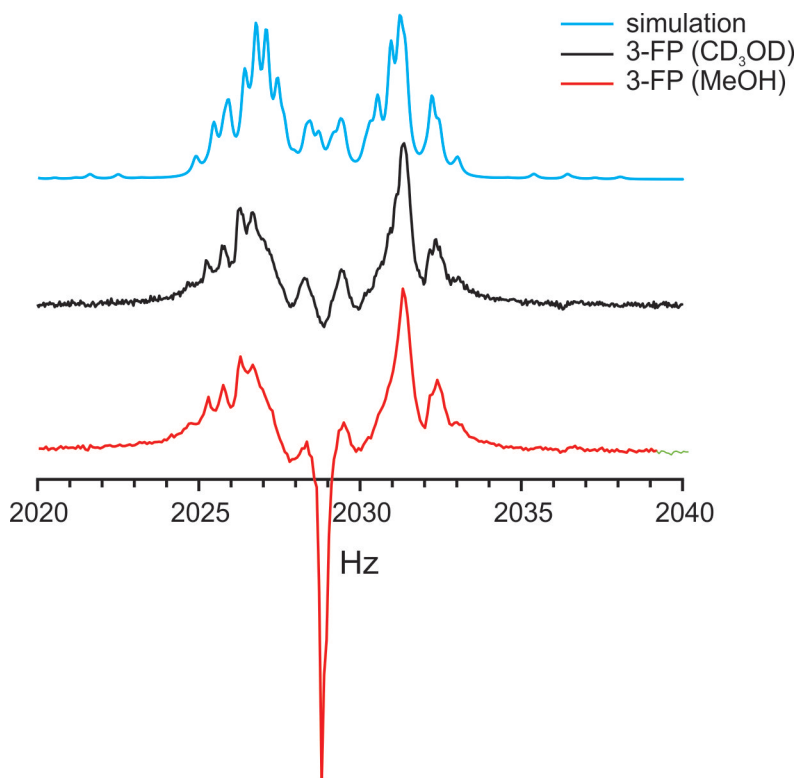


FIGURE 5.11: Comparison of the simulated EFNMR spectrum of 3-FP with the SABRE-polarised  $^1\text{H}$  EFNMR signals of 3-FP (50 equivalents relative to 5 mM of Ir-IMes) in 4 mL MeOH and  $\text{CD}_3\text{OD}$  solvent, acquired with 1 scan using a PTF of 6.4 mT and a  $t_{PTF}$  of 10 s. The sample containing MeOH displays a hyperpolarised  $^1\text{H}$  signal with an intense negative singlet at its centre that is not observed in the simulated signal or in the hyperpolarised  $^1\text{H}$  signal of the  $\text{CD}_3\text{OD}$  sample.

solution. A SABRE-polarised solvent signal reveals that MeOH is reversibly binding to the active catalyst and is therefore competing with 3-FP and  $p\text{-H}_2$  within the SABRE catalytic cycle.

SABRE polarisation of the OH proton of MeOH was identified by Olaru et al<sup>2</sup> at 500 MHz from a mildly acidic sample containing 3-FP and the Ir-IMes pre-catalyst, as a consequence of the formation of the  $\text{Ir}[(\text{IMes})(\text{H})_2(\text{sub})_2(\text{MeOH})]^+ \text{Cl}^-$  active catalyst. The presence of SABRE-polarised OH protons was also seen with samples containing 3,5-DFP and 2-fluoropyrazine. SABRE polarisation of MeOH with the Ir-IMes catalyst has also been studied across a range of PTFs and N-heterocyclic substrates.<sup>123</sup>

Although the intense negative singlet was not detected in the SABRE-polarised  $^1\text{H}$  spectrum of 3-FP in  $\text{CD}_3\text{OD}$ , there is a small negative component at the signal centre which is not replicated by the simulation. This may be observed because of the gradual exchange between the  $^2\text{H}$  nuclei in the solvent with the protons in the rest of the sample, leading to the formation of a small amount of the  $\text{Ir}[(\text{IMes})(\text{H})_2(\text{sub})_2(\text{MeOH})]^+ \text{Cl}^-$  which produces a very weak hyperpolarised solvent peak that slightly modifies the signal shape. To avoid disruption of the already complex SABRE-polarised EFNMR signals of fluorinated pyridines, all subsequent SABRE samples were prepared with  $\text{CD}_3\text{OD}$  which has the added benefit of decreasing the relaxation rates of the spins in

the hydride-metal-substrate complex, leading to an increase in the hyperpolarisation lifetime of the substrate.

### 5.3.3 *In situ* SABRE Polarisation of 3,5-difluoropyridine

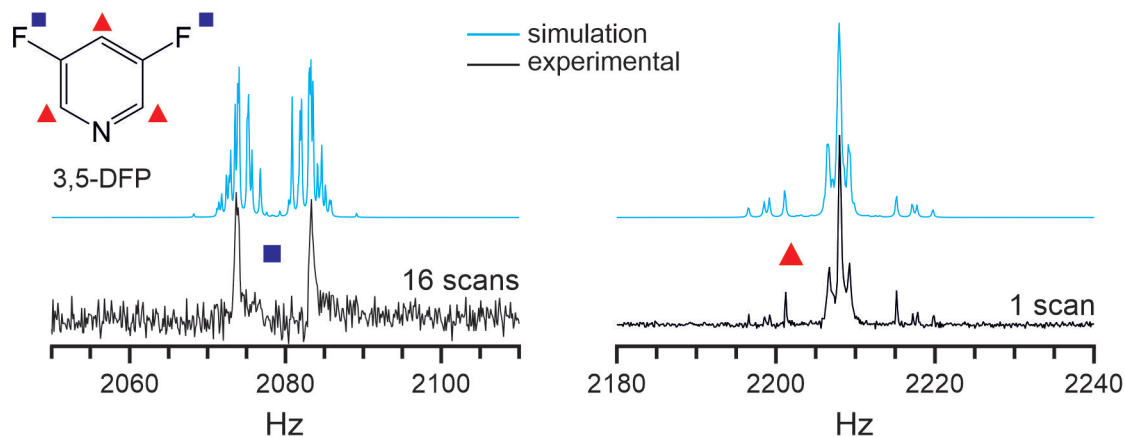


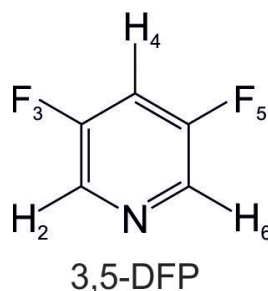
FIGURE 5.12: SABRE-polarised  $^1\text{H}$  and  $^{19}\text{F}$  EFNMR signals of 3,5-DFP (30 equivalents relative to 5 mM of Ir-IMes) in 4 mL  $\text{CD}_3\text{OD}$  acquired with a PTF of 9.0 mT and a  $t_{PTF}$  of 20 s with 1 and 16 scans of the mT SABRE-EFNMR experiment, respectively. The experimental spectra are overlaid with simulated spectra of 3,5-DFP for comparison. The hyperpolarised  $^1\text{H}$  and  $^{19}\text{F}$  EFNMR signals have been acquired from different experiments and have been phased separately. Simulations were acquired with  $\rho_0 = \sum_i \hat{I}_{zi}$  and  $\hat{I}_{obs} = \sum_i \hat{I}_i^-$  for all nuclei.

The mT SABRE-EFNMR experiment was run with a PTF of 9.0 mT to successfully acquire the hyperpolarised  $^1\text{H}$  and  $^{19}\text{F}$  EFNMR signal of 3,5-DFP (see FIGURE 5.12). The hyperpolarised  $^1\text{H}$  and  $^{19}\text{F}$  signals were acquired from separate mT SABRE-EFNMR experiments because 1 scan was not sufficient to observe the SABRE-polarised  $^{19}\text{F}$  signal which has a much lower SNR than the  $^1\text{H}$  signal. Therefore, the  $^{19}\text{F}$  spectrum of 3,5-DFP was acquired with 16 scans. Running separate experiments also allowed the probe to be tuned to the Larmor frequency of the  $^{19}\text{F}$  nucleus to amplify its signal and further increase the signal intensity.

The hyperpolarised  $^1\text{H}$  and  $^{19}\text{F}$  EFNMR signals of 3,5-DFP were overlaid with simulated  $^1\text{H}$  and  $^{19}\text{F}$  EFNMR signals. The values of the  $J$ -coupling interactions in 3,5-DFP are shown in Table 5.3. These were obtained using the optimisation experiments described in section 5.3.1. Since 3,5-DFP contains the  $J\{\text{F}_3, \text{F}_5\}$  coupling interaction between two magnetically inequivalent  $^{19}\text{F}$  nuclei that does not contribute to the  $^1\text{H}$  signal, its value could only be obtained and refined by repeating the optimisation experiments on the SABRE-polarised  $^{19}\text{F}$  EFNMR signal. Given that the  $^{19}\text{F}$  signal of 3,5-DFP acquired from the mT SABRE-EFNMR experiment is not an accurate representation of the  $^{19}\text{F}$  EFNMR signal, the  $J$ -coupling optimisation experiments were run on the  $^{19}\text{F}$  EFNMR signal acquired from the  $\mu\text{T}$  SABRE-EFNMR experiment, shown and discussed in Chapter 6.

Table 5.3: Table of optimised  $J$ -coupling values of 3,5-DFP.

$J$ -Coupling Interaction	Optimised Couplings (Hz)
$J\{H_2, H_4\}$	2.33
$J\{H_2, H_6\}$	3.39
$J\{H_2, F_3\}$	1.38
$J\{H_2, F_5\}$	-0.66
$J\{H_4, H_6\}$	2.33
$J\{H_4, F_3\}$	9.00
$J\{H_4, F_5\}$	9.00
$J\{H_6, F_3\}$	-0.66
$J\{H_6, F_5\}$	1.38
$J\{F_3, F_5\}$	2.09



The simulated  $^1\text{H}$  and  $^{19}\text{F}$  signals of 3,5-DFP were acquired with  $\rho_0 = \sum_i \hat{I}_{zi}$  and  $\hat{I}_{obs} = \sum_i \hat{I}_i^-$  for all nuclei. The SABRE-polarised  $^1\text{H}$  EFNMR signal is in excellent agreement with the SABRE-polarised  $^1\text{H}$  EFNMR spectrum. As with 3-FP, it can be concluded that SABRE polarisation transfer at 9.0 mT occurred mainly between the  $\mathbf{I}_1 \cdot \mathbf{I}_2$  state of the  $p$ - $\text{H}_2$  derived hydrides and the  $\hat{I}_z$  state of the  $^1\text{H}$  nuclei in 3,5-DFP. The SABRE-polarised EFNMR spectrum of 3,5-DFP is complex, but with EFNMR simulations and values for all of the  $J$ -coupling interactions in the substrate network, the spectrum can be interpreted and the peaks in the  $^1\text{H}$  and  $^{19}\text{F}$  signals can be assigned to better understand the form of the hyperpolarised signals.

EFNMR simulations of each  $^1\text{H}$  chemical environment were acquired to observe their contributions to the entire  $^1\text{H}$  EFNMR signal of 3,5-DFP (see FIGURE 5.13). This required running a simulation with  $\hat{I}_{obs} = \sum_{i=2,6} \hat{I}_i^-$ , and another simulation with  $\hat{I}_{obs} = \hat{I}_4^-$ . These simulations were also acquired with a lower apodisation and a larger number of points in comparison to the simulated  $^1\text{H}$  signals of 3,5-DFP in FIGURE 5.12 to improve spectral resolution and facilitate interpretation. The relative intensity of the signals is representative of the number of  $^1\text{H}$  nuclei in that chemical environment, therefore, the *ortho*-proton signal is a factor of two more intense than the *para*-proton signal.

The *ortho*-proton signal is produced from the four strong coupling interactions between the *ortho*-proton and the other four magnetically inequivalent nuclei in 3,5-DFP, including the second chemically equivalent *ortho*-proton. Under Pople nomenclature this 5-spin coupled system is described as an  $AA'BCD$  system, which produces a very complicated multiplet. The  $J$ -coupling interactions involving the *ortho*-proton are all different and small ( $\leq 3.39$  Hz), leading to numerous but narrow splitting of the signal, which in turn produces a central multiplet that is 3.5 Hz wide and exhibits high peak density (see FIGURE 5.13).

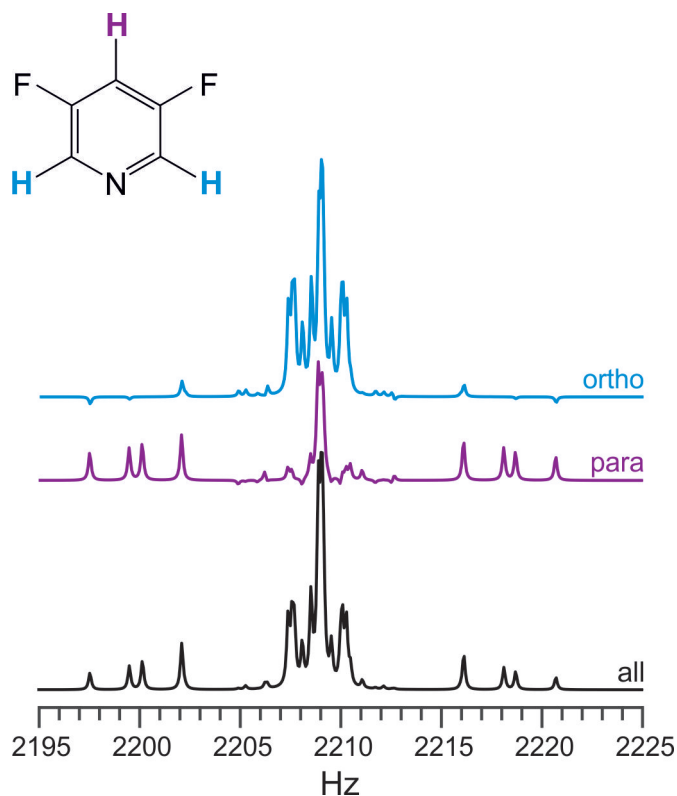


FIGURE 5.13: NMR simulations of the *ortho* and *para*-proton signals of 3,5-DFP, acquired with  $\hat{I}_{obs} = \sum_{i=2,6} \hat{I}_i^-$  and  $\hat{I}_{obs} = \hat{I}_4^-$ , respectively at 51.9  $\mu$ T. The two signals allow observation of the individual contribution to the simulated  $^1\text{H}$  signal by the *ortho* and *para*-proton environments.

On the other hand, the *para*-proton signal is much easier to interpret because of the symmetry in its strongly coupled interactions with the two  $^{19}\text{F}$  nuclei and the two *ortho*-protons. This 5-spin coupled system is described as an  $AB_2C_2$  system under Pople nomenclature, which is much simpler than the  $AA'BCD$  spin system. Consequently, the form of the *para*-proton signal of 3,5-DFP can be dissected for further interpretation by observing the contributions to the signal multiplicity by the individual  $J$ -coupling interactions within its coupled system. This was achieved by zeroing the unwanted  $J$ -coupling interactions from the Spinach code so they are not included into the Hamiltonian operator.

FIGURE 5.14 shows the simulated signal produced from the acquisition of the *para*-proton ( $\text{H}_4$ ) with a single  $J\{\text{H}_4, \text{F}_{3,5}\}$  coupling interaction to the two  $^{19}\text{F}$  nuclei. This interaction is described by a 3-spin  $AB_2$  system which forms a multiplet containing 4 peaks: two overlapping peaks at the signal centre separated by  $\sim 0.6$  Hz (2207.8 and 2208.4 Hz); two outer peaks at 2199 and 2217 Hz. Under weak coupling this interaction would yield a 1:2:1 triplet due to the degeneracy between two of the 3-spin product states in the Hamiltonian under the Zeeman basis. Under strong coupling the Hamiltonian is best described under the singlet-triplet basis, where the degeneracy between product states is broken and four peaks are observed instead of three. Addition of the  $J\{\text{H}_{2,6}, \text{H}_4\}$  coupling interaction between  $\text{H}_4$  and the *ortho*-protons ( $\text{H}_2$  and  $\text{H}_6$ ) into the simulation produces an EFNMR signal corresponding to an  $AB_2C_2$  spin system. This simulation shows that the four  $AB_2$  peaks undergo splitting, forming the complete  $\text{H}_4$  signal seen in FIGURE 5.13. The two central  $AB_2$  peaks at 2207.8 and

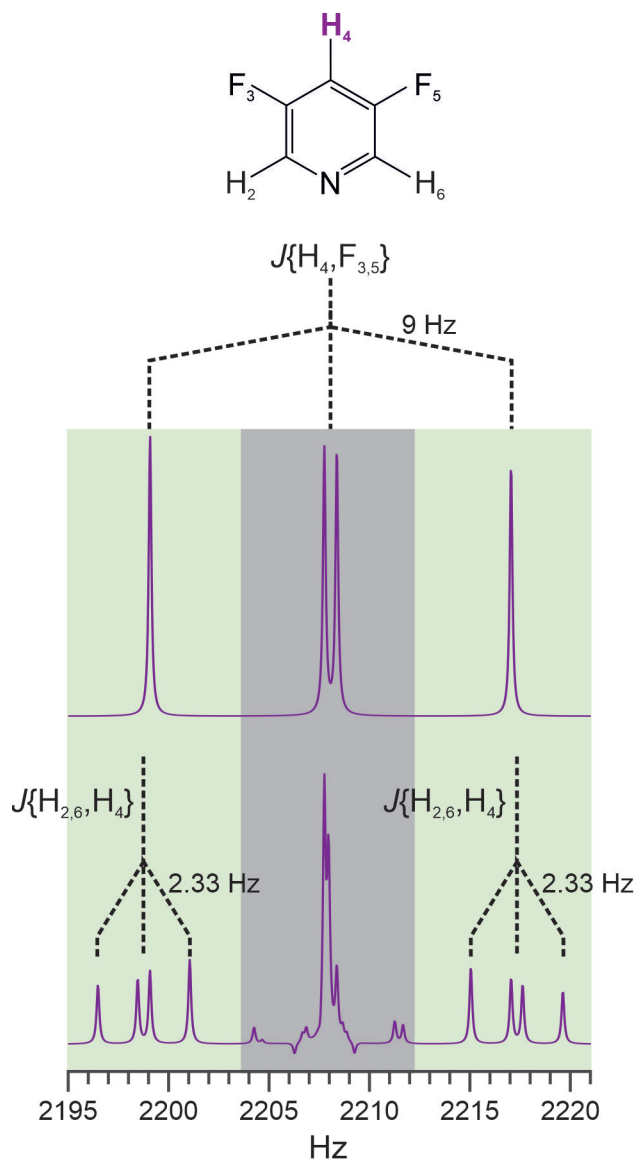


FIGURE 5.14: Simulated splitting tree of the  $H_4$  signal of 3,5-DFP at  $51.9 \mu\text{T}$ . When considered separately, the dominant  $9 \text{ Hz } J\{H_4, F_{3,5}\}$  coupling interaction represents an  $AB_2$  spin system and forms a multiplet of four peaks. The two outer split peaks (green) are further split by the  $2.33 \text{ Hz } J\{H_{2,6}, H_4\}$  coupling interaction forming a set of multiplets of four peaks. The two central split peaks (grey) are further split by the  $2.33 \text{ Hz } J\{H_{2,6}, H_4\}$  coupling interaction forming a complex multiplet of several peaks.

$2208.4 \text{ Hz}$  split to form a complex multiplet (grey shaded region) with significant peak overlap, whereas the outer  $AB_2$  peaks at  $2199$  and  $2217 \text{ Hz}$  undergo a  $2.33 \text{ Hz}$  splitting to form a set of four peaks (green shaded region). The strong coupling of  $H_4$  with  $H_2$  and  $H_6$  leads to the breaking of degenerate product states in the 5-spin system and the formation of a set of four split peaks instead of a set of 1:2:1 triplets.

Since the multiplet in the top  $H_4$  signal in FIGURE 5.14 is caused by the strong  $J\{H_4, F_{3,5}\}$  heteronuclear coupling interaction in 3,5-DFP, the roofing exhibited by the multiplet points toward the middle of the complete heteronuclear coupling pattern, which would also involve four  $^{19}\text{F}$  peaks at  $\sim 2080 \text{ Hz}$ . The outer multiplets in the green shaded region of the bottom  $H_4$  signal are caused by the strong  $J\{H_{2,6}, H_4\}$

homonuclear coupling interaction and therefore exhibit roofing that points toward the centre of the homonuclear coupling pattern. This roofing effect is observed in the experimental  $^1\text{H}$  signal of 3,5-DFP in FIGURE 5.12 and is replicated by the simulations.

Although the form of both the *para* and *ortho*-proton signals are complex, the lower number of interactions that the *para*-proton has with the other nuclei in 3,5-DFP leads to a simpler multiplet. Also, the 9.0 Hz  $J\{\text{H}_4, \text{F}_{3,5}\}$  interaction helps to disentangle the multiplet to increase signal resolution and facilitate signal interpretation.

The SABRE-polarised  $^{19}\text{F}$  EFNMR signal of 3,5-DFP (see FIGURE 5.12) appears to be a doublet with a splitting of 9.0 Hz, due to the  $J\{\text{H}_4, \text{F}_{3,5}\}$  coupling interaction. The simulated  $^{19}\text{F}$  signal of 3,5-DFP does not replicate this and shows a pseudo-doublet with a splitting of 9.0 Hz and a fine-structure of multiple split peaks caused by the small strong coupling interactions involving the  $^{19}\text{F}$  nuclei of -0.66 to 2.09 Hz (see Table 5.3). The reason for the difference between the experimental and simulated signals is not known, but it appears that only part of the  $^{19}\text{F}$  signal has been hyperpolarised in this experiment. A discussion of the SABRE-polarised  $^{19}\text{F}$  EFNMR signal of 3,5-DFP is presented in section 6.2.3 where acquisition of the  $^{19}\text{F}$  signal was achieved using  $\mu\text{T}$  PTFs.

It is also worth noting that the hyperpolarised  $^{19}\text{F}$  EFNMR signal is much weaker than the hyperpolarised  $^1\text{H}$  EFNMR signal. This is because a mT PTF drives efficient SABRE polarisation transfer to the  $^1\text{H}$  nuclei and the  $^{19}\text{F}$  nuclei become hyperpolarised via the transfer of polarisation from the SABRE-polarised  $^1\text{H}$  nuclei which is not as efficient. This can also be attributed to faster  $T_1$  relaxation of the  $^{19}\text{F}$  nuclei in comparison to the  $^1\text{H}$  nuclei, leading to a quicker decay of  $^{19}\text{F}$  hyperpolarisation.

### 5.3.4 *In situ* SABRE Polarisation of 3,5-bis(trifluoromethyl)pyridine

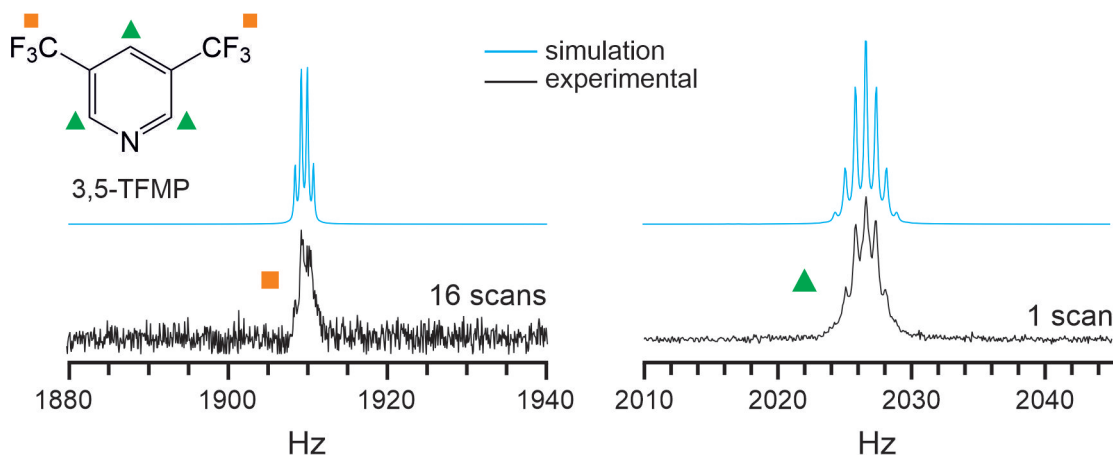


FIGURE 5.15: SABRE-polarised  $^1\text{H}$  and  $^{19}\text{F}$  EFNMR signals of 3,5-TFMP (50 equivalents relative to 5 mM of Ir-IMes) in 4 mL  $\text{CD}_3\text{OD}$  acquired with a PTF of 6.4 mT and a  $t_{PTF}$  of 30 s with 1 and 16 scans of the mT SABRE-EFNMR experiment, respectively, overlaid with the simulated EFNMR spectrum of 3,5-TFMP. The hyperpolarised  $^1\text{H}$  and  $^{19}\text{F}$  EFNMR signals have been acquired from different experiments and have been phased separately. Simulations were acquired with  $\rho_0 = \sum_i \hat{I}_{zi}$  and  $\hat{I}_{obs} = \sum_i \hat{I}_i^-$  for all nuclei.

The SABRE-polarised  $^1\text{H}$  and  $^{19}\text{F}$  EFNMR signals of 3,5-TFMP shown in FIGURE 5.15 were acquired separately with 1 and 16 scans of the mT SABRE-EFNMR experiment, respectively, using a 6.4 mT PTF. In each experiment the probe was tuned to the signal of interest for amplification of the signal intensity. The simulation of the EFNMR spectrum of 3,5-TFMP, acquired using the  $J$ -coupling values in Table 5.4, is included in FIGURE 5.15 for comparison and interpretation. The SABRE-polarised  $^1\text{H}$  EFNMR signal of 3,5-TFMP is in good agreement with the simulated signals acquired with  $\rho_0 = \sum_i \hat{I}_{zi}$  and  $\hat{I}_{obs} = \sum_i \hat{I}_i^-$  for all nuclei, however, the hyperpolarised  $^{19}\text{F}$  is not. The simulation indicates a dominant SABRE polarisation transfer pathway between the  $\mathbf{I}_1 \cdot \mathbf{I}_2$  state of the  $p\text{-H}_2$  derived hydrides and the  $\hat{I}_z$  state of the  $^1\text{H}$  in 3,5-TFMP at 6.4 mT.

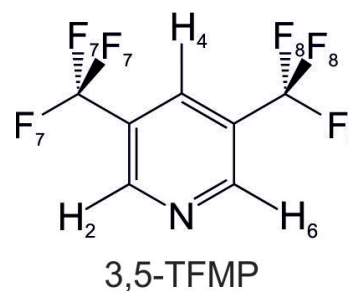
A pseudo-septet with a splitting of 0.7 Hz is observed for the hyperpolarised  $^1\text{H}$  signal of 3,5-TFMP due to the  $J\{\text{H}_4, \text{F}_8\}$  coupling interaction between the *para*-proton and the six  $^{19}\text{F}$  nuclei (see Table 5.4). In comparison to 3,5-DFP which is structurally very similar to 3,5-TFMP but displays a complex  $^1\text{H}$  EFNMR signal with numerous split peaks, the experimental and simulated  $^1\text{H}$  signal of 3,5-TFMP is simple and exhibits very little peak splitting. This is because the significantly smaller heteronuclear coupling interactions of 3,5-TFMP, due to the separation of the  $^{19}\text{F}$  nuclei from the aromatic protons by the methyl carbon bond, reduces the heteronuclear  $J$ -coupling interactions within the coupling network. Since it is the heteronuclear coupling interactions within the substrate coupling network that breaks the equivalence of the protons, allowing homonuclear coupling to be observed, it follows that 3,5-TFMP is below the limit of heteronuclear coupling to break that equivalence, hence homonuclear coupling is not observed.

This also helps to explain the lack of chemical structure and multiplicity exhibited by the hyperpolarised  $^{19}\text{F}$  EFNMR signal, which displays a broad multiplet with poor signal resolution. Although the six  $^{19}\text{F}$  nuclei are strongly coupled to three magnetically inequivalent  $^1\text{H}$  nuclei with different values (see Table 5.4), expected to produce a complex multiplet, it is likely the similarity in the values means the  $^{19}\text{F}$  nuclei are effectively coupled to three near-magnetically equivalent protons with a coupling value that is the average of the individual ones ( $[1 + 0.7 + 0.6]/3 = 0.75$ ). This interaction better explains the observed simulated multiplet in FIGURE 5.15.

A combination of the very small  $^1\text{H}$ - $^{19}\text{F}$  coupling interactions ( $\leq 1$  Hz) and the lack of a  $J\{\text{F}_7, \text{F}_8\}$  coupling produces hyperpolarised  $^1\text{H}$  and  $^{19}\text{F}$  EFNMR signals with minimal chemical information and fine structure, making it hard to analyse further.

Table 5.4: Table of optimised  $J$ -coupling values of 3,5-TFMP.

<b><math>J</math>-Coupling Interaction</b>	<b>Optimised Couplings (Hz)</b>
$J\{\text{H}_2, \text{H}_4\}$	2.20
$J\{\text{H}_2, \text{H}_6\}$	0.50
$J\{\text{H}_2, \text{F}_7\}$	1.00
$J\{\text{H}_2, \text{F}_8\}$	0.60
$J\{\text{H}_4, \text{H}_6\}$	2.20
$J\{\text{H}_4, \text{F}_7\}$	0.70
$J\{\text{H}_4, \text{F}_8\}$	0.70
$J\{\text{H}_6, \text{F}_7\}$	0.60
$J\{\text{H}_6, \text{F}_8\}$	1.00
$J\{\text{F}_7, \text{F}_8\}$	0.00



### 5.3.5 *In situ* SABRE Polarisation of 3-difluoromethylpyridine

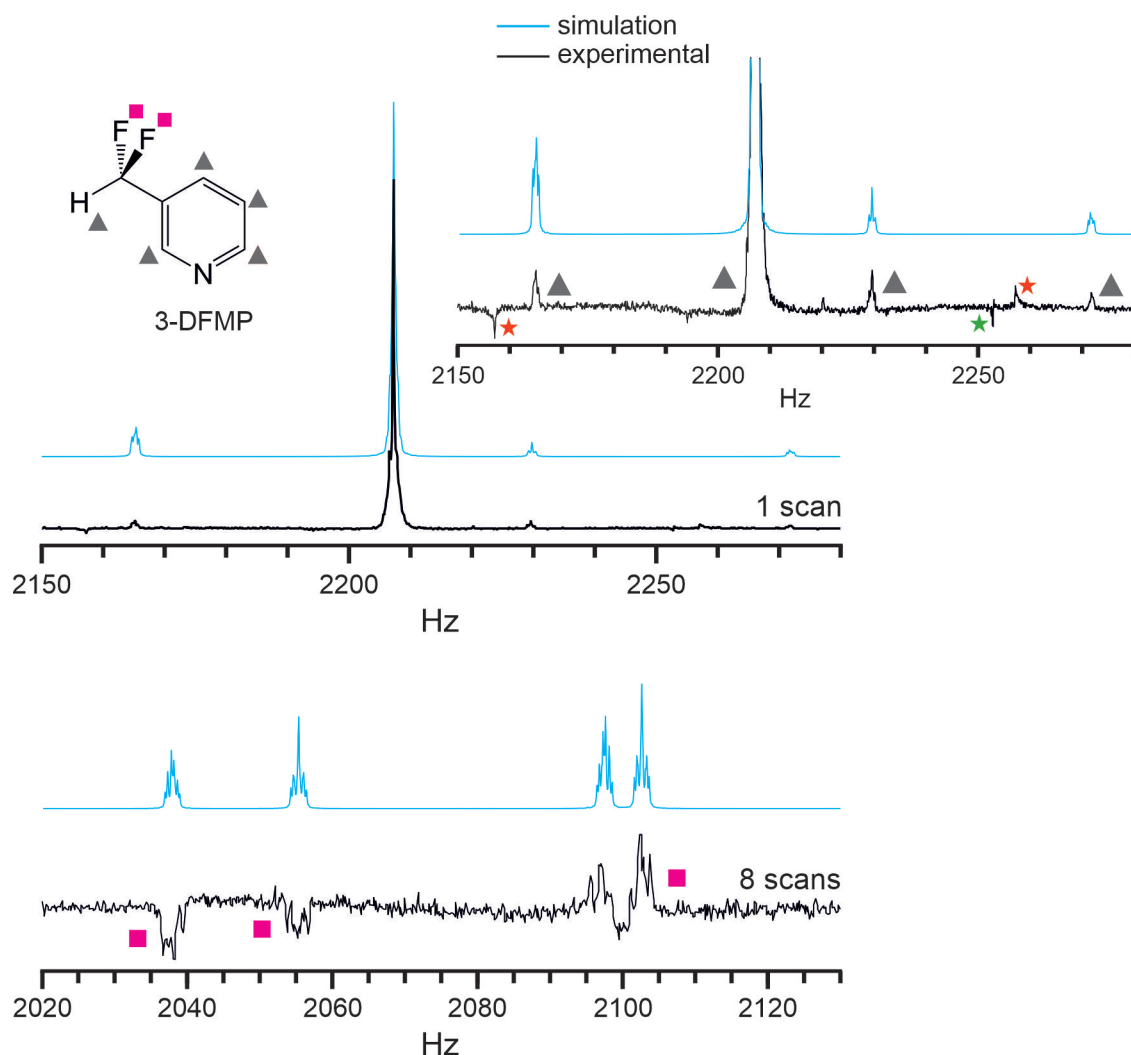


FIGURE 5.16: SABRE-polarised  $^1\text{H}$  and  $^{19}\text{F}$  EFNMR signals of 3-DFMP (50 equivalents relative to 5 mM of Ir-IMes) in 4 mL  $\text{CD}_3\text{OD}$  acquired with a PTF of 6.0 mT and a  $t_{\text{PTF}}$  of 30 s with 1 and 8 scans of the mT SABRE-EFNMR experiment, respectively, overlaid with the simulated EFNMR spectrum of 3-DFMP. The hyperpolarised  $^1\text{H}$  and  $^{19}\text{F}$  EFNMR signals have been acquired from different experiments and have been phased separately. Simulations were acquired with  $\rho_0 = \sum_i \hat{I}_{zi}$  and  $\hat{I}_{\text{obs}} = \sum_i \hat{I}_i^-$  for all nuclei. The peaks labeled with a red and green stars are artefacts from the instrumentation.

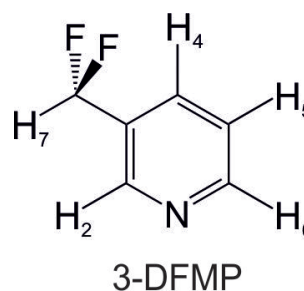
All SABRE polarised spectra of 3-DFMP in this chapter and Chapter 6 were acquired by Adrian Muller, under the supervision of myself and Dr Meghan Halse as part of a Master's project.

The SABRE-polarised  $^1\text{H}$  and  $^{19}\text{F}$  EFNMR signals of 3-DFMP shown in FIGURE 5.16 were acquired separately with 1 and 8 scans of the mT SABRE-EFNMR experiment, respectively, using a 6.0 mT PTF. In each experiment the probe was tuned to the signal of interest for amplification of the signal intensity. The experimentally acquired signals have also been overlaid with simulated EFNMR signals for comparison and interpretation. The simulations were acquired with  $\rho_0 = \sum_i \hat{I}_{zi}$  for all  $^1\text{H}$

nuclei, using the  $J$ -coupling values in Table 5.5 which were obtained by running the  $J$ -opt 1 experiment on the high-field  $^1\text{H}$  and  $^{19}\text{F}$  NMR spectra of 3-DFMP. Coupling interactions with a separation of five or more chemical bonds could not be retrieved from the high-field spectra as they do not have a visible influence on the signal shape, and hence were set to zero.

Table 5.5: Table of optimised  $J$ -coupling values of 3-DFMP.

<b><math>J</math>-Coupling Interaction</b>	<b>Optimised Couplings (Hz)</b>
$J\{\text{H}_2, \text{H}_7\}$	0.95
$J\{\text{H}_2, \text{H}_4\}$	1.00
$J\{\text{H}_2, \text{H}_5\}$	1.00
$J\{\text{H}_2, \text{H}_6\}$	1.40
$J\{\text{H}_2, \text{F}\}$	1.00
$J\{\text{H}_7, \text{H}_4\}$	0.30
$J\{\text{H}_7, \text{H}_5\}$	0.00
$J\{\text{H}_7, \text{H}_6\}$	0.00
$J\{\text{H}_7, \text{F}\}$	55.40
$J\{\text{H}_4, \text{H}_5\}$	8.00
$J\{\text{H}_4, \text{H}_6\}$	0.95
$J\{\text{H}_4, \text{F}\}$	0.94
$J\{\text{H}_5, \text{H}_6\}$	5.00
$J\{\text{H}_5, \text{F}\}$	0.17
$J\{\text{H}_6, \text{F}\}$	0.00



The  $J$ -opt 1 procedure was not repeated on the SABRE-polarised  $^1\text{H}$  and  $^{19}\text{F}$  EFNMR signals of 3-DFMP for the purpose of achieving further refinement of the  $J$ -coupling interactions because the structure of the 3-DFMP spectrum is dictated by the  $J\{\text{H}_7, \text{F}\}$  coupling interaction between the  $^1\text{H}$  and two  $^{19}\text{F}$  nuclei in the methyl group, the value of which was sufficiently refined after running the  $J$ -opt 1 experiment on the high-field data.

The methyl group represents a strongly coupled 3-spin  $AB_2$  system<sup>80</sup> which produces eight peaks: four peaks in the Larmor frequency region of spin A ( $^1\text{H}$ ) and four peaks in the Larmor frequency region of spin B ( $^{19}\text{F}$ ). The intensity of the hyperpolarised  $^1\text{H}$  peak at 2208 Hz, containing contributions from the aromatic and methyl protons, is a factor of 43 more intense than the hyperpolarised  $^1\text{H}$  peaks at 2165 and 2230 Hz belonging solely to the methyl proton (see zoomed-out  $^1\text{H}$  signal of 3-DFMP in FIGURE 5.16). From this observation it is clear that majority of hyperpolarisation was transferred from the  $p$ - $\text{H}_2$  derived hydrides to the aromatic protons at a PTF of 6 mT.

The EFNMR simulation of 3-DFMP in FIGURE 5.16 shows an excellent repli-

cation of the form of the experimental spectrum and accurate alignment of the eight signals. The three experimental  $^1\text{H}$  peaks at 2157, 2253 and 2257 Hz, labelled with red and green stars, do not appear in the simulation as they are artefacts. The peak at 2252 Hz (green star) is a noise peak that comes from the mains electricity and is observed at multiples of 50 Hz as this is the AC frequency in the UK. The anti-phase peaks at 2157 Hz and 2257 Hz (red star) are exactly  $\pm 50$  Hz from the centre of the  $^1\text{H}$  EFNMR signal and are typically observed with any sample that gives rise to a strong SABRE-polarised spectrum. Therefore, they are likely related to an external source such as instrument vibration during acquisition of the FID.

The good fit between the SABRE-polarised  $^1\text{H}$  EFNMR signal of 3-DFMP and the simulated  $^1\text{H}$  signal, acquired with  $\rho_0 = \sum_i \hat{I}_{zi}$  for all nuclei, suggests a dominant SABRE polarisation transfer pathway between the  $\mathbf{I}_1 \cdot \mathbf{I}_2$  state of the  $p\text{-H}_2$  derived hydrides and the  $\hat{I}_z$  state of the  $^1\text{H}$  nuclei of 3-DFMP at 6.0 mT. The structure of the SABRE-polarised  $^{19}\text{F}$  EFNMR signal is also well replicated by the simulation and the split peaks are well aligned, however, the phases are not. The hyperpolarised  $^{19}\text{F}$  signal was more accurately replicated by the simulation acquired with  $\rho_0 = \sum_i \hat{I}_{zi}$  for all  $^1\text{H}$  nuclei only and  $\hat{I}_{obs} = \sum_i \hat{I}_i^-$  for all nuclei (see FIGURE 5.17). Running the simulation in this way accounts for the fact that mT PTFs drive efficient SABRE polarisation transfer to  $^1\text{H}$ , however, its replication of the full SABRE-polarised EFNMR spectrum of 3-DFMP was unexpected, considering  $^1\text{H}$  and  $^{19}\text{F}$  EFNMR signals were generated from an initial spin density matrix ( $\rho_0$ ) containing only population of the  $^1\text{H}$  nuclei. Nonetheless, this observation can be understood if the nuclear spin system of 3-DFMP is represented by the singlet-triplet basis instead of the Zeeman basis.

The Zeeman basis, which is the preferred basis set to define the Hamiltonian operator under weak coupling conditions (for a two spin-1/2 system the Zeeman basis is made up of a linear combination of the  $|\alpha\alpha\rangle$ ,  $|\alpha\beta\rangle$ ,  $|\beta\alpha\rangle$  and  $|\beta\beta\rangle$  spin states, where the spin state on the left is assigned to spin 1 and the spin state on the right is assigned to spin 2.) considers the spins in a spin state separately as they are deemed distinguishable from each other. This is not the preferred basis set for the representation of a strongly coupled spin system. That being said, the SABRE polarised EFNMR spectra of 3,5-DFP and 3,5-TFMP, which represent strongly coupled spin systems in the ULF regime, were successfully interpreted by assigning the nuclear spin states to different nuclei (Zeeman-like approach). Spin systems like that of 3-DFMP are much more strongly coupled owing to the large 55.4 Hz coupling between the methyl nuclei ( $J\{\text{H}_7, \text{F}\}$ ), and the Hamiltonian of this system is more accurately defined by the singlet-triplet basis set (for a two spin-1/2 system the singlet-triplet basis is made up of a linear combination of the singlet spin state  $|S_0\rangle = \frac{1}{\sqrt{2}}(|\alpha\beta\rangle - |\beta\alpha\rangle)$  and the three components of the triplet spin state  $|T_{+1}\rangle = |\alpha\alpha\rangle$ ,  $|T_0\rangle = \frac{1}{\sqrt{2}}(|\alpha\beta\rangle + |\beta\alpha\rangle)$ , and  $|T_{-1}\rangle = |\beta\beta\rangle$ ) which considers the spin system as a superposition (mix) of the individual spin states because the spins in the spin states are near equivalent and thus indistinguishable from each other. It is important to acknowledge that mixing of the nuclear spin states of 3-DFMP is more significant in the  $\mu\text{T}$  regime, during EFNMR detection, and less so during exposure of the sample to the mT PTF.

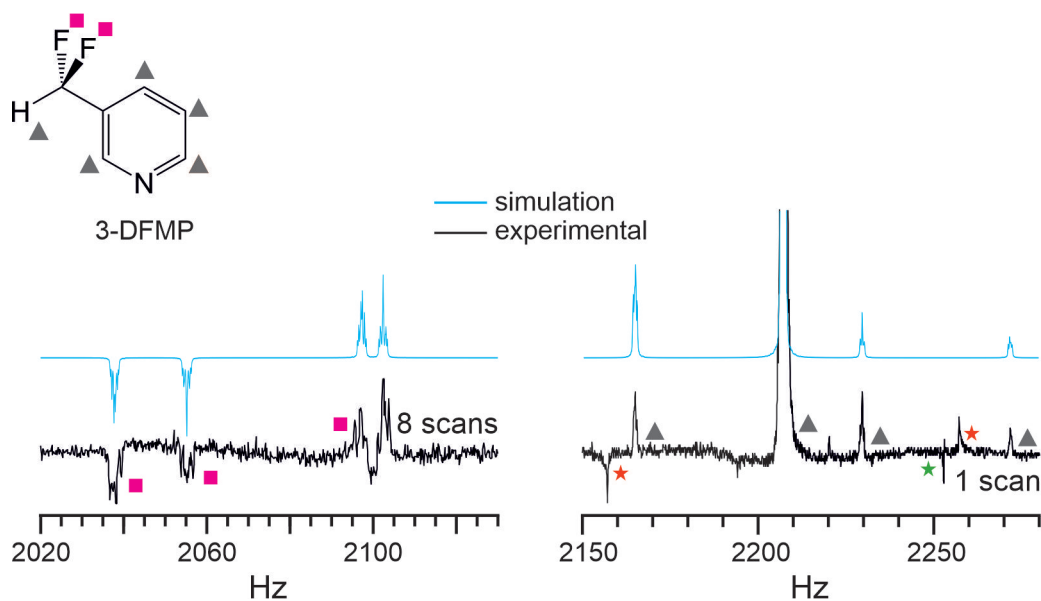


FIGURE 5.17: The EFNMR simulation of 3-DFMP acquired with  $\rho_0 = \sum_i \hat{I}_{zi}$  over all  $^1\text{H}$  nuclei and  $\hat{I}_{obs} = \sum_i \hat{I}_i^-$  over all nuclei fits well to the SABRE-polarised EFNMR spectrum of 3-DFMP  $^{19}\text{F}$  and also replicates the phase of the hyperpolarised peaks at the  $^{19}\text{F}$  region of the spectrum.

The SABRE-polarised EFNMR spectrum of 3-DFMP therefore arises from hyperpolarisation of the  $\hat{I}_z$  state of the  $^1\text{H}$  nuclei, as suggested by the EFNMR simulation acquired with  $\rho_0 = \sum_i \hat{I}_{zi}$  for all  $^1\text{H}$  nuclei and  $\hat{I}_{obs} = \sum_i \hat{I}_i^-$  over all nuclei. The eight hyperpolarised peaks (four in the  $^1\text{H}$  region and four in the  $^{19}\text{F}$  region of the EFNMR spectrum) are formed from the single coherence-order transitions between the mixed nuclear spin states of 3-DFMP in the  $\mu\text{T}$  detection field, after the  $\pi/2$  RF pulse.

Although there is accurate replication of the phase and structure of the SABRE-polarised EFNMR spectrum of 3-DFMP acquired with a PTF of 6 mT by the simulation, the relative intensity of the split peaks in both regions of the EFNMR spectrum are not in complete agreement. For example, the hyperpolarised peaks at 2165 and 2230 Hz have similar intensities experimentally but the simulation shows a more intense peak at 2165 Hz. The simulations also shows similar intensities between the four hyperpolarised peaks at 2036, 2056, 2098 and 2103 Hz, however the experimental result shows a weaker peak at 2056 and 2098 Hz. These differences may be a consequence of indirect polarisation transfer from the SABRE-polarised  $\hat{I}_z$  state of the  $^1\text{H}$  nuclei to other product states within the mixed nuclear spin system, which may result in the formation of hyperpolarised peaks in the same positions but with varying phases and intensities that add to or subtract from the dominant form of the spectrum.

Significant separation of the split peaks within the EFNMR signals of 3-DFMP compared to those of 3-FP, 3,5-DFP and 3,5-TFMP is caused by the large 55.4 Hz coupling. Reduced peak overlap improves signal resolution and allows for the observation of fine-structure on the multiplets that arises from the smaller homonuclear and heteronuclear  $J$ -coupling interactions involving the aromatic protons. The extra chemical information displayed by the SABRE-polarised  $^1\text{H}$  and  $^{19}\text{F}$  EFNMR signals is

beneficial for interrogating the SABRE polarisation transfer mechanism which requires observing changes in the form of hyperpolarised signals as a function of the SABRE polarisation transfer condition. The simulation shows a good fit to the fine structure displayed by the experimental  $^1\text{H}$  multiplets, but not the  $^{19}\text{F}$  multiplets. The heteronuclear couplings in Table 5.5 are therefore not completely accurate. In principle, refinement of these couplings could be achieved by running the  $J$ -opt 1 experiment on the SABRE-polarised  $^{19}\text{F}$  EFNMR signal of 3-DFMP. However, this was found to be ineffective because the multiplets are noisy due to low SNR.

### 5.3.6 Conclusion

The SABRE-polarised EFNMR spectra of 3,-FP, 3,5-DFP, 3,5-TFMP and 3-DFMP were acquired using the mT SABRE-EFNMR experiment. The SABRE-polarised  $^1\text{H}$  signals of 3,5-DFP and 3,5-TFMP acquired with 1 scan exhibited much higher levels of polarisation than the SABRE-polarised  $^{19}\text{F}$  signals acquired with 16 and 8 scans, respectively, as shown in FIGURE 5.18. This is because the mT PTF directs SABRE-polarisation transfer from the  $p\text{-H}_2$  derived hydrides to the  $^1\text{H}$  nuclei on the substrate, whereas the  $^{19}\text{F}$  nuclei become hyperpolarised indirectly via the transfer of SABRE polarisation from the  $^1\text{H}$  nuclei; a process that is mediated by the  $J$ -coupling network of the substrate and is inefficient. The combination of inefficient polarisation transfer to  $^{19}\text{F}$  at mT PTFs and heavy splitting of the hyperpolarised signals due to strong coupling led to an unobservable  $^{19}\text{F}$  EFNMR signal of 3-FP. The higher number of  $^{19}\text{F}$  nuclei in 3,5-DFP and 3,5-TFMP, combined with the fact that they are within simpler coupling networks, due to the symmetry of the substrates which minimises peak splitting and peak overlap, increases the SNR of the hyperpolarised  $^{19}\text{F}$  signals to enable their observation.

SABRE-polarised EFNMR signals in the  $^1\text{H}$  region of the 3-DFMP spectrum were also much more intense than the signals in the  $^{19}\text{F}$  region (see FIGURE 5.18), however, this is not related to differences in the efficiency of SABRE and indirect polarisation transfer, as the source of both sets of signals is SABRE polarisation of the  $^1\text{H}$  nuclei (predominantly the aromatic protons) followed by single coherence-order transitions between the mixed nuclear spin states of  $^1\text{H}$  and  $^{19}\text{F}$  after a  $\pi/2$  RF pulse. The hyperpolarised EFNMR signals of 3-DFMP in the  $^{19}\text{F}$  region of the spectrum, acquired with 8 scans, are therefore more intense than the  $^{19}\text{F}$  EFNMR signals of 3,5-DFP and 3,5-TFMP, acquired with 16 scans, as the 3-DFMP signals are produced from optimal SABRE polarisation to  $^1\text{H}$  and not inefficient hyperpolarisation of  $^{19}\text{F}$  at mT PTFs.

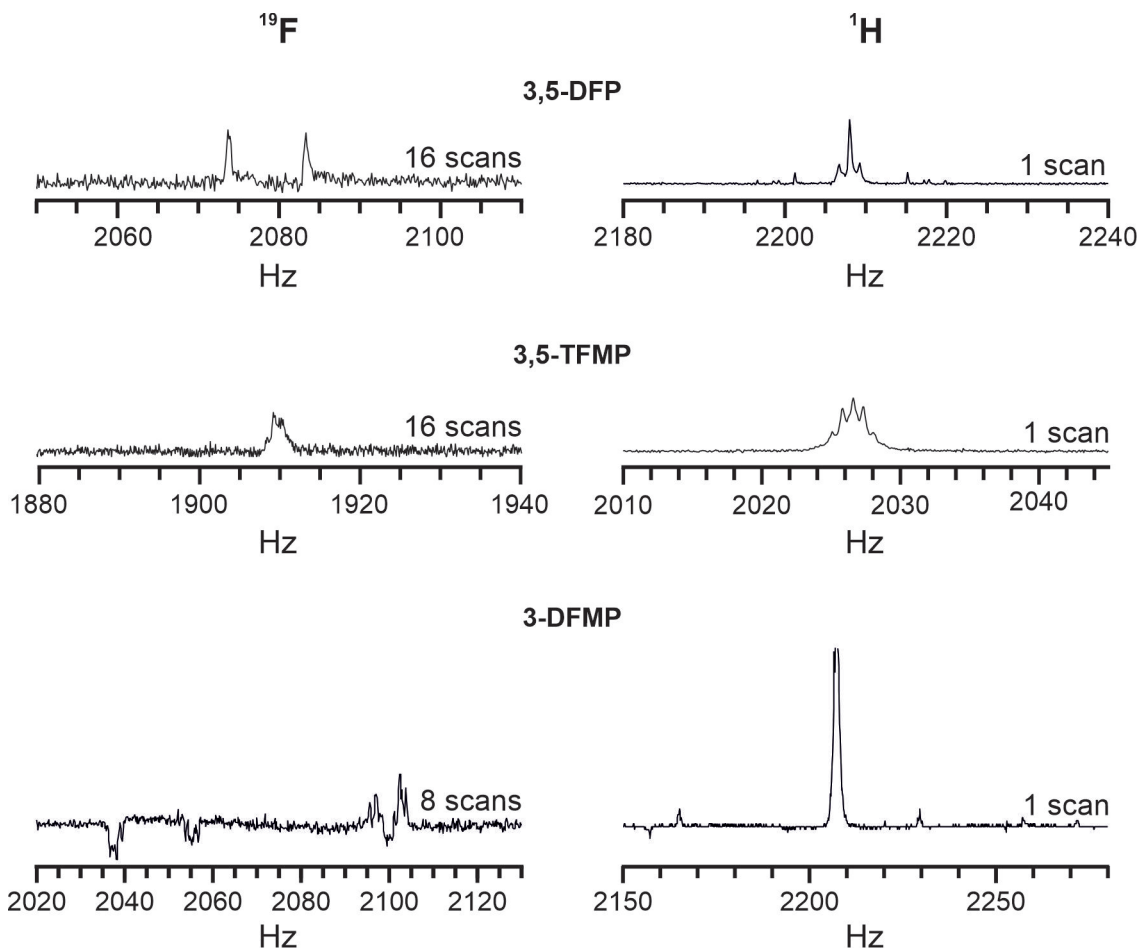


FIGURE 5.18: The SABRE-polarised  $^1\text{H}$  and  $^{19}\text{F}$  EFNMR signals of 3,5-DFP, 3,5-TFMP and 3-DFMP acquired using the mT SABRE-EFNMR experiment.

Indirect polarisation transfer to  $^{19}\text{F}$  on 3,5-DFP was shown to be more efficient than to  $^{19}\text{F}$  on 3,5-TFMP because both signals displayed comparable SNRs from an equal number of scans of the mT SABRE-EFNMR experiment, even though the latter contains  $3\times$  as many  $^{19}\text{F}$  nuclei. This was observed because indirect polarisation transfer is mediated by the substrate  $J$ -coupling network, therefore, the reduced  $J$ -coupling interactions involving the  $^{19}\text{F}$  nuclei in 3,5-TFMP ( $\leq 1$  Hz) versus 3,5-DFP ( $\leq 9$  Hz), due to the added chemical bond (methyl carbon) between  $^{19}\text{F}$  and the other substrate nuclei reduces the efficiency of transfer.

Comparison of all experimental EFNMR signals acquired from the mT SABRE-EFNMR experiment in FIGURE 5.18, with simulated EFNMR signals acquired using  $\hat{I}_{obs} = \sum_i \hat{I}_i^-$ , showed a dominant polarisation transfer pathway from the hyperpolarised  $\mathbf{I}_1 \cdot \mathbf{I}_2$  state of the  $p\text{-H}_2$  derived hydrides to the  $\hat{I}_z$  state of the protons. The form of the hyperpolarised  $^{19}\text{F}$  EFNMR signals of 3,5-DFP and 3,5-TFMP did not replicate the simulated  $^{19}\text{F}$  EFNMR signals well. This may be due to poor efficiency of indirect polarisation transfer to  $^{19}\text{F}$  in these substrates when using mT PTFs, or may be due to the hyperpolarisation of different spin states. In any case, the mT SABRE-EFNMR experiments were not sufficient to understand the simplified form of the  $^{19}\text{F}$  signals. Conclusions about the pathway of indirect polarisation transfer from the SABRE-

polarised  $^1\text{H}$  nuclei of 3-DFMP in the mT regime could not be made as the form of the hyperpolarised  $^{19}\text{F}$  EFNMR spectrum was dominated by mixing between states in the Earth's field following direct SABRE polarisation transfer to the  $\hat{I}_z$  state of  $^1\text{H}$  in the mT PTF.

Probing the SABRE polarisation transfer process requires hyperpolarised spectra that provide chemical information on the target substrate by the display of signals with fine structure. This allows both significant and subtle changes to the form of the hyperpolarised signals to be observed under variable SABRE conditions. Large coupling interactions within the substrate coupling network increases splitting of the EFNMR multiplets to reduce peak overlap and promote acquisition of EFNMR signals with more fine structure that are easier to interpret. For example, successful interpretation of the SABRE-polarised  $^1\text{H}$  signal of 3,5-DFP was made possible by its clear display of split peaks which enabled the use of simulations to dissect the signal into contributions from the different  $^1\text{H}$  environments (*para*, *ortho*), as shown in section 5.3.3. Similarly, the eight main signals of the SABRE-polarised 3-DFMP spectrum are a consequence of the dominant 3-spin  $AB_2$  interaction between the two  $^{19}\text{F}$  and  $^1\text{H}$  nuclei, and are greatly separated thanks to the 55.4 Hz coupling within the  $AB_2$  system. This allows improved signal resolution to observe even the small  $J$ -coupling interactions involving the aromatic and methyl protons. Therefore, the relatively large heteronuclear couplings of 9 and 55.4 Hz in 3,5-DFP and 3-DFMP, respectively, as well as mixing of the  $^1\text{H}$  and  $^{19}\text{F}$  spin states of 3-DFMP due to the fact that it represents a nuclear spin system that is very strongly coupled, make both substrates prime candidates for more detailed investigations of the magnetic field dependence of ULF SABRE polarisation transfer in the next chapter.

# 6 | Probing SABRE Polarisation Transfer with *in situ* EFNMR Detection

## 6.1 Introduction

In Chapter 5 the SABRE-polarised  $^1\text{H}$  and  $^{19}\text{F}$  EFNMR signals of 3,5-DFP and 3-DFMP were successfully acquired with mT PTFs using the mT SABRE-EFNMR experiment. The complex form and multiplicity of the hyperpolarised signals were interpreted via comparison with simulated EFNMR spectra. In this chapter, methods to explore the SABRE polarisation transfer to  $^1\text{H}$  and  $^{19}\text{F}$  in both mT and  $\mu\text{T}$  fields, *in situ* of NMR detection, will be developed and applied to 3,5-DFP and 3-DFMP. Both substrates exhibited well resolved hyperpolarised signals that were relatively straight-forward to interpret as a consequence of the sufficiently large  $^1\text{H}$  and  $^{19}\text{F}$  coupling interactions of 9 and 55.4 Hz in 3,5-DFP and 3-DFMP, respectively.

Generally speaking, polarisation transfer from the  $p\text{-H}_2$  derived hydrides to a target nucleus on the substrate is made more efficient when the PTC is met (see Eq. 2.35). The condition requires the frequency difference between the source and target of polarisation transfer to be matched to the dominant  $J$ -coupling interaction in the coupling network of the SABRE active catalyst ( $\text{Ir}\{\{\text{IMes}\}\{\text{H}\}_2\{\text{sub}\}_3\}^+$ ). SABRE polarisation transfer to  $^1\text{H}$  nuclei is therefore more efficient at mT fields, whereas SABRE polarisation transfer to heteronuclei is more efficient at  $\mu\text{T}$  fields.

The use of  $\mu\text{T}$  PTFs to direct SABRE polarisation transfer to heteronuclei has been illustrated on a wide range of isotopes using high-field NMR detection coupled with the *ex situ* SABRE polarisation transfer technique titled SABRE in SHield Enables Alignment Transfer to Heteronuclei<sup>2,36-40</sup> (SABRE-SHEATH). This method utilises a magnetic shield to houses the NMR tube and expose it to  $\mu\text{T}$  magnetic fields during the SABRE polarisation transfer step. The NMR tube within the magnetic shield is either shaken in the presence of  $p\text{-H}_2$  (shake and drop experiment) or bubbled with  $p\text{-H}_2$  before being transferred to the bore of the high-field NMR probe for detection. Enhancements of two orders of magnitude at 9.4 T have been reported in the literature for the  $^{19}\text{F}$  signals of fluorinated pyridines (up to  $\sim 200$  for the  $^{19}\text{F}$  signal of 3-FP<sup>37</sup>) using SABRE-SHEATH, however, these values are much smaller than the 4-5 order of magnitude enhancement of the  $^1\text{H}$  signals of N-heterocycles using mT PTFs in traditional SABRE experiments that use mT PTFs and detection in the high-field regime. The larger number of bonds separating the  $^{19}\text{F}$  nuclei in the target

analytes from the  $p$ -H<sub>2</sub> derived hydrides within the catalyst-bound  $p$ -H<sub>2</sub> and substrate species, reduces the strength of the  $J$ -coupling interaction between them. Since the efficiency of SABRE polarisation transfer is proportional to the  $J$ -coupling between the  $p$ -H<sub>2</sub> derived hydride and the nucleus receiving polarisation, the <sup>19</sup>F nuclei were less efficiently hyperpolarised. The shorter  $T_1$  relaxation times of <sup>19</sup>F nuclei (ranging between 3 and 5 s at 11.74 T<sup>2</sup>) also contributes to the lower enhancement levels as more hyperpolarisation is lost during automated sample transfer ( $\sim 5$  s) from the magnetic shield to the NMR probe.<sup>124</sup>

Demonstrated here is the use of the  $\mu$ T SABRE-EFNMR experiment to directly and immediately detect SABRE polarisation transfer to <sup>19</sup>F nuclei. The  $\mu$ T PTF enables the acquisition of SABRE-polarised <sup>19</sup>F signals of 3,5-DFP and 3-DFMP with higher polarisation levels and hence better signal resolution in comparison to what was observed using mT PTFs, where the <sup>19</sup>F nuclei were hyperpolarised indirectly via the inefficient transfer of hyperpolarisation on the SABRE-polarised <sup>1</sup>H nuclei. The focus of this chapter is the implementation of the the SABRE-EFNMR system to perform *in situ* mT and  $\mu$ T PTF-cycling experiments, allowing direct observation of the magnetic field dependence of the SABRE hyperpolarisation across the  $\mu$ T and mT regimes. Once more, simulations play a vital role in deciphering the product states responsible for the observed hyperpolarised signal shape to allow insight into, and compare, the polarisation transfer pathway to 3,5-DFP and 3-DFMP.

## 6.2 SABRE Polarisation Transfer to 3,5-difluoropyridine

### 6.2.1 Millitesla Polarisation Transfer Field Cycling

The mT PTF-cycling experiment was executed by repeating the mT SABRE-EFNMR experiment with linear increments of the mT field generated by the polarising coil. FIGURE 6.1 shows the mT PTF curve of 3,5-DFP, produced by plotting the normalised integral of the <sup>1</sup>H and <sup>19</sup>F EFNMR signals for every increment of the PTF. The data points in the <sup>1</sup>H PTF curve were acquired by integrating the central peak of the 3,5-DFP <sup>1</sup>H signal. Low SNR limited the analysis of the contribution to the PTF curve by the outer peaks of the 3,5-DFP <sup>1</sup>H signal.

The PTF curve of the <sup>1</sup>H signal shows the magnetic-field dependence of the efficiency of SABRE polarisation transfer to <sup>1</sup>H in 3,5-DFP in the mT regime, where the broad peak with a maximum between 8.5 and 9.5 mT outlines the optimal PTF for SABRE polarisation transfer to <sup>1</sup>H. The PTF curve of the <sup>19</sup>F signal shows a similar dependency with a maximum between 6 and 12 mT. This is expected under mT PTFs because the <sup>19</sup>F nuclei are hyperpolarised indirectly by the transfer of hyperpolarisation on the SABRE-polarised <sup>1</sup>H nuclei. It is worth noting that the data point at 0 mT in FIGURE 6.1 corresponds to 0 A through the polarising coil and therefore more accurately refers to a PTF of  $\sim 51.9 \mu$ T (detection field). Although

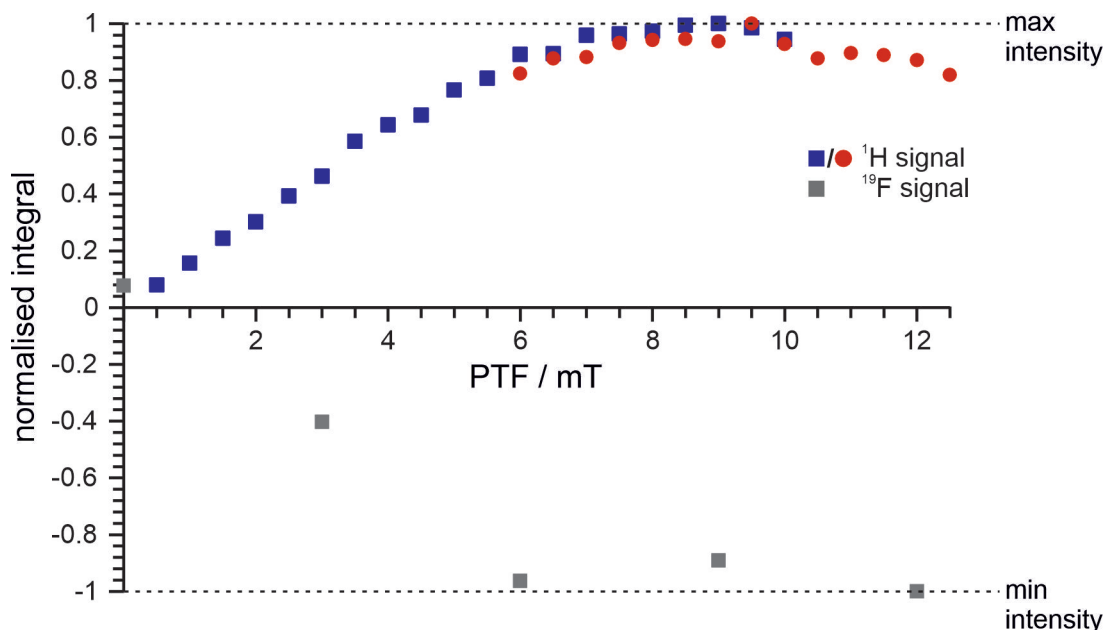


FIGURE 6.1: The  $^1\text{H}$  and  $^{19}\text{F}$  mT PTF curves of 3,5-DFP acquired by repeating the mT SABRE-EFNMR experiment with 1 and 16 scans, respectively and a  $t_{PTF} = 10$  s. The curves illustrate the magnetic field dependence of the efficiency of SABRE polarisation transfer to the  $^1\text{H}$  and  $^{19}\text{F}$  nuclei. Polarisation transfer to  $^1\text{H}$  is maximal between 8.5 and 9.5 mT, and hyperpolarisation of  $^{19}\text{F}$  is maximal between 6 and 12 mT. The efficiency of polarisation transfer to  $^1\text{H}$  and  $^{19}\text{F}$  as a function of the PTF follows similar trends as  $^{19}\text{F}$  receives its hyperpolarisation from the SABRE-polarised  $^1\text{H}$  nuclei at mT PTFs. The normalised integrals represented by red circles were acquired from the same sample on a different day but replicate the shape of the PTF curve demonstrating good reproducibility in the SABRE results.

heteronuclear SABRE polarisation transfer is coherent in the  $\mu\text{T}$  regime, coherent SABRE polarisation transfer to  $^{19}\text{F}$  requires  $\approx 4 \mu\text{T}$ .

There were no changes observed to the SABRE and indirect polarisation transfer pathways over the mT sweep experiment as the form of the hyperpolarised EFNMR signals were unchanged. The signals exhibited the same peak shapes as those presented in Chapter 5, where the  $^1\text{H}$  EFNMR signal corresponds to the dominant transfer of SABRE polarisation from the  $\mathbf{I}_1 \cdot \mathbf{I}_2$  state on the  $p\text{-h}_2$  derived hydrides to the  $\hat{I}_z$  state on the substrate  $^1\text{H}$  nuclei. The product state (or states) of 3,5-DFP involving  $^{19}\text{F}$  that receive hyperpolarisation from the  $\hat{I}_z$  state of  $^1\text{H}$  could not be deduced as the  $^{19}\text{F}$  EFNMR signal exhibited a fraction of the peaks illustrated by simulations. This may be a consequence of hyperpolarisation transfer to multiple product states that give rise to split peaks with intensities that cancel out. A dependency of the dominant pathway of SABRE and indirect polarisation transfer to  $^1\text{H}$  and  $^{19}\text{F}$ , respectively, was not observed across the sampled PTF range since the form of the hyperpolarised signals did not change.

A mT PTF curve of the hyperpolarised  $^1\text{H}$  and  $^{19}\text{F}$  signals in 3,5-DFP was previously acquired on an 11.74 T spectrometer by Olaru et al. (see FIGURE 6.2<sup>2</sup>) via *ex situ* SABRE polarisation transfer using an automated gas flow system to transport the sample from a reaction chamber that hosts SABRE polarisation transfer in a mT PTF to the NMR probe for detection. Due to chemical shift resolution in the high-field

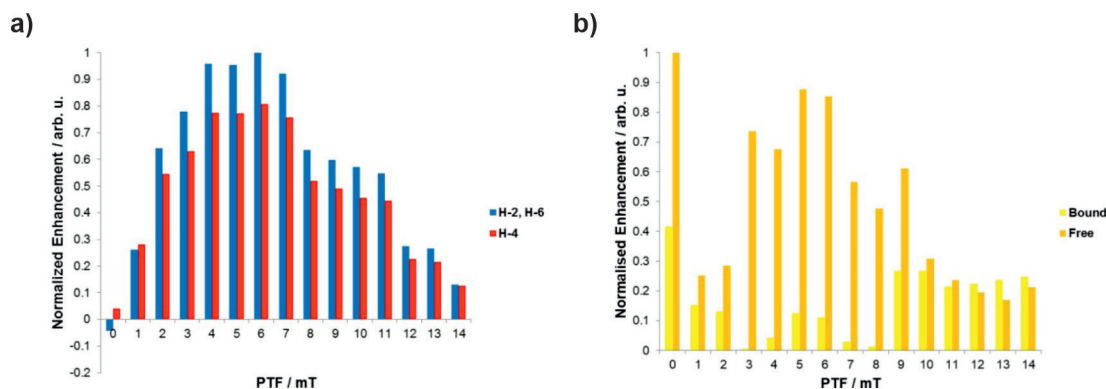


FIGURE 6.2: PTF curves plotted from the SABRE-polarised a)  $^1\text{H}$  and b)  $^{19}\text{F}$  signals of 3,5-DFP acquired via *ex situ* mT PTF-cycling experiments using an automated gas flow system for automated transfer from the PTF, generated by an external solenoid, to the 11.74 T detection field within the NMR spectrometer. Figures are reproduced without alteration from the SI of the publication by Olaru et al.<sup>2</sup> under the CC BY 4.0 license.

regime and efficient hyperpolarisation of the  $^1\text{H}$  nuclei (3-4 orders of magnitude), a PTF curve was acquired for both  $^1\text{H}$  environments of 3,5-DFP (*para* and *ortho*-protons). This also allowed the acquisition of a PTF curve for the  $^{19}\text{F}$  signals in catalyst-bound and free substrate.

The PTF curves of 3,5-DFP in FIGURE 6.2 acquired with an *ex situ* approach to PTF-cycling showed similarities to the PTF curves acquired in this work with an *in situ* approach. Both sets of curves show a broad range of PTFs for efficient hyperpolarisation of  $^1\text{H}$  and  $^{19}\text{F}$  up to  $\sim 11$  mT. While the *in situ* results display a smooth increase in SABRE polarisation transfer up to  $\sim 9.5$  mT and a gradual decrease beyond 12 mT, the *ex situ* results display more complex features. SABRE polarisation transfer to  $^1\text{H}$  was shown to be most efficient at 6 mT, followed by a fall to a rough plateau from 7-11 mT and then a significant drop at 12 mT. SABRE polarisation transfer to  $^{19}\text{F}$  in the free substrate was found to be optimal at 0 mT, although an additional broad peak of polarisation transfer efficiency was observed with a maximum around 5 mT, as well as apparent peaks at 3 and 9 mT. The PTF dependence of  $^{19}\text{F}$  hyperpolarisation was therefore quite noisy with *ex situ* SABRE polarisation transfer.

The *ex situ* PTF curves include more variability across the PTF values than what was observed in our *in situ* experiments. However, the results are difficult to directly compare because of key differences in the experimental protocol. Carrying out SABRE polarisation transfer *ex situ* of the detection field, with a  $\sim 5$  s duration for sample transfer from the polarisation transfer to detection field using an automated gas flow system, leads to a loss of hyperpolarisation due to  $T_1$  relaxation. In addition, other aspects of *ex situ* SABRE polarisation transfer act as sources of variability. For example, exposure to the magnetic environment of the lab during transfer, which includes the Earth's magnetic field and stray magnetic fields from the NMR spectrometer, also promotes  $T_1$  relaxation of the hyperpolarised spin system and may be slightly different for different steps in the experiment, leading to reduced reproducibility. In contrast, *in situ* SABRE polarisation transfer is detected without sample transfer and maintains a consistent 20 ms delay between the polarisation transfer and NMR detection steps, allowing for the advantageous capturing of the hyperpolarised response before significant

$T_1$  relaxation can occur, and with a higher level of reproducibility. On the other hand, *in situ* SABRE experiments suffer from a loss of chemical information due to NMR detection in the ULF regime, although in the case for 3,5-DFP, no significant differences were observed in the PTF curves for the different chemical environments (see FIGURE 6.2a).

In summary, while the PTF curves acquired from the two approaches cannot be directly compared, the enhancement variability displayed by the *ex situ* PTF curves are not likely due to variations in the efficiency of SABRE polarisation transfer, but rather reproducibility issues with the experimental procedure. This conclusion is supported by the magnetic field dependence of SABRE polarisation transfer displayed by the *in situ* PTF curves that do not show any similar structure but exhibit a smoother shape, which better represents what is expected when gradually moving toward and away from an LAC.

## 6.2.2 *In situ* SABRE Polarisation Transfer using Microtesla Polarisation Transfer Fields

Where the mT SABRE-EFNMR experiment (see Fig 5.2a) has been used thus far to coherently transfer polarisation from the *p*-H<sub>2</sub> derived hydrides to <sup>1</sup>H nuclei in 3,5-DFP, 3,5-TFMP and 3-DFMP, this section illustrates the use of the  $\mu$ T SABRE-EFNMR experiment (see Fig 5.2b) to drive coherent polarisation transfer to <sup>19</sup>F, as predicted by the PTC and LAC theory.

FIGURE 6.3a shows the SABRE-polarised EFNMR spectrum of 3,5-DFP acquired with 1 scan of the  $\mu$ T SABRE-EFNMR experiment using a 8  $\mu$ T PTF. The simulated signals are the same as those shown in section 5.3.3, acquired with  $\rho_0 = \sum_i \hat{I}_{zi}$  and  $\hat{I}_{obs} = \sum_i \hat{I}_i^-$  for all nuclei. The SABRE-polarised <sup>19</sup>F signal of 3,5-DFP using a 8  $\mu$ T PTF more accurately replicates the form and multiplicity of the simulated signal, although the relative intensity of the split peaks are not all well matched. This may be a consequence of SABRE polarisation transfer to other spin states within the nuclear spin system of 3,5-DFP that give rise to multiplet structures that when combined lead to peak cancelling and a reduction in peak intensity. As the split peaks of the <sup>19</sup>F EFNMR signal are very weak in comparison to the two main and most intense peaks (separated by 9 Hz due to the  $J\{H_4, F_{3,5}\}$  coupling interaction), they are likely hidden in the noise of the hyperpolarised <sup>19</sup>F EFNMR signal acquired via the mT SABRE-EFNMR experiment which had a very low SNR and displayed poor signal resolution. This may explain why it is only the two main peaks that appear in the indirectly hyperpolarised <sup>19</sup>F EFNMR signal of 3,5-DFP at 9 mT. Nonetheless, the simulation indicates a dominant polarisation transfer pathway from the  $\mathbf{I}_1 \cdot \mathbf{I}_2$  state of the *p*-H<sub>2</sub> derived hydrides to the  $\hat{I}_z$  state of the <sup>19</sup>F nuclei in 3,5-DFP at 5  $\mu$ T.

The hyperpolarised <sup>1</sup>H signal of 3,5-DFP acquired from the  $\mu$ T SABRE-EFNMR experiment shows a single peak that is antiphase with respect to the SABRE-polarised

$^{19}\text{F}$  EFNMR signal, in the same way that the SABRE-polarised  $^1\text{H}$  EFNMR signal of 3,5-DFP acquired from the mT SABRE-EFNMR experiment was also antiphase relative to the hyperpolarised  $^{19}\text{F}$  EFNMR signal. In FIGURE 5.12 in section 5.3.3 the SABRE-polarised EFNMR spectra of 3,5-DFP were acquired from separate mT SABRE-EFNMR experiments and were therefore phased separately to be displayed as absorbance signals. In FIGURE 6.3 the hyperpolarised  $^1\text{H}$  and  $^{19}\text{F}$  EFNMR spectra are from single experiments and have been phased so that the signal corresponding to the nuclei targeted by SABRE polarisation transfer is presented in absorbance mode. The antiphase nature of the hyperpolarised  $^1\text{H}$  and  $^{19}\text{F}$  EFNMR signals is representative of relayed transfer of hyperpolarisation between the nuclei (polarisation must be conserved, therefore transfer of polarisation between substrate nuclei leads to signals with opposite signs) and is therefore evidence of indirect transfer within the substrate molecule. The  $^{19}\text{F}$  signal hyperpolarised at  $8\ \mu\text{T}$  also appears to contain negative peaks that may correspond to the hyperpolarisation of multiple spin-order states (more clearly observed on the spectra acquired using negative PTFs in FIGURE 6.4b). These negative peaks are not replicated by the simulation acquired with a starting state of longitudinal magnetisation on all of the spins in 3,5-DFP ( $\rho_0 = \sum_i \hat{I}_{zi}$  for all nuclei) before the  $\pi/2$  RF pulse.

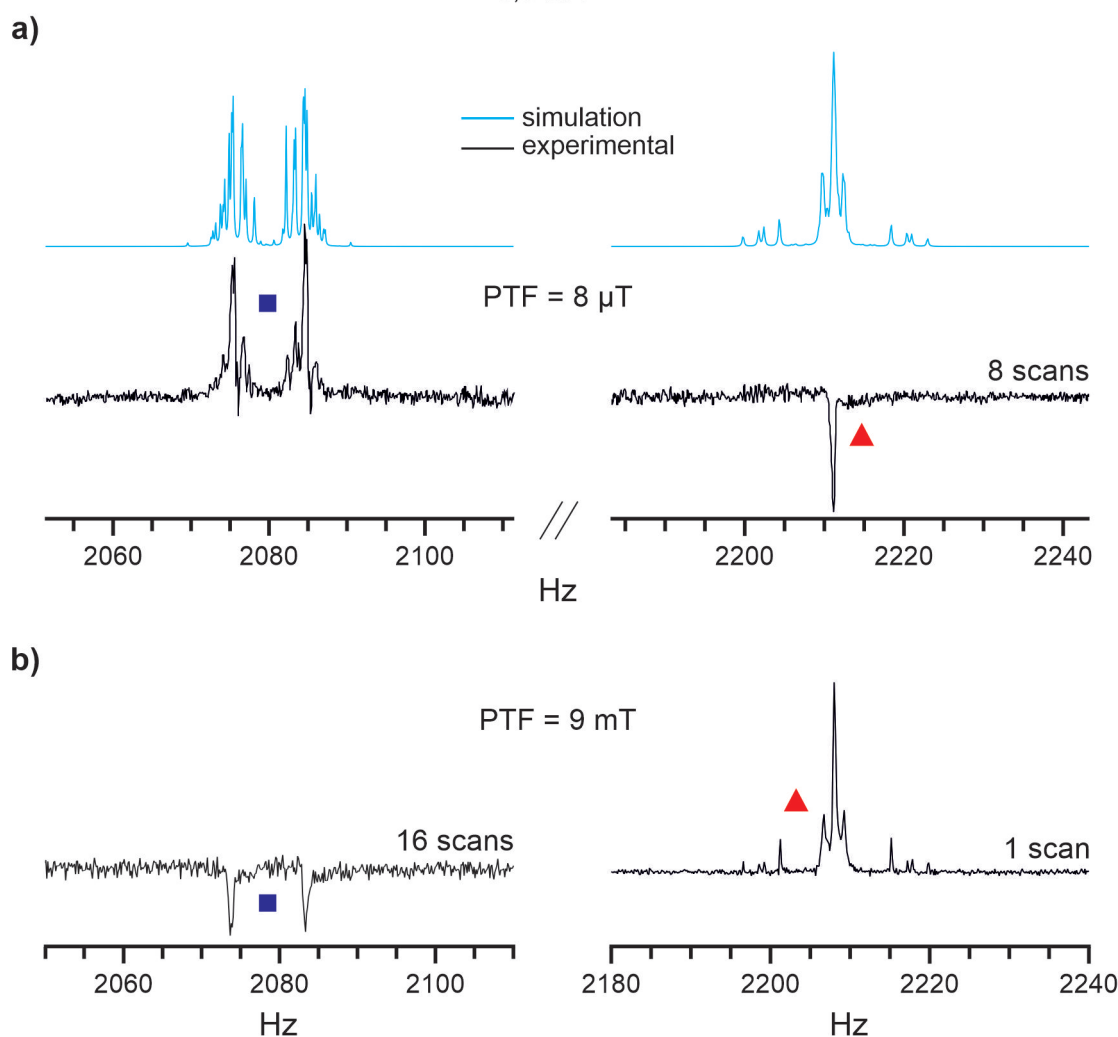
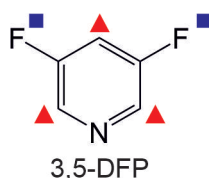


FIGURE 6.3: SABRE-polarised EFNMR spectrum of 3,5-DFP acquired using a) PTF = 8  $\mu$ T and  $t_{PTF}$  = 15 s with the  $\mu$ T SABRE-EFNMR experiment, and b) PTF = 9 mT with the mT SABRE-EFNMR experiment. The spectra have been phased so that the hyperpolarised signal from the target nucleus of SABRE polarisation transfer is an absorbance signal: a)  $^{19}\text{F}$  and b)  $^1\text{H}$ .

Poor signal resolution and low SNR of the hyperpolarised  $^1\text{H}$  EFNMR signal in FIGURE 6.3a is owed to the inefficient transfer of hyperpolarisation from the  $p\text{-H}_2$  derived hydrides to the  $^1\text{H}$  nuclei in the target substrate under  $\mu\text{T}$  PTFs, producing a hyperpolarised  $^1\text{H}$  peak that does not exhibit any fine structure. The  $^1\text{H}$  signal of 3,5-DFP is split up into contributions from the *para* and *ortho*-protons (see section 5.3.3). The *para*-proton is responsible for the 4 split peaks at the signal edges and contains a singlet-like peak in the centre of the signal, whereas the *ortho*-protons contribute to the multiplets at the centre of the signal that resemble a pseudo-triplet. The observed  $^1\text{H}$  peak from the  $\mu\text{T}$  SABRE-EFNMR experiment does not resemble a pseudo-triplet and the outer multiplets are not observed. The lack of pseudo-triplet structure at

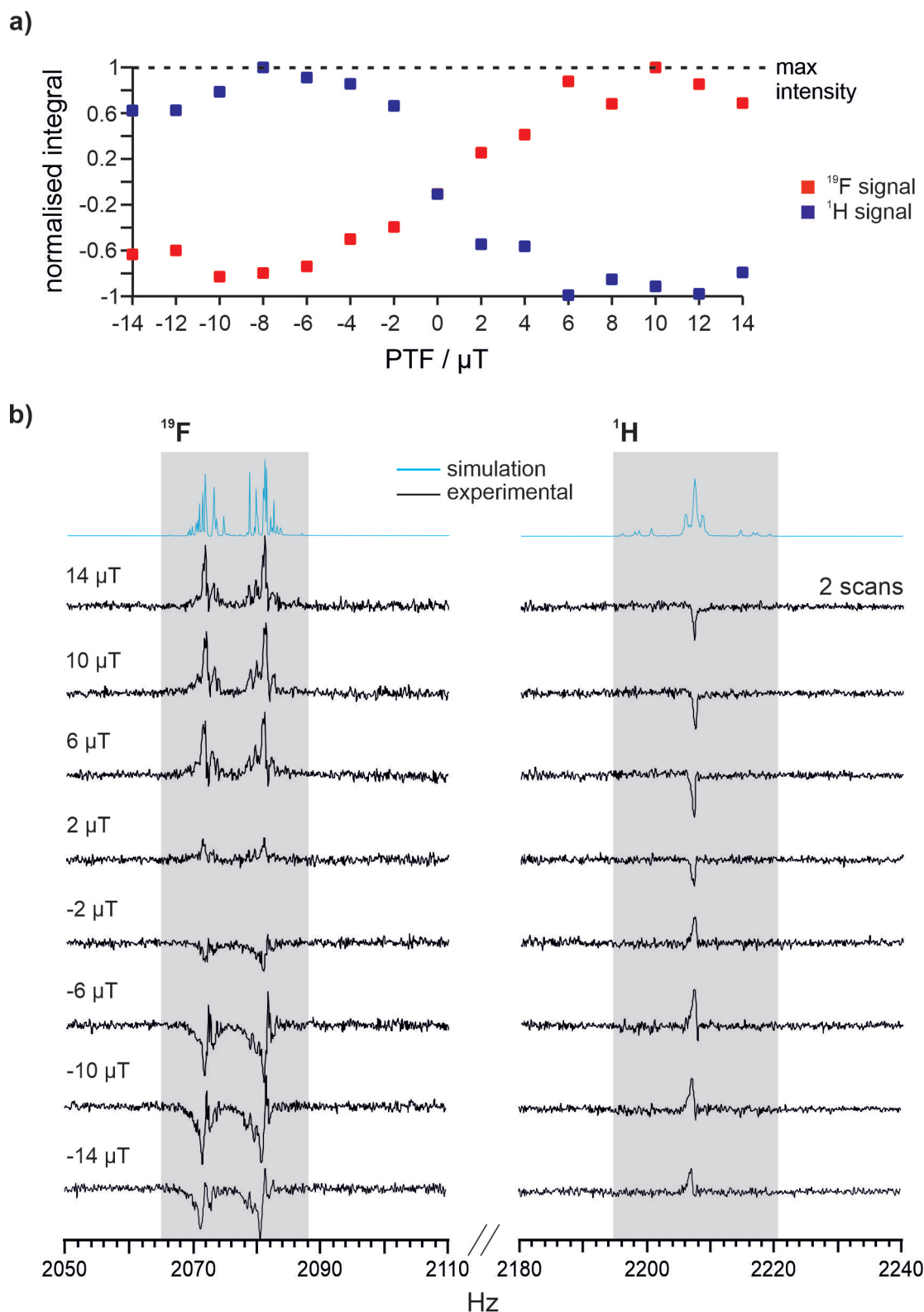
the centre of the  $^1\text{H}$  EFNMR signal may indicate the indirect polarisation transfer pathway from the SABRE-polarised  $^{19}\text{F}$  nuclei is more efficient to the *para*-proton, and it is likely that, as with the indirectly hyperpolarised  $^{19}\text{F}$  EFNMR signal in FIGURE 6.3b, the SNR of the  $^1\text{H}$  EFNMR signal is too low for the outer multiplets of the *para*-proton signal to appear above the noise. It is unlikely the  $^1\text{H}$  peak corresponds to the SABRE-polarised OH proton on the solvent as this would require mT PTFs for coherent SABRE polarisation transfer to  $^1\text{H}$ .

### 6.2.3 Microtesla Polarisation Transfer Field Cycling

A  $\mu\text{T}$  PTF-cycling experiment allows observation of the magnetic field dependence of the efficiency and pathway of SABRE polarisation transfer to  $^{19}\text{F}$  on the target substrate to progress toward improving the efficacy of SABRE. Repeatedly running the  $\mu\text{T}$  SABRE-EFNMR experiment over linear increments of the  $\mu\text{T}$  field generated by the z-Helmholtz coil enables execution of  $\mu\text{T}$  PTF-cycling. FIGURE 6.4a shows two  $\mu\text{T}$  PTF curves produced from the integration of the hyperpolarised  $^{19}\text{F}$  and  $^1\text{H}$  EFNMR signals of 3,5-DFP, acquired with 2 scans for each iteration of the  $\mu\text{T}$  SABRE-EFNMR experiment. The PTF curves were acquired by sweeping the PTF from -14 to 14  $\mu\text{T}$  in increments of 2  $\mu\text{T}$ .

A change in the sign of the signal intensity is observed when crossing 0  $\mu\text{T}$ ; however, both PTF curves appear symmetric about zero which demonstrates good reproducibility of SABRE polarisation. The change in sign is not accompanied by a change in the form of the hyperpolarised EFNMR signal as shown by the 3,5-DFP spectra in FIGURE 6.4b. The similarity in the trends of the  $^1\text{H}$  and  $^{19}\text{F}$  PTF curves is evidence the hyperpolarised  $^1\text{H}$  signals originate from the transfer of hyperpolarisation from  $^{19}\text{F}$  and do not correspond to hyperpolarisation of the solvent in this case, as may be perceived by the acquisition of a singlet-like  $^1\text{H}$  signal. The trend is also similar to what was seen with the  $^1\text{H}$  and  $^{19}\text{F}$  mT PTF curves of 3,5-DFP in FIGURE 6.1.

SABRE polarisation transfer from the *p*- $\text{H}_2$  derived hydrides to  $^{19}\text{F}$  in 3,5-DFP is shown by the PTF curves to be a broad peak with a maximum between 6 and 10  $\mu\text{T}$ , outlining the optimal PTF range for SABRE polarisation transfer to  $^{19}\text{F}$ . Significant changes to the form of the SABRE-polarised  $^{19}\text{F}$  EFNMR signals were not observed from -14-14  $\mu\text{T}$ . Despite this, the SABRE-polarised  $^{19}\text{F}$  signals from the  $\mu\text{T}$  PTF-cycling experiment displayed antiphase peaks (relative to the major component of the signal) with ranging intensities across the PTF sweep, where these peaks were most intense at -14, -10 and -6  $\mu\text{T}$ . These antiphase peaks also appeared on the SABRE-polarised  $^{19}\text{F}$  EFNMR signal of 3,5-DFP in FIGURE 6.3a acquired using a PTF of 8  $\mu\text{T}$ . The simulations in FIGURE 6.4b were acquired with  $\rho_0 = \sum_i \hat{I}_{zi}$  and  $\hat{I}_{obs} = \sum_i \hat{I}_i^-$  for all nuclei in 3,5-DFP and do not show antiphase peaks, suggesting that experimentally there may be hyperpolarisation of product states other than  $\hat{I}_z$ . Regardless, stronger SNRs are required to provide insight into the cause of these components, as well as the use of different flip angles ( $< \pi/2$ ).



A gradual shift in the phase of the hyperpolarised  $^1\text{H}$  EFNMR signal is observed over the  $\mu\text{T}$  PTF-cycling experiment from 2 - 14  $\mu\text{T}$  (see FIGURE 6.4b). The reason for this shift is due to gradual drifting of the external field ( $B^0$ ) over time on account of the naturally fluctuating Earth's magnetic field. A shift in  $B^0$  leads to a shift in the Larmor frequency of the spins, which will interact differently with the  $B^1$  field (RF pulse) of fixed frequency and gain zero-order phase proportional to the shift in Larmor frequency. The steps in the  $\mu\text{T}$  PTF-cycling experiment were acquired sequentially starting at -14  $\mu\text{T}$ , meaning the hyperpolarised  $^1\text{H}$  EFNMR signals acquired with positive PTFs were more significantly affected by the drifting  $B^0$  (frequency shifts of up to +1.5 Hz were recorded) and hence gained more phase. It is important to note that the  $B^0$  shift is not always linear over time as it is not only caused by variation in the Earth's magnetic field, but also by temporary magnetic fields in the vicinity of the EFNMR probe. This makes the use of automated post-processing procedures to correct for phase shifts more complicated.

A  $\mu\text{T}$  PTF curve of 3,5-DFP was also acquired by Olaru et al.<sup>2</sup> with an *ex situ* PTF-cycling experiment (see FIGURE 6.5). The magnetic field dependence of SABRE polarisation transfer illustrated by the *ex situ* and *in situ* PTF curves were very different. The *ex situ* PTF curve saw a 10-fold enhancement to the maximum from 10 to 20  $\mu\text{T}$  and fall to a plateau of minimum enhancement from 30 - 60  $\mu\text{T}$  where it remained until the final sampled PTF of 100  $\mu\text{T}$ . This deviates significantly from the smooth and broad maximum of the *in situ* PTF curve at 6 - 10  $\mu\text{T}$  (see FIGURE 6.4a). Also, the acquisition of multiple *in situ* PTF curves of 3,5-DFP all showed a gradual decay of the  $^1\text{H}$  and  $^{19}\text{F}$  hyperpolarisation away from the maximum toward higher PTFs, until the signals could not be observed beyond 26  $\mu\text{T}$  which is not replicated by the *ex situ* PTF curve in FIGURE 6.5. The maximal enhancement of the  $^{19}\text{F}$  signal of 3,5-DFP at 20  $\mu\text{T}$  suggested by the *ex situ* PTF curve is also quite far from the optimal PTF of  $\sim 4 \mu\text{T}$  predicted by the theory of LAC.<sup>54</sup>

As was the case when comparing the *ex situ* and *in situ* mT PTF curves of

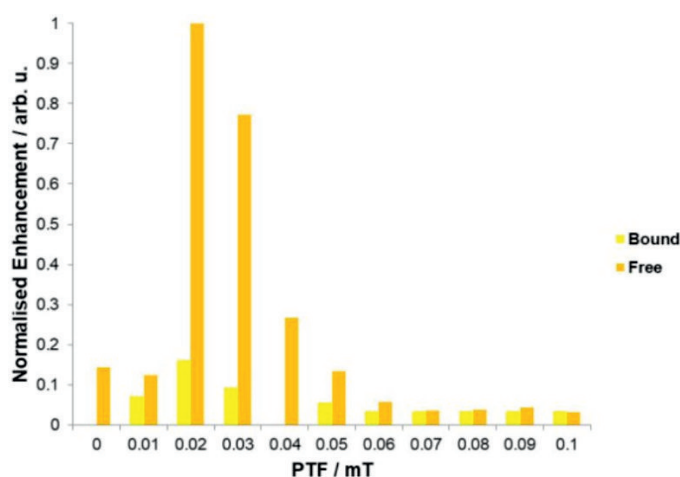


FIGURE 6.5: PTF curve plotted from the SABRE-polarised  $^{19}\text{F}$  signal of 3,5-DFP acquired via *ex situ*  $\mu\text{T}$  PTF-cycling experiments using an automated gas flow system for automated transfer from the PTF, generated by an external solenoid, to the 11.74 T detection field within the NMR spectrometer. Figure is reproduced without alteration from the SI of the publication by Olaru et al.<sup>2</sup> under the CC BY 4.0 license.

3,5-DFP, the  $\mu\text{T}$  PTF curves cannot be compared directly. The  $\mu\text{T}$  PTFs generated by the z-Helmholtz coil pair within the SABRE-EFNMR system can easily be calibrated and thus accurately generated. Calibration requires measuring the Larmor frequency of the spins in a sample across a range of positive and negative current values to calculate the  $\mu\text{T mA}^{-1}$  value and the magnitude of the Earth's magnetic field,  $B_E$ . Since the pair of y-Helmholtz coils produce a y-field that aligns  $B^0$  to the z-axis, the desired magnetic field is achieved by passing the required amount of positive or negative current through the z-Helmholtz coil to linearly add to or subtract from  $B_E$ , respectively. The instrumentation for *ex situ* SABRE polarisation transfer uses a solenoid located within a  $\mu$ -metal shield, where the solenoid generates  $\mu\text{T}$  fields and the  $\mu$ -metal shield attenuates the Earth's magnetic field by up to a factor of 300. The accuracy in the magnetic field exposed to the sample within the  $\mu$ -metal shield depends on the calibration of the  $\mu\text{T}$  field generated by the solenoid and how effectively the shield has been degaussed. In this case, Larmor frequency cannot be used to measure the magnetic field strength inside the  $\mu$ -metal shield and a gaussmeter is used instead. The issue here lies in the fact that the gaussmeter must also be calibrated but requires a well calibrated  $\mu$ -metal shield.

Furthermore, the power supply attached the Helmholtz coil array allowed the generation of  $\mu\text{T}$  magnetic fields with a much higher precision than that of the power supply attached to the solenoid within the  $\mu$ -metal shield ( $\pm 10 \mu\text{T}$ ). Consequently, the *in situ* approach enables a more reliable interrogation of the magnetic field dependence of SABRE polarisation transfer in the  $\mu\text{T}$  regime.

## 6.3 SABRE Polarisation Transfer to 3-difluoromethylpyridine

### 6.3.1 *In situ* SABRE Polarisation Transfer using Microtesla Polarisation Transfer Fields

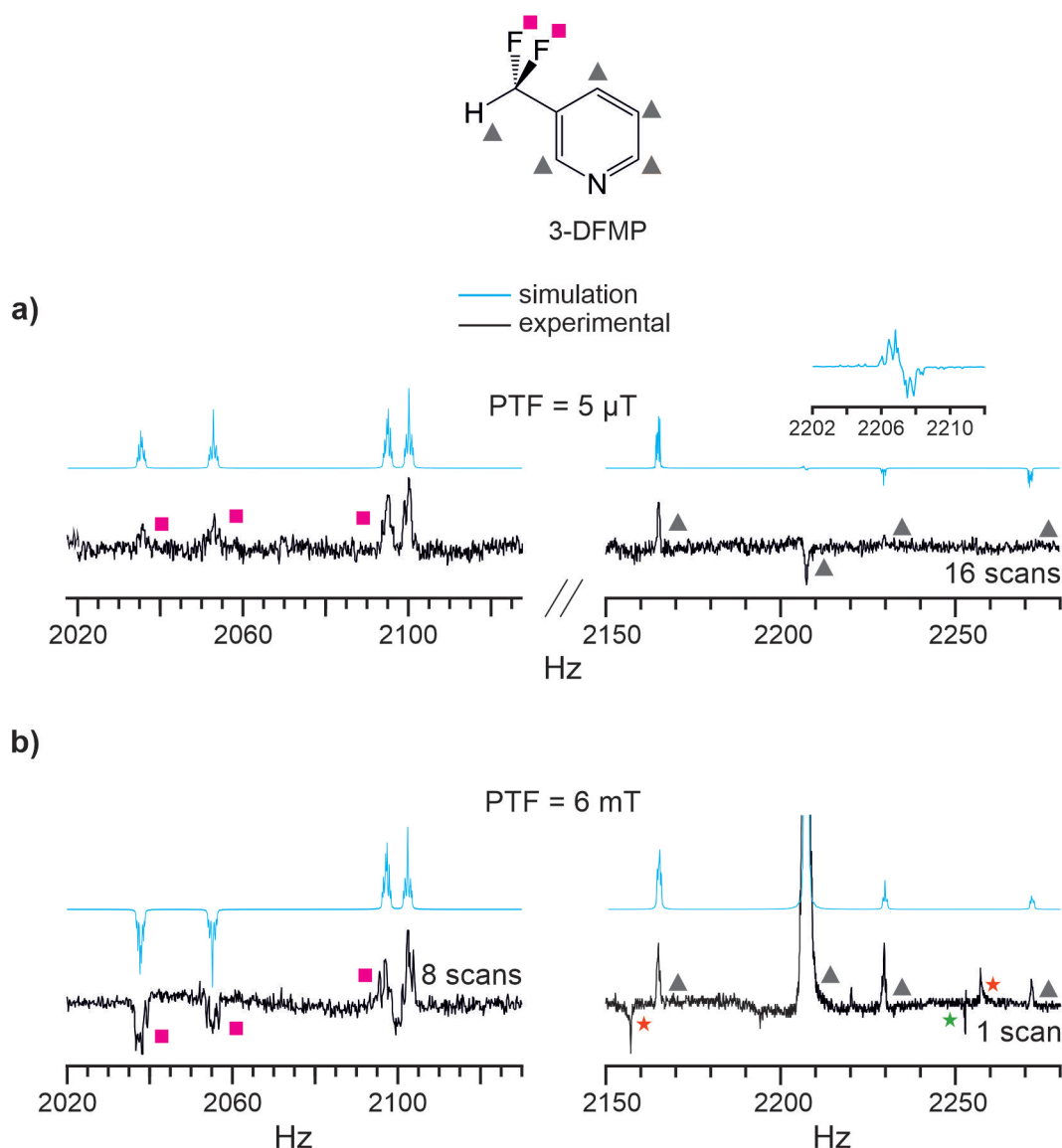


FIGURE 6.6: SABRE-polarised EFNMR spectrum of 3-DFMP acquired using a) PTF = 5  $\mu\text{T}$  and  $t_{PTF} = 12\text{s}$  with the  $\mu\text{T}$  SABRE-EFNMR experiment, and b) PTF = 6 mT with the mT SABRE-EFNMR experiment. The spectra have been phased so that the hyperpolarised signal from the target nucleus of SABRE polarisation transfer is an absorbance signal: a)  $^{19}\text{F}$  and b)  $^1\text{H}$ .

SABRE polarisation transfer was directed to  $^{19}\text{F}$  in 3-DFMP using a 5  $\mu\text{T}$  PTF in 16 scans of the  $\mu\text{T}$  SABRE-EFNMR experiment, producing the hyperpolarised EFNMR spectrum in FIGURE 6.6a. The hyperpolarised  $^1\text{H}$  and  $^{19}\text{F}$  EFNMR signals

of 3-DFMP acquired with a 6 mT PTF in 1 and 8 scans of the mT SABRE-EFNMR experiment (displayed in section 5.3.5) is shown in FIGURE 6.6b for comparison. Both spectra have been phased relative to the display of an absorbance signal for the nucleus targeted by SABRE polarisation transfer. The simulated EFNMR spectrum of 3-DFMP in FIGURE 6.6a was acquired with  $\rho_0 = \sum_i \hat{I}_{zi}$  for all  $^{19}\text{F}$  nuclei and  $\hat{I}_{obs} = \hat{I}_i^-$  for all nuclei, to account for the fact that SABRE polarisation transfer under  $\mu\text{T}$  PTFs is directed to  $^{19}\text{F}$ . The simulated EFNMR spectrum of 3-DFMP in FIGURE 6.6b was run in the same way but with  $\rho_0 = \sum_i \hat{I}_{zi}$  for all  $^1\text{H}$  nuclei since mT PTFs drive SABRE polarisation transfer to  $^1\text{H}$ .

As discussed previously, the large 55.4 Hz  $J\{\text{H}_7,\text{F}\}$  coupling interaction between the nuclei of the methyl group ( $\text{CHF}_2$ ) of 3-DFMP leads to a very strongly coupled nuclear spin system that is more accurately represented by the singlet-triplet basis which defines the nuclear spin system as a superposition or mixing of the individual spin states. Therefore, direct SABRE polarisation of the  $^{19}\text{F}$  nuclei in 3-DFMP produces hyperpolarised EFNMR signals at the Larmor frequency of  $^{19}\text{F}$  and  $^1\text{H}$ , where the observed splitting pattern of the EFNMR spectrum is dictated by the strongly coupled 3-spin  $\text{AB}_2$  system of the methyl nuclei. The simulation replicating direct SABRE polarisation transfer to the  $\hat{I}_z$  state of  $^1\text{H}$  in FIGURE 6.6b fit very well to the SABRE-polarised spectrum and replicated the phase of the split peaks. The simulation of direct SABRE polarisation transfer to the  $\hat{I}_z$  state of  $^{19}\text{F}$  in FIGURE 6.6a fit well to the SABRE-polarised absorbance signals in the  $^{19}\text{F}$  region of the EFNMR spectrum, but did not replicate the hyperpolarised signals in the  $^1\text{H}$  region. The simulation shows an absorbance signal at 2166 Hz, a weak antiphase signal at 2207 Hz and emission peaks at 2230 and 2273 Hz, whereas the experimental spectrum shows an absorbance and emission signal at 2166 Hz and 2207 Hz, respectively. The signals at 2230 and 2273 Hz are observed, but their phase and corresponding fit to the simulation cannot be commented on as they are mostly hidden in the noise.

The differences between the simulated and experimental EFNMR spectra suggests indirect transfer of hyperpolarisation from the SABRE-polarised  $\hat{I}_z$  state of the  $^{19}\text{F}$  nuclei to other product states within the mixed nuclear spin system. This would produce a resultant EFNMR spectrum of 3-DFMP that deviates from the simulation as it contains contributions from the indirectly hyperpolarised product states that each give rise to signals with the same splitting pattern but with different phases and intensities and combine to form a modified SABRE-polarised EFNMR spectrum. The presence of a hyperpolarised emission signal at 2207 Hz may therefore correspond to indirect polarisation transfer to the  $\hat{I}_z$  state of aromatic  $^1\text{H}$  nuclei that are known to produce an in-phase multiplet at this frequency and which would appear antiphase relative to the signal of the nucleus targeted by SABRE polarisation transfer ( $^{19}\text{F}$  in this case), as already discussed. It is also likely that this emission signal is overlapping with the much weaker antiphase peak illustrated by the simulation in FIGURE 6.6a. Low SNR prevents the observation of the peaks at 2230 and 2273 Hz to compare to the simulation, although the simulation shows that these peaks are very small in comparison to the peak at 2166 Hz which experimentally also has a low SNR. While the form of hyperpolarised signals at the  $^{19}\text{F}$  region of the EFNMR spectrum of 3-DFMP is replicated by the simulation, there appear to be differences in their relative intensities as the two peaks at 2036 and 2054 Hz are significantly weaker than the two peaks at

2095 and 2100 Hz. This further indicates indirect hyperpolarisation transfer from the  $\hat{I}_z$  state of the  $^{19}\text{F}$  nuclei to other product states within the mixed nuclear spin system of 3-DFMP that effects the shapes of the hyperpolarised signals at the  $^{19}\text{F}$  and  $^1\text{H}$  region of the EFNMR spectrum.

### 6.3.2 Microtesla Polarisation Transfer Field Cycling

The magnetic field dependence of the SABRE polarisation transfer to  $^1\text{H}$  and  $^{19}\text{F}$  in 3-DFMP was probed via the implementation of mT and  $\mu\text{T}$  PTF-cycling experiments. The mT PTF curves which have not been presented here showed a broad maximum for both nuclei at  $\sim 6$  mT without displaying any significant changes in the form of

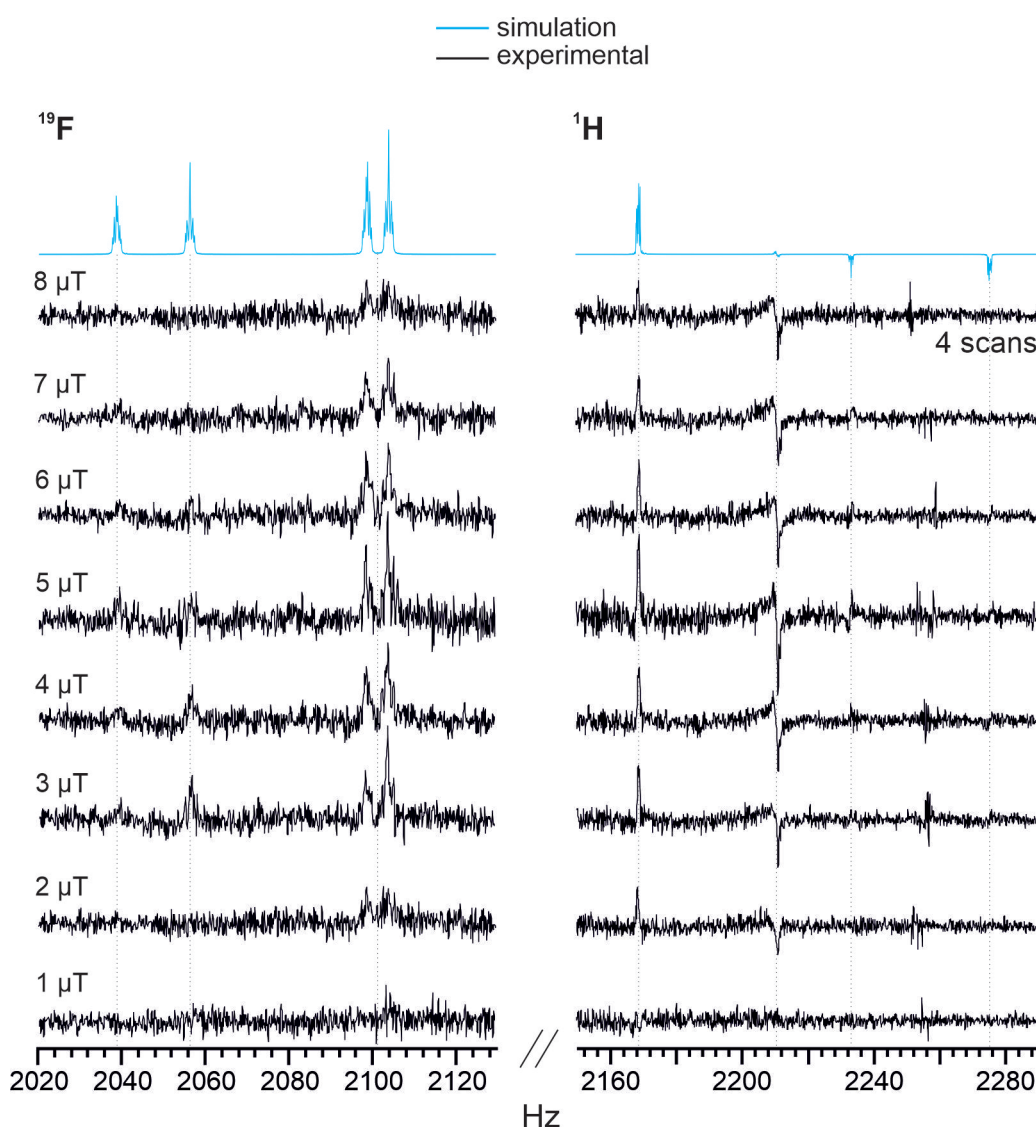


FIGURE 6.7: The hyperpolarised EFNMR spectra of 3-DFMP were acquired with 4 scans and a  $t_{PTF} = 12$  s for each PTF iteration of the  $\mu\text{T}$  SABRE-EFNMR experiment. The magnetic field dependency of the efficiency of SABRE polarisation transfer to  $^{19}\text{F}$ , and the efficiency of indirect polarisation transfer from  $^{19}\text{F}$  to  $^1\text{H}$  is shown to be the same across a PTF range of 1–8  $\mu\text{T}$ . The stacked spectra have been aligned along the frequency axis for illustrative purposes.

the hyperpolarised EFNMR spectrum across the sweep.

FIGURE 6.7 shows the SABRE-polarised EFNMR spectra of 3-DFMP acquired from a  $\mu\text{T}$  PTF-cycling experiment, where the  $\mu\text{T}$  SABRE-EFNMR experiment was repeated with 4 scans for each PTF value ranging from 1 to 8  $\mu\text{T}$ . SABRE polarisation transfer to  $^{19}\text{F}$  is seen to be most efficient at 5  $\mu\text{T}$  where the hyperpolarised 3-DFMP peaks in the  $^{19}\text{F}$  and  $^1\text{H}$  regions of the EFNMR spectrum have the largest signal intensity. The intensity of the hyperpolarised peaks are also shown to gradually decrease at PTFs above and below 5  $\mu\text{T}$ , in a similar way to the  $\mu\text{T}$  PTF curve of 3,5-DFP.

The first key point to note is that the intensity of all of the hyperpolarised peaks in both the  $^{19}\text{F}$  and  $^1\text{H}$  regions of the EFNMR spectra show the same trend in intensity as a function of PTF. This suggests that all peaks, including the peak at 2211 Hz, originate from the substrate and not from the solvent. This supports the hypothesis that the peak at 2212 Hz arises via indirect transfer of hyperpolarisation from the SABRE-polarised  $^{19}\text{F}$  nuclei to the aromatic  $^1\text{H}$  nuclei, in a manner similar to what was observed from 3,5-DFP. The negative phase of this peak relative to the  $^{19}\text{F}$  peaks is also consistent with this hypothesis and with the observations for 3,5-DFP. However, the phase of this peak does appear to deviate from pure emission, with the phase distortion becoming more prominent above 4  $\mu\text{T}$ . This cannot be attributed to a zero-order phase distortion due to drifting of the Earth's magnetic field and shifting of the Larmor frequencies (observed with the  $\mu\text{T}$  PTF-cycling experiment of 3,5-DFP) because the other peaks in the spectrum do not exhibit the same zero-order phase shifts. It could be attributed to a PTF dependency of hyperpolarisation of the antiphase component at 2211 Hz which is illustrated by the simulated signal. The hyperpolarised peak at 2224 Hz can be seen in FIGURE 6.7, particularly at PTFs of 5, 6 and 7  $\mu\text{T}$ , whereas the hyperpolarised peak at 2277 Hz can be seen at PTFs of 3,4 and 5  $\mu\text{T}$ . Both signals appear in-phase with the signal at 2168 Hz which is not illustrated by the simulation and would therefore indicate hyperpolarisation of product states other than  $\hat{I}_z$  on the  $^{19}\text{F}$  nuclei.

While changes to the form of the hyperpolarised EFNMR signals of 3-DFMP were observed across the sampled PTF range, there is insufficient SNR and signal resolution on the hyperpolarised EFNMR signals to understand the source of those changes. Furthermore, the dominant form of the SABRE polarised EFNMR spectrum was consistent across the sampled PTF range which suggests the prominent pathway of SABRE and indirect polarisation transfer was maintained.

## 6.4 Conclusions

Execution of SABRE in the  $\mu\text{T}$  regime via the  $\mu\text{T}$  SABRE-EFNMR experiment was shown to drive SABRE polarisation transfer from the  $\mathbf{I}_1 \cdot \mathbf{I}_2$  state of the  $p\text{-H}_2$  derived hydrides to the  $\hat{I}_z$  state of the  $^{19}\text{F}$  nuclei by comparison of experimental and simulated spectra (see FIGURE 6.3). The SABRE-polarised  $^{19}\text{F}$  EFNMR signal of 3,5-DFP was

acquired over a range of PTFs (-14- 14  $\mu\text{T}$ ) and exhibited a signal shape that better replicated the simulated  $^{19}\text{F}$  EFNMR signal acquired with  $\rho_0 = \sum_i \hat{I}_{zi}$  and  $\hat{I}_{obs} = \hat{I}_i^-$  for all nuclei in 3,5-DFP (see FIGURE 6.4), in comparison to the  $^{19}\text{F}$  EFNMR signal of 3,5-DFP which was hyperpolarised inefficiently and indirectly at 9 mT and exhibited only a fraction of the  $^{19}\text{F}$  EFNMR signal.

The  $\mu\text{T}$  SABRE-EFNMR experiment was also performed on 3-DFMP using a PTF of 5  $\mu\text{T}$  and gave rise to a SABRE-polarised EFNMR spectrum containing interesting signal shapes with in-phase and antiphase relationships (see FIGURE 6.6). The nuclei in 3-DFMP are very strongly coupled in the ULF regime due to the 55.4 Hz coupling between the methyl nuclei. This causes significant mixing of the nuclear spin states under  $\mu\text{T}$  fields and led to the acquisition of SABRE-polarised signals in the  $^1\text{H}$  and  $^{19}\text{F}$  region of the EFNMR spectrum that arise from hyperpolarisation of the  $\hat{I}_z$  state of the  $^{19}\text{F}$  nuclei. Comparison of the experimental EFNMR spectrum of 3-DFMP acquired from the  $\mu\text{T}$  SABRE-EFNMR experiment, with the simulated spectrum acquired using  $\rho_0 = \sum_i \hat{I}_{zi}$  for all  $^{19}\text{F}$  nuclei and  $\hat{I}_{obs} = \hat{I}_i^-$  for all nuclei provided some insight into the potential pathways of indirect polarisation transfer from the  $\hat{I}_z$  state of  $^{19}\text{F}$  to, for example, the  $\hat{I}_z$  state of the aromatic  $^1\text{H}$  nuclei. This was speculated based on the emission signal of 3-DFMP at  $\sim 2207$  Hz which does not appear in the simulation.

Successful implementation of the mT and  $\mu\text{T}$  PTF-cycling experiments by repetition of the mT and  $\mu\text{T}$  SABRE-EFNMR experiments with varying PTF values allowed the optimisation of SABRE polarisation transfer to  $^1\text{H}$  and  $^{19}\text{F}$ . Maximal transfer to  $^1\text{H}$  and  $^{19}\text{F}$  in 3,5-DFP and 3-DFMP was read out from the maximum of the acquired PTF curves. For 3,5-DFP, SABRE and indirect polarisation transfer was found to be optimal at 8- 10 mT and 6- 10  $\mu\text{T}$ . For 3-DFMP, SABRE and indirect polarisation transfer was found to be optimal at  $\sim 6$ ,mT and  $\sim 5$   $\mu\text{T}$ . The optimisation of mT and  $\mu\text{T}$  SABRE polarisation transfer to  $^1\text{H}$  and  $^{19}\text{F}$  in 3,5-DFP by Olaru et al.<sup>2</sup> via *ex situ* SABRE polarisation transfer provided an opportunity for comparison to the *in situ* approach performed in this work. The PTF curves could not be compared directly due to the differences between the experimental methods. However, the consequence of more accurate and precise field control provided by the EFNMR-SABRE setup, as well as higher reproducibility of the *in situ* SABRE results supported by the ability to immediately detect SABRE polarisation after the PTF, was illustrated by the *in situ* PTF curves which displayed less variability in the efficiency of SABRE polarisation transfer across the sampled PTF range. That being said, both approaches produced similar mT PTF curves of the  $^1\text{H}$  and  $^{19}\text{F}$  nuclei in 3,5-DFP. Lower reliability and precision of the *ex situ* instrumentation in generating  $\mu\text{T}$  PTFs led to significantly different and incomparable  $\mu\text{T}$  PTF curves.

In regards to the magnetic field dependency of the pathway of SABRE polarisation transfer, subtle changes to the form of the SABRE-polarised spectra were observed for 3,5-DFP and 3-DFMP across the  $\mu\text{T}$  PTF-cycling experiments, however much higher levels of hyperpolarisation of the substrates are required at mT and  $\mu\text{T}$  PTFs to understand and interrogate these. Achieving this will improve interrogation of SABRE polarisation transfer in order to further probe the mechanism and pathway of SABRE polarisation transfer to  $^1\text{H}$  and  $^{19}\text{F}$ .

# 7 | *sel*-SHARPER on a Benchtop NMR System

## 7.1 Introduction

The work presented in this chapter was undertaken during the first lockdown of the COVID-19 pandemic as part of a collaboration with the Uhrin group at the University of Edinburgh. Closure of the University of York from March-July 2020 meant that all lab work had to be carried out remotely, therefore, research toward probing of the SABRE polarisation transfer mechanism was suspended as it requires the flow of pressurised H<sub>2</sub> gas. Since the collaborative project involved the design of the SHARPER experiment on a benchtop NMR spectrometer using a water sample, it could be carried out remotely.

NMR Reaction monitoring relies on tracking the signal intensity of a reactant over the course of a chemical reaction for the calculation of reaction rates. This is well established on high-field NMR systems,<sup>125-127</sup> but also on benchtop NMR systems<sup>7,128,129</sup> as its compactness and low cost is appealing for reaction and process monitoring in industrial settings. Sensitive, Homogeneous, And Resolved PEaks in Real time<sup>3</sup> (SHARPER) is a pure-shift NMR technique<sup>130-132</sup> that is complementary to NMR reaction monitoring. Like all pure-shift techniques, SHARPER removes homonuclear and heteronuclear scalar-couplings to collapse multiplets into singlets, but requires only one scan, although a second scan helps to improve spectral quality with the removal of artefacts. Since reaction monitoring depends on the process of reactant signal integration, peak splitting can be disruptive, and the structural information provided by multiplets is often not required. Also, the lack of *J*-coupling information in the spectrum reduces signal overlap and increases SNR because the signal intensity is not distributed between split peaks. This enhances the sensitivity of NMR and enables the use of smaller sample volumes. The faster experiment time of SHARPER enables the monitoring of faster chemical reactions. SHARPER is especially advantageous for the monitoring of signals in <sup>1</sup>H spectra that exhibit high signal density due to narrow chemical shift dispersion and extensive proton-proton coupling. Chemical reactions that involve gas sparging are generally disruptive to NMR acquisition and hence reaction monitoring because the magnetic susceptibility difference between spins in the sample at the gas-liquid interface creates inhomogeneities in the local magnetic field, however, SHARPER is also able to eliminate the effects of magnetic field inhomogeneity for the acquisition of extremely narrow singlets.

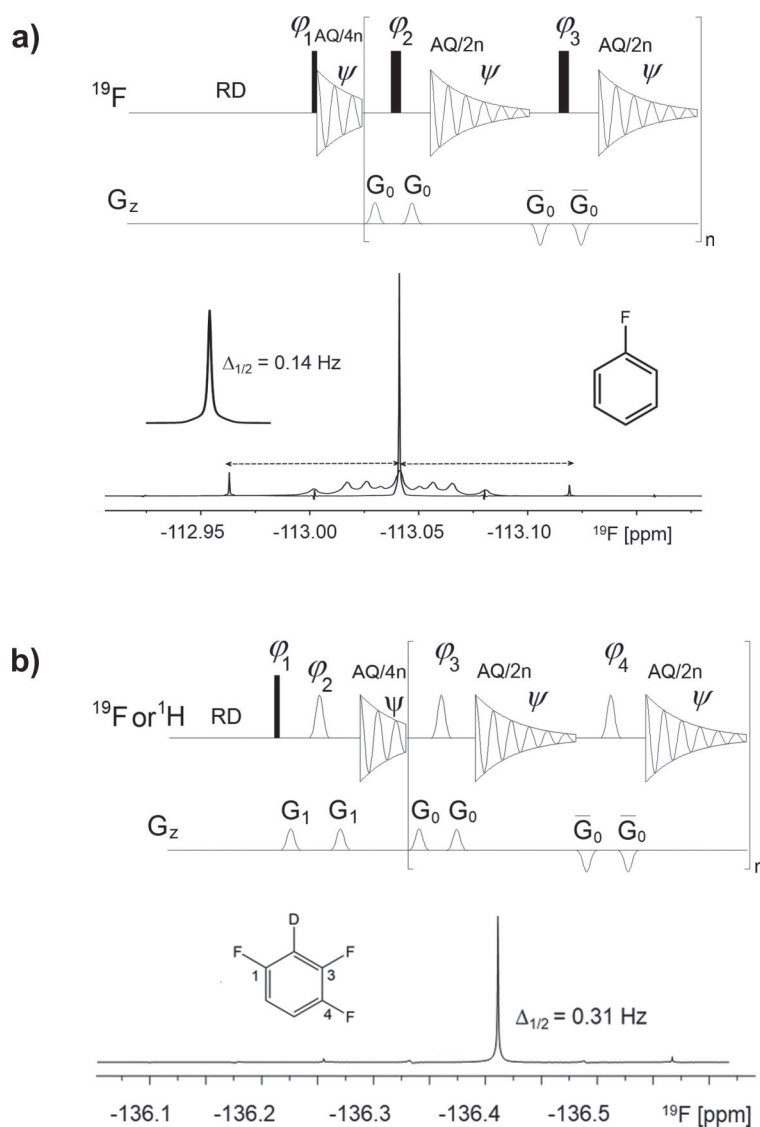


FIGURE 7.1: Pulse sequence for the a) SHARPER and b) *sel*-SHARPER experiment with the corresponding  $^{19}\text{F}$  SHARPER spectra of fluorobenzene and 2-deutero-1,3,4-trifluorophenyl displaying linewidths of 0.14 and 0.31 Hz, respectively. Solid rectangles represent hard  $\pi/2$  pulses and unfilled Gaussian shapes represent soft  $\pi$  pulses. Sine-shaped pulsed field gradients were applied at  $G_0 = 1\%$  for the SHARPER and *sel*-SHARPER experiments. The phase cycle:  $\phi_1 = 2x, 2(-x), 2y, 2(-y)$ ;  $\phi_2 = 2(y,-y), 2(x,-x)$ ;  $\phi_3 = 2(-y,y), 2(-x,x)$ ; and  $\Psi = 2x, 2(-x), 2y, 2(-y)$  was used for the SHARPER experiment. The phase cycle:  $\phi_1 = 4x, 4(-x), 4y, 4(-y)$ ;  $\phi_2 = 2y, 2x, 2(-y), 4(-x), 2y, 2x, 2(-y)$ ;  $\phi_3 = 4(y,-y), 4(x,-x)$ ;  $\phi_4 = 4(-y,y), 4(-x,x)$ ; and  $\Psi = 2x, 4(-x), 2x, 2y, 4(-y), 2y$  was used for the *sel*-SHARPER experiment.  $G_1$  was applied at 30%. Figures a) and b) have been reproduced with permission from the literature<sup>3</sup> (<https://pubs.acs.org/doi/10.1021/acs.analchem.7b02437>). Further permissions related to the material excerpted should be directed to the American Chemical Society.

The implementation of SHARPER and selective-SHARPER (*sel*-SHARPER) was reported in 2017<sup>3</sup> on a 400 MHz Bruker NMR spectrometer, and was shown to successfully collapse the multiplets of fluorinated heterocycles to singlets with sub-hertz linewidths (see FIGURE 7.1). Both experiments begin with the use of a  $\pi/2$  pulse to place the spins along the transverse plane, followed by a chain of  $\pi$  (refocusing) pulses. Acquisition of the FID occurs in short chunks after each refocusing pulse, and post-processing is required to stitch the chunked FIDs together.

The constant refocusing of chemical shift evolution and the short acquisition of the FID chunk leads to a final FID that is void of  $J$ -coupling evolution and the effects of magnetic field inhomogeneities. This allows for the collapse of heteronuclear couplings in SHARPER and *sel*-SHARPER without the need for an X-channel. The collapse of homonuclear couplings is achieved with the selective  $\pi$  pulses in *sel*-SHARPER. The SHARPER and *sel*-SHARPER experiments also make possible the acquisition of sub-hertz linewidths without prior shimming of the NMR probe.

In contrast to the SHARPER experiment, which utilises hard pulses to achieve heteronuclear decoupling of all of the signals in the spectrum, the *sel*-SHARPER experiment offers the ability to achieve both heteronuclear and homonuclear decoupling of signals in a band-selective region of the spectrum. This is achieved when a Pulsed Field Gradient (PFG),  $G_0$  and  $G_1$ , is placed either side of the soft  $\pi$  pulses (see FIGURE 7.1) to ensure the transverse magnetisation of only the active spins is refocused, whilst causing a loss in coherence of the passive spins.

As is typical of real time pure-shift NMR experiments,<sup>133</sup> the first FID chunk is half as long as the subsequent ones. The reason for this can be explained by considering the evolution of the  $J$ -coupling during the SHARPER and *sel*-SHARPER pulse sequence. The  $J$ -coupling is refocused at the centre of the echo FIDs that are generated after each  $\pi$  pulse. By acquiring the FID for a short time before and after the  $J$ -coupling is refocused means the duration of the FID chunk can be doubled without increasing  $J$ -evolution, since the amount of  $J$ -evolution either side of the point of refocusing is the same. This cannot be done with the first FID chunk in the SHARPER experiment, which comes immediately after a  $\pi/2$  pulse, because the FID is not an echo and it begins from a point of refocused  $J$ -coupling. Increasing the duration of the FID chunk is beneficial as it means more data points are acquired per chunk which helps to reduce experimental times whilst maintaining the collapse of multiplets.

The work presented in this chapter describes the design of Gaussian RF pulses on a (1 T) Magritek Spinsolve Carbon benchtop NMR spectrometer to perform *sel*-SHARPER on a low-field NMR system. This is motivated by the push toward NMR reaction monitoring in more compact and cost-effective NMR systems. Performing SHARPER on a benchtop NMR spectrometer improves its accessibility and broadens its range of applications in research and industry. The inherent challenges associated with reaction monitoring using low-field NMR systems (1-2 T), such as the drop in sensitivity and the reduction of chemical shift resolution, is overcome by *sel*-SHARPER as it enables the acquisition of extremely narrow linewidths with significantly increased SNRs. The *sel*-SHARPER pulse sequence used in high-field NMR (see FIGURE 7.1) was simplified for use on the Spinsolve spectrometer to remove the need for gradient coils, which are not available on many benchtop NMR spectrometers.

Reaction monitoring of organofluorine compounds plays a major role in the production of pharmaceuticals<sup>134</sup> and agrochemicals,<sup>135</sup> and motivated the design of SHARPER by Jones et al.<sup>3</sup> (2017) who first demonstrated its execution on the  $^{19}\text{F}$  signals of fluorinated heterocycles. This collaborative project follows the same motivation, outlining the performance of *sel*-SHARPER on the Spinsolve benchtop

NMR spectrometer when tested on the  $^{19}\text{F}$  signals of three fluoropyridines: 3-FP, 3,5-DFP and 3,5-TFMP. The application to fluoropyridines was motivated by their suitability for SABRE hyperpolarisation, as explored in Chapters 5 and 6, and therefore would provide an opportunity to explore the combined sensitivity enhancement effects of SABRE and SHARPER for the first time.

The Larmor frequency of  $^1\text{H}$  and  $^{19}\text{F}$  nuclei at low field is close enough that a single RF channel is used by the Spinsolve spectrometer to interact with both; however, the coil is tuned to the  $^1\text{H}$  Larmor frequency, which leads to a less efficient interaction between the RF pulse and the  $^{19}\text{F}$  nuclei. Nonetheless,  $^{19}\text{F}$  NMR provides broader chemical shift dispersion of signals to facilitate the development and implementation of selective excitation.

The first section of this chapter focuses on the methodology that was devised to allow creation and calibration of Gaussian  $\pi$  pulses on the Spinsolve benchtop NMR spectrometer, required for the selective refocusing of spins in the *sel*-SHARPER experiment. The development of the Gaussian pulse was carried out on the  $^1\text{H}$  signal of water, but its implementation within the *sel*-SHARPER experiment was extended to  $^{19}\text{F}$  NMR. The excitation profile of the Gaussian pulse was then acquired to visualise and verify the accuracy of its synthesis by the Spinsolve spectrometer. After the Gaussian  $\pi$  pulse was implemented in a selective spin-echo experiment to show the selective excitation of the active  $^{19}\text{F}$  spins in a sample, the acquisition of  $^{19}\text{F}$  *sel*-SHARPER spectra was carried out and is discussed in the last section of the chapter, where sub-Hertz  $^{19}\text{F}$  singlets of 3-FP, 3,5-DFP and 3,5-TFMP were acquired.

## 7.2 Selective Pulse Design

### 7.2.1 Gaussian RF Pulse

RF pulses can be used to manipulate the orientation of the magnetic spins ( $I > 0$ ) in an NMR sample through the interaction of the oscillating and finite RF pulse with the magnetic moments of the spins. This interaction leads to nutation of the net nuclear magnetization. Just as the spins precess around the static field,  $B^0$ , of an NMR spectrometer orientated along the longitudinal plane, the net magnetization also precess around the magnetic field of the RF pulse,  $B^1$ , which lies along the transverse plane due to the positioning of the RF coil in the probe. Nutation of the magnetization is most efficient when the precession frequency of the spins,  $\omega^0$ , is on resonance with the frequency of the RF field,  $B^1$ . The difference in these two frequencies is generally referred to as the offset frequency.

All forms of electromagnetic radiation obey the time-energy uncertainty relation (Eq. 7.1), where  $\Delta T$  and  $\Delta E$  are the uncertainties in time and energy, respectively, and  $\hbar$  is the reduced Planck's constant. In terms of NMR,  $\Delta E$  is better interpreted as the energy bandwidth of the RF pulse, whilst  $\Delta T$  is better interpreted as the duration

of the RF pulse,  $t_{RF}$ . According to the time-energy uncertainty relation the two are inversely proportional. Therefore, short RF pulses have wider energy bandwidths than long RF pulses and so are less frequency selective. Generally speaking, the energy bandwidth of a pulse can be estimated from the inverse of its duration, for example, a 1000  $\mu\text{s}$  RF pulse will have an energy (excitation) bandwidth of  $\sim 1000$  Hz ( $1/1000 \times 10^{-6}$  s). In a 400 MHz NMR spectrometer this corresponds to a selectivity of 2.5 ppm.

$$\Delta T \Delta E \geq \frac{\hbar}{2} \quad (7.1)$$

As well as duration, the shape of the RF pulse, dictated by the RF amplitude as a function of time, is an important factor to be considered when accomplishing the selective excitation of spins. Long RF pulses are generally shaped (non-rectangular) and are referred to as selective or ‘soft’. The more common short RF pulses are rectangular and are referred to as non-selective or ‘hard’. A hard pulse is instantaneously turned on with a fixed amplitude until it is instantaneously turned off after  $t_{RF}$ , thus depicted as a rectangular pulse in the time domain, although practically there is a finite rise and decay time for any switched pulse so it will not resemble a perfect rectangle. Shaped pulses are not switched on and off instantaneously and instead have a range of amplitude values along the time axis. The Fourier transform of the pulse shape in the time domain produces the pulse shape in the frequency domain and is a visualisation of the pulse excitation profile.

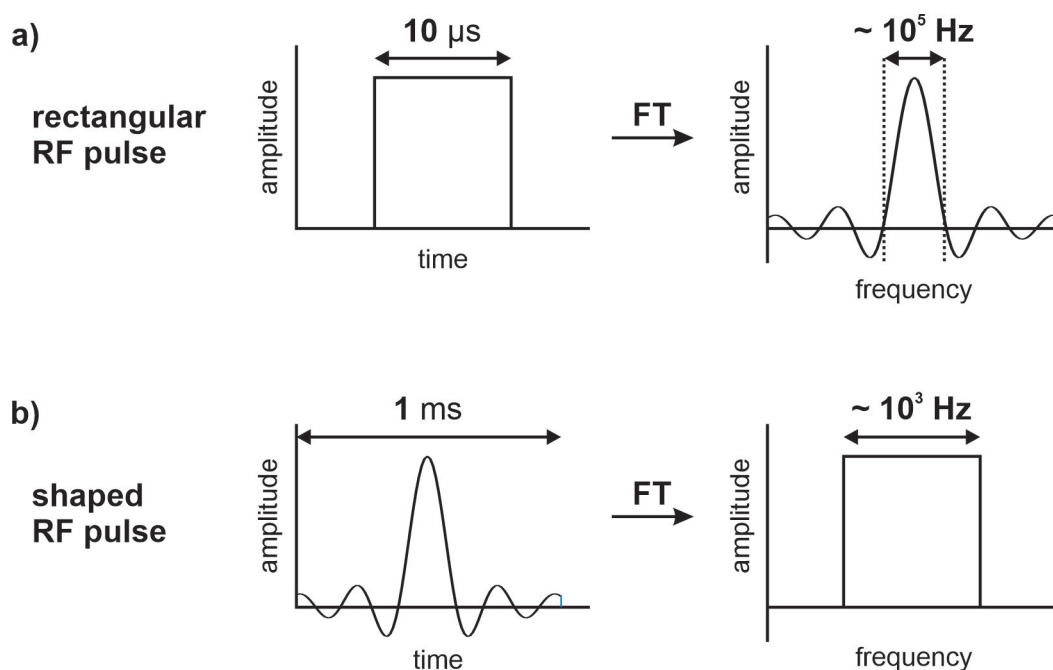


FIGURE 7.2: Schematic illustrating the difference between the excitation profile shapes (right) of a) rectangular and b) shaped RF pulses, generated from the Fourier transform of the pulse shapes (left). The difference in the excitation bandwidth of rectangular ( $10^5$  Hz) and shaped pulses ( $10^3$  Hz) were calculated from typical  $t_{RF}$  values of  $10 \mu\text{s}$  and  $1$  ms, respectively. The sinc pulse shape is used here as the example of a shaped RF pulse.

The Fourier transform of a hard pulse with a very short duration generates a sinc function with a very broad frequency range. As depicted in FIGURE 7.2, a  $10\ \mu\text{s}$  rectangular pulse produces a sinc function with a central peak around  $10^5\ \text{Hz}$  wide. A  $^1\text{H}$  NMR spectrum is typically  $10^3 - 10^4\ \text{Hz}$  wide and would therefore lie within the tip of the sinc function's central peak. This means all peaks within the  $^1\text{H}$  spectrum effectively experience the same RF amplitude and undergo the same amount of nutation. For this reason, hard pulses are considered to be non-selective.

Increasing the duration of a hard rectangular pulse to achieve the required excitation bandwidth is simple but not always practical. A  $1000\ \mu\text{s}$  rectangular pulse will have a sinc excitation profile with a central peak of approximately  $1\ \text{kHz}$  wide. The NMR spectrum ( $10^3 - 10^4\ \text{Hz}$ ) spans across more of the sinc profile in this case as it is much narrower. Since selective pulses are fundamentally designed to place the selected (active) spins within their excitation bandwidth, whilst placing the non-selected spins (passive) outside of the excitation bandwidth, long rectangular pulses can be problematic for selective excitation. This is because there is little control over the shape of the sinc profile to ensure the passive spins lie on the nodes of the pulse, and the spins may instead experience a range of positive and negative RF amplitudes depending on their offset frequency relative to the RF pulse. Non-rectangular pulses with specialised shapes can be used to solve these issues. One such example is the sinc pulse illustrated in FIGURE 7.2. As it corresponds to a rectangular excitation profile there is a well outlined excitation bandwidth which can be set to the desired range by changing the pulse length. It is important to note that the RF amplifiers and spectrometers, even on expensive high-field NMR systems, are not accurate enough to generate a sinc pulse that produces a perfectly rectangular excitation profile; sinc-like oscillations are always present at the edges of the pulse in practice.

The Gaussian RF pulse<sup>136</sup> was chosen to perform the selective refocusing of spins in *sel*-SHARPER on the Spinsolve Carbon benchtop NMR system due to its simple shape (see FIGURE 7.3). The Gaussian pulse is the easiest selective pulse to synthesise and was seen as a good starting point for pulse shape design on the benchtop NMR spectrometer. Also, the Gaussian pulse produces a Gaussian excitation profile after Fourier transformation, which is an easy shape to design and visualise, thus simplifying

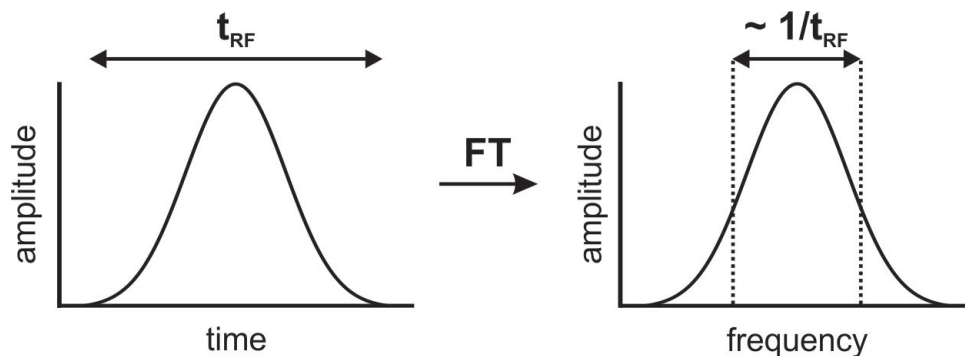


FIGURE 7.3: Gaussian pulse shapes are very simple and easy to synthesise on low-field NMR systems that are less sophisticated than high-field NMR systems. The Gaussian pulse produces a Gaussian excitation profile in which active and passive spins experience only positive RF amplitude values at a frequency range calculated from the inverse of the pulse duration,  $t_{RF}$ .

its optimisation in order to achieve the desired selective excitation. For these reasons, Gaussian pulses are widely used in standard high-field NMR.<sup>137–139</sup>

## 7.2.2 Synthesis of Gaussian RF Pulse

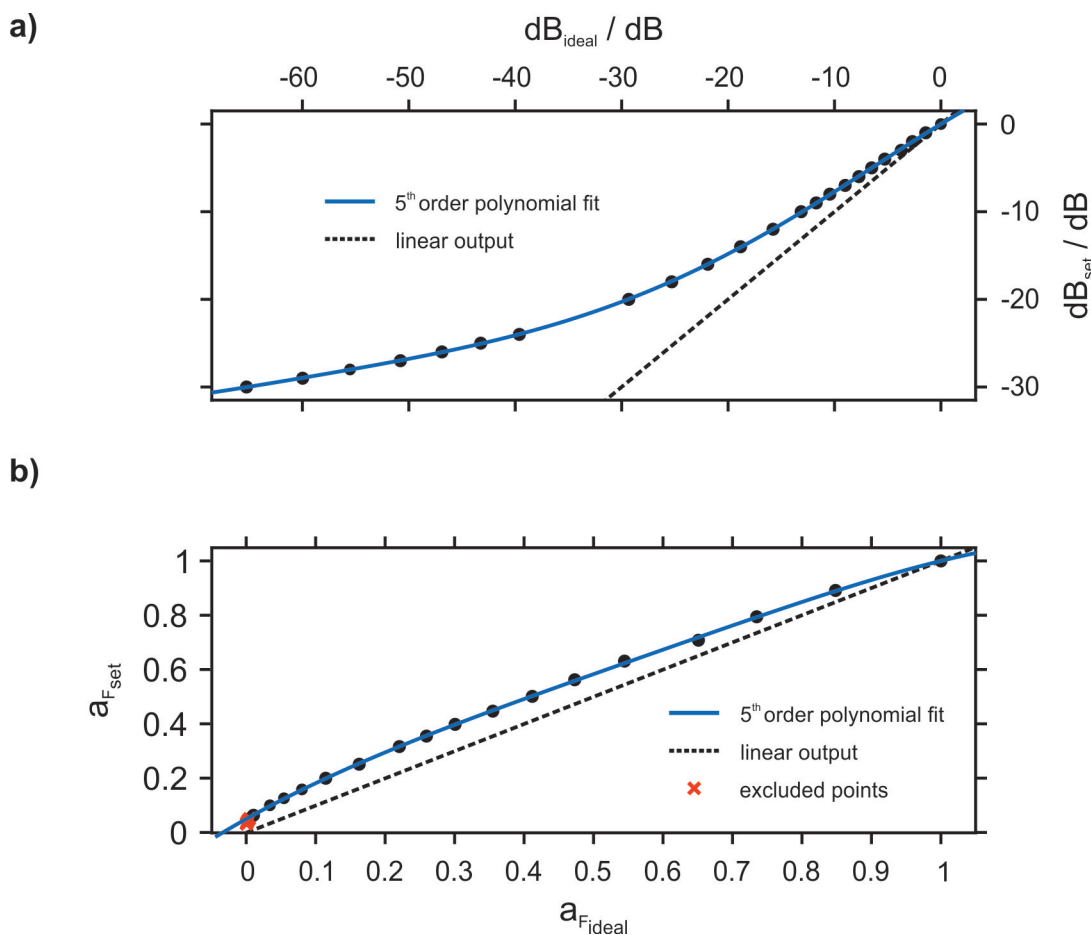


FIGURE 7.4: Calibration curve showing the non-linear power output of the RF amplifier on the Spinsolve spectrometer in the a) dB scale and b) linear scale. Both sets of data were fit to a 5th order polynomial to calculate the amplitude value to be set on the spectrometer,  $\text{dB}_{\text{set}}$  or  $a_{F\text{set}}$ , for execution of the desired pulse amplitude,  $\text{dB}_{\text{ideal}}$  or  $a_{F\text{ideal}}$ . The lowest 5 data points in b) were excluded from the fit because  $A_{RF}$  cannot be accurately defined below a linear attenuation of 0.01. The equation and corresponding polynomial coefficients of the fit to the data in plot a) can be found in Eq. 7.3 and Table 7.1, and in plot b) can be found in Eq. 7.7 and Table 7.2, respectively.

The Spinsolve benchtop NMR spectrometer defines the amplitude of the RF pulse,  $A_{RF}$ , in decibels (dB), a unit based on a logarithmic scale of power ratio rather than a standard linear scale (e.g. Volts, Amps, etc.). A dB describes power amplification ( $\text{dB} > 0$ ) or attenuation ( $\text{dB} < 0$ ) relative to a reference power value (see Eq. 7.2a). An  $A_{RF}$  of 0 dB is the maximum power output of the RF amplifier on the Spinsolve spectrometer, and represents the reference power value. This means that the RF pulse power can only be attenuated and is never amplified ( $P_{\text{out}}/P_{\text{ref}} \leq 1$ ). It can be more

convenient in NMR to express dB as a ratio of nutation frequencies,  $\omega_1$ , instead of a power ratio, since  $\omega_1$  is directly related to the pulse amplitude and power is not (see Eq. 7.2b).

$$dB = 10 \log_{10} \left( \frac{P_{out}}{P_{ref}} \right) \quad (7.2a)$$

$$\text{since } P \propto \omega_1^2, \quad \text{where } \omega_1 \propto \frac{1}{t_{RF}},$$

$$dB = 20 \log_{10} \left( \frac{\omega_1^{out}}{\omega_1^{ref}} \right) = 20 \log_{10} \left( \frac{t_{\pi/2}^{ref}}{t_{\pi/2}^{exp}} \right) \quad (7.2b)$$

The RF amplifier of the early-version Magritek Spinsolve 43 Carbon is known to have a non-linear power output that leads to discrepancies between the  $A_{RF}$  value set on the pulse program macro, and the  $A_{RF}$  value that is outputted by the RF amplifier.<sup>140</sup> The non-linear response of the RF amplifier had to be corrected to ensure an accurate formation of the selective pulses whose shape is defined by  $A_{RF}$  values. The presence of distortions in the shape of the selective pulse would distort its excitation profile and the desired selectivity would not be achieved.

Using a water sample, RF duration-sweep nutation curves with hard pulses were acquired for a range of user-defined  $A_{RF}$  values, denoted  $dB_{set}$ , using the built in '1PulseDurationSweep-H' experiment. The RF pulse duration that corresponds to a  $\pi/2$  rad nutation of the spins,  $t_{\pi/2}$ , was calculated for each  $dB_{set}$  value and is quoted as  $t_{\pi/2}^{exp}$ . These values were put through Eq. 7.2b which describes dB in terms of a  $t_{\pi/2}$  ratio ( $t_{\pi/2}^{ref} = t_{\pi/2}$  at 0 dB) instead of a power ratio. The output of the equation is the experimental  $A_{RF}$  experienced by the spins in the sample during the RF duration-sweep experiment, denoted  $dB_{ideal}$ . The non-linear behaviour of the RF amplifier was observed when  $dB_{set}$  was plotted against  $dB_{ideal}$  in FIGURE 7.4a. A 5<sup>th</sup> order polynomial represented by Eq. 7.3 was required to fit the data. The polynomial coefficients are tabulated in Table 7.1.

$$y = P_5 x^5 + P_4 x^4 + P_3 x^3 + P_2 x^2 + P_1 x \quad (7.3)$$

The curve deviated significantly from linearity which is represented by the dashed black line. Although the fit is non-linear, it allows conversion from the  $dB_{ideal}$  value to the  $dB_{set}$  value. In other words, the polynomial provides the  $A_{RF}$  value that should be set on the pulse program macro in order for the RF amplifier to output the desired  $A_{RF}$  value, thus correcting for the non-linear behaviour.

Table 7.1: Table of coefficients of the 5<sup>th</sup> order polynomial that is fit to the calibration curve of the RF amplifier defined along a logarithmic (dB) attenuation scale.

Polynomial Coefficient	Value
P <sub>1</sub>	0.7365
P <sub>2</sub>	-8.224 × 10 <sup>-3</sup>
P <sub>3</sub>	-5.414 × 10 <sup>-4</sup>
P <sub>4</sub>	-7.771 × 10 <sup>-6</sup>
P <sub>5</sub>	-3.679 × 10 <sup>-8</sup>

$$G = b^{(4x^2)} \quad \text{between } -0.5 \leq x \leq 0.5 \quad (7.4)$$

The shape of the Gaussian pulse is outlined by tabulated  $A_{RF}$  values in the pulse program macro of the SpinsolveExpert software (version 1.30) that operates the Spinsolve spectrometer. These values are outputted one at a time by the RF amplifier over the duration of the pulse. The table of  $A_{RF}$  values were generated in this work using Eq. 7.4 which produces a Gaussian curve with a maximum amplitude of  $G = 1$  at  $x = 0$ , and a cut-off amplitude at  $x = \pm 0.5$  determined by the parameter  $b$ , which is quoted as a percentage of the maximum amplitude and controls the width of the curve. It is important to note that the size of the table of  $A_{RF}$  ( $G$ ) values is dictated by the number of  $x$  values used to describe the Gaussian pulse (see Eq. 7.4), where more  $x$  values leads to a more accurate representation of the Gaussian shape. The duration of the RF pulse is also controlled by the number of  $x$  values since the RF amplifier takes a minimum of 10  $\mu\text{s}$  to step through each tabulated  $A_{RF}$  value. Therefore, a Gaussian defined by 100  $x$  values has a duration of 1000  $\mu\text{s}$  ( $100 \times 10 \mu\text{s}$ ).

$$\begin{aligned} dB &= 20 \log_{10} \left( \frac{\omega_1^{out}}{\omega_1^{ref}} \right) \\ \Rightarrow a_{F_{set}} &= 10^{\left(\frac{dB}{20}\right)} \quad \text{where } a_F = \left( \frac{\omega_1^{out}}{\omega_1^{ref}} \right) \end{aligned} \quad (7.5)$$

In order for the RF amplifier to output the Gaussian pulse, the  $A_{RF}$  values must be represented as 14-bit numbers. A value of 0 corresponds to the highest possible attenuation of the RF pulse, and a value of  $2^{14}-1$  (16383) corresponds to an unattenuated RF pulse (0 dB). Representation of the Gaussian amplitude values as 14-bit numbers was achieved within the pulse program macro in 3 steps. The first step required converting the RF attenuation, which is defined by the user in dB ( $\text{dB}_{set}$ ), into a linear attenuation factor,  $a_{F_{set}}$ . This was calculated using Eq. 7.5, which describes attenuation as a ratio of  $\omega_1$ . The  $A_{RF}$  values defining the Gaussian shape,  $G$ , are then multiplied by  $a_{F_{set}}$  to attenuate each of them by the desired amount (see Eq. 7.6), producing a Gaussian curve with a maximum of  $G_{att} = a_{F_{set}}$  at  $x = 0$ . For example, a  $\text{dB}_{set}$  of -6 dB is equivalent to an  $a_{F_{set}}$  of 0.5, and corresponds to the output of an RF pulse with  $A_{RF}$  values that are half that of the reference pulse at 0 dB.

$$G_{att} = a_{F_{set}} G \quad (7.6)$$

The second step required the correction of the calculated  $G_{att}$  values to overcome the non-linear output of the RF amplifier. The correction curve in FIGURE 7.4a was used to correct the  $A_{RF}$  values in dB, but cannot be used to correct the  $G_{att}$  values which are defined along a linear scale. Instead, Eq. 7.5 was used to convert the dB attenuation values into linear attenuation factors to produce the correction curve in FIGURE 7.4b which plots set attenuation,  $a_{F_{set}}$ , against ideal attenuation,  $a_{F_{ideal}}$ . A 5<sup>th</sup> order polynomial was fit to this data and is shown in Eq. 7.3, where the values of the polynomial coefficients are tabulated in Table 7.1. The corrected  $A_{RF}$  values,  $G_{corr}$ , were acquired by passing the attenuated  $A_{RF}$  values,  $G_{att}$ , through the polynomial. The fit is designed to fix the polynomial to coordinates (1,1), where  $G_{corr} = 1$  when  $G_{att} = 1$ . This is done to ensure the unattenuated reference RF pulse of 0 dB exhibits a linear power output.

$$G_{corr} = p_5(G_{att}-1)^5 + p_4(G_{att}-1)^4 + p_3(G_{att}-1)^3 + p_2(G_{att}-1)^2 + p_1(G_{att}-1) + 1 \quad (7.7)$$

Table 7.2: Table of coefficients of the 5<sup>th</sup> order polynomial that is fit to the calibration curve of the RF amplifier defined along a linear attenuation scale.

Polynomial Coefficient	Value
p <sub>1</sub>	0.6281
p <sub>2</sub>	-0.8736
p <sub>3</sub>	-1.329
p <sub>4</sub>	-0.8460
p <sub>5</sub>	-0.0677

The Gaussian curve and its corrected version is illustrated in FIGURE 7.5 for  $\text{dB}_{set}$  values of 0 and -12 dB. All Gaussian curves were generated with 1000 points in the  $-0.5 \leq x \leq 0.5$  range, and with a cut-off amplitude of  $b = 0.01$ . The linear polynomial correction is seen to have a larger effect on the shape of the Gaussian at lower amplitudes as this is the region of the correction curve where the RF amplifier significantly deviated from linearity (see FIGURE 7.4).

The third and final step takes the corrected  $A_{RF}$  values,  $G_{corr}$ , and multiplies them by 16383 ( $2^{14}-1$ ) to represent them as 14-bit numbers that the spectrometer can interpret and use to produce the desired Gaussian RF pulse.

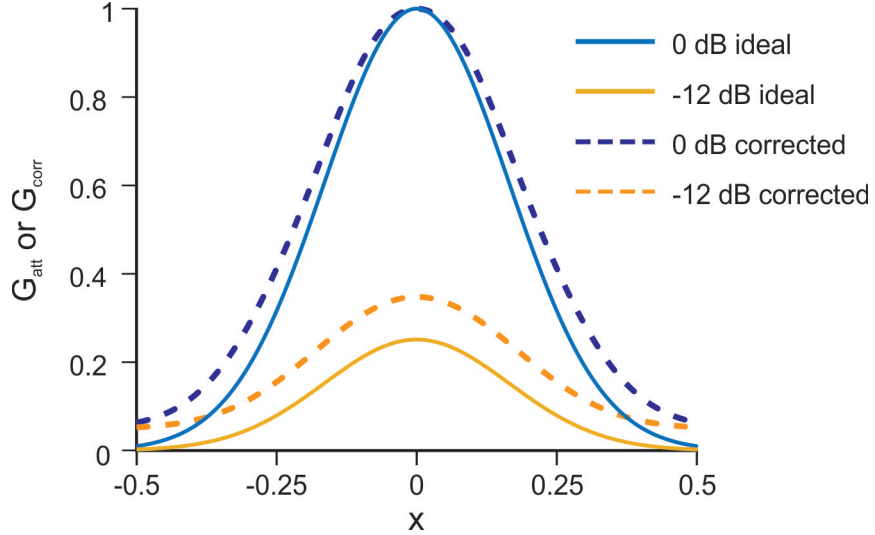


FIGURE 7.5: A plot of Gaussian curves with  $\text{dB}_{\text{set}} = 0$  and  $-12$  dB plotted with Eq. 7.4 using 1000 amplitude values and a cut-off amplitude of  $b = 0.01$ . The curves represented by solid and dashed lines depict the ideal and corrected versions of the Gaussian, respectively, where the corrected versions involve passing the  $G_a$  values through the 5<sup>th</sup> order polynomial fit in Eq. 7.3 from the linear correction curve in FIGURE 7.4b.

### 7.2.3 Calibration of Gaussian Refocusing Pulse

The *sel*-SHARPER pulse sequence requires the use of selective  $\pi$  pulses, which means that the Gaussian pulse must be calibrated for a  $\pi$  rad nutation of the spins. The duration,  $t_{RF}$ , and amplitude,  $A_{RF}$ , of the Gaussian affects the nutation angle of the spins when they interact with the RF pulse (see section 3.3.3), however,  $t_{RF}$  is chosen based on the required excitation bandwidth (selectivity) of the RF pulse so only  $A_{RF}$  needs to be considered and calibrated. Whereas nutation curves acquired from RF amplitude or RF duration sweep experiments are typically used to calibrate hard RF pulses, the Gaussian  $\pi$  pulse was calibrated by a combination of the RF amplitude sweep experiment with the Single Pulsed Field Gradient Spin Echo (SPFGSE) experiment, illustrated in FIGURE 7.6.

The SPFGSE experiment is similar to a spin echo as the pulse sequence follows the spin echo experiment (90-delay-180-delay), but the rectangular  $\pi$  pulse is replaced with a selective  $\pi$  pulse that is bracketed by two homospoil gradient pulses of equal gradient strength and phase. The first gradient pulse causes a loss in the coherence of the spins along the transverse plane, produced by the initial  $\pi/2$  pulse, and in turn destroys transverse magnetisation. The selective refocusing pulse inverts the magnetic moment of the active spins, and the second field gradient reverts the effect of the first field gradient, thus refocusing the transverse magnetisation but only for the spins that experienced the selective  $\pi$  pulse. The passive spins that did not experience the  $\pi$  pulse are therefore not refocused and are not detected. As is the case for all spin echo experiments, the delay,  $t_{\text{echo}}$ , before and after the refocusing pulse must be exactly the same to achieve maximal refocusing of the transverse magnetisation, which occurs after a time  $t_{\text{echo}}$  from the moment the  $\pi$  pulse is applied (see FIGURE 7.6). Refocusing of the transverse magnetisation is most effective when the spins undergo a full  $\pi$  rad

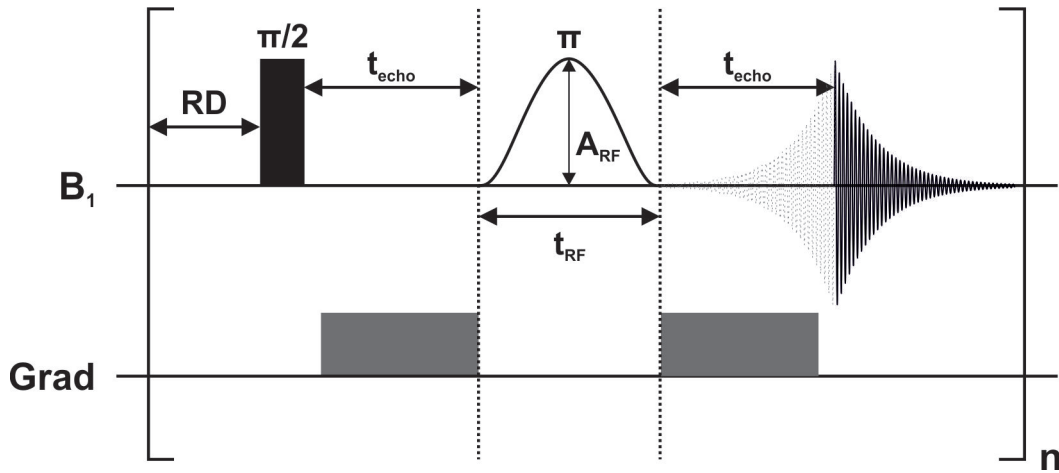


FIGURE 7.6: Pulse sequence for the SPFGSE experiment, where the filled rectangle represents a hard  $\pi/2$  RF pulse and the unfilled Gaussian shape represents a selective  $\pi$  RF pulse. Repeating this experiment with a range of amplitude values allows calibration of the selective  $\pi$  pulse for a given  $t_{RF}$ .

nutations, therefore, the SPFGSE experiment can be repeated with varying  $A_{RF}$  values to produce a curve of signal intensity against  $A_{RF}$ , whereby the value that gives rise to the strongest signal corresponds to a  $\pi$  rad nutation of the spins with the Gaussian pulse,  $\text{dB}_\pi$ .

The SPFGSE amplitude sweep experiment was performed on a water sample with 0.5 dB  $A_{RF}$  steps for the calibration of 2, 3 and 4 ms  $\pi$  Gaussian pulses (see FIGURE 7.7). The calibration curve shows a maximum signal intensity at -33, -38.5 and -46 dB, respectively, and equals the  $\text{dB}_\pi$  value for each pulse. The data shows that longer RF pulses require lower amplitudes, or larger attenuation, to achieve the same nutation angle which is expected since  $A_{RF}$  and  $t_{RF}$  are inversely proportional.

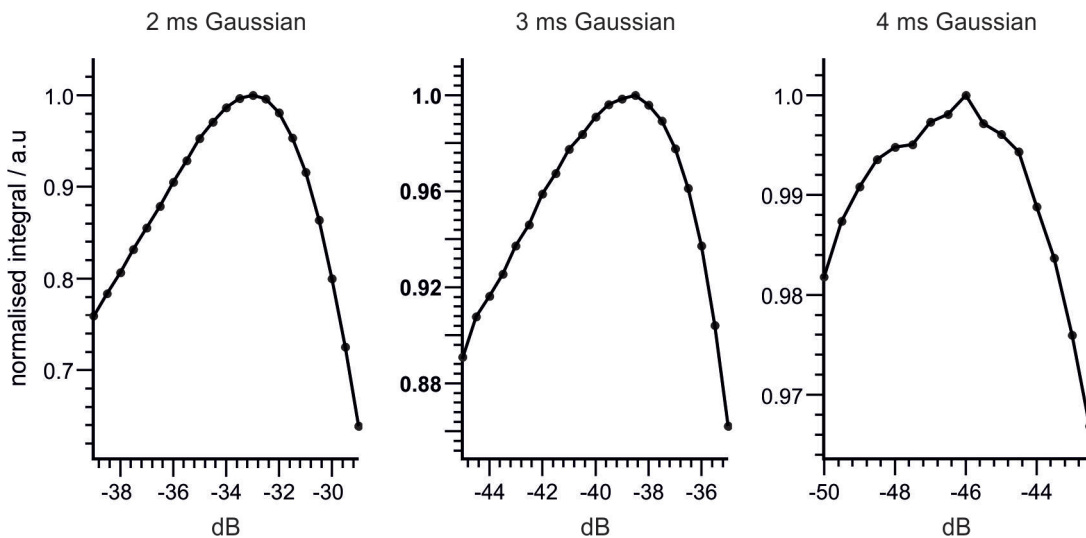


FIGURE 7.7: Results from the SPFGSE amplitude sweep experiment showing that -33, -38.5 and -46 dB are required to achieve  $\pi$  rad nutations for 2, 3 and 4 ms Gaussian RF pulses, respectively.

With calibrated  $\pi$  pulses the excitation profile and selectivity of the Gaussian can be visualised to confirm that the shape generated by the RF amplifier resembles a Gaussian. This was done by performing the SPFGSE experiment with an RF (offset) sweep, where the offset frequency of the RF pulse relative to the signal of interest is linearly varied along positive and negative frequencies. The intensity of the signal at each iteration of the RF offset is integrated and plotted to produce the excitation profile. Since the pulse amplitude that a spin experiences depends on its Larmor frequency, and only the spins on-resonance to the shaped pulse experience the  $\text{dB}_\pi$  RF amplitude, shifting the RF offset frequency varies the nutation angle of the spins. For a Gaussian pulse, the further away from the centre of the Gaussian that the signal is, the lower the RF amplitude and the lower the nutation angle. As the signal intensity is dependant on the successful inversion of the active spins which is dependent on the RF amplitude experienced by the spins, the plot of signal integral with respect to the RF offset provides an outline of the excitation profile of the Gaussian pulse with a maximum integral at an offset of 0 ppm that decays as the offset increases in the positive and negative directions.

The Spinsolve spectrometer cannot set different offset frequencies for different pulses within the same RF sequence, however, this was not a problem for the SPFGSE experiment because the only other pulse is the rectangular  $\pi/2$  pulse which has a

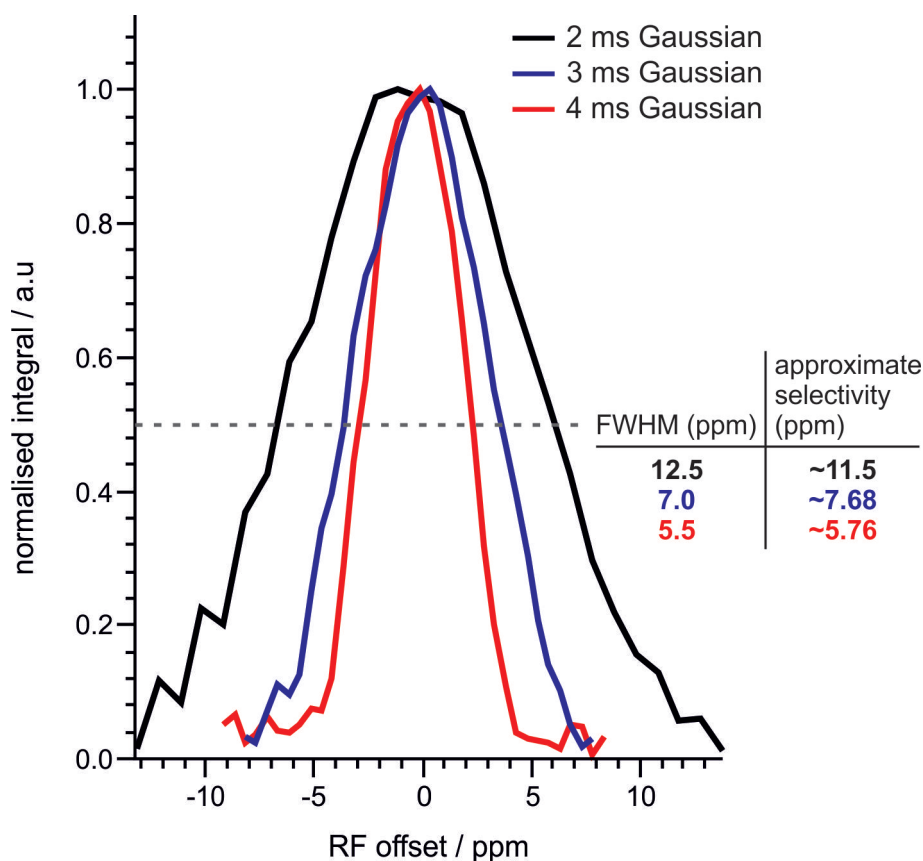


FIGURE 7.8: Excitation profile of the 2, 3 and 4 ms Gaussian pulses showing that the Gaussian excitation profiles become narrower as  $t_{RF}$  increases which is in agreement with the time-energy uncertainty relation. The excitation bandwidths (selectivity) of the Gaussian pulses are approximated from the FWHM of the Gaussian excitation profiles and are very close to the theoretical values calculated from the reciprocal of  $t_{RF}$ .

broad excitation bandwidth of tens of ppm. Hard pulses with offsets less than 10 ppm will have a negligible effect on the spin nutations.

FIGURE 7.8 shows the excitation profile of the 2, 3 and 4 ms Gaussian pulses acquired from a water sample. The offset sweep experiment was performed in 0.5 ppm steps. The excitation profiles indicate that the Gaussian pulse has been correctly synthesised. The shape of all 3 excitation profiles appear Gaussian and also become narrower as  $t_{RF}$  increases, indicating that the Gaussian pulse is also becoming more selective as it has a narrower excitation bandwidth. The FWHM of the Gaussian excitation profiles, denoted by the dashed line in FIGURE 7.8, can be used as an approximation of their selectivity. The values are in good agreement with the approximate selectivity of the pulses, calculated from the inverse of  $t_{RF}$ , which are only slightly narrower.

## 7.2.4 Selective Excitation of Fluorine

Excitation of  $^{19}\text{F}$  nuclei on the Spinsolve spectrometer required the re-calibration of the hard and soft (Gaussian) RF pulses, that had previously been calibrated for  $^1\text{H}$  nuclei via the RF duration-sweep nutation curve and RF amplitude-sweep SPFGSE experiments, respectively. This was achieved by adapting  $^{19}\text{F}$  variants of the NMR experiments illustrated thus far for  $^1\text{H}$ . This was simple to do because the Spinsolve spectrometer uses the same single X-channel to interact with both the  $^1\text{H}$  and  $^{19}\text{F}$  nuclei. Re-calibration of the RF pulse was necessary because of the difference in gyromagnetic ratio between the  $^1\text{H}$  ( $\gamma_{^1\text{H}} = 267.522 \text{ rad s}^{-1} \text{ T}^{-1}$ ) and  $^{19}\text{F}$  ( $\gamma_{^{19}\text{F}} = 251.815 \text{ rad s}^{-1} \text{ T}^{-1}$ ) nuclei. The lower gyromagnetic ratio of the  $^{19}\text{F}$  nucleus means it will have a weaker interaction with the RF pulse in comparison to the  $^1\text{H}$  nucleus, leading to a slower nutation frequency,  $\omega_1$ .

The  $^{19}\text{F}$  spectrum in FIGURE 7.9a was acquired from a sample containing 250 mM of 3-FP in deuterated methanol with 8 scans of a pulse-acquire experiment in which a rectangular  $\pi/2$  pulse of duration,  $t_{RF} = 100 \mu\text{s}$ , and amplitude,  $A_{RF} = 0 \text{ dB}$  is used to place the spins along the transverse plane for acquisition of the FID. Although 3-FP contains one  $^{19}\text{F}$  nucleus and hence one  $^{19}\text{F}$  peak at -127.2 ppm, a much broader signal was observed at -72.3 ppm due to the presence of  $^{19}\text{F}$  nuclei in the plastic within the Spinsolve NMR probe. While this background signal is a disruptive feature of the probe, it provided an ideal scenario to test the selectivity of the Gaussian RF pulse. The large chemical shift difference between the background and substrate signals ensures the selective refocusing and subsequent observation of the sample's  $^{19}\text{F}$  nuclei if the Gaussian has been accurately synthesised.

The SPFGSE experiment was run on the same sample with 8 scans using a Gaussian  $\pi$  pulse of duration,  $t_{RF} = 5 \text{ ms}$ , and amplitude,  $A_{RF} = -19 \text{ dB}$ , which offers a theoretical selectivity of  $\sim 4.9 \text{ ppm}$ . The RF pulse was placed on-resonance to the  $^{19}\text{F}$  signal at -127.2 ppm and produced the  $^{19}\text{F}$  spectrum shown in FIGURE 7.9b. The  $^{19}\text{F}$  signal from the active 3-FP spins was observed in the spectrum but the background

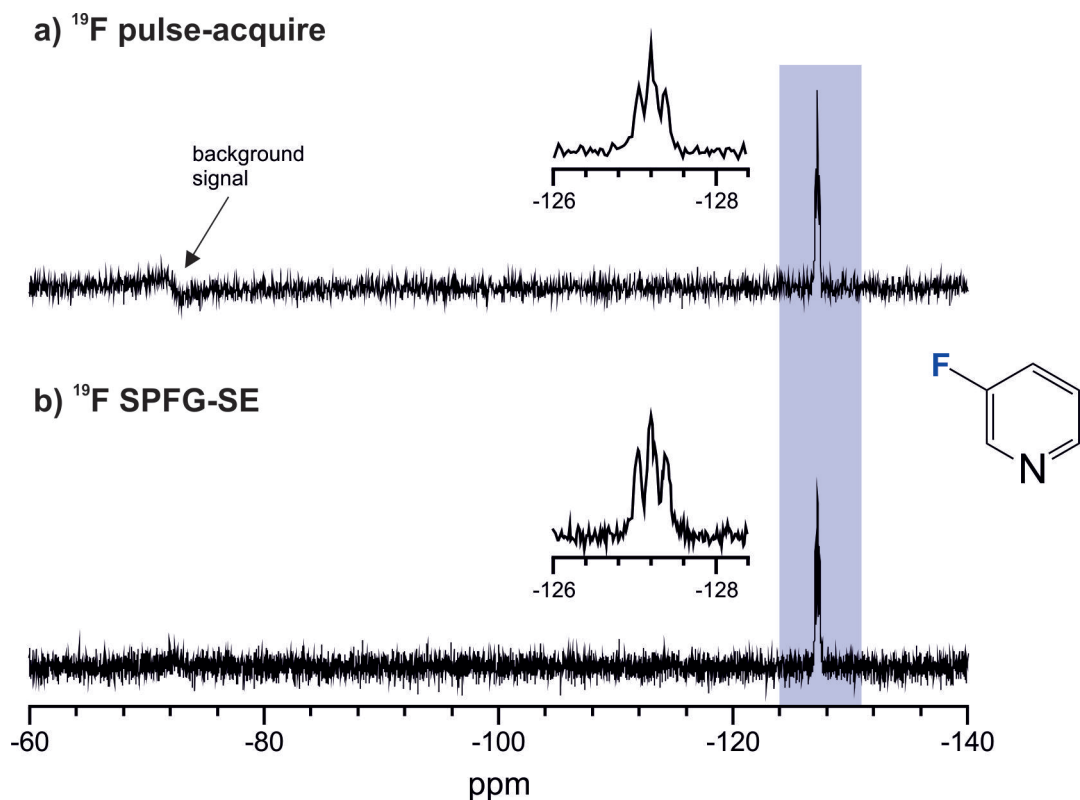


FIGURE 7.9: Spectra of 3-FP acquired from 8 scans of a) a  $^{19}\text{F}$  pulse-acquire experiment and b) a  $^{19}\text{F}$  SPFGSE experiment using a 5 ms Gaussian  $\pi$  pulse that offers a theoretical selectivity of 4.9 ppm. The lack of the background signal on the  $^{19}\text{F}$  SPFGSE spectrum at -72.3 ppm and the observation of the 3-FP multiplet in both spectra at -127.2 ppm demonstrates the successful implementation of the Gaussian RF pulse which selectively interacted and refocused the  $^{19}\text{F}$  nuclei in the sample only.

signal from the passive spins, which are outside the excitation bandwidth of the 5 ms Gaussian pulse, was not. This suggests that the 5 ms Gaussian  $\pi$  pulse within the SPFGSE experiment was successful at selectively exciting and inverting the active  $^{19}\text{F}$  spins in the sample whilst not appearing to interact with and nutate the passive spins 55 ppm away.

### 7.3 *sel*-SHARPER of Fluoropyridines

The development of the Gaussian  $\pi$  pulse on the Spinsolve benchtop NMR spectrometer is pivotal to the execution of *sel*-SHARPER on a low-field NMR system for the band-selective inversion of spins within the SHARPER experiment. This provides the ability to acquire SHARPER singlets for the selected signals without detecting the signals associated with the passive spins that do not experience the Gaussian pulse.

The *sel*-SHARPER experiment in FIGURE 7.10 was developed for use with the Spinsolve benchtop NMR spectrometer. The pulse sequence begins with an SPFGSE which effectively acts as a selective  $\pi/2$  pulse, nutating the active spins to

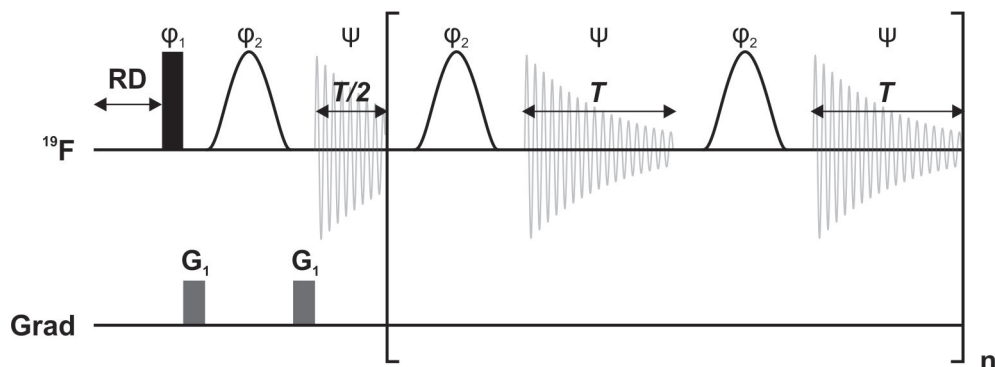


FIGURE 7.10: Pulse sequence for *sel*-SHARPER on the Spinsolve benchtop NMR spectrometer. A filled rectangle represents a hard  $\pi/2$  pulse and the unfilled Gaussian shape represents a Gaussian  $\pi$  pulse. The experiment is run with only one scan using phases of  $\phi_1 = \Psi = x$ , and  $\phi_2 = y$ , where  $\Psi$  corresponds to the phase of the receiver. The homospoil gradients used for refocusing the active spins are labelled  $G_1$ .

the transverse plane. It is followed by an FID chunk of duration  $T/2$ , and then a train of Gaussian  $\pi$  pulses interweaved with acquisition chunks of duration  $T$ . This version of *sel*-SHARPER differs slightly from the version developed for high-field NMR on a Bruker NMR spectrometer.<sup>3</sup> The low-field NMR version is run with one scan and the PFGs have been replaced with homospoil gradients produced by the shim coils. Also, the low-field *sel*-SHARPER experiment does not utilise any form of gradient pulses within the train of  $\pi$  pulses. This simplification relies on a specialised phase cycle ( $\phi_1 = \psi = x$ ,  $\phi_2 = y$ ) and on the success of the SPFGSE sequence to effectively execute selective refocusing of the active spins so that they evolve with coherence throughout the chain of soft pulses, while the passive spins retain their loss of coherence.

The  $^{19}\text{F}$  *sel*-SHARPER experiment was run on three different samples containing 250 mM of either 3-FP, 3,5-DFP or 3,5-TFMP in deuterated methanol (see FIGURE 7.11) with 10 ms Gaussian  $\pi$  pulses, an FID chunk duration of  $T = 20.6$  ms and  $n = 159$ . A 10 ms Gaussian pulse provided a theoretical selectivity of  $\sim 2.5$  ppm. The *sel*-SHARPER spectra are overlaid with the spectra acquired from 8 scans of the  $^{19}\text{F}$  pulse-acquire experiment, for comparison. A collapse of the  $^{19}\text{F}$  multiplets of 3,FP, 3,5-DFP and 3,5-TFMP at -127.2, -125 and -63.9 ppm, into singlets with linewidths,  $\Delta_{1/2}$ , of 0.39, 0.30 and 0.46 Hz, respectively, was observed from the  $^{19}\text{F}$  *sel*-SHARPER spectra. Also, the background signal at -72.3 ppm does not appear on the  $^{19}\text{F}$  *sel*-SHARPER spectra, but it is clearly visible in the  $^{19}\text{F}$  pulse-acquire experiments of 3-FP, 3,5-DFP and  $^{19}\text{F}$ .

The  $^{19}\text{F}$  *sel*-SHARPER spectrum of 3,5-TFMP shows a singlet with a  $\Delta_{1/2}$  of 0.48 Hz, as well as 48 Hz sidebands. These occur due to the chunking of the FID and are referred to as chunking artefacts. The frequency of the chunking artefacts is correlated to the sampling rate of acquisition of each FID chunk, equal to the inverse of  $T$ . All of the  $^{19}\text{F}$  *sel*-SHARPER spectra were acquired with a  $T$  of 20.6 ms, and hence an acquisition rate of  $48.5 \text{ s}^{-1}$  (Hz). The presence of sidebands can only be observed on the  $^{19}\text{F}$  *sel*-SHARPER signal of 3,5-TFMP due to its significantly larger SNR compared to that of 3-FP and 3,5-DFP, as a consequence of the higher concentration of  $^{19}\text{F}$  nuclei, which raises the sidebands above the noise level.

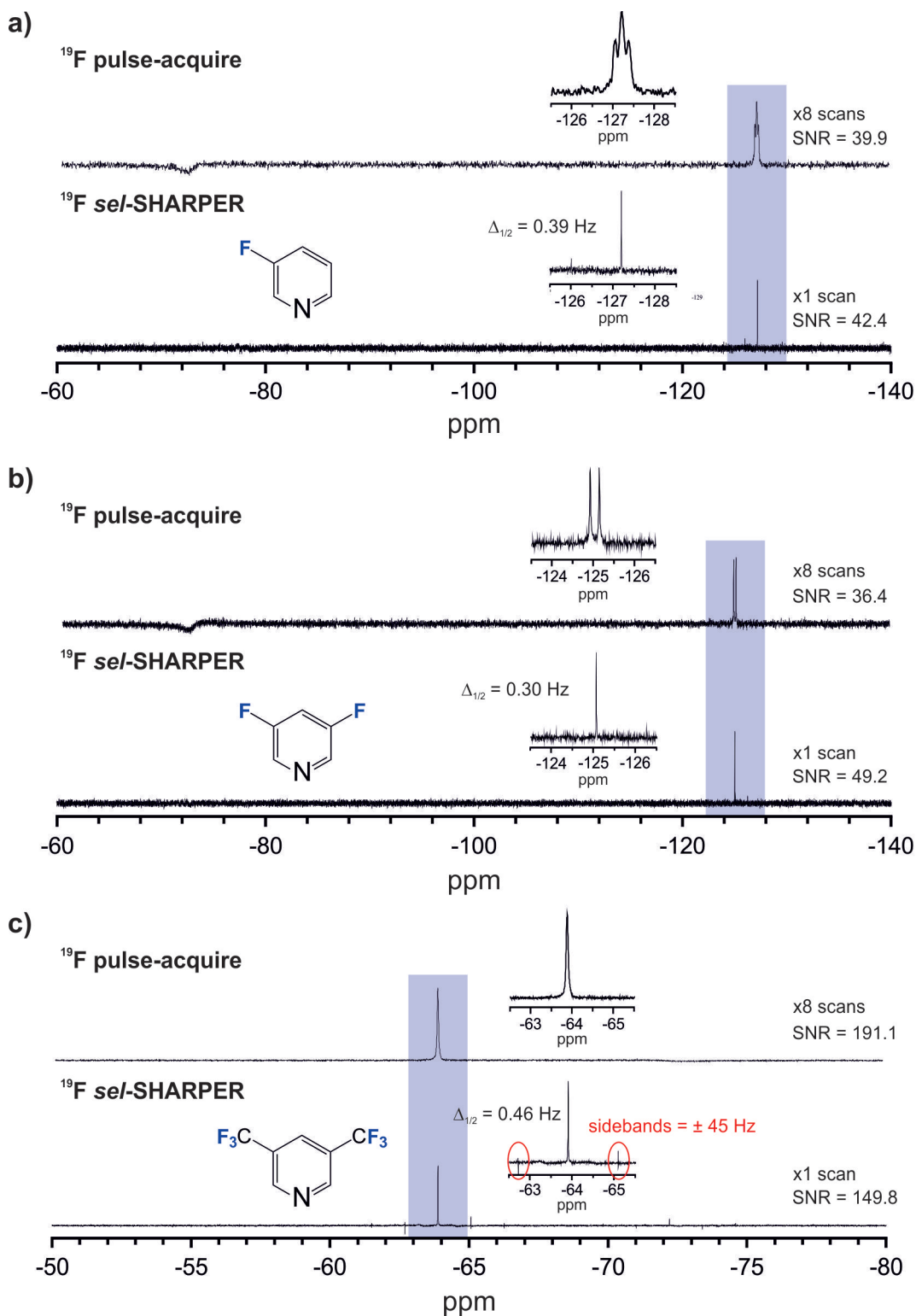


FIGURE 7.11:  $^{19}\text{F}$  pulse acquire and *sel*-SHARPER spectra of a) 3-FP, b) 3,5-DFP and c) 3,5-TFMP acquired with 8 and 1 scan, respectively. The *sel*-SHARPER spectra show the collapse of the  $^{19}\text{F}$  multiplets at -127.2, -125 and -63.9 ppm of 3-FP, 3,5-DFP and 3,5-TFMP, respectively, into narrow singlets with linewidths below 0.5 Hz. The background signal was also not observed in the *sel*-SHARPER spectra which utilised Gaussian  $\pi$  pulses on resonance to the heteronuclear  $^{19}\text{F}$  peaks with a selectivity of 4.9 ppm. Chunking artefacts were observed in the  $^{19}\text{F}$  *sel*-SHARPER spectrum of 3,5-TFMP with separation of 48 Hz due to its stronger signal intensity.

One of the many benefits of the SHARPER experiment is the increase in SNR that is achieved because the signal intensity is no longer distributed between split peaks (collapse of multiplets) and the linewidths are reduced from the increase in  $T_2$  relaxation times. This was observed for the  $^{19}\text{F}$  signal of 3-FP (42.4) and 3,5-DFP (49.2) acquired from 1 scan of the *sel*-SHARPER experiment in FIGURE 7.11, which showed a larger SNR than the  $^{19}\text{F}$  signals acquired from 8 scans of the pulse-acquire experiment of 39.9 and 36.4, respectively. For the 3,5-TFMP sample, the SNR of the  $^{19}\text{F}$  signal acquired from 1 scan of the *sel*-SHARPER experiment of 149.8 was not larger than the SNR of the  $^{19}\text{F}$  signal acquired from 8 scans of the pulse-acquire experiment of 191.1, although the values are close. This is not a surprise since the  $^{19}\text{F}$  *sel*-SHARPER singlet of 3,5-TFMP exhibited the largest linewidth of  $\Delta_{1/2} = 0.46$  Hz.

These observations indicate that the *sel*-SHARPER sequence was successfully designed and implemented. The collapse of multiplets of varying multiplicity to very narrow singlets ( $\Delta_{1/2} < 0.5$  Hz) indicates that the successive refocusing of the spins with the Gaussian  $\pi$  pulses, together with the acquisition of short FID chunks, effectively compiles a full FID that contains a minimal amount of heteronuclear and homonuclear  $J$ -evolution whilst increasing its  $T_2$  relaxation time. The removal of the broad background signal indicates that the selectivity of the 10 ms Gaussian ( $\sim 2.5$  ppm) was maintained throughout the entirety of the *sel*-SHARPER experiment which consisted of 319 Gaussian  $\pi$  pulses. It also indicates that a single PFG is sufficient to ensure destruction of the magnetisation of the passive spins.

The SHARPER sequence in FIGURE 7.12a was also implemented on the Spin-solve spectrometer. It is made up of an initial rectangular  $\pi/2$  pulse followed by an FID half chunk, and a subsequent chain of rectangular  $\pi$  pulses accompanied by FID acquisition chunks. The RF pulses and acquisition chunks are all separated by an acquisition delay of 20  $\mu\text{s}$ . This sequence is similar to the SHARPER sequence developed on the Bruker NMR spectrometer (see FIGURE 7.1), but has been simplified to not require PFGs and to be carried out with 1 scan. The phases of the rectangular pulses are the same as those used in the benchtop NMR *sel*-SHARPER sequence (see FIGURE 7.10), where  $\phi_1 = \psi = x$ , and  $\phi_2 = y$ .

The SHARPER experiment was run on the 250 mM sample of 3-FP with 1 scan, an FID chunk duration of  $T = 20.6$  ms and  $n = 159$ . The  $\pi$  and  $\pi/2$  pulses were pulsed on resonance to the  $^{19}\text{F}$  signal at -127.2 ppm and run with amplitudes of 0 dB, and durations of 100 and 225  $\mu\text{s}$ , respectively. The  $^{19}\text{F}$  SHARPER spectrum in FIGURE 7.12b shows the two signals of the  $^{19}\text{F}$  nucleus on 3-FP at -127.2 ppm and the  $^{19}\text{F}$  background signal at -72.3 ppm. The SHARPER singlet of 3-FP was acquired with a linewidth of 1.20 Hz and an SNR of 47.7. The background signal also experienced the hard RF pulses in the SHARPER experiment and was therefore an active spin. While it seems to display a collapse of the multiplicity and linewidth, it gave rise to multiple sidebands of  $\pm 48.5$  Hz across a  $\sim 40$  ppm range. These artefacts are also observed around the  $^{19}\text{F}$  signal of 3-FP but with a much lower intensity, and are correlated to the sampling rate of the FID chunks of 48.5 Hz.

The SHARPER singlet of 3-FP acquired from 1 scan of the  $^{19}\text{F}$  SHARPER and *sel*-SHARPER experiments are also different has an SNR of 47.7 and 42.4, and a

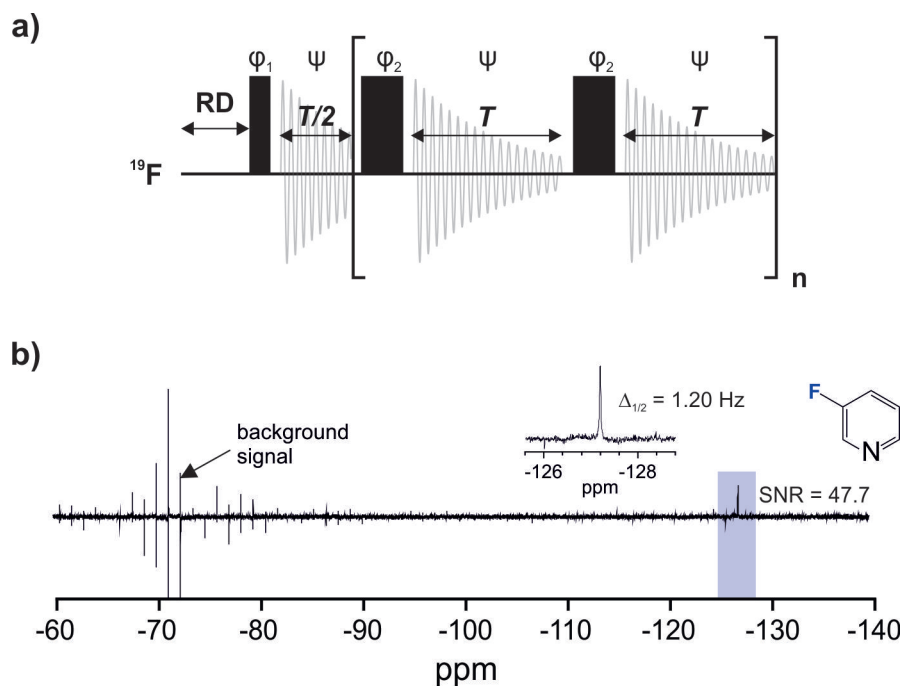


FIGURE 7.12: Illustration of a) the pulse sequence for the SHARPER experiment for implementation on the Spinsolve NMR spectrometer where a filled thin and wide rectangle represents a hard  $\pi/2$  and  $\pi$  pulse, respectively. The corresponding SHARPER spectrum of 3-FP in b) shows collapse of the  $^{19}\text{F}$  multiplet into a singlet with linewidth = 1.2 Hz and SNR = 47.7. A series of intense FID chunking artefacts with a frequency of  $\pm 48.5$  Hz were observed between -90 and -60 ppm due to the collapse of the broad solid-state-like (background)  $^{19}\text{F}$  signal at -72.3 ppm. The same FID chunking artefacts are observed around the  $^{19}\text{F}$  peak of 3-FP with a much lower intensity as a consequence of the 48.5 Hz sampling rate of each FID chunk. The SHARPER experiment is performed with 1 scan using phases of  $\phi_1 = \Psi = x$  and  $\phi_2 = y$ .

linewidth of 1.20 Hz and 0.39 Hz, respectively. The appreciable increase in the linewidth of the  $^{19}\text{F}$  SHARPER singlet by a factor of three compared to the *sel*-SHARPER singlet suggests that the refocusing of the coherence by the hard RF pulses to nullify the effects of homogeneous  $T_2$  relaxation, was less effective than the Gaussian RF pulses which were also combined with homospoil gradients pulses for selective refocusing of the active spins. Nonetheless, the SNR of the  $^{19}\text{F}$  SHARPER singlet of 47.7 was higher than that of the  $^{19}\text{F}$  *sel*-SHARPER singlet of 42.4, despite having a larger linewidth. This could be attributed to some relaxation of the spin system during the *sel*-SHARPER pulse sequence due to long Gaussian pulses (10 ms) that are used multiple times ( $n = 319$ ) in a single scan.

The result of the  $^{19}\text{F}$  SHARPER spectrum of 3-FP clearly demonstrates the benefit of carrying out the *sel*-SHARPER sequence which allows the acquisition of narrower SHARPER singlets on the band-selected region of the spectrum, without acquiring any signals corresponding to the passive spins in the experiment. This was observed in FIGURE 7.11 with the removal of the background signal in the  $^{19}\text{F}$  *sel*-SHARPER spectra of all samples. The *sel*-SHARPER experiment therefore provides the ability to produce much cleaner spectra which is favourable for procedures such as reaction monitoring that rely on the accurate integration of signals of interest.

## 7.4 Conclusion and Future Work

The collaboration between the Halse and Uhrin research groups involved the design of Gaussian shaped RF pulses on the Spinsolve benchtop NMR spectrometer to allow implementation of the *sel*-SHARPER sequence on a low-field NMR instrument. Performing the SHARPER experiment on a benchtop NMR system improves its scope for reaction monitoring in a laboratory and industrial setting due to its ability to simplify NMR spectra by removing *J*-coupling information and minimising the effects of magnetic field inhomogeneity to yield sharp singlets with enhanced SNRs.

The Gaussian RF pulse was successfully generated by the RF amplifier in the Spinsolve spectrometer through the creation of a table of  $A_{RF}$  values on the pulse program macro within the Spinsolve Expert software that outlines the shape of the pulse. The tabulated values are outputted by the RF amplifier in fixed intervals, where the total number of  $A_{RF}$  values dictates the duration of the pulse. The RF amplifier was found to have a non-linear power output, meaning the attenuation of the RF pulse that is set by the user on the pulse program is different to the attenuation of the RF pulse that is outputted by the RF amplifier. This was more pronounced at higher attenuations. The non-linearity was corrected using a calibration curve that was produced from a 5<sup>th</sup> order polynomial fit to a plot of the attenuation value set by the user,  $\text{dB}_{set}$ , against the outputted attenuation value,  $\text{dB}_{ideal}$ , which was extracted from pulse calibration data. The fit allowed correction of the tabulated  $A_{RF}$  values to achieve an accurate synthesis of the desired RF pulse shape in spite of the RF amplifier's non-linear behaviour.

An SPFGSE experiment was written for the Spinsolve spectrometer to calibrate the Gaussian RF pulse by calculating the  $A_{RF}$  value required for a  $\pi$  rad nutation. The duration of the pulse is chosen based on the desired excitation bandwidth, approximated as the inverse of the pulse duration. The SPFGSE experiment was also used to produce an excitation profile of the Gaussian pulse to verify its shape and measure its excitation bandwidth, which was shown to be close to the theoretical excitation bandwidth for durations of 2, 3 and 4 ms. The Gaussian RF pulse was utilised in an SPFGSE experiment and shown to selectively excite and refocus the  $^{19}\text{F}$  nuclei of 3-FP, but not the  $^{19}\text{F}$  nuclei in the plastic of the Spinsolve probe responsible for a broad  $^{19}\text{F}$  peak at -72.3 ppm. From this result the Gaussian  $\pi$  pulse was implemented on the *sel*-SHARPER sequence which was run on 250 mM samples of 3-FP, 3,5-DFP and 3,5-TFMP, where the single  $^{19}\text{F}$  multiplets of all samples were collapsed to singlets with linewidths  $< 0.5$  Hz.

The success of the *sel*-SHARPER sequence on the Spinsolve Benchtop NMR spectrometer was reported to the Uhrin group at the University of Edinburgh and multiple remote meetings took place to explain the specifics of the method behind the design and implementation of the Gaussian  $\pi$  pulse. This included sharing of the pulse program macro on the SpinsolveExpert software that enables creation of the Gaussian shape by the RF amplifier, as well as the procedure to acquire the calibration curve to correct for the non-linearity of the RF amplifier's power output. The collaboration resulted in a joint publication in which I am a co-author,

demonstrating the implementation of SHARPER on a 60 MHz Spinsolve Ultra NMR spectrometer for SHARPER-enhanced benchtop NMR of organofluorine compounds.<sup>141</sup>

Due to the end of the initial COVID lockdown and the return to laboratory work, my involvement in the development of SHARPER on a benchtop NMR system was terminated. The project was passed onto another member of the Halse group who demonstrated the integration of SABRE with the SHARPER and *sel*-SHARPER sequences on the benchtop spectrometer to produce hyperpolarised SHARPER signals from samples containing mixture of fluorinated N-heterocycles. The work has recently been submitted for publication.<sup>43</sup>

## 8 | Conclusions and Future Work

Presented in this thesis is a new approach to directly probe the ULF SABRE polarisation transfer mechanism via *in situ* NMR detection, thus eliminating the need for sample transfer between the polarisation transfer and detection fields. This was achieved with an EFNMR instrument (Magritek Terranova-MRI) that, due to its compact and accessible nature, was integrated with a triaxial Helmholtz coil array and an automated  $p\text{-H}_2$  gas flow system, to make a complete SABRE-EFNMR system.

The gas flow system made-up of a  $p\text{-H}_2$  generator, a Bruker polariser control unit and a glass reaction cell that hosts the SABRE reaction was employed to carry out *in situ*  $p\text{-H}_2$  bubbling of the SABRE sample (pre-catalyst + substrate + solvent) required for *in situ* NMR detection. Optimisation of the gas flow procedures within the  $p\text{-H}_2$  generator and the polariser enabled a stable and reproducible flow of  $p\text{-H}_2$  gas into the reaction cell. This was vital in ensuring the acquisition of reproducible SABRE results since the hyperpolarisation of the sample is proportional to both  $p\text{-H}_2$  pressure and bubbling rate; therefore, variations in the flow of  $p\text{-H}_2$  lead to variability in the observed enhancement level of substrates. Gas flow conditions of +0.25 bar pressure differential at a 4 bar forward pressure were found to yield sufficient sample hyperpolarisation without significant depletion of the output pressure of  $p\text{-H}_2$  from the generator, thus permitting multiple repetitions of  $p\text{-H}_2$  bubbling experiments, provided a sufficiently long delay between repeats ( $t_{rep} > 40$  s) is in place to allow recovery of  $p\text{-H}_2$  pressure in the generator.

The Helmholtz coil pairs were used to generate a field that combines with the Earth's magnetic field, shown to have an axial tilt of  $\sim 26^\circ$  within the local environment of the lab, to generate a resultant field that is parallel to the vertical axis of the laboratory frame in order to align the spin (dictated by orientation of  $B^0$ ) and laboratory (dictated by the  $B^1$  coil) frames of reference. This alignment led to improvements on the operation of standard NMR procedures such as spin nutation via RF pulses and NMR detection, both of which are optimal when  $B_0$  and the  $B_1$  field produced by the  $B^1$  coil are perpendicular. This allowed the calibration of an off-resonance RF pulse to simultaneously nutate the  $^1\text{H}$  and  $^{19}\text{F}$  nuclei by  $\pi/2$  rad to achieve simultaneous acquisition of both nuclei which are only separated by  $\sim 130$  Hz in the Earth's magnetic field. The alignment was also crucial in providing reliable control over the external field in the  $\mu\text{T}$  regime as linear changes in the current through the z-Helmholtz coil produced linear changes to  $B^0$ . The use of internal power supplies originally designed to power the shim coils allowed precise control in the positive and negative directions, over the strength of the external field, as

well as facile control of their timing within an NMR experiment through parameters defined on the pulse program of the software (Prospa) operating the instrument. This enables facile switching between the PTF and detection field required to execute the  $\mu\text{T}$  SABRE-EFNMR experiment. Since EFNMR detection is carried out in the same field regime as the SABRE polarisation transfer process, only small changes in current were required ( $< 200\text{ mA}$ ). The built-in polarising coil designed for pre-polarisation of the sample provided precise and accurate control over the external field in the mT regime which is required to execute the mT SABRE-EFNMR experiment. Therefore, the EFNMR-Helmholtz system offers access to the full SABRE PTF range for probing of SABRE polarisation transfer to  $^1\text{H}$  (5-10 mT) and  $^{19}\text{F}$  ( $< 50\ \mu\text{T}$   $\{B^E\}$ ).

NMR experiments were designed to incorporate communication with the Bruker polariser control unit to initiate  $p\text{-H}_2$  bubbling, as well as communication with the polarising and z-Helmholtz coil pair to generate the mT and  $\mu\text{T}$  PTF, respectively, prior to the NMR experiment, which consisted of an RF pulse to simultaneously excite  $^1\text{H}$  and  $^{19}\text{F}$ , followed by acquisition of the FID. These were labelled the mT and  $\mu\text{T}$  SABRE-EFNMR experiments, and together demonstrated the successful hyperpolarisation and *in situ* detection of the SABRE-enhanced EFNMR signals of four fluoropyridines: 3-FP, 3,5-DFP, 3,5-TFMP and 3-DFMP.

A hyperpolarised  $^{19}\text{F}$  EFNMR signal of 3-FP at 6.4 mT was not observed from the mT SABRE-EFNMR experiment primarily due to the fact that mT PTFs drive coherent SABRE polarisation transfer to  $^1\text{H}$ , where  $^{19}\text{F}$  hyperpolarisation is a consequence of indirect polarisation transfer from the SABRE-polarised  $^1\text{H}$  nuclei. However, the lack of a hyperpolarised  $^{19}\text{F}$  EFNMR signal of 3-FP, which was not the case for the other substrates, was attributed to the substrate itself as it has only one  $^{19}\text{F}$  nucleus that is strongly coupled to four magnetically inequivalent protons. This causes significant splitting and corresponding distribution of the signal intensity and gives rise to a signal with low SNR.

NMR simulations acquired on Matlab using the Spinach library<sup>122</sup> were employed as an interpretation tool for the complex EFNMR signals which lack chemical shift resolution and are formed from strongly coupled nuclear spin systems. Since the acquisition of an NMR simulation requires defining a Hamiltonian operator from which the defined spin density matrix can evolve under throughout the simulated NMR experiment, the  $J$ -coupling interactions within the coupling network of all four substrates had to be deciphered. Coupling values measured from high-field NMR spectra that display good chemical shift and signal resolution were used to calibrate high-field NMR simulations. Comparison of the simulated and experimental high-field NMR spectra for different  $J$ -coupling values across a user defined range via the Nelder-Mead method allowed refinement of the measured coupling values. Comparison of simulated and experimental EFNMR spectra then allowed further optimisation of the  $J$ -coupling values by comparing their fit when different relative signs of the coupling interactions were introduced into the simulation. A single coupling interaction on 3-FP and 3,5-DFP were found to be negative. This elucidation of the relative signs of the coupling interactions is a unique feature of the strong coupling regime that exists in the Earth's magnetic field.

The simulated EFNMR spectrum of 3-FP supported the hypothesis that the lack of a hyperpolarised  $^{19}\text{F}$  peak is attributed to heavy splitting of the  $^{19}\text{F}$  signal. NMR simulations were also vital in understanding not only the form of the EFNMR signals of 3,5-DFP, 3,5-TFMP and 3-DFMP by deciphering how the  $^1\text{H}$  nuclei in different chemical environments contribute to the complex multiplet observed, but also in gaining insight into the dominant SABRE polarisation transfer pathway across the PTF range. The SABRE polarised  $^1\text{H}$  signals of 3,5-DFP, 3,5-TFMP and 3-DFMP acquired using a 9, 6.4 and 6 mT PTF, respectively, represented a dominant polarisation transfer pathway from the  $\mathbf{I}_1 \cdot \mathbf{I}_2$  ( $S_0$ ) state of the  $p\text{-H}_2$  derived hydrides to the  $\hat{I}_z$  state of the  $^1\text{H}$  nuclei of the catalyst-bound substrate. The weak heteronuclear  $J$ -coupling interactions of 3,5-TFMP fail to effectively break the magnetic equivalence of the protons for the observation of homonuclear  $J$ -coupling interactions, and therefore gave rise to a simulated and hyperpolarised EFNMR spectrum that exhibited very little multiplicity, fine structure and signal resolution, preventing any form of interpretation or conclusions about potential indirect polarisation transfer pathways to  $^{19}\text{F}$ . The relatively large 9 Hz heteronuclear coupling of 3,5-DFP produced a well resolved  $^1\text{H}$  EFNMR signal with minimal peak overlap and sufficient fine structure to interpret the  $^1\text{H}$  multiplet shape, where simulations demonstrated the contributions of the *para* and *ortho*-protons to different regions of the  $^1\text{H}$  multiplet. The indirectly hyperpolarised  $^{19}\text{F}$  EFNMR signal contained only two peaks instead of the complex multiplet illustrated by the simulation. While the reason for this could not be established definitively, it did exhibit observable hyperpolarisation. The antiphase nature of the hyperpolarised  $^{19}\text{F}$  EFNMR signal of 3,5-DFP and 3,5-TFMP relative to their respective hyperpolarised  $^1\text{H}$  EFNMR signals, is consistent with the hyperpolarisation of  $^1\text{H}$  being the source of hyperpolarisation on  $^{19}\text{F}$  through indirect transfer within the substrate.

The SABRE polarised EFNMR spectrum of 3-DFMP exhibited well resolved multiplets with good signal resolution owing to the very large 55.4 Hz heteronuclear  $J$ -coupling interaction between the magnetically equivalent  $^{19}\text{F}$  nuclei and the  $^1\text{H}$  nucleus. The form of the 3-DFMP spectrum resembled that of an  $AB_2$  spectrum, indicating the strongly coupled 3-spin  $AB_2$  system of the  $\text{CHF}_2$  functional group in 3-DFMP is the dominant interaction. The NMR simulation of 3-DFMP acquired with  $\rho_0 = \sum_i \hat{I}_{zi}$  and  $\hat{I}_{obs} = \sum_i \hat{I}_i^-$  for all nuclei replicated the hyperpolarised  $^1\text{H}$  EFNMR signal and emphasised the greater efficiency of SABRE polarisation transfer to the aromatic  $^1\text{H}$  nuclei over the methyl  $^1\text{H}$  nucleus. The  $^{19}\text{F}$  EFNMR signal was not replicated by the aforementioned simulation because it exhibited antiphase peaks. Simulations run with  $\rho_0 = \sum_i \hat{I}_{zi}$  for all  $^1\text{H}$  nuclei only and  $\hat{I}_{obs} = \sum_i \hat{I}_i^-$  for all nuclei were shown to replicate the entire experimental spectrum of 3-DFMP, suggesting that while it is accurate to assume mT PTFs drive SABRE polarisation transfer to the  $\hat{I}_z$  state of the  $^1\text{H}$  nuclei only, the observed signals at the  $^1\text{H}$  and  $^{19}\text{F}$  regions of the EFNMR spectrum are associated with single (-1) quantum coherences between highly strongly coupled and heavily mixed nuclear spin states (more accurately described under the singlet-triplet basis), where the signals can no longer be assigned independently to a particular nuclear species.

Successful hyperpolarisation and *in situ* EFNMR detection of 3,5-DFP at 8  $\mu\text{T}$  was achieved using the  $\mu\text{T}$  SABRE-EFNMR experiment. With SABRE polarisation transfer now being coherently directed to  $^{19}\text{F}$  in this regime, a SABRE-polarised  $^{19}\text{F}$

EFNMR signal of 3,5-DFP was acquired that fit much more closely to the NMR simulation and represented a dominant SABRE polarisation transfer pathway from the  $\mathbf{I}_1 \cdot \mathbf{I}_2$  state on the hydride to the  $\hat{I}_z$  state on the  $^{19}\text{F}$  nuclei. The indirectly hyperpolarised  $^1\text{H}$  EFNMR signal of 3,5-DFP was antiphase relative to the  $^{19}\text{F}$  EFNMR signal as expected; however, it exhibited a broad central peak which is only a portion of the  $^1\text{H}$  EFNMR signal. This may have been due to a less efficient polarisation pathway, with the rest of the peaks hidden in the noise, or predominant hyperpolarisation of the *ortho*-protons (the outer peaks on the edges of the signal associated with the *para*-proton were not observed). Either way, higher SNR is required to interpret the signal shape further, as well as the indirect polarisation transfer pathway. The SABRE-polarised EFNMR spectrum of 3-DFMP in the  $\mu\text{T}$  regime displayed SABRE-polarised peaks at the  $^1\text{H}$  and  $^{19}\text{F}$  regions of the EFNMR spectrum, where the latter were absorption signals this time and the signals in the  $^1\text{H}$  region were antiphase. The simulation acquired with  $\rho_0 = \sum_i \hat{I}_{zi}$  for all  $^{19}\text{F}$  nuclei only and  $\hat{I}_{obs} = \sum_i \hat{I}_i^-$  for all nuclei fit well with the EFNMR signals at the  $^{19}\text{F}$  region, but not to those in the  $^1\text{H}$  region. While this could be partly due to low SNR that caused some of the split peak intensities to fall below the noise, the observed negative peak at  $\sim 2210$  Hz (peak corresponds to the aromatic protons in 3-DFMP), which was not present in the simulation, could suggest indirect polarisation transfer to other product states, for example, the  $\hat{I}_z$  state on  $^1\text{H}$ , that might give rise to the resultant spectrum observed. As with 3,5-DFP, higher SNR was required to make more concrete conclusions about the observed form of the SABRE-polarised 3-DFMP spectrum.

Finally, *in situ* mT and  $\mu\text{T}$  PTF-cycling experiments were run on 3,5-DFP and 3-DFMP by repeating the SABRE-EFNMR experiments with linear increments in the current through the polarising coil or z-Helmholtz coil pair. The acquired PTF curve from the PTF-cycling experiment allowed visualisation of the magnetic field dependence of SABRE polarisation transfer efficiency. The mT PTF curves acquired from the  $^1\text{H}$  and  $^{19}\text{F}$  EFNMR signals of 3,5-DFP were swept from 0. - 12.5 mT. A smooth increase in SABRE polarisation transfer efficiency up to the maximum at  $\sim \pm 9.5$  mT was observed, followed by a gradual decrease beyond  $\pm 12$  mT. The synchronised and inverse trend in the  $^1\text{H}$  and  $^{19}\text{F}$  EFNMR signal intensities across the mT regime provided further evidence the hyperpolarisation of  $^{19}\text{F}$  in the mT regime is linked to the efficiency of coherent SABRE polarisation transfer to  $^1\text{H}$ . The mT PTF curve of 3-DFMP showed a similar smooth trend with a maximum at 6 mT. The  $\mu\text{T}$  PTF curves acquired from the  $^1\text{H}$  and  $^{19}\text{F}$  EFNMR signals of 3,5-DFP and 3-DFMP were also smooth, and showed a gradual increase and decrease to and from the maxima at 8 and 5  $\mu\text{T}$ , respectively.

The PTF curves acquired from the *in situ* PTF-cycling experiment on 3,5-DFP were compared to *ex situ* PTF-cycling results in the literature on 3,5-DFP.<sup>2</sup> Both approaches displayed similar results from the  $^1\text{H}$  and  $^{19}\text{F}$  mT PTF curves between 0- 14 mT, and hence illustrated a comparable magnetic field dependence of SABRE polarisation transfer efficiency to 3,5-DFP in the mT regime. The differences in the results, however, highlighted the benefits of performing SABRE polarisation transfer *in situ* of NMR detection. The *ex situ* approach produced PTF curves with observable variability in SABRE polarisation that was likely a consequence of lower reproducibility in experimental procedures such as PTF strength and duration. Sample transfer times

of  $\sim 5$  s, even when carried out in an automated fashion is also a source of experimental variation. The  $\mu\text{T}$  PTF curves were not directly comparable as they were performed across a different range of PTF values. Nonetheless, this again highlighted the benefits of the SABRE-EFNMR system that provides precise control over the PTF. The symmetry about  $0\ \mu\text{T}$  that was observed from the shape of the  $\mu\text{T}$  PTF curves of 3,5-DFP from  $-14$ - $14\ \mu\text{T}$  further illustrated the higher level of reproducibility in SABRE hyperpolarisation via *in situ* EFNMR detection using the SABRE-EFNMR system.

The magnetic field dependence of the SABRE and indirect polarisation transfer in the mT or  $\mu\text{T}$  regime can also be interrogated from PTF curves. While subtle changes to the form of the SABRE-polarised  $^1\text{H}$  and  $^{19}\text{F}$  EFNMR signals of 3,5-DFP and 3-DFMP were observed, the SNR and signal resolution was insufficient to interrogate the causes and draw conclusions about what product states are receiving hyperpolarisation.

In conclusion, a robust method to allow direct interrogation of ULF SABRE polarisation transfer to  $^1\text{H}$  and  $^{19}\text{F}$  has been developed that offers excellent reproducibility in SABRE hyperpolarisation. The SABRE-EFNMR system allowed the design of the mT and  $\mu\text{T}$  SABRE-EFNMR experiments to achieve the immediate acquisition of hyperpolarised EFNMR signals across the entire PTF range. Numerical simulations were coupled with EFNMR detection to aid in interpreting EFNMR spectra and to provide insight into the SABRE polarisation transfer pathway under varying SABRE conditions.

Moving forward with the current SABRE-EFNMR system, the design of new experiments can allow further probing of SABRE polarisation transfer. Thus far, SABRE polarisation is detected immediately after switching from the PTF to the detection field ( $\sim 51.9\ \mu\text{T}$ ). While this provides information on the coherent pathway of SABRE polarisation transfer that takes place within the PTF, the effect that switching to the detection field has on the nuclear spin states and hence the indirect polarisation transfer mechanism within the hyperpolarised substrate is unexplored. In the case when coherent SABRE polarisation transfer occurs in the  $\mu\text{T}$  regime, switching to the detection field will not have a significant effect on the nuclear spin state, however, moving from a mT PTF to the  $\mu\text{T}$  detection field leads to increased mixing between the nuclear spin states. Therefore, the design of a variant of the mT SABRE-EFNMR experiment that introduces a variable delay between the moment the fields are switched, to the moment the spins are excited by the RF pulse will provide a route to more closely observing how the polarisation is transferred across the target substrate during acquisition of the FID. The variable delay could then also be carried out under a range of  $\mu\text{T}$  fields to further explore the magnetic field dependence of indirect polarisation transfer.

To progress toward the implementation of new and improved SABRE-EFNMR experiments the low SNR displayed by the hyperpolarised signals in this work must be addressed. Two brute force approaches can be implemented: higher  $p\text{-H}_2$  pressure and flow rate through the sample to increase the efficiency of SABRE;<sup>39,60,99</sup> and a larger glass reaction cell to increase the volume of the SABRE sample and hence the

concentration of hyperpolarised substrate in solution. The latter simply requires the design of a new and larger glass reaction cell since the one utilised in this work did not completely fill the diameter of the Terranova-MRI probe. Within the current automated gas flow system, the former cannot be achieved because the  $p$ -H<sub>2</sub> generator cannot cope with the  $p$ -H<sub>2</sub> flow rate demands associated with an increase in either the 4 bar forward pressure or the 0.25 bar pressure differential. This is because it is being limited by the formation rate of H<sub>2</sub> by the current H<sub>2</sub> generator. If replaced for one with a higher H<sub>2</sub> output pressure, the automated gas flow system would be able to supply a higher  $p$ -H<sub>2</sub> pressure and flow rate into the cell. Since increasing the formation rate of  $p$ -H<sub>2</sub> would reduce the recovery time  $t_{rep}$  (currently > 40 s) of the  $p$ -H<sub>2</sub> generator, more signal averaging per experiment time would be possible to further maximise the SNR of hyperpolarised signals.

Another approach to improve SNR within the SABRE-EFNMR system would be with the use of an external power supply to power the z-Helmholtz coil. As discussed in Chapter 3, re-wiring of the y-shim coil power supply to the z-Helmholtz coil introduced a significant amount of electrical noise into the probe and hence in the spectrum at frequencies > 2000 Hz. A requirement of the external power supply would be that it can maintain the timing and current precision offered by the internal power supply so as to not lose reproducibility in the SABRE results, as well as the ability to switch the polarisation of the current. Connecting such a power supply to the x and y-Helmholtz coils as well would unlock the ability to carry out controlled field switching perpendicular to  $B^0$  in order to execute quadrupolar decoupling via Singlet–Triplet Oscillations through Rotating Magnetic fields (STORM) pulses.<sup>142,143</sup> While quadrupolar nuclei such as <sup>2</sup>H and <sup>14</sup>N ( $I = 1$ ) generally do not contribute to  $T_1$  relaxation, in near-zero magnetic fields this is no longer the case. Consequently, in the  $\mu$ T fields used for coherent SABRE polarisation transfer to <sup>19</sup>F (< 10  $\mu$ T), the  $J$ -coupling interactions between the <sup>14</sup>N nuclei in 3-FP, 3,5-DFP, 3,5-TFMP and 3-DFMP, with all the other nuclei in the molecule act as sources of relaxation and reduce the lifetime of hyperpolarisation. Therefore, the use of STORM pulses to decouple quadrupolar relaxation would contribute to longer  $T_1$  relaxation times of the hyperpolarisation on the substrate and higher detected enhancement levels.

Combining the existing SABRE-EFNMR system with the improvements to SNR by the methods and approaches suggested above would produce a system that offers a high level of control over the SABRE experiment and high reproducibility of the SABRE results. With such a system, other aspects of the SABRE mechanism could be interrogated, such as the effects of temperature on the exchange rate of  $p$ -H<sub>2</sub> and substrate molecules to the SABRE catalyst.

## 9 | Experimental Details

### 9.1 Sample Preparation

EFNMR samples were prepared by mixing 5 mM (12.8 mg) of the pre-catalyst,  $[\text{IrCl}(\text{COD})(\text{IMes})]$  (IMes = 1,3-bis(2,4,6-trimethylphenyl)imidazol-2-ylidene and COD = cis,cis-1,5-cyclooctadiene) in 4 mL of either methanol or methanol-d<sub>4</sub> (as indicated in the text). Once dissolved the desired molar equivalents of the substrate were added to form the final solution. Sonication was typically used to speed up dissolution of the catalyst and substrate, if solid, in the solvent. The final sample was transferred into a glass reaction cell built in-house by injecting it via the cell inlet and through the frit. Sample degassing prior to the dissolution of *p*-H<sub>2</sub> was not required since bubbling of the solution with *p*-H<sub>2</sub> during the *in-situ* catalyst activation setup achieves this.

The pre-catalyst was synthesized in-house by Dr Victoria Annis according to a literature procedure.<sup>144,145</sup> The substrates were purchased from Merck Life Science UK Limited (3-difluoromethylpyridine), Fluorochem (3-fluoropyridine/3,5-difluoropyridine) and Sigma-Aldrich (3,5-bis{trifluoromethyl}pyridine) and used without further modification.

Prior to any hyperpolarisation experiments, the sample was typically activated by repeating the mT SABRE-EFNMR experiment 20-30 times (the number of repetitions depends on the duration of *p*-H<sub>2</sub> bubbling per repeat) until the SABRE response is observed to plateau, indicating full activation of the pre-catalyst from  $[\text{IrCl}(\text{COD})(\text{IMes})]$  to  $[\text{Ir}(\text{IMes})(\text{H})_2(3,5\text{-DFP})_3]^+ \text{Cl}^-$ . Activation of the catalyst is typically followed by a colour change from dark orange (pre-catalyst) to light yellow or clear solution.

### 9.2 Hyperpolarised EFNMR Data Acquisition

All hyperpolarised EFNMR spectra were acquired on a Magritek Terranova-MRI probe as part of the SABRE-EFNMR system described in Chapters 3 and 4. SABRE was carried out with mixing of the liquid sample with 4 bar *p*-H<sub>2</sub> at a 0.25 bar pressure differential across the reaction cell. The mT and  $\mu\text{T}$  SABRE-EFNMR experiments required to acquire hyperpolarised EFNMR signals were setup and run on the Terra-

novaExpert (version 0.97) software from a controlling PC. Table 9.1 contains typical values for the parameters in the mT and  $\mu$ T SABRE-EFNMR experiments.

Table 9.1: Table of values for the experimental parameters of the mT and  $\mu$ T SABRE-EFNMR experiments.

Parameter	Value
$B_{HZ}$ (detection field)	14.9 $\mu$ T (46 mA)
$B_1$	2160 Hz
dwel time	< 167 $\mu$ s
$V_{\pi/2}$	1.1 V
$t_{\pi/2}$	8 cycles
$t_{acq}$	20 ms
$B_{Hy}$ ( $B^0$ alignment field)	21.3 $\mu$ T (70 mA)
$t_{RD}$	20 ms
$t_{rep}$	> 40 s

The mT and  $\mu$ T PTF and  $t_{PTF}$  values are reported in the figure captions of the SABRE-polarised EFNMR spectra in Chapter 5 and 6. The  $t_{PTF}$  values were optimised via  $t_{PTF}$  duration sweep experiments as described in Chapter 5. PTF values were optimised via PTF-cycling as described in Chapter 6.

The Terranova-MRI system acquires the FID in the laboratory frame, producing an NMR spectrum from  $-swh/2$  -  $swh/2$  after FT. For a Larmor frequency of proton at  $\sim 2210$  Hz, a minimum sweep width of 6000 Hz was sufficient to encapsulate the entire NMR spectrum, leaving enough room to account for the splitting of the  $^1\text{H}$  signal ( $^1\text{H}$  peak observed at 2280 Hz for 3-DFMP). Therefore, the maximum dwell time was 167  $\mu$ s. In all cases, the value of the total number of acquisition points was set to ensure a sufficiently long acquisition period to capture the entire FID.

The minimum value for  $t_{rep}$  is 40 s to allow recovery of the  $p\text{-H}_2$  generator between  $p\text{-H}_2$  bubbling experiments. The long repetition time also ensures out-gassing of the SABRE sample in between  $p\text{-H}_2$  bubbling experiments.

### 9.3 EFNMR Data Processing

All EFNMR spectra acquired on the Terranova-MRI spectrometer were processed using the Prospa (version 3.40) software package which operates the Terranova-MRI spectrometer. The post-processing of EFNMR data typically included zero-filling and a zero- and first-order phase correction.

Spectra acquired from pseudo-2D NMR experiments ( $B_1$  amplitude sweep, PTF-cycling,  $t_{PTF}$  sweep, etc.) were aligned to facilitate peak integration and phasing

across stacked plots that saw Larmor frequency drifts across repeats due to fluctuations in the Earth's magnetic field. The 2D matrix of FIDs acquired from the pseudo-2D experiment is first Fourier transformed to generate a 2D matrix of spectra. The built-in 'phase2D' Prospa procedure is then used to auto-phase a user-selected peak that appears on all of the spectra in the 2D matrix, followed by the calculation of a frequency value for all the auto-phased peaks. The frequency shift is calculated by subtracting the maximum frequency value from the frequency of each peak. A  $1 \times n$  matrix (row x column) of zeros is then merged with each spectrum at the negative end of the two-sided spectrum to shift the spectra along the frequency axis and align it with the spectrum that experienced the largest Larmor frequency shift. To maintain the number of data points as a power of 2, the number of zeros added to each spectrum is deleted on the positive end of the two-sided spectrum.

## 9.4 Benchtop NMR Data Acquisition and Processing

All benchtop NMR experiments were performed on a Magritek Spinsolve 43 MHz benchtop NMR spectrometer (1 T). The NMR pulse programs were setup and run on the SpinsolveExpert (version 1.30) software from a controlling PC. Post processing was carried out using SpinsolveExpert and Prospa.

## 9.5 NMR Simulations

NMR simulations were acquired using Matlab (version R2020a) and the Spinach library<sup>122</sup> (version 2.4.5157). Many of the user inputs required to run and acquire the NMR simulations using Spinach were specific to the target molecule. These include the list of isotopes, their chemical shifts and the  $J$ -coupling interactions of each isotope on the substrate coupling network, all of which were different for 3-FP, 3,5-DFP, 3,5-TFMP and 3-DFMP. The chemical shift values were only necessary for high-field NMR simulations and hence were zeroed for the EFNMR simulations. The experimental parameters such as the external field strength, offset frequency, sweep width and number of points in the FID were extracted from experimental files of the spectra to be compared. For simulations based on EFNMR and benchtop NMR experiments run on Prospa with the Magritek instruments (Terranova-MRI and Spinsolve) the experimental parameters were imported from the 'acqu.par' file saved during each experiment using a simple 'cell2mat' Matlab function. Simulations based on high-field NMR experiments run on Topspin used the RBNMR Matlab function<sup>146</sup> designed to read and import Bruker NMR data into Matlab.

NMR parameters such as those to define the spin density matrix and the simulated RF pulse sequence also were required. All EFNMR simulations were acquired with the 'hp\_acquire' Matlab function from the Spinach library which replicates a pulse( $\pi/2$ )-acquire NMR experiment. The function was run with a  $\pi/2_x$  RF pulse, where the phase

was defined as  $\hat{\mathbf{I}}_{\mathbf{x}} = (\hat{\mathbf{I}}^+ + \hat{\mathbf{I}}^-)/2$ , and the flip angle defined as  $\pi/2$  radians. Coherence selection within this function, as well as more complex RF pulse sequences, were not utilised in this work. The starting and detection state of the spin density matrix for each simulation is indicated in the main text. For example, the interpretation of the SABRE-polarised  $^1\text{H}$  and  $^{19}\text{F}$  EFNMR signals in Chapters 5 and 6 required the acquisition of individual nuclei or isotopes, but were generally acquired with  $\rho_0 = \sum_i \mathbf{I}_{zi}$  for all isotopes. All high-field NMR simulations were acquired with the 'acquire' Matlab function from the Spinach library which replicates NMR acquisition and therefore requires a starting state of  $\rho_0 = \sum_i \mathbf{I}^+$  for all isotopes. All EFNMR and high-field NMR simulations were run with the detection of (-1) quantum coherence via  $\hat{\mathbf{I}}_{obs} = \sum_i \mathbf{I}_i^-$ , to accurately simulate NMR acquisition.

Spinach functions to define base symmetry groups on the molecule were utilised to reduce the simulation time of 3,5-TFMP as it contains 9 spins. The functions were used with the following commands:

```
bas.sym_group=('S3'),('S3');
bas.sym_spins=[2 3 4],[6 7 8];
```

where the two 'S3' values and the two sets of numbers [2, 3, 4] and [6 7 8] refer to the 3 magnetic equivalent  $^{19}\text{F}$  nuclei in both  $\text{CF}_3$  functional groups of 3,5-TFMP.

The high-field and EFNMR simulations were also run with different parameters. One difference was the assumption argument that is used for the 'liquid' Matlab function from the Spinach library which carries out the NMR experiment under the chosen NMR pulse sequence and user defined spin system and experimental parameters. For high-field and EFNMR simulations the assumption is set to 'nmr' and 'labframe', respectively. The 'nmr' assumption runs the simulation with simplified spin dynamics (e.g. secular approximation of the Hamiltonian operator, rotating frame approximations, etc.), whereas the 'labframe' assumption does not utilise any simplifications (e.g. full Hamiltonian operator, laboratory frame, etc.). Another difference is that high-field NMR simulations require defining a single isotope for 'parameter.spins' with a corresponding 'parameters.offset' value to mimic high-field NMR acquisition where one RF channel is assigned to each nuclear species. Since the Terranova-MRI probe contains a single RF channel and NMR acquisition of  $^1\text{H}$  and  $^{19}\text{F}$  is simultaneous, the EFNMR simulations were run with both  $^1\text{H}$  and  $^{19}\text{F}$  defined for 'parameter.spins'. This must be followed by defining 'parameters.offset' as a 1x2 array, with each value corresponding to each spin, to prevent an error. The offset value sets the middle of the spectrum, therefore the same value was given to each nucleus.

The remainder of the Spinach code to define the basis set and the nuclear spin system is shown below:

```
bas.formalism='sphten-liouv';
bas.approximation='IK-2';
bas.connectivity='scalar_couplings';
bas.space_level=1;
```

Parameters for definition of relaxation in the nuclear spin system is made available to the user in the Spinach library but was not utilised for any of the simulations.

## List of Abbreviations

3,5-DFP	3,5-difluoropyridine.
3,5-TFMP	3,5-bis(trifluoromethyl)pyridine.
3-DFMP	3-difluoromethylpyridine.
3-FP	3-fluoropyridine.
AF	Audio Frequency.
COD	cis,cis-1,5-cyclooctadiene.
CSV	Comma Separated Values.
DNP	Dynamic Nuclear Polarisation.
EFNMR	Earth's Field NMR.
EPR	Electron Paramagnetic Resonance.
FEP	Fluorinated Ethylene Propylene.
FID	Free Induction Decay.
FWHM	Full Width Half Maximum.
IMes	1,3-bis(2,4,6-trimethylphenyl)imidazol-2-ylidene.
LAC	Level Anti-Crossing.
MRI	Magnetic Resonance Imaging.
NHC	N-Heterocyclic Carbene.
NMR	Nuclear magnetic resonance.
PFG	Pulsed Field Gradient.
PHIP	<i>Para</i> -Hydrogen Induced Polarisation.
PTC	Polarisation Transfer Condition.
PTF	Polarisation Transfer Field.
RF	Radio Frequency.
RMS	Root Mean Square.
SABRE	Signal Amplification By Reversible Exchange.

SABRE-SHEATH	SABRE in SHield Enables Alignment Transfer to Heteronuclei.
sel-SHARPER	selective-SHARPER.
SEOP	Spin-Exchange Optical Pumping.
SNR	Signal to Noise Ratio.
SPFGSE	Single Pulsed Field Gradient Spin-Echo.
TFE	2,2,2-trifluoroethanol.
TMS	Tetramethylsilane.
TTL	Transistor-Transistor Logic.
ULF	Ultra-Low-Field.

# Bibliography

- [1] Magritek. Terranova-MRI EFNMR User’s Manual. Technical report, Magritek Limited, 2005.
- [2] Alexandra M. Olaru, Thomas B.R. Robertson, Jennifer S. Lewis, Alex Antony, Wissam Iali, Ryan E. Mewis, and Simon B. Duckett. Extending the Scope of  $^{19}\text{F}$  Hyperpolarization through Signal Amplification by Reversible Exchange in MRI and NMR Spectroscopy. *ChemistryOpen*, 7(1):97–105, 1 2017.
- [3] Ariana B. Jones, Guy C. Lloyd-Jones, and Dušan Uhrín. SHARPER Reaction Monitoring: Generation of a Narrow Linewidth NMR Singlet, without X-Pulses, in an Inhomogeneous Magnetic Field. *Analytical Chemistry*, 89(18):10013–10021, 9 2017.
- [4] A. McDowell and E. Fukushima. Ultracompact NMR:  $^1\text{H}$  Spectroscopy in a Subkilogram Magnet. *Applied Magnetic Resonance 2008 35:1*, 35(1):185–195, 11 2008.
- [5] Vasiliki Demas and Pablo J. Prado. Compact magnets for magnetic resonance. *Concepts in Magnetic Resonance Part A*, 34A(1):48–59, 1 2009.
- [6] Ernesto Danieli, Juan Perlo, Bernhard Blümich, Federico Casanova, E Danieli, J Perlo, B Blümich, and F Casanova. Small Magnets for Portable NMR Spectrometers. *Angewandte Chemie International Edition*, 49(24):4133–4135, 6 2010.
- [7] Thomas Castaing-Cordier, Dylan Bouillaud, Jonathan Farjon, and Patrick Girardeau. Recent advances in benchtop NMR spectroscopy and its applications. *Annual Reports on NMR Spectroscopy*, 103:191–258, 1 2021.
- [8] Bernhard Blümich. Low-field and benchtop NMR. *Journal of Magnetic Resonance*, 306:27–35, 9 2019.
- [9] Simon K. Küster, Ernesto Danieli, Bernhard Blümich, and Federico Casanova. High-resolution NMR spectroscopy under the fume hood. *Physical Chemistry Chemical Physics*, 13(29):13172–13176, 7 2011.
- [10] Alina Adams. Non-destructive analysis of polymers and polymer-based materials by compact NMR. *Magnetic Resonance Imaging*, 56:119–125, 2 2019.
- [11] Anton Duchowny, Oliver Mohnke, Holger Thern, Pablo Matias Dupuy, Hege Christin Widerøe, Audun Faanes, Anfinn Paulsen, Markus Küppers, Bernhard Blümich, and Alina Adams. Composition analysis of natural gas by

- combined benchtop NMR spectroscopy and mechanistical multivariate regression. *Energy Reports*, 8:3661–3670, 11 2022.
- [12] David S. Wishart. Quantitative metabolomics using NMR. *TrAC Trends in Analytical Chemistry*, 27(3):228–237, 3 2008.
- [13] Abdul Hamid Emwas, Raja Roy, Ryan T. McKay, Leonardo Tenori, Edoardo Saccenti, G. A. Nagana Gowda, Daniel Raftery, Fatimah Alahmari, Lukasz Jaremko, Mariusz Jaremko, and David S. Wishart. NMR Spectroscopy for Metabolomics Research. *Metabolites 2019, Vol. 9, Page 123*, 9(7):123, 6 2019.
- [14] Lloyd Lumata, Zoltan Kovacs, Craig Malloy, A Abragam, and M Goldman. Reports on Progress in Physics Principles of dynamic nuclear polarisation A Abragdm and M Goldman. *Rep. Prog. Phys*, 41, 1978.
- [15] Jan H. Ardenkjær-Larsen, Björn Fridlund, Andreas Gram, Georg Hansson, Lennart Hansson, Mathilde H. Lerche, Rolf Servin, Mikkel Thaning, and Klaes Golman. Increase in signal-to-noise ratio of  $> 10,000$  times in liquid-state } NMR. *Proceedings of the National Academy of Sciences of the United States of America*, 100(18):10158, 9 2003.
- [16] Thad G. Walker and William Happer. Spin-exchange optical pumping of noble-gas nuclei. *Reviews of Modern Physics*, 69(2):629, 4 1997.
- [17] Boyd M. Goodson. Nuclear Magnetic Resonance of Laser-Polarized Noble Gases in Molecules, Materials, and Organisms. *Journal of Magnetic Resonance*, 155(2):157–216, 4 2002.
- [18] John P. Mugler and Talissa A. Altes. Hyperpolarized  $^{129}\text{Xe}$  MRI of the human lung. *Journal of Magnetic Resonance Imaging*, 37(2):313–331, 2 2013.
- [19] M. A. Bouchiat, T. R. Carver, and C. M. Varnum. Nuclear Polarization in  $^3\text{He}$  Gas Induced by Optical Pumping and Dipolar Exchange. *Physical Review Letters*, 5(8):373, 10 1960.
- [20] Thomas C. Eisenschmid, Rein U. Kirss, Paul P. Deutsch, Sven I. Hommeltoft, Richard Eisenberg, Joachim Bargon, Ronald G. Lawler, and Alan L. Balch. Para Hydrogen Induced Polarization in Hydrogenation Reactions. *Journal of the American Chemical Society*, 109(26):8089–8091, 12 1987.
- [21] Lars T. Kuhn and Joachim Bargon. Transfer of parahydrogen-induced hyperpolarization to heteronuclei. *Topics in Current Chemistry*, 276:25–68, 2007.
- [22] Roman V. Shchepin, Aaron M. Coffey, Kevin W. Waddell, and Eduard Y. Chekmenev. PASADENA hyperpolarized  $^{13}\text{C}$  phospholactate. *Journal of the American Chemical Society*, 134(9):3957–3960, 3 2012.
- [23] Eleonora Cavallari, Carla Carrera, Silvio Aime, and Francesca Reineri. Studies to enhance the hyperpolarization level in PHIP-SAH-produced  $^{13}\text{C}$ -pyruvate. *Journal of Magnetic Resonance*, 289:12–17, 4 2018.

- [24] C. Russell Bowers and Daniel P. Weitekamp. Transformation of Symmetrization Order to Nuclear-Spin Magnetization by Chemical Reaction and Nuclear Magnetic Resonance. *Physical Review Letters*, 57(21):2645, 11 1986.
- [25] Qingxia Gong, Ali Gordji-Nejad, Bernhard Blümich, and Stephan Appelt. Trace analysis by low-field NMR: Breaking the sensitivity limit. *Analytical Chemistry*, 82(17):7078–7082, 9 2010.
- [26] Kevin W. Waddell, Aaron M. Coffey, and Eduard Y. Chekmenev. In situ detection of PHIP at 48 mT: Demonstration using a centrally controlled polarizer. *Journal of the American Chemical Society*, 133(1):97–101, 1 2011.
- [27] Stephan Berner, Andreas B. Schmidt, Frowin Ellermann, Sergey Korchak, Eduard Y. Chekmenev, Stefan Glöggler, Dominik von Elverfeldt, Jürgen Hennig, and Jan Bernd Hövener. High field para hydrogen induced polarization of succinate and phospholactate. *Physical Chemistry Chemical Physics*, 23(3):2320–2330, 1 2021.
- [28] Keunhong Jeong, Soonmo Kwon, Sein Min, Heelim Chae, and Sung Keon Namgoong. Low Cost and Portable Parahydrogen Generator for the PHIP. *Journal of the Korean Magnetic Resonance Society*, 21(4):126–130, 2017.
- [29] Benjamin Chapman, Baptiste Joalland, Collier Meersman, Jessica Ettetdgui, Rolf E. Swenson, Murali C. Krishna, Panayiotis Nikolaou, Kirill V. Kovtunov, Oleg G. Salnikov, Igor V. Koptuyug, Max E. Gemeinhardt, Boyd M. Goodson, Roman V. Shchepin, and Eduard Y. Chekmenev. Low-Cost High-Pressure Clinical-Scale 50% Parahydrogen Generator Using Liquid Nitrogen at 77 K. *Analytical Chemistry*, 93(24):8476–8483, 6 2021.
- [30] Yash Mhaske, Elodie Sutter, James Daley, Christopher Mahoney, and Nicholas Whiting. 65% Parahydrogen from a liquid nitrogen cooled generator. *Journal of Magnetic Resonance*, 341:107249, 8 2022.
- [31] Ralph W. Adams, Juan A. Aguilar, Kevin D. Atkinson, Michael J. Cowley, Paul I.P. Elliott, Simon B. Duckett, Gary G.R. Green, Iman G. Khazal, Joaquin Lopez-Serrano, and David C. Williamson. Reversible interactions with parahydrogen enhance NMR sensitivity by polarization transfer. *Science (New York, N. Y.)*, 323(5922):1708–1711, 3 2009.
- [32] Philip Norcott, Michael J. Burns, Peter J. Rayner, Ryan E. Mewis, and Simon B. Duckett. Using  $^2\text{H}$  labelling to improve the NMR detectability of pyridine and its derivatives by SABRE. *Magnetic Resonance in Chemistry*, 56(7):663–671, 7 2018.
- [33] Haifeng Zeng, Jiadi Xu, Joseph Gillen, Michael T. McMahon, Dmitri Artemov, Jean Max Tyburn, Joost A.B. Lohman, Ryan E. Mewis, Kevin D. Atkinson, Gary G.R. Green, Simon B. Duckett, and Peter C.M. Van Zijl. Optimization of SABRE for polarization of the tuberculosis drugs pyrazinamide and isoniazid. *Journal of Magnetic Resonance*, 237:73–78, 12 2013.

- [34] Stefan Glögger, Rafael Müller, Johannes Colell, Meike Emondts, Martin Dabrowski, Bernhard Blümich, and Stephan Appelt. Para-hydrogen induced polarization of amino acids, peptides and deuterium – hydrogen gas. *Physical Chemistry Chemical Physics*, 13(30):13759–13764, 7 2011.
- [35] Ryan E. Mewis, Richard A. Green, Martin C.R. Cockett, Michael J. Cowley, Simon B. Duckett, Gary G.R. Green, Richard O. John, Peter J. Rayner, and David C. Williamson. Strategies for the hyperpolarization of acetonitrile and related Ligands by SABRE. *Journal of Physical Chemistry B*, 119(4):1416–1424, 1 2015.
- [36] Soumya S. Roy, Philip Norcott, Peter J. Rayner, Gary G.R. Green, and Simon B. Duckett. A Simple Route to Strong Carbon-13 NMR Signals Detectable for Several Minutes. *Chemistry – A European Journal*, 23(44):10496–10500, 8 2017.
- [37] Nikita V. Chukanov, Oleg G. Salnikov, Roman V. Shchepin, Alexandra Svyatova, Kirill V. Kovtunov, Igor V. Koptuyug, and Eduard Y. Chekmenev. 19F Hyperpolarization of 15N-3-19F-Pyridine via Signal Amplification by Reversible Exchange. *Journal of Physical Chemistry C*, 122(40):23002–23010, 10 2018.
- [38] Vladimir V. Zhivonitko, Ivan V. Skovpin, and Igor V. Koptuyug. Strong 31P nuclear spin hyperpolarization produced via reversible chemical interaction with parahydrogen. *Chemical Communications*, 51(13):2506–2509, 1 2015.
- [39] Milton L. Truong, Thomas Theis, Aaron M. Coffey, Roman V. Shchepin, Kevin W. Waddell, Fan Shi, Boyd M. Goodson, Warren S. Warren, and Eduard Y. Chekmenev. 15N Hyperpolarization by Reversible Exchange Using SABRE-SHEATH. *Journal of Physical Chemistry C*, 119(16):8786–8797, 4 2015.
- [40] Roman V Shchepin, Danila A Barskiy, Aaron M Coffey, Boyd M Goodson, Eduard Y Chekmenev, R V Shchepin, D A Barskiy, A M Coffey, and E Y Chekmenev. NMR Signal Amplification by Reversible Exchange of Sulfur-Heterocyclic Compounds Found In Petroleum. *ChemistrySelect*, 1(10):2552–2555, 7 2016.
- [41] Alexandra M. Olaru, Alister Burt, Peter J. Rayner, Sam J. Hart, Adrian C. Whitwood, Gary G.R. Green, and Simon B. Duckett. Using signal amplification by reversible exchange (SABRE) to hyperpolarise 119 Sn and 29 Si NMR nuclei. *Chemical Communications*, 52(100):14482–14485, 12 2016.
- [42] Daniel A. Taylor, Louise S. Natrajan, Mathias Nilsson, and Ralph W. Adams. SABRE-enhanced real-time pure shift NMR spectroscopy. *Magnetic Resonance in Chemistry*, 59(12):1244–1252, 12 2021.
- [43] Ana S. Terra, Matheus Rossetto, Claire L. Dickinson, George Peat, Dusan Uhrin, and Meghan E. Halse. SABRE-SHARPER: Enhancing 19F benchtop NMR by combining hyperpolarisation and multiplet refocusing. *Submitted*, 2022.
- [44] Olga Semenova, Peter M. Richardson, Andrew J. Parrott, Alison Nordon, Meghan E. Halse, and Simon B. Duckett. Reaction Monitoring Using SABRE-Hyperpolarized Benchtop (1 T) NMR Spectroscopy. *Analytical Chemistry*, 91(10):6695–6701, 5 2019.

- [45] Peter J. Rayner, Marianna Fekete, Callum A. Gater, Fadi Ahwal, Norman Turner, Aneurin J. Kennerley, and Simon B. Duckett. Real-Time High-Sensitivity Reaction Monitoring of Important Nitrogen-Cycle Synthons by  $^{15}\text{N}$  Hyperpolarized Nuclear Magnetic Resonance. *Journal of the American Chemical Society*, 144, 2022.
- [46] Thomas Tennant, Matthew C. Hulme, Thomas B.R. Robertson, Oliver B. Sutcliffe, and Ryan E. Mewis. Benchtop NMR analysis of piperazine-based drugs hyperpolarised by SABRE. *Magnetic Resonance in Chemistry*, 58(12):1151–1159, 12 2020.
- [47] Nan Eshuis, Bram J A van Weerdenburg, Martin C Feiters, Floris P J T Rutjes, Sybren S Wijmenga, Marco Tessari, N Eshuis, B J A van Weerdenburg, M C Feiters, F P J T Rutjes, S S Wijmenga, and M Tessari. Quantitative Trace Analysis of Complex Mixtures Using SABRE Hyperpolarization. *Angewandte Chemie*, 127(5):1501–1504, 1 2015.
- [48] Wissam Iali, Peter J. Rayner, and Simon B. Duckett. Using parahydrogen to hyperpolarize amines, amides, carboxylic acids, alcohols, phosphates, and carbonates. *Science Advances*, 4(1), 1 2018.
- [49] Anand Manoharan, Peter J. Rayner, Marianna Fekete, Wissam Iali, Philip Norcott, V. Hugh Perry, and Simon B. Duckett. Catalyst-Substrate Effects on Biocompatible SABRE Hyperpolarization. *ChemPhysChem*, 20(2):285–294, 1 2019.
- [50] Anand Manoharan, Peter J. Rayner, Wissam Iali, Michael J. Burns, V. Hugh Perry, and Simon B. Duckett. Achieving Biocompatible SABRE: An invitro Cytotoxicity Study. *ChemMedChem*, 13(4):352–359, 2 2018.
- [51] Jan Bernd Hövener, Niels Schwaderlapp, Thomas Lickert, Simon B. Duckett, Ryan E. Mewis, Louise A.R. Highton, Stephen M. Kenny, Gary G.R. Green, Dieter Leibfritz, Jan G. Korvink, Jürgen Hennig, and Dominik Von Elverfeldt. A hyperpolarized equilibrium for magnetic resonance. *Nature Communications* 2013 4:1, 4(1):1–5, 12 2013.
- [52] Wissam Iali, Soumya S. Roy, Ben J. Tickner, Fadi Ahwal, Aneurin J. Kennerley, and Simon B. Duckett. Hyperpolarising Pyruvate through Signal Amplification by Reversible Exchange (SABRE). *Angewandte Chemie*, 131(30):10377–10381, 7 2019.
- [53] Elizabeth J. Fear, Aneurin J. Kennerley, Peter J. Rayner, Philip Norcott, Soumya S. Roy, and Simon B. Duckett. SABRE hyperpolarized anticancer agents for use in  $^1\text{H}$  MRI. *Magnetic Resonance in Medicine*, 88(1):11–27, 7 2022.
- [54] Andrey N. Pravdivtsev, Alexandra V. Yurkovskaya, Hans Martin Vieth, Konstantin L. Ivanov, and Robert Kaptein. Level anti-crossings are a key factor for understanding para-hydrogen-induced hyperpolarization in SABRE experiments. *ChemPhysChem*, 14(14):3327–3331, 10 2013.

- [55] Thomas Theis, Milton L. Truong, Aaron M. Coffey, Roman V. Shchepin, Kevin W. Waddell, Fan Shi, Boyd M. Goodson, Warren S. Warren, and Eduard Y. Chekmenev. Microtesla SABRE enables 10% nitrogen-15 nuclear Spin polarization. *Journal of the American Chemical Society*, 137(4):1404–1407, 2 2015.
- [56] Andrey N Pravdivtsev, Konstantin L Ivanov, Alexandra V Yurkovskaya, Pavel A Petrov, Hans-Heinrich Limbach, Robert Kaptein, and Hans-Martin Vieth. Spin polarization transfer mechanisms of SABRE: A magnetic field dependent study. *Journal of Magnetic Resonance*, 261:73–82, 2015.
- [57] Peter M. Richardson, Scott Jackson, Andrew J. Parrott, Alison Nordon, Simon B. Duckett, and Meghan E. Halse. A simple hand-held magnet array for efficient and reproducible SABRE hyperpolarisation using manual sample shaking. *Magnetic Resonance in Chemistry*, 56(7):641–650, 7 2018.
- [58] Ben J. Tickner, Olga Semenova, Wissam Iali, Peter J. Rayner, Adrian C. Whitwood, and Simon B. Duckett. Optimisation of pyruvate hyperpolarisation using SABRE by tuning the active magnetisation transfer catalyst. *Catalysis Science & Technology*, 10(5):1343–1355, 3 2020.
- [59] Lyrelle S Lloyd, Ralph W Adams, Michael Bernstein, Steven Coombes, Simon B Duckett, Gary G R Green, Richard J Lewis, Ryan E Mewis, and Christopher J Sleight. Utilization of SABRE-Derived Hyperpolarization To Detect Low-Concentration Analytes via 1D and 2D NMR Methods. *Journal of the American Chemical Society*, 2012.
- [60] Ryan E. Mewis, Kevin D. Atkinson, Michael J. Cowley, Simon B. Duckett, Gary G.R. Green, Richard A. Green, Louise A.R. Highton, David Kilgour, Lyrelle S. Lloyd, Joost A.B. Lohman, and David C. Williamson. Probing signal amplification by reversible exchange using an NMR flow system. *Magnetic Resonance in Chemistry*, 52(7):358–369, 7 2014.
- [61] Peter M Richardson, Andrew J Parrott, Olga Semenova, Alison Nordon, Simon B Duckett, and Meghan E Halse. SABRE hyperpolarization enables high-sensitivity 1 H and 13 C benchtop NMR spectroscopy. *Analyst*, 143:3442, 2018.
- [62] Petr Štěpánek, Clara Sanchez-Perez, Ville Veikko Telkki, Vladimir V. Zhivonitko, and Anu M. Kantola. High-throughput continuous-flow system for SABRE hyperpolarization. *Journal of Magnetic Resonance*, 300:8–17, 3 2019.
- [63] Patrick TomHon, Evan Akeroyd, Sören Lehmkuhl, Eduard Y. Chekmenev, and Thomas Theis. Automated pneumatic shuttle for magnetic field cycling and parahydrogen hyperpolarized multidimensional NMR. *Journal of Magnetic Resonance*, 312:106700, 3 2020.
- [64] Thomas Theis, Milton Truong, Aaron M. Coffey, Eduard Y. Chekmenev, and Warren S. Warren. LIGHT-SABRE enables efficient in-magnet catalytic hyperpolarization. *Journal of Magnetic Resonance*, 248:23–26, 11 2014.

- [65] Andrey N. Pravdivtsev, Alexandra V. Yurkovskaya, Hans Martin Vieth, and Konstantin L. Ivanov. RF-SABRE: A Way to Continuous Spin Hyperpolarization at High Magnetic Fields. *Journal of Physical Chemistry B*, 119(43):13619–13629, 10 2015.
- [66] Andrey N. Pravdivtsev, Alexandra V. Yurkovskaya, Herbert Zimmermann, Hans Martin Vieth, and Konstantin L. Ivanov. Transfer of SABRE-derived hyperpolarization to spin-1/2 heteronuclei. *RSC Advances*, 5(78):63615–63623, 7 2015.
- [67] Bernhard Blümich, Federico Casanova, Juan Perlo, Sophia Anferova, Vladimir Anferov, Kai Kremer, Nicolae Goga, Klaus Kupferschläger, and Michael Adams. Advances of unilateral mobile NMR in nondestructive materials testing. *Magnetic Resonance Imaging*, 23(2):197–201, 2 2005.
- [68] Dimitris Sakellariou, Carlos A. Meriles, and Alexander Pines. Advances in ex-situ Nuclear Magnetic Resonance. *Comptes Rendus Physique*, 5(3):337–347, 4 2004.
- [69] Martin Packard and Russell Varian. Free nuclear induction in the earth’s magnetic field. *Physical Review*, 93:941, 1954.
- [70] P. T. Callaghan, R. Dykstra, C. D. Eccles, T. G. Haskell, and J. D. Seymour. A nuclear magnetic resonance study of Antarctic sea ice brine diffusivity. *Cold Regions Science and Technology*, 29(2):153–171, 8 1999.
- [71] Jeremy N. Robinson, Andrew Coy, Robin Dykstra, Craig D. Eccles, Mark W. Hunter, and Paul T. Callaghan. Two-dimensional NMR spectroscopy in Earth’s magnetic field. *Journal of Magnetic Resonance*, 182(2):343–347, 10 2006.
- [72] Meghan E. Halse, Andrew Coy, Robin Dykstra, Craig Eccles, Mark Hunter, Rob Ward, and Paul T. Callaghan. A practical and flexible implementation of 3D MRI in the Earth’s magnetic field. *Journal of Magnetic Resonance*, 182(1):75–83, 9 2006.
- [73] Danila A. Barskiy, Michael C.D. Tayler, Irene Marco-Rius, John Kurhanewicz, Daniel B. Vigneron, Sevil Cikrikci, Ayca Aydogdu, Moritz Reh, Andrey N. Pravdivtsev, Jan Bernd Hövener, John W. Blanchard, Teng Wu, Dmitry Budker, and Alexander Pines. Zero-field nuclear magnetic resonance of chemically exchanging systems. *Nature Communications 2019 10:1*, 10(1):1–9, 7 2019.
- [74] Seong-Joo Lee, Kiwoong Kim, Chan Seok Kang, Seong-min Hwang, and Yong-Ho Lee. Pre-polarization enhancement by dynamic nuclear polarization in SQUID-based }ultra-low-field nuclear magnetic resonance. *Superconductor Science and Technology*, 23(11):115008, 10 2010.
- [75] Matthew P. Augustine, Annjoe Wong-Foy, Jeffery L. Yarger, Marco Tomaselli, Alexander Pines, Dinh M. Tonthat, and John Clarke. Low field magnetic resonance images of polarized noble gases obtained with a dc superconducting quantum interference device. *Applied Physics Letters*, 72(15):1908, 6 1998.

- [76] V. V. Yashchuk, J. Granwehr, D. F. Kimball, S. M. Rochester, A. H. Trabesinger, J. T. Urban, D. Budker, and A. Pines. Hyperpolarized xenon nuclear spins detected by optical atomic magnetometry. *Physical Review Letters*, 93(16):160801, 10 2004.
- [77] Daniel J. Kennedy, Scott J. Seltzer, Ricardo Jiménez-Martínez, Hattie L. Ring, Nicolas S. Malecek, Svenja Knappe, Elizabeth A. Donley, John Kitching, Vikram S. Bajaj, and Alexander Pines. An optimized microfabricated platform for the optical generation and detection of hyperpolarized  $^{129}\text{Xe}$ . *Scientific Reports* 2017 7:1, 7(1):1–10, 3 2017.
- [78] T. Theis, P. Ganssle, G. Kervern, S. Knappe, J. Kitching, M. P. Ledbetter, D. Budker, and A. Pines. Parahydrogen-enhanced zero-field nuclear magnetic resonance. *Nature Physics* 2011 7:7, 7(7):571–575, 5 2011.
- [79] John W. Blanchard, Teng Wu, James Eills, Yinan Hu, and Dmitry Budker. Zero-to ultralow-field nuclear magnetic resonance J-spectroscopy with commercial atomic magnetometers. *Journal of Magnetic Resonance*, 314:106723, 5 2020.
- [80] H. J. Bernstein, J. A. Pople, and W. G. Schneider. THE ANALYSIS OF NUCLEAR MAGNETIC RESONANCE SPECTRA: I. SYSTEMS OF TWO AND THREE NUCLEI. *Canadian Journal of Chemistry*, 35(1):65–81, 1 1957.
- [81] Andrei N. Matlachov, Petr L. Volegov, Michelle A. Espy, John S. George, and Robert H. Kraus. SQUID detected NMR in microtesla magnetic fields. *Journal of Magnetic Resonance*, 170(1):1–7, 9 2004.
- [82] Stephan Appelt, F. Wolfgang Häsing, Holger Kühn, Ulrich Sieling, and Bernhard Blümich. Analysis of molecular structures by homo- and hetero-nuclear J-coupled NMR in ultra-low field. *Chemical Physics Letters*, 440(4-6):308–312, 6 2007.
- [83] A. Farkas. Orthohydrogen, parahydrogen and heavy hydrogen. *Cambridge University Press*, 1935.
- [84] Peter M. Richardson, Richard O. John, Andrew J. Parrott, Peter J. Rayner, Wissam Iali, Alison Nordon, Meghan E. Halse, and Simon B. Duckett. Quantification of hyperpolarisation efficiency in SABRE and SABRE-Relay enhanced NMR spectroscopy. *Physical Chemistry Chemical Physics*, 20(41):26362–26371, 10 2018.
- [85] J. Jugel, G. M. Schwab, and J. Voitländer. Magnetocatalytic effect on rare earth oxides. *The Journal of Chemical Physics*, 78(7):4755, 8 1998.
- [86] D. H. Weitzel and O. E. Park. Iron Catalyst for Production of Liquid parahydrogen. *Review of Scientific Instruments*, 27(1):57, 12 2004.
- [87] R. Eldo Svadlenak and Allen B. Scott. The Conversion of Ortho- to Parahydrogen on Iron Oxide-Zinc Oxide Catalysts. *Journal of the American Chemical Society*, 79(20):5385–5388, 1957.
- [88] K. F. Bonhoeffer and P. Harteck. About Para- and Orthohydrogen. *Zeitschrift für Physikalische Chemie*, 4B(1):113–141, 6 1929.

- [89] G. E. Schmauch and A. H. Singleton. Technical aspects of ortho-parahydrogen conversion. *Industrial and Engineering Chemistry*, 56(5):20–31, 5 1964.
- [90] Bibo Feng, Aaron M. Coffey, Raul D. Colon, Eduard Y. Chekmenev, and Kevin W. Waddell. A pulsed injection parahydrogen generator and techniques for quantifying enrichment. *Journal of magnetic resonance (San Diego, Calif. : 1997)*, 214(1):258–262, 1 2012.
- [91] Ronald M. Bliesner, Jacob W. Leachman, and Patrick M. Adam. Parahydrogen–Orthohydrogen Conversion for Enhanced Vapor-Cooled Shielding of Liquid Oxygen Tanks. <https://doi.org/10.2514/1.T4366>, 28(4):717–723, 10 2014.
- [92] Zhao Yanxing, Gong Maoqiong, Zhou Yuan, Dong Xueqiang, and Shen Jun. Thermodynamics analysis of hydrogen storage based on compressed gaseous hydrogen, liquid hydrogen and cryo-compressed hydrogen. *International Journal of Hydrogen Energy*, 44(31):16833–16840, 6 2019.
- [93] Richard A. Green, Ralph W. Adams, Simon B. Duckett, Ryan E. Mewis, David C. Williamson, and Gary G.R. Green. The theory and practice of hyperpolarization in magnetic resonance using parahydrogen. *Progress in Nuclear Magnetic Resonance Spectroscopy*, 67:1–48, 11 2012.
- [94] Kevin D. Atkinson, Michael J. Cowley, Paul I.P. Elliott, Simon B. Duckett, Gary G.R. Green, Joaquín López-Serrano, and Adrian C. Whitwood. Spontaneous transfer of Parahydrogen derived spin order to pyridine at low magnetic field. *Journal of the American Chemical Society*, 131(37):13362–13368, 9 2009.
- [95] Michael J. Cowley, Ralph W. Adams, Kevin D. Atkinson, Martin C.R. Cockett, Simon B. Duckett, Gary G.R. Green, Joost A.B. Lohman, Rainer Kerssebaum, David Kilgour, and Ryan E. Mewis. Iridium N-heterocyclic carbene complexes as efficient catalysts for magnetization transfer from para -hydrogen. *Journal of the American Chemical Society*, 133(16):6134–6137, 4 2011.
- [96] Bram J.A. van Weerdenburg, Stefan Glöggler, Nan Eshuis, A. H.T. Engwerda, Jan M.M. Smits, René de Gelder, Stephan Appelt, Sybren S. Wymenga, Marco Tessari, Martin C. Feiters, Bernhard Blümich, and Floris P.J.T. Rutjes. Ligand effects of NHC–iridium catalysts for signal amplification by reversible exchange (SABRE). *Chemical Communications*, 49(67):7388–7390, 7 2013.
- [97] Stephan Knecht, Andrey N. Pravdivtsev, Jan Bernd Hövener, Alexandra V. Yurkovskaya, and Konstantin L. Ivanov. Quantitative description of the SABRE process: rigorous consideration of spin dynamics and chemical exchange. *RSC Advances*, 6(29):24470–24477, 3 2016.
- [98] Danila A. Barskiy, Stephan Knecht, Alexandra V. Yurkovskaya, and Konstantin L. Ivanov. SABRE: Chemical kinetics and spin dynamics of the formation of hyperpolarization. *Progress in Nuclear Magnetic Resonance Spectroscopy*, 114–115:33–70, 10 2019.
- [99] Lyrelle S. Lloyd, Aziz Asghar, Michael J. Burns, Adrian Charlton, Steven Coombes, Michael J. Cowley, Gordon J. Dear, Simon B. Duckett, Georgi R.

Genov, Gary G.R. Green, Louise A.R. Highton, Alexander J.J. Hooper, Majid Khan, Iman G. Khazal, Richard J. Lewis, Ryan E. Mewis, Andrew D. Roberts, and Amy J. Ruddlesden. Hyperpolarisation through reversible interactions with parahydrogen. *Catalysis Science and Technology*, 4(10):3544–3554, 9 2014.

- [100] Danila A. Barskiy, Kirill V. Kovtunov, Igor V. Koptuyug, Ping He, Kirsten A. Groome, Quinn A. Best, Fan Shi, Boyd M. Goodson, Roman V. Shchepin, Aaron M. Coffey, Kevin W. Waddell, and Eduard Y. Chekmenev. The feasibility of formation and kinetics of NMR signal amplification by reversible exchange (SABRE) at high magnetic field (9.4 T). *Journal of the American Chemical Society*, 136(9):3322–3325, 3 2014.
- [101] Kate M. Appleby, Ryan E. Mewis, Alexandra M. Olaru, Gary G.R. Green, Ian J.S. Fairlamb, and Simon B. Duckett. Investigating pyridazine and phthalazine exchange in a series of iridium complexes in order to define their role in the catalytic transfer of magnetisation from para -hydrogen. *Chemical Science*, 6(7):3981–3993, 6 2015.
- [102] Peter J. Rayner, Michael J. Burns, Alexandra M. Olaru, Philip Norcott, Marianna Fekete, Gary G.R. Green, Louise A.R. Highton, Ryan E. Mewis, and Simon B. Duckett. Delivering strong  $^1\text{H}$  nuclear hyperpolarization levels and long magnetic lifetimes through signal amplification by reversible exchange. *Proceedings of the National Academy of Sciences of the United States of America*, 114(16):E3188–E3194, 4 2017.
- [103] Peter J. Rayner and Simon B. Duckett. Signal Amplification by Reversible Exchange (SABRE): From Discovery to Diagnosis. *Angewandte Chemie - International Edition*, 57(23):6742–6753, 6 2018.
- [104] Philipp Rovedo, Stephan Knecht, Tim Bäumlisberger, Anna Lena Cremer, Simon B. Duckett, Ryan E. Mewis, Gary G.R. Green, Michael Burns, Peter J. Rayner, Dieter Leibfritz, Jan G. Korvink, Jürgen Hennig, Gerhard Pütz, Dominik Von Elverfeldt, and Jan Bernd Hövener. Molecular MRI in the Earth’s Magnetic Field Using Continuous Hyperpolarization of a Biomolecule in Water. *Journal of Physical Chemistry B*, 120(25):5670–5677, 6 2016.
- [105] Nan Eshuis, Niels Hermkens, Bram J.A. Van Weerdenburg, Martin C. Feiters, Floris P.J.T. Rutjes, Sybren S. Wijmenga, and Marco Tessari. Toward nanomolar detection by NMR through SABRE hyperpolarization. *Journal of the American Chemical Society*, 136(7):2695–2698, 2 2014.
- [106] Fraser Hill-Casey, Aminata Sakho, Ahmed Mohammed, Matheus Rossetto, Fadi Ahwal, Simon B Duckett, Richard O John, Peter M Richardson, Robin Virgo, and Meghan E Halse. In Situ SABRE Hyperpolarization with Earth’s Field NMR Detection. *Molecules*, 24(22), 2019.
- [107] Philip Norcott, Peter J. Rayner, Gary G.R. Green, and Simon B. Duckett. Achieving High  $^1\text{H}$  Nuclear Hyperpolarization Levels with Long Lifetimes in a Range of Tuberculosis Drug Scaffolds. *Chemistry – A European Journal*, 23(67):16990–16997, 12 2017.

- [108] P. T. Callaghan, C. D. Eccles, T. G. Haskell, P. J. Langhorne, and J. D. Seymour. Earth's Field NMR in Antarctica: A Pulsed Gradient Spin Echo NMR Study of Restricted Diffusion in Sea Ice. *Journal of Magnetic Resonance*, 133(1):148–154, 1998.
- [109] P T Callaghan, A Coy, R Dykstra, C D Eccles, M E Halse, M W Hunter, O R Mercier, and J N Robinson. New Zealand Developments in Earth's Field NMR. *Appl. Magn. Reson*, 32:63–74, 2007.
- [110] Meghan E. Halse and Paul T. Callaghan. A dynamic nuclear polarization strategy for multi-dimensional Earth's field NMR spectroscopy. *Journal of Magnetic Resonance*, 195(2):162–168, 2008.
- [111] Meghan E. Halse, Paul T. Callaghan, Brett C. Feland, and Roderick E. Wasylshen. Quantitative analysis of Earth's field NMR spectra of strongly-coupled heteronuclear systems. *Journal of Magnetic Resonance*, 200(1):88–94, 9 2009.
- [112] Ryan E. Mewis. Developments and advances concerning the hyperpolarisation technique SABRE. *Magnetic Resonance in Chemistry*, 53(10):789–800, 10 2015.
- [113] Alastair F. Donaldson and Alice Miller. A Computational Group Theoretic Symmetry Reduction Package for the Model Checker. *Lecture Notes in Computer Science*, 4019:374–380, 2006.
- [114] Andrey N Pravdivtsev, Alexandra V Yurkovskaya, Herbert Zimmermann, Hans-Martin Vieth, and Konstantin L Ivanov. Transfer of SABRE-derived hyperpolarization to spin-1/2 heteronuclei †. *Royal Society of Chemistry*, 2015.
- [115] Alexandra Svyatova, Ivan V. Skovpin, Nikita V. Chukanov, Kirill V. Kovtunov, Eduard Y. Chekmenev, Andrey N. Pravdivtsev, Jan Bernd Hövener, and Igor V. Koptuyug. <sup>15</sup>N MRI of SLIC-SABRE Hyperpolarized <sup>15</sup>N-Labelled Pyridine and Nicotinamide. *Chemistry - A European Journal*, 25(36):8465–8470, 6 2019.
- [116] Jens Barkemeyer, Mathias Haake, and Joachim Bargon. Hetero-NMR Enhancement via Parahydrogen Labeling. *Journal of the American Chemical Society*, 117(10):2927–2928, 1995.
- [117] Lars T. Kuhn, Ute Bommerich, and Joachim Bargon. Transfer of parahydrogen-induced hyperpolarization to <sup>19</sup>F. *Journal of Physical Chemistry A*, 110(10):3521–3526, 3 2006.
- [118] Haukur Jóhannesson, Oskar Axelsson, and Magnus Karlsson. Transfer of parahydrogen spin order into polarization by diabatic field cycling. *Comptes Rendus Physique*, 5(3):315–324, 2004.
- [119] Eleonora Cavallari, Carla Carrera, Tommaso Boi, Silvio Aime, and Francesca Reineri. Effects of Magnetic Field Cycle on the Polarization Transfer from Parahydrogen to Heteronuclei through Long-Range J-Couplings. *Journal of Physical Chemistry B*, 119(31):10035–10041, 8 2015.
- [120] Mathias Haake, Johannes Natterer, and Joachim Bargon. Efficient NMR pulse sequences to transfer the parahydrogen-induced polarization to hetero nuclei. *Journal of the American Chemical Society*, 118(36):8688–8691, 9 1996.

- [121] Gabriele Stevanato, James Eills, Christian Bengs, and Giuseppe Pileio. A pulse sequence for singlet to heteronuclear magnetization transfer: S2hM. *Journal of Magnetic Resonance*, 277:169–178, 4 2017.
- [122] H. J. Hogben, M. Krzystyniak, G. T.P. Charnock, P. J. Hore, and Ilya Kuprov. Spinach – A software library for simulation of spin dynamics in large spin systems. *Journal of Magnetic Resonance*, 208(2):179–194, 2 2011.
- [123] Karlos X. Moreno, Khaled Nasr, Mark Milne, A. Dean Sherry, and Warren J. Goux. Nuclear spin hyperpolarization of the solvent using signal amplification by reversible exchange (SABRE). *Journal of Magnetic Resonance*, 257:15–23, 8 2015.
- [124] Roman V. Shchepin, Boyd M. Goodson, Thomas Theis, Warren S. Warren, and Eduard Y. Chekmenev. Toward Hyperpolarized <sup>19</sup>F Molecular Imaging via Reversible Exchange with Parahydrogen. *ChemPhysChem*, 18(15):1961–1965, 8 2017.
- [125] Victor Sans, Luzian Porwol, Vincenza Dragone, and Leroy Cronin. A self optimizing synthetic organic reactor system using real-time in-line NMR spectroscopy. *Chemical Science*, 6(2):1258–1264, 1 2015.
- [126] Paper P John Lowe, Ulrich Hintermair, Andrew M R Hall, Jonathan C Chouler, Anna Codina, Peter T Gierth, and John P Lowe. Practical aspects of real-time reaction monitoring using multi-nuclear high resolution FlowNMR spectroscopy. *Catalysis Science & Technology*, 6(24):8406–8417, 12 2016.
- [127] Christiane Schotten, Joseph L. Howard, Robert L. Jenkins, Anna Codina, and Duncan L. Browne. A continuous flow-batch hybrid reactor for commodity chemical synthesis enabled by inline NMR and temperature monitoring. *Tetrahedron*, 74(38):5503–5509, 9 2018.
- [128] Michel Goldbach, Ernesto Danieli, Juan Perlo, Bernard Kaptein, Victor M. Litvinov, Bernhard Blümich, Federico Casanova, and Alexander L.L. Duchateau. Preparation of Grignard reagents from magnesium metal under continuous flow conditions and on-line monitoring by NMR spectroscopy. *Tetrahedron Letters*, 57(1):122–125, 1 2016.
- [129] Bernhard Blümich and Kawarpal Singh. Desktop NMR and Its Applications From Materials Science To Organic Chemistry. *Angewandte Chemie International Edition*, 57(24):6996–7010, 6 2018.
- [130] Juan A Aguilar, Stephen Faulkner, Mathias Nilsson, Gareth A Morris, J A Aguilar, M Nilsson, G A Morris, and S Faulkner. Pure Shift 1H NMR: A Resolution of the Resolution Problem? *Angewandte Chemie International Edition*, 49(23):3901–3903, 5 2010.
- [131] Klaus Zangger. Pure shift NMR. *Progress in Nuclear Magnetic Resonance Spectroscopy*, 86-87:1–20, 4 2015.
- [132] Ralph W. Adams. Pure Shift NMR Spectroscopy. *eMagRes*, 3(4):295–310, 2014.

- [133] N. Helge Meyer and Klaus Zangger. Simplifying Proton NMR Spectra by Instant Homonuclear Broadband Decoupling. *Angewandte Chemie International Edition*, 52(28):7143–7146, 7 2013.
- [134] Munenori Inoue, Yuji Sumii, and Norio Shibata. Contribution of Organofluorine Compounds to Pharmaceuticals. *ACS Omega*, 5(19):10633–10640, 5 2020.
- [135] Yuta Ogawa, Etsuko Tokunaga, Osamu Kobayashi, Kenji Hirai, and Norio Shibata. Current Contributions of Organofluorine Compounds to the Agrochemical Industry. *iScience*, 23(9):101467, 9 2020.
- [136] Christopher Bauer, Ray Freeman, Tom Frenkiel, James Keeler, and A. J. Shaka. Gaussian Pulses. *Journal of Magnetic Resonance (1969)*, 58(3):442–457, 1984.
- [137] Nathan B. Ley, Michelle L. Rowe, Richard A. Williamson, and Mark J. Howard. Optimising selective excitation pulses to maximise saturation transfer difference NMR spectroscopy. *RSC Advances*, 4(14):7347–7351, 1 2014.
- [138] Danielle DiCara, Chiara Rapisarda, Julie L. Sutcliffe, Shelia M. Violette, Paul H. Weinreb, Ian R. Hart, Mark J. Howard, and John F. Marshall. Structure-Function Analysis of Arg-Gly-Asp Helix Motifs in  $\alpha\beta6$  Integrin Ligands. *Journal of Biological Chemistry*, 282(13):9657–9665, 3 2007.
- [139] Ray Freeman. Shaped radiofrequency pulses in high resolution NMR. *Progress in Nuclear Magnetic Resonance Spectroscopy*, 32(1):59–106, 2 1998.
- [140] S Watson. *Automated, quantitative process analysis by NMR*. PhD thesis, University Of Strathclyde, 2019.
- [141] Claire L. Dickson, George Peat, Matheus Rossetto, Meghan E. Halse, and Dušan Uhrín. SHARPER-enhanced benchtop NMR: improving SNR by removing couplings and approaching natural linewidths. *Chemical Communications*, 58(36):5534–5537, 5 2022.
- [142] Laurynas Dagys, Christian Bengs, Gamal A.I. Moustafa, and Malcolm H. Levitt. Deuteron-Decoupled Singlet NMR in Low Magnetic Fields: Application to the Hyperpolarization of Succinic Acid\*. *ChemPhysChem*, page e202200274, 2022.
- [143] Laurynas Dagys and Christian Bengs. Hyperpolarization read-out through rapidly rotating fields in the zero- and low-field regime. *Physical Chemistry Chemical Physics*, 24(14):8321–8328, 4 2022.
- [144] Olga Torres, Marta Martín, and Eduardo Sola. Labile N-heterocyclic carbene complexes of iridium. *Organometallics*, 28(3):863–870, 2 2009.
- [145] Peter J. Rayner, Philip Norcott, Kate M. Appleby, Wissam Iali, Richard O. John, Sam J. Hart, Adrian C. Whitwood, and Simon B. Duckett. Fine-tuning the efficiency of para-hydrogen-induced hyperpolarization by rational N-heterocyclic carbene design. *Nature Communications 2018 9:1*, 9(1):1–11, 10 2018.
- [146] N. Nyberg. RBNMR (<https://www.mathworks.com/matlabcentral/fileexchange/40332-rbnmr>), 9 2022.